(Photo)Electrochemical Performance Predictions and Electrocatalytic Measurements for Wastewater Nutrient Recovery and Solar Hydrogen Production

by

Luisa Barrera

A dissertation submitted in partial fulfillment
of the requirements for the degree of
Doctor of Philosophy
(Mechanical Engineering)
in the University of Michigan
2023

Doctoral Committee:

Assistant Professor Rohini Bala Chandran, Chair
Associate Professor Neil Dasgupta
Assistant Professor Nirala Singh
Professor Margaret Wooldridge

Luisa Barrera

luisab@umich.edu

ORCID iD: 0000-0002-5278-958X

Dedication

To my mom and dad, Anita and Rafael Barrera, for supporting me in everything that I do. Without them, none of this would have been possible. To my brother, Sebastian Barrera, for always believing in me. And to my partner, Alexis Prel, for his unbounded enthusiasm to talk all things science and his ability to always put a smile on my face.

Acknowledgements

I would like to thank first and foremost my advisor Rohini Bala Chandran. It’s been a privilege and an honor to work alongside you for the past five years, and I remain astounded by the depths of your knowledge in all the fields TREE Lab works on. How the group has grown so quickly and so well is a testament to your hard work, and I am excited to see what comes next.

I would also like to thank my committee members, Profs. Margaret Wooldridge, Neil Dasgupta, and Nirala Singh, for their guidance and support throughout my graduate studies. In addition, I would like to thank Profs. Shane Ardo, Daniel Esposito, and Steven Skerlos for their fantastic insight on the different projects I’ve worked on. Finally, I would also like to thank funding sources from the Department of Mechanical Engineering at University of Michigan and M-Cubed, as well as the Water Splitting Materials Consortium, established as part of the Energy Materials Network under the U.S. Department of Energy, Office of Energy Efficiency and Renewable Energy, Hydrogen and Fuel Cell Technologies Office, under Award Number DE-EE0008838.

I would especially like to thank TREE Lab as a whole: Bingjia, Bryan, Mike, Rachel, Zijie, and past members Erika, Aishwarya, Emily, and Kate. Having lived through the quiet and lonely first year where I was the only student in lab, I cannot fully express how happy it makes me to see the office crammed with 6 desks, with 3 conversations going on at once, and the adjoining laboratory space bustling with activity. If only I could tell first-year Luisa how good it was going to get! I am truly proud of how the lab has blossomed, and I hope that whoever joins next procrastibakes as well so group meetings remain well-stocked with sugary treats.

Grad school isn't easy, and I have gotten through thanks to caffeine, stubbornness, and, most importantly, friends. Truly, truly great friends. Thank you Jaclyn for being there for me and for letting me co-parent your cat. Thank you Rosa for being the sister of my heart, and allowing me to chill out with your dog whenever I needed it. Thank you Keara for the fantastic hugs and for always being ready to lend an ear, not to mention the countless drives to and from the airport. Thank you Andrea and Mario for showing me how to grad school those first few years and for reminding me that work isn't everything in life. Thank you Yves for making me laugh obnoxiously loud in the workplace. Thank you James for the remote IT help, and for putting up with my coding questions at any time of day. Thank you Connie for sharing my interest in books and bourbon. Thank you Cécile, Irina, Alex (Sailsman!), Isabel, Xitlali, Kelli, Fernanda, Colin, Abdiel, Lea, and Thelonia, for simply being in my life. We might not chat or hang out as often as I would like due to general busyness and geographic distance, but my life is infinitely richer from simply having met you.

Finally, I would like to thank my family. Thank you Mama for being my closest confidante and literally waking me up in the morning so I could make it to meetings on time. I would not have been able to do half the work I've done without you in my corner. Thank you Papa for your never-ending support and for leading by example. Thank you Bas for pushing me to go big and for reminding me not to take life too seriously. Thank you Zoe for always having good advice and for bringing good cheer to the family dinners. And thank you Alexis for the incredible trips, the heart-warming phone calls, and the overall willingness to listen to me rant about Butler-Volmer kinetics. You see me for who I truly am and I could not have gotten through the final stretch without your love and support. Thank you.

Table of Contents

Dedication ii

Acknowledgements iii

List of Tables viii

List of Figures x

List of Appendices xviii

Nomenclature xix

Abstract xxiii

Chapter 1 Introduction 1

1.1 Wastewater Resource Recovery 2

1.2 Photocatalytic Solar Water Splitting to Produce Hydrogen 6

1.3 Thesis Outline & Research Contributions 10

Chapter 2 Concentration, pH, and Polycrystalline Copper Electrode Surface Affects Nitrate Reduction Activity and Selectivity to Ammonia and Nitrite 13

2.1 Introduction 13

2.2 Experimental Set-up and Methods 16

2.2.1 Selection of NO_3^- Concentrations and pH Conditions 16

2.2.2 Reagents, Solution and Electrode Preparation 17

2.2.3 Cyclic Voltammetry 18

2.2.4 Chronoamperometry and Electrochemical Impedance Spectroscopy 20

2.2.5 Concentration Measurements for NO_3^-, NO_2^-, and NH_3 25

2.2.6 Error Quantification 27

2.2.7 Performance metrics 28

2.3 Results and Discussion 29

2.3.1 Concentration and pH Effects on Cu Disk Electrodes 29

2.3.2 Activity, Selectivity and Stability Measurements on Cu Planar Electrodes 38

2.3.3 Energy Intensity for NH_3 Recovery 44

2.3.4 Correlating Impedance Measurements with Trial-to-Trial Variations 47

2.4 Conclusion 50

Chapter 3 Harnessing Photoelectrochemistry for Wastewater Nitrate Treatment Coupled with Resource Recovery 53

3.1 Introduction 53

3.2 Photoelectrochemical Device for Wastewater Nitrate Treatment 56

3.3 Theory & Numerical Model 57

3.3.1 Light Absorber 59

3.3.2 Electrochemical Reactions 61

3.3.3 Modeling Competing Reactions 64

3.3.4 Performance Metrics 65

3.4 Results & Discussion 66

3.4.1 Solar-to-Chemical Efficiencies and Nitrogen Removal/Recovery Rates 66

3.4.2 Comparison with state-of-the-art nitrogen-removal technologies 75

3.5 Conclusions 78

Chapter 4 Revealing the Role of Competing Reactions and Mass-Transfer Effects in Photocatalytic Solar Hydrogen Production Systems 80

4.1 Introduction 80

4.2 Theory & Numerical Model 83

4.2.1 Light absorber behavior 84

4.2.2 Selective coating implementation 86

4.2.3 Electrochemical reactions 87

4.2.4 Solver set-up 90

4.2.5 Performance metrics 92

4.3 Parametric sweeps for a single slab 93

4.4 Parametric sweep for an ensemble of light absorbers 100

4.5 Conclusion 105

Chapter 5 Summary and Future Work 107

5.1 Thesis summary and limitations 107

5.1.1 Wastewater resource recovery – experimental and modeling findings 107

5.1.2 Photocatalytic solar water-splitting 110

5.2 Thesis impact 111

5.3 Future work 112

5.3.1 Effects of competing ions present in real waste streams 112

5.3.2 Nitrate reduction in an electrochemical flow reactor 113

5.3.3 Resolving local species concentrations in tandem with reaction rate predictions 113

5.3.4 Case study with a suspension of particles instead of an ensemble of thin semitransparent slabs 114

Bibliography 155

List of Tables

Table 2-1: Potential ranges used in the CA and expected faradaic efficiency from the CV study24

Table 2-2: Error associated with different components of the experimental set-up 27

Table 3-1: List of the governing equations for the semiconductor light absorber in the equivalent circuit (0-D) model 60

Table 3-2: Reactions modeled with relevant pH, reference exchange current density, $j_{0,\mathrm{ref}}$; charge transfer coefficients, α_c and $\alpha_{a;}$ N/A for the charge-transfer coefficients implies the use of the irreversible equation form (Eq. (3-12)); bulk reference concentrations, $c_{\mathrm{bulk,ref}}$, extracted from the literature or from own experiments for the catalysts are listed; pH 1 used for N_2O and pH 8 and 14 data used for NH_3 production 64

Table 3-3: Process description, nitrogen-removal rates and mass-specific energy intensity comparisons for the Sharon-Annamox, electrochemical flow reactor for ammonia stripping and the photoelectrochemical approach discussed in this work. 76

Table 4-1: Assumed constants and parameter space.. 89

Table A-1: Tafel kinetics extracted for each concentration/pH pairing shown in Figure A-4 ... 117

Table A-2: Tafel kinetics extracted for each concentration/pH pairing shown in Figure A-5. .. 118

Table B-1: pH Specific Electrode Areas Used in the Chronoamperometry Results 119

Table C-1: Extracted fit values and confidence intervals for EIS curve fitting parameters for 1 M $NaNO_3$ at pH 8 trials. Confidence intervals are shown to the right of each fitted parameter in the same units as the parameter. i: initial, f: final. 124

Table C-2: Extracted fit values and confidence intervals for EIS curve fitting parameters for 0.1 M $NaNO_3$ at pH 8 trials. Confidence intervals are shown to the right of each fitted parameter in the same units as the parameter. i: initial, f: final. 124

Table C-3: Extracted fit values and confidence intervals for EIS curve fitting parameters for 1 M $NaNO_3$ at pH 10 trials. Confidence intervals are shown to the right of each fitted parameter in the same units as the parameter. i: initial, f: final. 125

Table C-4: Extracted fit values and confidence intervals for EIS curve fitting parameters for 0.1 M $NaNO_3$ at pH 10 trials. Confidence intervals are shown to the right of each fitted parameter in the same units as the parameter. i: initial, f: final. 125

Table C-5: Extracted fit values and confidence intervals for EIS curve fitting parameters for 1 M $NaNO_3$ at pH 14 trials. Confidence intervals are shown to the right of each fitted parameter in the same units as the parameter. 126

Table C-6: Extracted fit values and confidence intervals for EIS curve fitting parameters for 0.1 M $NaNO_3$ at pH 14 trials. Confidence intervals are shown to the right of each fitted parameter in the same units as the parameter. 126

Table D-1: Species-specific concentration ranges used to make the calibration curves, and the species-specific wavelengths used to extract the molar absorption coefficients. 130

Table D-2: Equations and constant values for K_a (for phosphoric acid in water at 25°C)[248] used for equilibrium speciation calculations of a phosphate buffer 133

Table E-1: Errors from the calibration curves NO_3^-, NO_2^-, and NH_3 at the relevant wavelengths 136

Table E-2: Pipettes specifications for SCILOGEX MicroPipette Pipettors 138

Table E-3: Inputs for the systematic error calculation 138

Table E-4: Trial-to-trial error across all pH and concentration combinations 140

Table E-5: Measured $FENO2-$ and $FENH3$ with the associated error ($sc, NO2, \mathrm{f}cNO2, \mathrm{f}, m$ and $sc, NH3, \mathrm{f}cNH3, \mathrm{f}, m$) without considering the contributions from trial-to-trial variation). The total species error is calculated as the sum of these errors and can be compared to the unaccounted charge in each trial. 142

List of Figures

Figure 1-1: Concentrations of biological oxygen demand (mg-O_2/L), nitrogen species, and phosphate (mg-PO_4^{3-}/L) in different waste streams. Percentage breakdown of nitrogen species – NO_3^- (mg-NO_3^-/L), NO_2^- (mg-NO_2^-/L) and NH_4^+ (mg-NH_4^+/L) is indicated for each source. Data was compiled from the US Environmental Protection Agency (EPA) development documents,[15,16] EPA's database for industrial wastewater treatment technologies,[17] and pertinent journal papers.[18–40] EPA's specifications for nitrogen-contaminants in drinking water: < 44.3 mg-NO_3^-/L (dashed blue line) and < 3.3 mg-NO_2^-/L.[14] 3

Figure 1-2: Schematic depicting the electrochemical reduction of wastewater nitrates (from sources like ion-exchange brine and industrial effluent) into N-species products (NH_3, N_2O, N_2) for water recovery, nutrient (NH_3), and energy (N_2O). The paired reaction at the anode was assumed to be water oxidation. The energy input to the system can be any renewable electron source. 5

Figure 1-3: Schematics depicting standard architectures for photovoltaic + electrolyzer, photoelectrochemical cell, and photocatalysis water-splitting approaches. Inset shows the charge separation occurring on the particle in suspension evolving H_2. D/D^+: redox shuttle species 7

Figure 1-4: Suspension of particles undergoing photocatalytic water-splitting for the generation of H_2 and O_2 in a Z-scheme photocatalyst reactor. Schematic representations of thermodynamic driving forces for both forward and backward reactions at the conduction and valence bands. A selectively permeable coating allows for only the desired reactions (hydrogen evolution reaction and oxidation of D^+/D) to occur as a result of the modified mass-transport toward the catalyst surface. 10

Figure 2-1: (a) Three-electrode cell set-up for cyclic voltammetry and chronoamperometry tests. REF: reference electrode, CE: counter electrode, WE: working electrode, Gas: gas inlet. (b) Electrodes used: (left) Cu disk electrode for the cyclic voltammetry studies and (right) Cu planar electrode for the chronoamperometry studies. 21

Figure 2-2: (a) Circuit diagram with a constant phase element, CPE, in parallel with a Faradaic resistance, Rt, and impedance from a Warburg element, Zw, and both are in series with a solution resistance, Re. A potential is applied at the working electrode (WE) with respect to the reference electrode (REF), while current flows between the WE and counter electrode (not shown). (b) Order of tests first conducted on the blank and then on the experiments with the species present. Open circuit voltage (OCV) measurements subject the WE to a potential where there is a negligibly small current passed between the WE and the counter electrode (not shown). pH measurements were completed before and after the whole series of tests for both the blank and the NO_3^- species experiments. Note that CV: cyclic voltammetry, CA: chronoamperometry, EIS: electrochemical impedance spectrometry. 22

Figure 2-3: Cyclic voltammograms for 0.1 M, 0.5 M and 1 M $NaNO_3$ for (a) pH 8, (b) pH 10, and (c) pH 14 using a Cu disk electrode (Figure 2-1) with a scan rate of 20 mV s^{-1} and stir rate of 900 rpm. Average current density for the last and steady cycle is shown as a bold line with the shaded regions representing the standard deviation over at least 3 trials computed at every potential. Arrows indicate the direction of the sweep. Data in Figure 2-3(a) and Figure 2-3(b) for pH 8 and pH 10 is a selected subset of more experimental trials. 30

Figure 2-4: Cyclic voltammograms for pH and 1 M $NaNO_3$ and 1 M $NaNO_2$ concentrations for a Cu disk electrode obtained with a scan rate of 20 mV s^{-1} and a stir rate of 900 rpm at: (a) pH 8, (b) pH 10, and (c) pH 14. The blanks associated with each trial condition are shown as dotted lines. The onset of the blank is indicated by the vertical dashed line. Average current density for the last and steady cycle is shown as a bold line, with the shaded regions representing the standard deviation over all trials calculated at each potential. 32

Figure 2-5: Tafel kinetics extracted from the CVs obtained with a Cu disk electrode for all pH and $NaNO_3$ concentrations in the NO_3^- to NO_2^- onset potential region: (a) exchange current densities $j0$ (mA cm^{-2}) and (b) charge transfer coefficients αc. The filled markers indicate the values extracted for the average behavior across all trials and the vertical lines with empty markers as endpoints indicate the range of values covered by the individual trials. 35

Figure 2-6: Cyclic voltammograms for 0.5 M $NaNO_3$ for a Cu disk electrode with a scan rate of 20 mV s^{-1} and a stir rate of 900 rpm at (a) pH 8, (b) pH 10 and (c) pH 14. For (a) and (c), two different clusters of measured datasets are observed and average current density values over multiple trials (at least 2) are shown in bold and the shaded regions represent the standard deviation. For (b), data from all trials are shown. 37

Figure 2-7: Chronoamperometry studies for pH 8, 10, and 14 for $NaNO_3$ concentrations of (a) 0.1 M and (b) 1 M. Average current density for all trials is shown in the bold line, with the shaded regions representing the standard deviation of 3 experimental trials. Experiments were completed with planar Cu electrodes with geometric areas in Table B-1, where the working electrode was subject to the voltages in Table 2-1, and with a stir rate of 900 rpm. 39

Figure 2-8: (a) Average and standard deviations in Faradaic efficiency to NH_3 (green) and NO_2^- (purple) at pH 8, 10, and 14 for 0.1 M and 1 M NaNO3. (b) Average and standard deviations in measured NO_3^- consumption (blue) and estimated NO_3^- consumption (teal); (c) trial-to-trial breakdown of Faradaic efficiency to NO_2^-, NH_3, predicted H_2, and unaccounted products. All data for this figure are from experiments completed with planar Cu electrodes with geometric areas in Table C-1, where the working electrode was subject to the voltages in Table 2-1, and with a stir rate of 900 rpm. Average values in 2-8(a) and 2-8(b) are obtained by averaging over all trials in Figure 2-7, and error bars account for both random (trial-to-trial) and systematic errors (Table 2-2); 2-8(c) does not show uncertainties in the Faradaic efficiency to NO_2^- and NH_3. Instead, the red box indicates the portion of the unaccounted products that lies outside of the systematic error coming from the NH_3 and NO_2^- measurements. 42

Figure 2-9: Energy intensity for ammonia recovery, $ENH3$ (MJ kg_N^{-1}), and rate of ammonia production, $rNH3$ (g_N m^{-2} day^{-1}), as a function of pH 8, 10, and 14 for 0.1 M and 1 M $NaNO_3$. Energy intensity values estimated for the standard biological nitrification-denitrification approach (green star), and for the Sharon-Anammox process (yellow star) are included for comparison. All data for this figure are from experiments completed with planar Cu electrodes with geometric areas in Table B-1, where the working electrode was subject to the voltages in Table 2-1, and with a stir rate of 900 rpm. Average values for energy intensity and rate of ammonia production are obtained by averaging over all trials in Figure 2-7, and error bars account for both random (trial-to-trial) and systematic errors (Table 2-2). 45

Figure 2-10: Correlation, using trial-by-trial experimental data, between the average of initial and final values of the charge-transfer resistance, Rt, and the charge passed for NO_3^- reduction to NO_2^- and NH_3, $QNO2-+QNH3$, for 0.1 M and 1 M $NaNO_3$ at pH 8, 10, and 14. Best-fit charge-transfer resistance values are obtained from electrochemical impedance spectroscopy data measured with planar Cu electrodes at a potential of -0.1 V. Lower Rt leads to higher charge passed to NO_3^- reduction products, as shown by the fit line. Systematic errors in the determination of $QNO2-+QNH3$ (Table 2-2) is not explicitly shown in this dataset. 47

Figure 2-11: Correlations using trial-by-trial experimental data between the net charge passed and the average of the initial and final effective double-layer capacitance, $Ceff$. (a, b) show the charge for NO_2^-, NH_3, and unaccounted products and (c, d) only consider NO_2^- and NH_3. The $Ceff$ is split by concentration, with (a, c) showing 0.1 M and (b,d) showing 1 M $NaNO_3$ for pH 8, 10, and 14. Trendlines in the data (dotted and dashed) are included at every pH. Best-fit double-layer capacitance values are calculated from electrochemical impedance spectroscopy data obtained with planar Cu electrodes at a potential of -0.1 V. The error bars for $QNO2-+QNH3$ include the contributions from systematic error (Table 2-2). 48

Figure 3-1: Schematic of a photoelectrochemical device for treating wastewater nitrate contaminants. Selective water oxidation at the photoanode and only NO_3^- reduction to form NH_3 (R1), N_2O (R2) or N_2 (R3) are depicted for simplicity. All the standard potentials, $E0$, for aqueous solutions at 25˚C are reported vs. NHE based on a 1 atm standard state for H_2. Unless otherwise mentioned all species are in the aqueous phase.[170,171] A negative $E0$ for a net reaction indicates that it is thermodynamically uphill, while a positive $E0$ indicates reaction spontaneity............. 56

Figure 3-2: Equivalent circuit diagram to model the operation and performance of the photoelectrochemical device in Figure 3-1. The semiconductor light-absorber was modeled as a photodiode and the electrochemical reactions as variable resistors with minimum electrical loads corresponding to the thermodynamic potentials for the corresponding reactions. Selective oxygen evolution reaction (OER) at the anode and parallel reactions were modeled at the cathode including the desired NO3RR, and the competing HER and ORR. Desired reactions in the circuit are indicated by the solid lines and the undesired and competing reactions at the cathode are indicated by the dashed lines. 59

Figure 3-3: (a) Solar-to-chemical energy conversion efficiencies, $\eta\mathrm{solar-to-chemical}$, for water oxidation and NO_3^- reduction to NH_3 (green) and N_2O (purple) with RuO_2, Cu (pH 14) and IrO_2, Sn-Pt (pH 1) catalysts for the OER and the NO3RR, respectively. Solar-to-hydrogen efficiency in the inset was computed for RuO_2 (OER) and Pt (HER) catalysts at pH=1; maximum solar-to-H_2 efficiency is represented as a star.[153] The thick solid lines and the thin solid lines represent efficiencies with state-of-the-art and ideal nitrate reduction catalysts. Total kinetic overpotential, ηtotal, and the split between the oxidation (OER) overpotential, ηOER, (dark shaded area) and the NO3RR overpotential, ηNO3RR, (light shaded area) is shown for (b) NH_3 (green) and (c) N_2O (purple). Standard state potential from Eq. (3-3) was used and a 100 mM NO_3^- species concentration was modeled; $E\text{NO3RR0} = 0.835$ V vs NHE. 68

Figure 3-4: Concentration effects on the solar-to-chemical efficiencies ((a) and (b)) and the nitrogen-removal rates ((c) and (d)) with complete selectivity to desired reactions assumed: for (a) and (c), for the NO_3^--to-NH_3 conversion at pH 14, selective OER on IrO_2 and selective NO3RR on Cu was assumed; for (b) and (d), for the NO_3^--to-N_2O conversion at pH 1, selective OER on RuO_2 and selective NO3RR on Sn-Pt was assumed. For all these calculations, a headspace with standard atmospheric conditions (1 atm, 25˚C) with 20.9% of O_2, trace amounts of H_2 (0.5 ppm) and balance N_2 was assumed to determine thermodynamic reaction potentials. 70

Figure 3-5: Concentration effects on the solar-to-chemical efficiencies ((a) and (b)) and the nitrogen-removal rates ((c) and (d)) with measured Faradaic efficiencies to desired reactions assumed: for (a) and (c), for the NO_3^--to-NH_3 conversion at pH 14, selective OER on IrO_2 and FE = 39.5% for NO3RR on Cu was assumed; for (b) and (d), for the NO_3^--to-NH_3 conversion at pH 8, selective OER on CoMnOx and FE = 46% (gray) and FE = 25% (blue) for NO3RR on Cu was assumed. Bold solid lines represent the FE implemented for the concentration at which it was measured (Chapter 2), dashed lines represent an assumed FE value being implemented. For all these calculations, a headspace with standard atmospheric conditions (1 atm, 25˚C) with 20.9% of O_2, trace amounts of H_2 (0.5 ppm) and balance N_2 was assumed to determine thermodynamic reaction potentials. 71

Figure 3-6: Solar-to-chemical efficiency for (a) NH_3 production and (c) N_2O production when competing HER and ORR reactions are implemented at the cathode with *worst-case* kinetic parameter values (Table 3-2). (b,d) To further illustrate the driving forces for the competing reactions, the current-voltage behavior for the diode (black) assuming $BiVO_4$ with a band gap of 2.5 eV and the parallel and competing electrochemical reactions at the cathode. Open symbols on the current-voltage plot represent models that assumed selective reactions whereas the filled symbols include the competing reactions. The operating point, $j$op and Vop, is shown on the diode curve (black circles); the cathode potential and current densities for (b) NH_3 production (green) or (d) N_2O production (purple); HER (yellow); and ORR (blue). 74

Figure 4-1: Particle schematics and equivalent circuit diagrams for (a) the state-of-the-art scenario, where only desired reduction (H^+/H_2) and desired oxidation (D/D^+) reactions are taking place, and (b) the hereby proposed scenario, where additional competing back-reactions (indicated by the dashed lines) are allowed. Intersection plots of the diode curve (black) with the reaction curves (green for the redox shuttle reaction (RS), blue for the hydrogen reaction (H2)) (c) when only selective reactions are implemented and (d) competing reactions are considered as well, with desired reactions shown as full markers and competing reactions shown as empty markers. The operating point of the device is indicated by the black marker on the diode curve. Governing equations for the current densities implemented shown in the box. 82

Figure 4-2: Schematics depicting (a) a single (N = 1) optically thick light absorber and (a) an ensemble of optically thin light absorbers with Beer's Law implemented, with τ/N representing the optical thickness of each light absorber assumed to be present. 85

Figure 4-3: Intersection plots depicting diode curve (black), individual reaction curves (H2: hydrogen in blue, RS: redox shuttle in green), and summed reaction curve (yellow), showing (a) mass-transport limited behavior, (b) light-limited behavior, and (c) kinetically limited behavior. The desired reaction are shown by the filled markers, the undesired competing reaction shown by the empty markers, and the behavior at the conduction band and valence band are indicated by VCB and VVB, respectively. For all cases shown, $\alpha a, RS$ = 0.5, gl, VB = 1e-1, gl, CB = 1e-1, and $jl, H2, c/jsc$ = -1000. 90

Figure 4-4: Algorithm flow chart with intersection plots depicting steps 3, 4, and 6 for both cases (undershot and overshot). Step 3: the intersection of the diode and summed curves is the starting point (Vin, $j$in shown as the yellow marker) that determines the initial VCB, in and VVB, in. Step 4: shifting the operating point to larger (undershot) or smaller (overshot) current densities. Step 6: When the stopping criteria is met, the operating points on each curve can be calculated, with the desired reaction shown with the filled markers, the undesired competing reaction shown with the empty markers, and the behavior at the conduction band and valence band indicated by VCB, i and VVB, i, respectively. 91

Figure 4-5: Solar-to-hydrogen efficiencies for selective reactions (dashed lines) and with competing reactions (solid lines) for (a) $jl, RS, a/jsc$ = 1 and (b) $jl, RS, a/jsc$ = 1e-2. Selectivity ($Srxn$) towards the desired reaction (when competing reactions are implemented) for $jl, RS, a/jsc$ = 1 at (c) the valence band (VB) (d) the conduction band (CB). Black line indicates the maximum possible STH efficiency that could be reached assuming a fully ideal redox reaction. The light absorber was assumed to be optically thick (absorptance A of 0.99) with a band gap of 1.55 eV. The additional limiting current densities assumed were: $gl, VB = jl, H2, a/jl, RS, a$ = 1e-1, gl, CB = $|jl, RS, c|jRS, a,$ = 1e-1, and $jl, H2, c/jsc$ = -1000. The redox shuttle pair assumed here was Fe(III)/Fe(II). All Si = 1. RS: redox shuttle reaction. H2: hydrogen reaction. 94

Figure 4-6: Solar-to-hydrogen efficiencies for competing reactions implemented for different redox shuttle pairs: (a) $ERS0$ = 0.77 V (Fe^{3+}/Fe^{2+}), (b) $ERS0$ = 1 V (I^-/IO_3^-), and (c) $ERS0$ = 1.23 V (H_2O/O_2). (d) RS reaction curves for different assumed $ERS0$ values (solid lines for 0.77 V and dash-dot lines for 1.23 V) as $gl, CB = jl, RS, c/jl, RS, a$ is varied from 1e-4 (light green) to 10 (dark green). (e) H2 reaction curves for $gl, VB = jl, H2, a/jl, RS, a$ varied from 1e-4 (light blue) to 10 (dark blue). For all plots, $jl, RS, a/jsc$ = 1e-2, $j0, RS$ = 10 A m^{-2} and $\alpha a, RS$ = 0.5, all Si = 1, and a single optically thick light absorber with an absorptance A of 0.99 and optical thickness of 4.61, with a band gap of 1.55 eV was considered. RS: redox shuttle. H2: hydrogen. 96

Figure 4-7: (a) Solar-to-hydrogen efficiencies for $jl, RS, a/jsc$ = 1, $gl, VB = jl, H2, a/jl, RS, a$ = 1e-2 and SO, RS = 1 for varying $gl, CB = jl, RS, c/jl, RS, a$ and SR, RS values. Inset depicting intersection plot for SR, RS = 1e-2 - 10 when gl, CB = 1e-2. (b) Solar-to-hydrogen efficiencies for $jl, RS, a/jsc$ = 1, gl, VB = 1e-2 and gl, CB = 1e-4 for varying SO, RS and SR, RS values. Inset depicting intersection plot for SO, RS = 10 and 1e-1 when SR, RS = 1. The light absorber was assumed to be optically thick (absorptance A of 0.99) with a band gap of 1.55 eV. The redox shuttle pair assumed here was Fe(III)/Fe(II). 99

Figure 4-8: Solar-to-hydrogen efficiencies for an increasing number of light absorbers for (a) $gl, CB = |jl, RS, c|/jl, RS, a$ = 0.01 and (b) gl, CB = 1, with $gl, VB = jl, H2, a/jl, RS, a$ = 1e-4 – 10. (c) Maximum solar-to-hydrogen efficiencies and (d) corresponding number of slabs are tracked with respect to gl, CB and gl, VB. For all plots, $jl, RS, a/jsc$ = 1e-2, $j0, RS$ = 10 A m^{-2}, $\alpha a, RS$ = 0.5, and Si = 1. The total absorptance A was maintained at 0.99 for an ensemble of semitransparent optically thin slabs with a band gap of 1.55 eV. The redox shuttle pair assumed here was Fe(III)/Fe(II). 101

Figure 4-9: Maximum solar-to-hydrogen efficiencies for (a) $gl, CB = jl, RS, c/jl, RS, a$ = 1e-2 and $gl, VB = jl, H2, a/jl, RS, a$ = 1e-2 and (b) gl, CB = 1e-1 and gl, VB = 1. The number of light absorbers required to reach the maximum solar-to-hydrogen efficiencies are listed for each $jl, RS, a/jsc$ combination. For (a), $jl, RS, a/jsc$ = 1 reaches its maximum values for a decreasing number of light absorbers as SR, RS increases, going from 3 to 1. For all plots, the total absorptance A was maintained at 99%, $j0, RS$ = 10 A m^{-2} and $\alpha a, RS$ = 0.5, SO, RS = 1, and the redox shuttle pair assumed here was Fe(III)/Fe(II). 102

Figure A-1: (a) Cyclic voltammogram for 1 M $NaNO_3$ at pH 14 for cycles 1 through 30. The blank cycles are shown as dotted lines. (b) Cycle stability calculated for each sequential pair of cycles (ex: the stability of cycle 30 was calculated as the change in current density over all potentials with respect to cycle 29). A CV was considered stable if the last five cycles were over 95% stable (cut-off shown as dashed line).. 115

Figure A-2: Cyclic voltammogram for the average blank response at each pH (8, 10, 14) for (a) 0.1 M $NaNO_3$, (b) 0.5 M $NaNO_3$, and (c) 1 M $NaNO_3$. The average was taken across all trials (before the $NaNO_3$ was run) using the last cycle. This response was removed from the stable responses for each pH/concentration combination to obtain Figure 2-3. 115

Figure A-3: Cyclic voltammograms for pH 10 and 0.1 M $NaNO_3$ and 0.1 M $NaNO_2$ concentrations. The blanks associated with each trial condition are shown as dotted lines. The onset of the blank is indicated by the dashed line. Average current density for the last cycle is shown as a bold line, with the shaded regions representing the standard deviation between the different runs calculated at each potential point. Scan rate: 20 mV s^{-1}; stir rate: 900 rpm. 116

Figure A-4: Average Tafel current density with respect to overpotential ($\eta = V_{WE} - E^0_{RDS}$), where E^0_{RDS} = 0.835 vs RHE for the (a) LCD cases at pH 8 and all $NaNO_3$ concentrations, (b) HCD cases at pH 8 and 0.1 M and 0.5 M $NaNO_3$, (c) pH 10 and all $NaNO_3$ concentrations, and (d) both types (LCD for all $NaNO_3$ concentrations and HCD for 0.5 M $NaNO_3$) at pH 14. Stable current density values from the cathodic sweep are used with the blank current deducted for each data type. Low current density (LCD) runs are shown as solid lines and high current density (HCD) runs are shown as dashed lines.. 116

Figure A-5: Exchange current densities $j0$ (mA cm^{-2}) extracted from the CVs for all pH and $NaNO_3$ concentrations in the NO_3^- to NO_2^- onset potential region using the fixed αc values listed in Table A-2. The filled markers indicate the values extracted for the average behavior across all trials and the vertical lines with empty markers as endpoints indicate the range of values covered by the individual trials. All values can be found in Table A-2. 117

Figure B-1: Optical microscope images of the pH 8 electrode, showing significant surface roughness and scratches. Image taken at 20 times zoom. Scale bar shown on image............... 120

Figure B-2: Optical microscope images of the pH 10 electrode, showing significantly reduced scratching than the pH 8 electrode. Pitting of the Cu surface is present. Image taken at 20 times zoom. Scale bar shown on image.. 120

Figure B-3: Optical microscope images of the pH 14 electrode, showing significantly reduced scratching than the pH 8 electrode but also lesser pitting compared to pH 10 electrode. Image taken at 20 times zoom. Scale bar shown on image. 121

Figure B-4: Predicted efficiency towards NH_3 formation and predicted rate of NH_3 formation vs working potential for all pH and concentrations, using the average current density response from the CVs shown in Figure 2-3. 122

Figure C-1: Nyquist impedance data points and best fit curves for all pH 8 data. All trials have both an initial and final data fit. 1 M $NaNO_3$ data is show by + and 0.1 M data is shown by * symbols. pH 8 1 M data was fit using a Warburg impedance element in series with a CPE, to account for the mass transfer limitation seen in the shape of the curve. 124

Figure C-2: Nyquist Impedance data points and best fit curves for all pH 10 data. All trials have both an initial and final data fit. 1 M $NaNO_3$ data is show by + and 0.1 M data is shown by * symbols. The inset of the plot shows a close-up view of the 1M $NaNO_3$ data.......................... 125

Figure C-3: Nyquist Impedance data points and best fit curves for all pH 14 data. All trials have both an initial and final data fit. 1 M $NaNO_3$ data is show by + and 0.1 M data is shown by * symbols. The inset of the plot shows a close-up view of the 1 M $NaNO_3$ data, which is nearly 1 order of magnitude smaller than the 0.1 M $NaNO_3$ data. 126

Figure C-4: Showing the EIS voltage in relation to different reaction onsets. (a) EIS operating voltage is more positive than the onset of HER in all blanks tested. (b) In the pH 8 solution, the EIS operating voltage takes place after the onset of the 1 M $NaNO_3$ data, but before the onset of the 1 M $NaNO_2$ data. (c) In the pH 10 solution, both 1 M and 0.1 M $NaNO_3$ onsets occur before the EIS onset, but the 0.1 M and the 1 M $NaNO_2$ onset occurs after. (d) In the pH 14 solution, the onset of the 1M $NaNO_3$ takes place more positive of the EIS potential, while the 1 M $NaNO_2$ onset is observed more negative of the EIS potential. 127

Figure C-5: The OCV in the first 20 seconds following the completion of the CA experiment for each trial at (a) pH 8, (b) pH 10, and (c) pH 14. The rapid drop shows the local and bulk concentrations of anions coming into equilibrium. Since this is a hydroxide producing reaction, OH^- is expected to be present in significant amounts. As OCV relaxes back to steady-state, any local pH gradient would have dissipated, meaning that our operating voltage for EIS is now a steady value vs RHE. 129

Figure D-1: (a) Wavelength-dependent absorbance for NO_3^- concentrations ranging from 10 mM to 100 mM, with the NO_3^- characteristic peak centered around 303 nm (b) Concentration-dependent maximum absorbance reached at 303 nm, fitted using Beer's Law......................... 131

Figure D-2: (a) Wavelength-dependent absorbance for NO_2^- concentrations ranging from 1 mM to 50 mM, with the NO_2^- characteristic peak centered around 355 nm and secondary peak around 303 nm (b) Concentration-dependent maximum absorbance reached at 355 nm, and secondary peak at 303 nm, fitted using Beer's Law. 131

Figure D-3: (a) Prepared calibration samples using the salicylate method after 1 hour (b) Wavelength-dependent absorbance for NH_3 concentrations ranging from 10 µM to 50 µM as detected using the salicylate method, with the NH_3 characteristic peak centered around 650 nm (c) Concentration-dependent maximum absorbance reached at 650 nm, fitted using Beer's Law.. 132

Figure D-4: UV-Vis reading for a trial at 0.1 M $NaNO_3$ and pH 14, compared to NO_3^- and NO_2^- calibration curves. (inset) Wavelength range where unexplained signal is taking place........... 132

Figure D-5: Phosphate Bjerrum plot (calculated from the state equations listed in Table D-2) from 0 to 14 pH at 25°C with a total concentration of 0.4 M (as in the case of the pH 10 solutions used in this study). As pH 8 and 10 locally develop a higher pH, the phosphate species close to the electrode will shift based on the local pH. As pH 10 shifts locally, an increasing amount of PO_4^{3-} ions will develop. As pH 8 shifts higher locally, the amount of PO_4^{3-} ions will still be insignificant. 134

Figure F-1: Relative difference (RE (%)) of the solar-to-chemical efficiencies with and without competing reactions as a function of NO_3^- concentration for Si (red), MoS_2 (orange), $BiVO_4$ (yellow) and TiO_2 (purple) as discussed in Figure 3-6 for the (a) NO_3^--to-NH_3 transformation and (b) NO_3^--to-N_2O transformation. RE value of 100% indicates that the solar-to-chemical efficiency with competing reactions is 0; smaller the RE value lesser the effect of competing reactions on the efficiency.......... 144

List of Appendices

Appendix A: Cyclic Voltammetry Studies 115

Appendix B: Chronoamperometry Experiments 119

Appendix C: Electrochemical Impedance Spectroscopy 123

Appendix D: Species Behavior in Solution 130

Appendix E: Error Quantification 135

Appendix F: Estimated Solar-to-Chemical Efficiencies and Nitrogen Removal/Recovery Rates 143

Appendix G: Derivation for Equivalent Circuit Model: Selective Coating Implementation 146

Nomenclature

Symbols	
a	activity of modeled aqueous/dissolved species, unitless with $a_{\mathrm{O/R}} = \frac{c_{\mathrm{O/R}}}{c_{\mathrm{O/R,ref}}}$
A	absorbance
A_{total}	total optical absorptance
$\bar{A}_\iota$	average absorbance at a calibration concentration c_i
c	speed of light, 3.0 × 10^8 m s^{-1}
$\boldsymbol{c}_i$	concentration of modeled species i, mol m^{-3}
$\boldsymbol{c}_{i,s}$	concentration of modeled species i at the electrode surface, mol m^{-3}
$\boldsymbol{c}_i^*$	concentration of modeled species i in the coating, mol m^{-3}
$\bar{c}$	average concentration across all solutions, in M
c_i	final concentration of species i, in M
C	double layer capacitance, in F
C_s	area-specific capacitance of the surface, in F
D	diffusion coefficient of modeled species, m^2 s^{-1}
e^-	electrons
E^0	standard state potential, in V
E_{eq}	Nernst potential, V
E_g	band gap of the semiconductor material, eV
E_{N}	specific energy intensity to form N-products, in MJ kg_{N}^{-1}
F	Faraday's constant, 96485 C mol^{-1}
$g_{l,b}$	asymmetry factor, competing vs desired reaction limiting current density for each band (VB, CB)
Δg^0	standard state free energy change associated with a reaction, kJ mol^{-1}
h	Planck constant, 6.626 × 10^{-34} J s
i	discrete step taken in the stepwise solving algorithm (Chapter 4)
$\boldsymbol{i}$	imaginary number, $\sqrt{-1}$
$I(t)$	measured time-dependent current density, in mA cm^{-2}
j	current density, in mA cm^{-2} (Chapter 2) or A m^{-2} (Chapter 3)
j_0	exchange current density, in mA cm^{-2} (Chapter 2) or A m^{-2} (Chapter 3)
k	electrochemical reaction rate, m s^{-1}
k_{B}	Boltzmann constant, 1.38 × 10^{-23} J K^{-1}
k_{mf}	thermal voltage, $k_{mf} = F/R_c\,T$
K	equilibrium constant
l	optical pathlength through cuvette used in spectroscopy, 1 cm
m	mass, in g
M_{i}	molar mass of species i, in g mol^{-1}
n_d	ideality factor of the diode, here assumed to be 1

n_e	number of electrons
N	(Chapter 2) number of data points for the calibration curves (Chapter 4) number of light absorbers assumed in ensemble
N_i	flux of species i through a medium (boundary-layer, coating)
N_t	number of measurements across all trials for a pH/concentration combination
P	permeability of coating for species i, m^2 s^{-1}
q_e	elementary charge, 1.6021×10^{-19} C
$\boldsymbol{Q}$	constant phase element fitting parameter, unitless
Q_i	charge passed during the experiment to species i, Coulombs
$\dot{r}$	rate of nitrogen-removal and nitrogen-recovery, in g_N m^{-2} day^{-1}
R	D/C resistance, in Ohms
R_c	gas constant, 8.314 J mol^{-1} K^{-1}
$\dot{R}$	molar flux, in mol m^{-2} s^{-1}
s	error
S	partition coefficient for a species (S = 1 when no coating is present)
$S_{rxn,b}$	selectivity of a band b towards the desired reaction
STH	solar-to-hydrogen efficiency, %
t	time, in s
t_c	coating thickness, m
t_{CA}	duration of the experiment, 40 min or 2400 s or 0.0278 days
t_{day}	number of seconds in a day, 86400 s day^{-1}
T	ambient temperature (also the diode temperature), 298.15˚K
U	surface electrochemical potential, V
V	voltage/applied potential, in V
$\cancel{V}$	volume, in L
x	distance from the electrode surface into the bulk solution, m
Z	A/C Impedance, in Ohm

Greek

$\boldsymbol{\alpha}$	constant phase element fitting parameter, unitless
α	charge-transfer coefficient
δ_{BL}	boundary-layer thickness, μm
ε	molar absorption coefficient, L mol^{-1} cm^{-1}
ϵ	small value
η	overpotential, V or efficiency (solar-to-chemical subscript)
η_s	surface overpotential, V
υ	photon frequency, s^{-1}
ν	stoichiometric coefficient for modeled reactions
σ	diffusion constant function (σ = 0 when no mass-transfer limit)
τ	optical thickness
ϕ	frequency-dependent photon flux, s^{-1} m^{-2}
ω	frequency, Hz

Subscripts	
a	pertinent to the anode
avg	pertinent to the average value
A	pertinent to absorbance error in calibration curves
b	pertinent to the semiconductor band (conduction or valence)
bulk	pertinent to species concentration in the bulk electrolyte
c	pertinent to concentration or cathode (when paired with α)
CB	pertinent to the conduction band
cal	pertinent to calibration curves
$cell$	pertinent to the entire cell
$coat$	pertinent to the semipermeable coating
comp	pertinent to efficiency calculation with competing reactions
CPE	pertinent to the Constant Phase element
DBL	pertinent to the diffusion boundary layer
dil	pertinent to the error coming from dilution
e	pertinent to the electrolyte solution
eff	effective
ϵ	pertinent to the molar absorptivity
f	pertinent to the final state
fit	pertinent to the line fit
g	indicating the min. frequency of photons that can be absorbed by the diode
$H2$	pertinent to the hydrogen (evolving/oxidation) reaction
i	pertinent to the species i
i	pertinent to the initial state
k	pertinent to the electrochemical reaction k
k or kin	pertinent to the kinetic overpotential
l	pertinent to the limiting current density
λ	pertinent to a specific wavelength of λ
m	pertinent to measured value
mt	pertinent to the mass-transport overpotential
no comp	pertinent to efficiency without competing reactions
N	pertinent to the basis of N
NH_3	pertinent to the NH_3 species
NO_2^-	pertinent to the NO_2^- species
op	pertinent to the operating current density and potential of the device
O	pertinent to the oxidized species
r	pertinent to the reaction r
ref	pertinent to the reference value from the literature
rr	pertinent to the radiative recombination current density
R	pertinent to the reduced species
RDS	pertinent to the NO_3^- to NO_2^- rate-determining reduction step
RS	pertinent to the redox shuttle (reduction/oxidation) reaction
s	pertinent to the prepared solution
sc	pertinent to the short-circuit current density
solar	pertinent to the incident solar spectrum
$stock$	pertinent to the stock solution

sys	pertinent to the systematic error
t	pertinent to the charge transfer reaction
$t-t$	pertinent to the trial-to-trial error
total	total
u	pertinent to the unaccounted charge
VB	pertinent to the conduction band
w	pertinent to the Warburg impedance
WE	pertinent to the Working Electrode

Other

AM1.5	air mass 1.5 reference spectrum for terrestrial solar insolation
BOD	biological oxygen demand, mg-O_2/L
CA	Chronoamperometry
CE	Counter Electrode
CPE	Constant Phase Element
CV	Cyclic Voltammogram
e^-/h^+	electron/hole pair
ECSA	Electrochemical Surface Area
EIS	Electrochemical Impedance Spectroscopy
EPA	U.S. Environmental Protection Agency
FE	Faradaic Efficiency
HCD	High Current Density
HER	hydrogen evolution reaction
LCD	Low Current Density
NO3RR	nitrate reduction reaction
OCV	Open Circuit Voltage
OER	oxygen evolution reaction
ORR	oxygen reduction reaction
R1	net reaction 1, where nitrates are converted to ammonia
R2	net reaction 2, where nitrates are converted to nitrous oxide
R3	net reaction 3, where nitrates are converted to nitrogen
RE	relative difference
REF	Reference Electrode
RHE	Reversible Hydrogen Electrode, used as a reference
SA	Surface Area
WE	Working Electrode
~	on the same order of magnitude

Abstract

Increasing food demand due to the growing global population underlines the surging dependence on the Haber-Bosch process to produce ammonia (NH_3), which is a vital fertilizer for high crop yields. This process is energy and carbon intensive due to H_2 feedstock production and high temperature and pressure requirements. Motivated by these challenges, this doctoral dissertation evaluates the performance of: (a) (photo)electrochemical systems for nitrogen nutrient recovery from wastewater to enable renewable NH_3 production and (b) solar hydrogen production pathways to mitigate H_2 production energy requirements.

Wastewater nitrates (NO_3^-) represent an untapped source for nutrient and energy recovery, with pH and NO_3^- concentrations varying substantially depending on the source. We investigated the effects of NO_3^- concentration (0.1M – 1M) and pH (8 – 14) on the catalytic performance of polycrystalline Cu electrodes. Cyclic voltammograms indicate pH and concentration-dependent reaction kinetics and chronoamperometry experiments achieved maximum NH_3 Faradaic efficiencies of 46% ± 11% for 1M $NaNO_3$ at pH 14 at -0.55V vs RHE, with a minimum of 25% ± 6% for 1M $NaNO_3$ at pH 8. Large trial-to-trial uncertainties motivate the application of *in situ* electrochemical impedance spectroscopy, where trial-to-trial changes in the electrochemically active surface area are more dominant for 0.1M $NaNO_3$ solutions, whereas, for 1M $NaNO_3$, variations in the facet composition of the Cu catalyst surface play a significant role.

High energy requirements needed to drive NO_3^- reduction to NH_3 hinder its competitiveness with other treatment technologies. To probe solar-driven wastewater nutrient recovery, we developed a numerical model analogous to detailed-balance calculations for photovoltaic cells, with additional electrochemical loads. This model quantifies the dependence of solar-to-chemical efficiencies on light-absorber band gaps, electrocatalytic kinetic parameters, competing oxygen reduction and hydrogen reduction, and NO_3^- concentrations. With a single light-absorber and state-of-the-art catalysts, optimal solar-to-chemical efficiencies of 7% and 10% are predicted for NO_3^- reduction to NH_3 and N_2O respectively.

Equivalent circuit modeling was also applied for solar water splitting to produce hydrogen and oxygen. We studied Z-scheme photocatalytic suspension reactors in the presence of aqueous redox shuttles to facilitate 3-D photoelectrochemistry while avoiding the co-production of hydrogen and oxygen on the same photocatalyst. The modeling framework was used to understand the role of competing reactions and mass-transfer effects on solar-to-hydrogen efficiencies for individual and ensembles of light absorbers mimicking a photocatalytic particle suspension. Parameters of interest are the electrocatalytic reaction kinetics, the limiting current densities, the redox shuttle thermodynamic potentials, the presence of a selective coating and the number of light absorbers considered in the ensemble. The extent of the competing reactions effect was found to be dependent on the redox shuttle thermodynamic potentials: for small potentials, the efficiencies did not depend on the hydrogen oxidation implemented; for large potentials, both hydrogen oxidation and redox shuttle reduction affected the solar-to-hydrogen efficiency. In addition, increasing the number of light absorbers for severely mass-transport limited cases resulted in an optimum efficiency due to the additive gains of having multiple absorbers competing with the downside of light-limited reduction in operating potentials.

Overall, electrocatalytic measurements quantify sensitivity of nitrate reduction to pH, concentration, and surface composition on copper electrodes, and motivate future investigations of ammonia recovery in wastewater streams with more complex compositions. Equivalent-circuit

based models that account for competing reactions and mass-transfer limitations provide a powerful framework to predict performance limits for photocatalytic and photoelectrochemical systems.

Chapter 1 Introduction

Moving away from a linear economy towards a circular economy will be key to addressing upcoming environmental crises. The world's food demand is projected to increase by at least 54% by 2050 due to the combined effect of the global population growing from 8 billion to 9.7 billion people and socio-economic trends leading to higher food consumption.[1,2] This results in an increasing demand for nitrogen and phosphorus-based fertilizers, as these are integral to sustaining high crop yields.[3–6] The state-of-the-art method for nitrogen fertilizer production is the Haber-Bosch process, which involves dissociating widely available gaseous N_2 in the presence of H_2 and an Fe-based catalyst under high pressure (> 100 bar) and high temperature (~ 500˚C) conditions.[7] It currently represents 1-2% of the world's energy consumption and 1.44% of its CO_2 emissions.[7] Phosphorus production, on the other hand, depends on extracting non-renewable phosphate rock resources, which are liable to become depleted in the upcoming century.[3] All of these factors combined motivate the development of a circular economy, where the energy-intensive nitrogen nutrients and the resource-limited phosphorus nutrients are captured and repurposed as opposed to lost in the water cycle. In this work, my first area of focus is specifically on nitrogen nutrient recovery from wastewater, where we have experimentally characterized the performance of a well-studied Cu electrocatalyst and made predictions to assess the viability of photoelectrochemical pathways for nutrient recovery.

Integral to the production of ammonia, H_2 is also valuable as a chemical and feedstock for various other applications, such as steel production, hydrogenation in food applications, and in fuel cells for power generation.[8] In the US, ≥ 95% of H_2 production comes from an endothermic steam-methane reforming process, where high-temperature steam (700˚C – 1,000˚C) is used to produce H_2 from a methane (CH_4) source, such as natural gas.[9] This process is technologically mature and cost-competitive, costing between \$1.43/kg to \$2.27/kg depending on the market natural gas price,[9] but poses two critical climate challenges. First, it necessitates the use of a fossil-fuel source for H_2 production, defeating the purpose of using it as a replacement for fossil fuels. Second, it causes CO_2 emissions both from the reforming reaction ($CH_4 + 2H_2O$ (+ heat) $\rightarrow CO_2 + 4H_2$) and the use of fossil-fuel sources to provide the high-quality heating required to drive the endothermic reactions. This motivates the need for H_2 production pathways that integrate renewable energy sources. In this work, my second area of focus is on artificial photosynthesis systems, specifically photocatalytic particle suspension systems, where we have modeled the dependencies of the overall solar-to-chemical efficiencies on the considered reaction kinetics, competing reactions, and mass-transport limitations.

1.1 Wastewater Resource Recovery

The composition of wastewater nutrient contaminants, including organic, nitrogen (NO_3^-, NO_2^- and NH_4^+) and phosphorous (PO_4^{3-}) contaminants, is extremely source-dependent (Figure 1-1). Biological oxygen demand (BOD) quantifies the amount of the dissolved oxygen required to biologically oxidize the organic contaminants. Therefore, the larger the BOD value, the larger the organics concentration.[10] Organic species overshadow nutrient contaminants in municipal wastewater effluents and oil/gas processes, and could be harnessed to produce methane-rich biogas.[11–13] Phosphates, while present in every wastewater stream, consistently have the lowest concentrations amongst all the other pollutants considered. Currently pursued techniques for phosphate recovery include chemical precipitation, where the phosphate is recovered as struvite, and osmotic membrane bioreactors, where the phosphate is either recovered as struvite or calcium phosphate.[13] The nitrogen contaminants (NO_3^-, NO_2^- and NH_4^+) dominate in nuclear wastes (159,000 mg/L total nitrogen species), ion-exchange brines (5,270 mg/L), and power production processes (300 mg/L). More than 80% of all nitrogen-contaminants are in the form of NO_3^- in all the point sources considered, except for oil/gas processes where the NH_4^+ species predominates. In all these sources, except for municipal wastewater effluents, nitrogen-contaminant concentrations exceed the limit established by the U.S. Environmental Protection Agency (EPA) for drinking water – 44.3 mg-NO_3^- L^{-1} and 3.3 mg-NO_2^- L^{-1}.[14] Nitrates are stringently regulated since they pose a dire threat to both human and environmental health. Increased nitrate concentrations result in methemoglobinemia in infants and induce large-scale algal bloom over

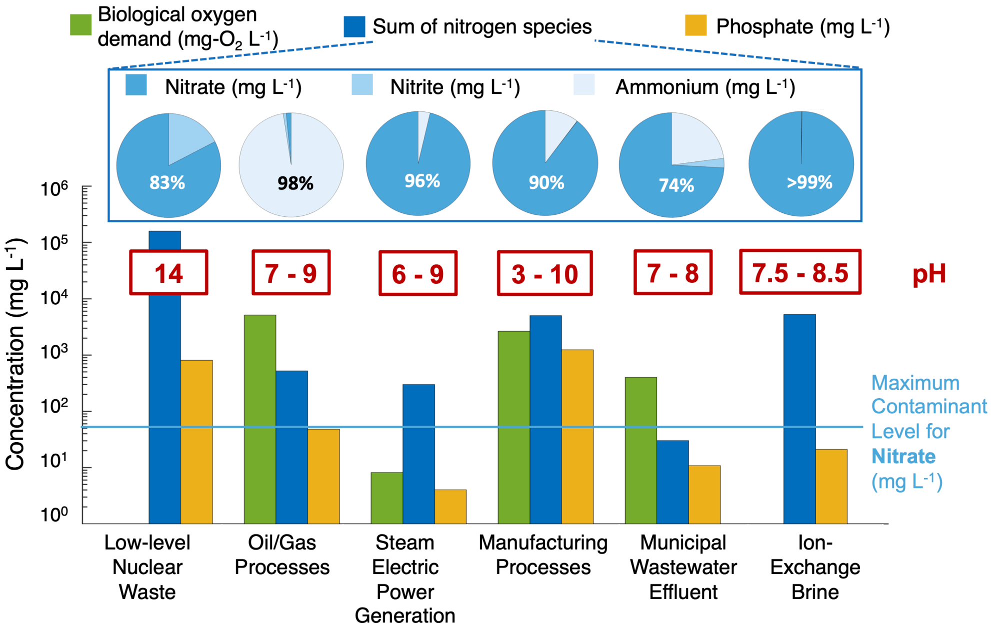

Figure 1-1: Concentrations of biological oxygen demand (mg-O_2/L), nitrogen species, and phosphate (mg-PO_4^{3-}/L) in different waste streams. Percentage breakdown of nitrogen species – NO_3^- (mg-NO_3^-/L), NO_2^- (mg-NO_2^-/L) and NH_4^+ (mg-NH_4^+/L) is indicated for each source. Data was compiled from the US Environmental Protection Agency (EPA) development documents,[15,16] EPA's database for industrial wastewater treatment technologies,[17] and pertinent journal papers.[18–40] EPA's specifications for nitrogen-contaminants in drinking water: < 44.3 mg-NO_3^-/L (dashed blue line) and < 3.3 mg-NO_2^-/L.[14]

bodies of water, which is a leading cause of dead zones.[41–43] This source-dependent fluctuation in the NO_3^- concentrations and the resulting variations in pH motivates our study to quantify these effects on reaction selectivity for the NO_3^--to-NH_3 conversion and solar-to-chemical process efficiencies for NO_3^- transformation to various reduced products including NH_3, N_2O and N_2.

State-of-the-art nitrate treatments are biological nitrification-denitrification processes for water treatment, and ion-exchange reactors for drinking water applications. Biological wastewater treatment is a two-step process where microbes first aerobically and sequentially oxidize NH_4^+ to NO_2^-, followed by NO_2^- to NO_3^-, and then anaerobically reduce NO_3^- to N_2 with the aid of a carbon-donor.[44] This process has an estimated energy intensity of nearly 45 MJ kg_N^{-1} including parasitic energy costs for pumping, aeration and deaeration. For proof-of-concept bioprocesses like Sharon-Anammox, the energy intensity is even more competitive and estimated to be 10-16 MJ kg_N^{-1}.[45,46] These lower energy requirements are tied to Sharon-Anammox's benefits over traditional nitrification-denitrification techniques: lower oxygen levels, donor carbon demand, sludge production, and N_2O emissions are all due to an optimization between the effluent from the Sharon process, which does the partial nitrification step, and the Anammox process, which forms the N_2.[47] Because even the traditional nitrification-denitrification process is competitive and unbeaten on an energy basis, it has been adopted for large-municipality-scales of wastewater treatment (10^3 – 10^6 m^3 day^{-1} depending on the size of the population served.[48] However, a drawback of these approaches is the lost opportunity to recover the nitrogen nutrients. Additionally, microbial cultures can be highly sensitive to operating environments, especially pH (6.8 – 7.3), oxygen content (1.1 – 3.8 mg L^{-1}), carbon-donor loading (0.27 – 0.36 kg m^{-3} day^{-1}), and temperature (19.8 – 26.0˚C).[48–51] This factor will preclude the use of biological processes for direct treatment of most point sources of wastewater (Figure 1-1). For drinking water applications, ion-exchange reactors selectively remove nitrates with the use of selectively permeable resins. To continuously use these resins, they need to be regenerated, which results in the production of a nitrate-concentrated wastewater brine (Figure 1-2).[52]

Overall, there is a need for processes that are compatible to treat varying concentrations and pH conditions of wastewater streams while facilitating recovery of value-added products and restricting the generation of secondary waste streams. Electrocatalytic reduction of NO_3^- offers a promising route to harness renewable energy (solar, wind, etc.) to recover wastewater NO_3^- as NH_3, nitrous oxide (N_2O), and N_2 (Figure 1-2). Converting NO_3^- to NH_3 would not only remove the harmful pollutant from the source stream but also recover nutrients, as dissolved NH_3 can be repurposed as a fertilizer (aqua ammonia).[53] Gaseous NH_3 can be used as a fuel as well as a H_2 carrier but would require additional energy inputs to separate the highly soluble ammonia from the aqueous solution phase.[45,54,55] Even though N_2O is a potent greenhouse gas, it can be used as a powerful oxidizer when it is used during a combustion reaction instead of O_2.[56] For example, in the combustion of CH_4, this switch increases the energy released by the reaction by 37%.[57,58]

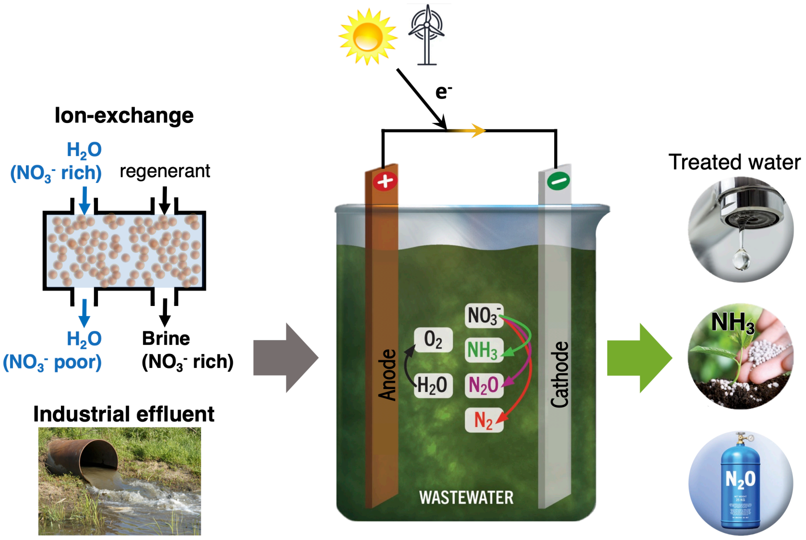

Figure 1-2: Schematic depicting the electrochemical reduction of wastewater nitrates (from sources like ion-exchange brine and industrial effluent) into N-species products (NH_3, N_2O, N_2) for water recovery, nutrient (NH_3), and energy (N_2O). The paired reaction at the anode was assumed to be water oxidation. The energy input to the system can be any renewable electron source.

The electrocatalytic reduction of NO_3^- can also be powered by sunlight with the use of photoactive materials for water oxidation at the anode in Figure 1-2. Relative advantages of this (photo)electrochemical process in comparison with biological and ion-exchange treatment processes include the recovery of NO_3^- as nutrients (NH_3) or energy (N_2O, NH_3) without the generation of additional waste. Prior work has extensively investigated the electrocatalytic reduction of NO_3^- to N_2 on Pt and Pd catalysts and NO_3^- to NH_3 on Cu, Fe, and Ni catalysts.[59–61] Cu is of particular interest due to its low cost, high affinity to NO_3^- adsorption, and selectivity towards NH_3 production.[59] The majority of these studies have been performed within a limited window of solution compositions, either highly alkaline (pH $\geq$ 12) and concentrated NO_3^- solutions ($\geq$ 0.1 M) or neutral pH (pH 6 – 8) and dilute NO_3^- (< 15 mM) solutions, whereas wastewater stream compositions vary much more widely (Figure 1-1).[61–63] In the alkaline pH region, quantitative studies on the kinetic behavior and stability for different pH and concentration conditions have been sparse, in particular for Cu.[61–63] My work focuses on experimentally characterizing the influence of pH and NO_3^- concentration, using representative combinations from different wastewater streams, on the activity, stability, and selectivity of a commercially-available polycrystalline Cu electrode.

1.2 Photocatalytic Solar Water Splitting to Produce Hydrogen

The development of artificial photosynthetic systems can enable the conversion of solar energy, which is a plentiful resource that is limited by its intermittency and its diffuse nature, into storable chemical bonds like hydrogen and oxygen from water splitting.[64,65] Figure 1-3 depicts examples of different architectures that can drive the thermodynamically uphill water splitting reaction using solar energy, including photovoltaic-assisted electrolysis, photoelectrochemical

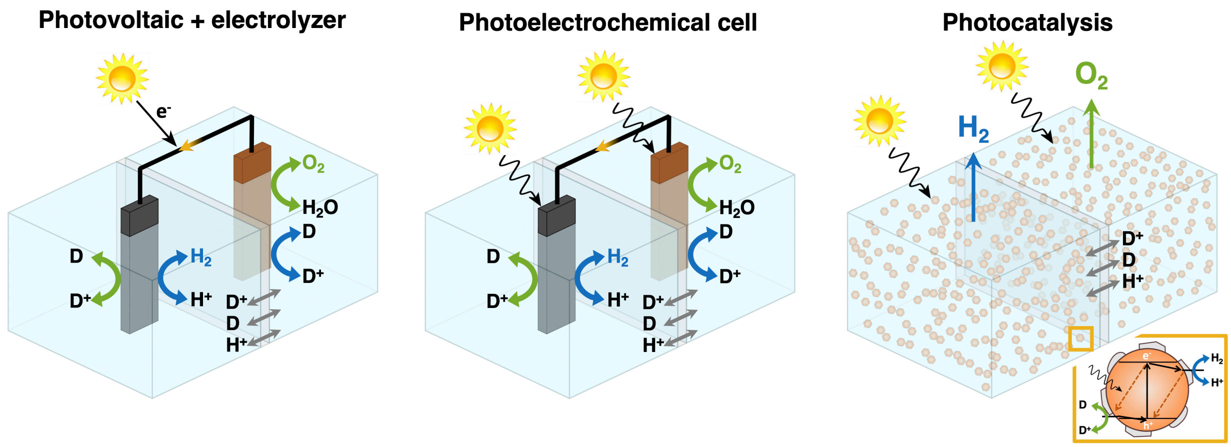

Figure 1-3: Schematics depicting standard architectures for photovoltaic + electrolyzer, photoelectrochemical cell, and photocatalysis water-splitting approaches. Inset shows the charge separation occurring on the particle in suspension evolving H_2. D/D^+: redox shuttle species

devices, and photocatalysis. In photovoltaic-powered electrolyzers (PV-electrolyzer), electricity from photovoltaic cells are current matched with an electrolyzer to produce H_2. Photoelectrochemical devices integrate charge-carrier generation with chemical reactions at functional semiconductor-electrolyte interfaces. While these systems can also attain comparable efficiencies to PV-electrolyzer concepts with high-efficiency solar-cell materials, the durability of such photoactive materials is a critical challenge.[66] In photocatalytic systems, typically oxide-based semiconductor materials, which are stable in water, generate photo-excited charge carriers as dictated by the semiconductor material band gap. Charge carriers that are transported to the surface can effect at least one reduction reaction at the conduction band and one oxidation reaction at the valence band (Figure 1-3) on the photocatalyst surface. Photocatalysis with aqueous suspensions of particles present a potentially cost-competitive H_2 production pathway driven by low cost materials and reactor designs, but cogeneration of H_2 and O_2 is a drawback (Figure 1-3).[66] Large scale proof-of-concept reactors have been developed using panels made with immobilized Al-doped $SrTiO_3$ photocatalysts, with a bandgap of 3.2 eV, which attained up to 0.76% solar-to-hydrogen (STH) efficiencies under natural sunlight.[67,68]

Z-scheme photocatalyst suspension reactors are inspired by natural photosynthesis and can facilitate the separation of H_2 and O_2 products generated while retaining many of the expected cost advantage from particle-suspension reactor designs.[69,70] These reactors comprise of two reaction compartments with different (or identical) light absorbers suspended in an aqueous solution. On the surface of the oxygen evolving light absorber (e.g. $BiVO_4$, Mo-doped $BiVO_4$, TiO_2),[71–73] ideally, water oxidation is coupled with reduction of an aqueous redox shuttle represented by D^+/D in Figure 1-4. The reduced form of the redox shuttle, D, is transported via a membrane/porous separator, to the other reaction compartment, where the hydrogen evolving light absorber (e.g. TiO_2, Rh-doped $SrTiO_3$, Ir-doped $SrTiO_3$)[70,71,74] should ideally effect the oxidation reaction (D to D^+) while simultaneously reducing H^+ or H_2O to H_2. The onus of performance in these Z-scheme reactors is critically reliant on (a) highly selective reactions on the photocatalysts despite the prevalence of thermodynamic and kinetic driving forces to drive the back reactions for the redox shuttle (as indicated by the dashed arrows on Figure 1-4), and (b) rapid transport of redox shuttles between the two compartments. Prior work by Bala Chandran et al. has demonstrated the need for asymmetry in the redox shuttle kinetics on the co-catalysts, with the smallest rates of competing shuttle reduction found for anodic charge transfer coefficients of 0.9 and optimal exchange current densities.[69] Symmetric charge transfer coefficients result in high rates of shuttle reduction taking place, for all exchange current densities considered. Additionally, H_2 oxidation was also demonstrated to be a significant competing reaction.[69] Keene et al. have demonstrated that the STH efficiencies are sensitive to the exchange current density assumed for the redox shuttle reaction, even when only considering selective reactions.[75] As a mitigation strategy, prior work has shown that competing reactions can be prevented and therefore solar-to-hydrogen conversion efficiencies can be boosted through the introduction of a selective coatings.[70] For example, CrOx coatings for Rh co-catalysts on oxide semiconductors and carbon-modified SiO_x films on Pt thin film electrodes have been shown to be effective in preventing the back reaction of O_2 reduction by preventing O_2 transport through the surface.[70] These additional layers affect the mass-transport of species to the catalyst and particle reactive surface (Figure 1-4), and can therefore affect the reaction kinetics as well.

The operation of a semiconductor material driving electrochemical reactions has been widely modeled using equivalent circuit models. The semiconductor material can be modeled as a photodiode in series with electrochemical loads, which can represent the kinetics of the electrochemical reactions taking place, the ohmic/solution resistance, and the mass-transport limitations of the species present. Additional competing reactions can be added as parallel branches for the relevant electrode. This approach can predict solar-to-fuel efficiencies as the material thermodynamic properties, reaction kinetic parameters, and species mass-transport behavior are varied. Prior work in the water-splitting field has established the expected behavior of a photodiode, ideal and non-ideal, in series with electrochemical loads, accounting for reaction kinetics and solution resistance.[76–78] The effect of competing back-reactions, however, remains unexplored in these models even though it is a widely known issue for photocatalysts with additional catalysts on the particle surface.[70] In this work, the effects of competing reactions, species mass-transport, and the presence of a selective coating on the STH efficiency and selectivity were explored using an equivalent circuit model.

This framework is applied not only for water splitting to produce H_2, but to also predict solar-to-chemical efficiencies for a photoelectrochemical system that converts wastewater nitrates to ammonia. The dependencies of the solar-to-chemical efficiencies on the semiconductor band

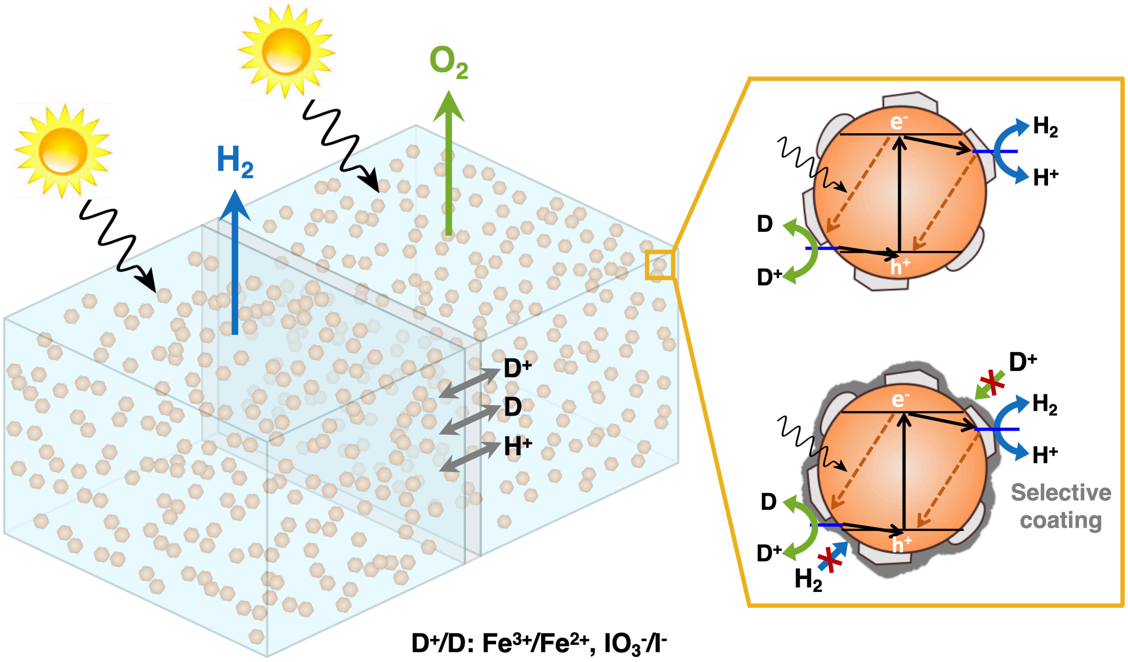

Figure 1-4: Suspension of particles undergoing photocatalytic water-splitting for the generation of H_2 and O_2 in a Z-scheme photocatalyst reactor. Schematic representations of thermodynamic driving forces for both forward and backward reactions at the conduction and valence bands. A selectively permeable coating allows for only the desired reactions (hydrogen evolution reaction and oxidation of D^+/D) to occur as a result of the modified mass-transport toward the catalyst surface.

gap, the concentration of nitrates in solution, the presence of competing electrochemical reactions and their respective reaction kinetics were all considered.

1.3 Thesis Outline & Research Contributions

This work includes both experimental data and modeling work probing nitrate reduction to ammonia and photo-induced water-splitting.

Chapter 2 is adapted from a manuscript recently submitted for publication. It explores the dependencies of the nitrate reduction to ammonia reaction on concentration, pH, and surface composition for a copper catalyst. These effects were studied using common techniques such cyclic voltammetry and chronoamperometry, with additional spectroscopy techniques, such as *in situ* electrochemical impedance spectroscopy and UV-Vis spectrophotometry, used to further quantify the dependencies. This work has equal contributions from two lead authors – Barrera and

Silcox; Barrera, Silcox, and Bala Chandran conceived and implemented this research. Barrera, Silcox, and Bala Chandran designed the cyclic voltammetry experiments. Barrera, Silcox, Giammalvo, Brower, and Isip conducted the cyclic voltammetry experiments. Barrera, Silcox, and Bala Chandran designed the chronoamperometry experiments and Silcox designed the electrochemical impedance spectroscopy (EIS) experiments as well as the EIS analysis approach. Both Barrera and Silcox conducted the chronoamperometry and EIS experiments, developed the energy analysis and analyzed all results; Barrera conducted the Tafel kinetics analysis; Barrera designed and conducted the UV-Vis spectroscopy calibration, measurements and analysis; Bala Chandran and Barrera developed and implemented the error quantification approach; writing and data analyses were done by Barrera, Silcox, and Bala Chandran.

Chapter 3 has been modified from a paper published in ACS Sustainable Chemistry & Engineering.[46] It presents the feasibility of harnessing solar energy to convert nitrates into ammonia and nitrous oxide for different band gaps, concentrations of nitrates, and competing reactions by using an equivalent circuit model framework. Bala Chandran and supervised conceived this research; Barrera and Bala Chandran performed calculations, data-analyses, and wrote the paper. In addition, measured product selectivity toward NH_3 production and reaction kinetics for the Cu catalyst from Chapter 2 were used to project solar-to-chemical process efficiencies using the equivalent circuit model.

Chapter 4 presents an equivalent circuit model formulation for photo-induced water-splitting that accounts for mass-transfer effects and competing reactions and that was used to explore the effect of competing undesired reactions, limiting current densities, redox shuttle kinetics, and the implementation of a selective coating to favor the desired reactions. This chapter has been modified from a manuscript currently in preparation and includes inputs from contributors outside of University of Michigan through a collaborative project funded by the U.S. Department of Energy (DE-EE0008838)

Finally, Chapter 5 presents concluding remarks and possible avenues for future work.

Supplementary information is included in the Appendices A through G.

Chapter 2 Concentration, pH, and Polycrystalline Copper Electrode Surface Affects Nitrate Reduction Activity and Selectivity to Ammonia and Nitrite

Adapted from a manuscript under review: *Barrera, L.*, Silcox, R.*, Giammalvo, K., Brower, E., Isip, E., Bala Chandran, R., "Concentration, pH, and Polycrystalline Copper Electrode Surface Affects Nitrate Reduction Activity and Selectivity to Ammonia and Nitrite".*

2.1 Introduction

Excessive anthropogenic production of nitrogen fertilizers has disrupted the natural nitrogen cycle. This imbalance has resulted in the global contamination of groundwater and surface water with reactive nitrogen contaminants, including nitrates (NO_3^{-}), nitrites (NO_2^{-}), ammonia/ ammonium (NH_3/NH_4^{+}), causing environmental threats such as dead zones and health risks in humans and aquatic wildlife.[41–43] However, these contaminants, especially NO_3^- that is dominantly present in many waste streams, represent an untapped resource for nutrient (nitrogen) and energy recovery.[79–82] This study focuses on evaluating the effects of NO_3^- concentration, pH and polycrystalline electrode surfaces on the electrochemical conversion of NO_3^- to NH_3 by copper catalysts.

The state-of-the-art nitrate treatments are biological nitrification-denitrification for wastewater treatment and physical separation technologies, such as ion-exchange and reverse osmosis, for drinking water.[83,84] These approaches are effective for removing NO_3^- in the form of N_2 (biological nitrification-denitrification) or for moving the NO_3^- into a separate, more concentrated secondary waste stream (ion-exchange, reverse osmosis). Recent work has explored electrochemical techniques to convert NO_3^- to NH_3 to recover the nitrogen nutrients present in waste streams.[9-23] The electrocatalytic behavior of metallic catalysts (Cu, Ni, Ti, Pt, Pd),[61,62,84–86] bimetallic catalysts (CuNi, CuPd),[61,62,84] and single-crystal electrodes (Cu, Pd, Pt)[87–90] has been reported with model electrolyte solutions, for select NO_3^- concentrations and pH conditions. In particular, Cu and Cu-based materials have been extensively studied due to its high affinity for NO_3^- adsorption and its low cost relative to more commonly used noble metals.[60,84,91,92] Many prior investigations have either considered dilute NO_3^- solutions (< 15 mM) for neutral conditions (pH 6 – 8) and concentrated NO_3^- solutions (≥ 0.1 M) for strongly alkaline media (pH ≥ 12).[61–63] Current-potential behavior for nitrate reduction, specifically probing the rate-determining two electron transfer step that reduces NO_3^- to NO_2^-,[85,93] have been widely reported for Cu under alkaline conditions (pH ≥ 12).[85,94,95] While new electrocatalysts are being modeled and measured for enhanced activity and selectivity in neutral pH conditions,[61–63] experimental measurements for polarization behavior, kinetic behavior, and stability assessments are generally sparse, including for Cu catalysts. Additionally, source-dependent variability in wastewater composition leads to a wide range of pH and NO_3^- concentrations that should be considered. In prior work, we reported that NO_3^- concentrations can vary from 1 mM to 2 M depending on the source of the waste stream[46] and pH values of these streams can range from 3 to 14.[18,21,34,96] Therefore, even with a widely studied material like Cu, comprehensive measurements are required to quantify pH and concentration dependence of its activity and selectivity for nitrate reduction.

Distinct from the effects of concentration and pH, the electrode surface facets have also been reported to influence the kinetic performance of Cu catalysts.[87,97] Pérez-Gallent et al. experimentally showed that Cu(100) exhibited higher current densities for NO_3^- reduction as compared to Cu(111) with 2 mM $NaNO_3$ at pH 13, whereas Cu(111) has lower current densities despite a lower onset potential because of sensitivity to surface poisoning effects.[87] In contrast, Hu et al. have demonstrated using density functional theory models that for neutral and alkaline conditions, Cu(111) drives the nitrate reduction more efficiently than hydrogen evolution when compared to the Cu(100) and Cu(110) surfaces.[97] These outcomes motivate the question of how the different facets present in commercially available polycrystalline Cu electrodes can influence its kinetic behavior and affect experimental trial-to-trial uncertainties. To this effect, many excellent reviews highlight the value of electrochemical impedance spectroscopy to characterize the effects of polycrystals,[98,99] pH,[100,101] concentration,[100] grain boundaries,[98,102] and surface non-homogeneity of the electrode-electrolyte interface.[99,102] Prior studies have obtained capacitances, derived from constant phase elements, and charge-transfer resistances from impedance measurements to probe reaction mechanism dependencies on applied potential.[103] On Fe-doped $SrTiO_3$ electrodes, large statistical variation in surface capacitance values were measured through microcontact impedance spectroscopy and attributed to variations that stem from a polycrystalline surface.[104] To this end, we performed electrochemical impedance measurements of the same polycrystalline Cu surface over several trials and correlated capacitance and resistance with activity and selectivity measurements. To the authors' knowledge, such correlational analyses have not been done in prior work for Cu electrodes performing NO_3^- reduction reactions to probe measurement uncertainties.

Motivated by the outlined knowledge gaps, this study has two main objectives. The primary objective of this study is to experimentally quantify the influence of pH and NO_3^- concentration on the electrocatalytic performance of a polycrystalline Cu electrode. A secondary objective is to understand and interpret trial-to-trial variabilities observed with our measurements on these electrodes. Cyclic voltammetry and chronoamperometry were performed to evaluate electrochemical performance in 0.1 M, 0.5 M, and 1 M $NaNO_3$ solutions at pH 8, 10, and 14. Cyclic voltammograms inform the landscape of electron-transfer reactions and quantify influences of NO_3^- concentration and pH on kinetic behavior. Chronoamperometry measurements probe activity and selectivity towards NH_3 and NO_2^- formation at a fixed potential and enable stability assessments as a function of pH. These results are further interpreted to determine how concentration and pH influences the process energy intensity to recover reactive nitrogen contaminants as NH_3. Electrochemical impedance spectroscopy was applied as a diagnostic tool to correlate double layer capacitance and charge-transfer resistance with measured faradaic efficiencies and currents for NO_3^- to NO_2^- conversion. This analysis provides insights to delineate effects of the electrochemically active surface area and the facets present in a polycrystalline electrode on uncertainties in the activity and the selectivity measurements. Notable advancements in this study include comprehensive pH and concentration dependent quantification of activity, selectivity, and stability of polycrystalline Cu electrodes to form NO_2^- and NH_3, as well as the use of electrochemical impedance measurements to deconvolute underlying factors that resulted in trial-to-trial variabilities using the same polycrystalline Cu electrode.

2.2 Experimental Set-up and Methods

2.2.1 Selection of NO_3^- Concentrations and pH Conditions

The pH values of the electrolyte were set to be 8, 10, and 14 to reflect typical conditions in ion-exchange brines,[105] electrical component manufacturing,[19] and low-level nuclear waste,[18] respectively. The concentration range was chosen using the corresponding NO_3^- concentrations for ion-exchange brines[105] (0.1 M) and low-level alkaline nuclear wastes[18] (1 M). The effects of competing ionic species were not considered in this study for the sake of simplicity and to isolate effects of NO_3^-/NO_2^- species on measured quantities.

2.2.2 Reagents, Solution and Electrode Preparation

Sodium nitrate ($NaNO_3$) (99.995% trace metals basis, Sigma-Aldrich, or 99.999% trace metals basis, Thermo Scientific) and sodium nitrite ($NaNO_2$) (99.999% trace metals basis, Sigma-Aldrich) were used to make the salt solutions. An analytical balance (W3100 Series, Accuris Instruments) was used to measure the weights of the salts required. All solutions were prepared using DI water (CENTRA R200, VEOLIA), diluted solutions of concentrated sodium hydroxide (NaOH) (50% in H_2O, Sigma-Aldrich) and a buffer solution to adjust the pH to 8, 10 and 14. All glassware used for solution preparation were washed thoroughly and rinsed with DI water prior to use. For pH 14, the sample solution was prepared using a 1 M NaOH solution without any other salt/buffer additions to the solution. At this pH, the solution conductivity is high and minimizes ohmic potential losses in the solution. For the lower pH tests, buffer salts were added to maintain the pH and to achieve comparable solution conductivities to the pH 14 tests. For pH 10, the solution was buffered with 0.4 M of sodium phosphate dibasic (Na_2HPO_4) (≥99.0%, Sigma-Aldrich) and 0.095 mM of NaOH. For pH 8, the solution was buffered by 0.5 M of sodium phosphate dibasic and 0.04 M of sodium phosphate monobasic monohydrate ($NaH_2PO_4 \cdot H_2O$) (≥98%, Sigma-Aldrich). The pH 8 buffer concentration was optimized to maintain the pH very close to a value of 8, even after the addition of 1 M $NaNO_3$, while keeping the buffer species concentrations within their solubility limits. Buffer salt concentrations used at pH 8 and 10 led to similar ionic conductivities (8.21 S m^{-1} for pH 8 and 6.29 S m^{-1} for pH 10) and remained somewhat comparable to the ionic conductivity at pH 14 (24.81 S m^{-1}), without the presence of $NaNO_3/NaNO_2$ salts. Solution pH was measured using a pH meter (STARTER 2200 pH Bench

Meter, OHAUS) with a measurement precision of ± 0.01 pH. All starting pH values are within 0.3 pH points from the desired pH, with the largest difference occurring for pH 8 at 1 M $NaNO_3$ due to increased interference of NO_3^- with the buffer.

2.2.3 Cyclic Voltammetry

Cyclic voltammetry (CV) studies were run in a three-electrode cell (Figure 2-1) using a BioLogic potentiostat (BioLogic VSP Potentiostat), with a 20 mV s^{-1} scan rate and a stir rate of 900 rpm. The scan rate was chosen to be slow enough to probe interesting features in the polarization curves, but fast enough to be time efficient to run many trials. Different from prior CV studies on copper electrodes, the electrolyte was stirred to probe the influences of surface kinetics while avoiding confounding effects due to mass-transfer limitations. The stir rate was chosen to be large enough to facilitate bubble detachment on the surface of the disk electrode while resulting in minimal lateral shaking of the stir plate (Corning PC-410D), which occurred for stir rates larger than 900 rpm. The working electrode potential ranges for the CV studies were scanned from 0.2 V to -0.65 V versus the reversible hydrogen electrode (RHE), such that the spanned potentials were all more negative as compared to the onset of NO_3^- reduction to NO_2^- without driving significant competing hydrogen evolution on the copper surface. The maximum value was limited by the pH-specific copper oxidation potentials.[106] All potential values unless otherwise noted are referenced against RHE in this study.

A polycrystalline copper disk electrode (3 mm in diameter, BASi) was used as the working electrode and a Pt wire (99.95% purity, BASi) was used as the counter electrode for all the CV measurements. The current densities were calculated using the current response and the geometric area of the working electrode. For the reference electrode, depending upon the pH of the solutions tested, either an Ag/AgCl electrode (3 M KCl, BASi, for pH 8 and 10) or a Hg/HgO electrode (1 M

NaOH, BASi, for pH 14) were used as the reference electrodes. All potential values unless otherwise noted are referenced against RHE in this study. The working electrode was polished using a polishing alumina suspension (0.05 μm particle size, BASi) and rinsed with DI water (CENTRA R200, VEOLIA) prior to use. Solutions are degassed by sparging with inert gases (blank solution with N_2 (99.95% purity, Cryogenic Gases) and the $NaNO_3$/$NaNO_2$ species solution with Ar (99.999% purity, Cryogenic Gases)) for at least 5 minutes with flow rates of 1-2 standard liters per minute, as measured using a mechanical flowmeter (2500 Series, BROOKS Instruments). Due to the small volume (10 mL) of the cells used in these tests, the solution was saturated with the sparging gas within 5 minutes.

Each CV study was preceded by an open-circuit voltage study (OCV) that was run for 10 minutes or until the potential stabilized, as determined by the potentiostat. The stable OCV potential value was used as a starting point for the CV test. For every study, a “blank” solution without the $NaNO_3$/$NaNO_2$ salts was first run for at least 25 cycles, until stable and repeatable polarization curves were measured. This test was immediately followed by the CV with the reacting species, NO_3^-/NO_2^-, present, and run for ~35 cycles or until stable polarization behavior is recorded. The electrodes were moved from the blank to the species solution as quickly as possible to minimize the amount of time the copper electrode that was exposed to air and water without a potential being applied. Cycle-to-cycle stability in the polarization curves was quantified by calculating the average of the change in current at any potential between two sequential cycles for the last five cycles. Stability is achieved when average change for any of the last five cycles is less than 5%. The pH of the bulk solution was measured before and after the experiment.

For most pH conditions, the NO_3^- to NO_2^- reduction (Eq. (2-1)) has been determined as the rate-determining step of the nitrate reduction process.[93,107]

$$NO_3^- + H_2O + 2e^- \rightarrow NO_2^- + 2OH^- \tag{2-1}$$

The Tafel kinetic parameters – j_0 and α_c – were extracted for this step using Eq.(2-2),[108]

$$j = j_0 \exp\left(\frac{-\alpha_c\, F\, \eta}{R_c\, T}\right) \tag{2-2}$$

where, j (in mA cm^{-2}) is the measured current density, j_0 (in mA cm^{-2}) is the exchange current density dependent on species concentration, α_c is the charge transfer coefficient, $\eta = V_{WE} - E^0_{RDS}$ is the overpotential defined with respect to the working potential and the standard state NO_3^--to-NO_2^- reduction potential of 0.835 V vs RHE (Eq. (2-1)), $F = 96485$ C mol^{-1} is the Faraday's constant, $R_c = 8.314$ J mol^{-1} K^{-1} is the gas constant, and $T = 298.15$ K is the temperature. The current-potential data for extracting these parameters are obtained from cyclic voltammograms at various NO_3^- concentrations and pH conditions tested. The potential ranges to extract this data are shown in Figure S4, and best-fit values for the exchange current density j_0 (y-intercept) and the charge transfer coefficient α_c (slope) were independently obtained (Table A-1).

2.2.4 Chronoamperometry and Electrochemical Impedance Spectroscopy

The chronoamperometry (CA) studies were also run in the same three-electrode cell (Figure 2-1) as the CV studies but using a different working electrode. The working electrode geometry was changed from a downward facing surface to a side-facing surface to improve bubble detachment, which is especially important when operating at large current densities. One working electrode was made for each pH tested from a polycrystalline copper plate (99.9%, McMaster-Carr, # 9821K11) with an exposed surface area of ~0.3 cm^2 (see Table B-1 for the exact area measurements of the pH-specific electrodes). The current densities were calculated using the current response and the measured geometric area of the pH-specific working electrode. Surfaces were initially polished using sequentially smaller diamond polish (15, 3, 1 μm Diamond Polish,

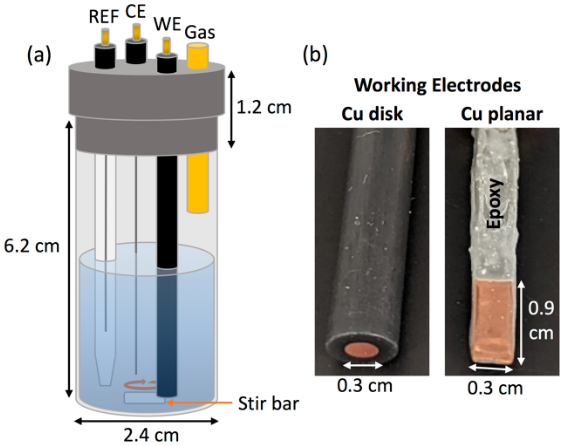

Figure 2-1: (a) Three-electrode cell set-up for cyclic voltammetry and chronoamperometry tests. REF: reference electrode, CE: counter electrode, WE: working electrode, Gas: gas inlet. (b) Electrodes used: (left) Cu disk electrode for the cyclic voltammetry studies and (right) Cu planar electrode for the chronoamperometry studies.

BASi) and unpolished surfaces of the working electrode were protected from the solution using epoxy (EA 9460 Loctite®). Between experiments, the planar working electrodes were polished using the same procedure as the CV experiments listed in Section 2.2.3. Solutions were also degassed with the same sparging treatment as described previously in Section 2.2.3.

Electrochemical impedance spectroscopy (EIS) measurements were conducted to quantitatively probe trial-to-trial changes in the double layer capacitance (C_{eff}), electrolyte solution resistance (R_e), and the charge transfer resistance for nitrate reduction (R_t).[109–111] The impedance channel in the potentiostat was used in these measurements without any extension cables and without a faraday cage. The EIS measurements were completed with the working electrode subjected to -0.1 V vs RHE for all pH, with an amplitude of 5 mV, from 50 kHz – 10 Hz, and with 8 data points collected per frequency decade. The voltage of -0.1 V was chosen to probe the charge transfer resistance of the nitrate reduction step (Eq. (2-1)). As will be shown in Figure 2-4, at more negative potentials NO_2^- reduction and hydrogen evolution can occur and therefore interfere in the charge-transfer resistance measurements for the NO_3^- to NO_2^- reduction step.

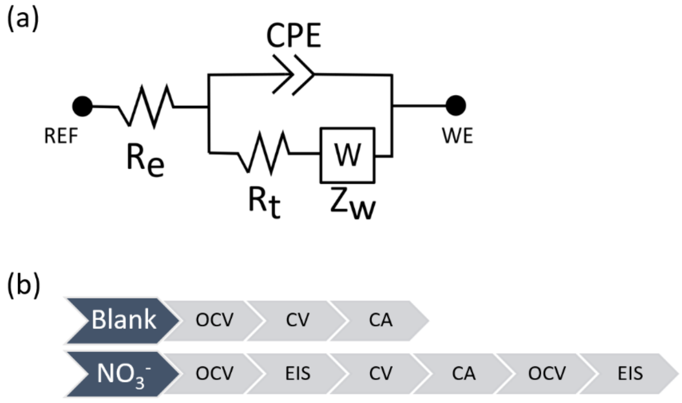

Figure 2-2: (a) Circuit diagram with a constant phase element, CPE, in parallel with a Faradaic resistance, R_t, and impedance from a Warburg element, Z_w, and both are in series with a solution resistance, R_e. A potential is applied at the working electrode (WE) with respect to the reference electrode (REF), while current flows between the WE and counter electrode (not shown). (b) Order of tests first conducted on the blank and then on the experiments with the species present. Open circuit voltage (OCV) measurements subject the WE to a potential where there is a negligibly small current passed between the WE and the counter electrode (not shown). pH measurements were completed before and after the whole series of tests for both the blank and the NO_3^- species experiments. Note that CV: cyclic voltammetry, CA: chronoamperometry, EIS: electrochemical impedance spectrometry.

To analyze the Nyquist plots generated from EIS measurements, the data for the real and imaginary portion of the impedance as a function of frequency was fit to a *R-CPE* circuit shown in Figure 2-2(a) with a constant phase element (CPE) with an impedance, Z_{CPE}, described by two parameters, Q and $\boldsymbol{\alpha}$ (Eq. (2-3)),

$$Z_{CPE} = \frac{1}{(\omega\, \boldsymbol{i})^{\boldsymbol{\alpha}}\, Q} \tag{2-3}$$

where, Z_{CPE} is the impedance of a constant phase element, $\boldsymbol{i}$ is $\sqrt{-1}$, ω (in Hz) is the frequency, and Q and $\boldsymbol{\alpha}$ are fitting parameters dictated by the double layer capacitance and a time delay associated with surface roughness or non-ideal conditions. This CPE is in parallel with a Faradaic or charge transfer resistance, R_t, and both are in series with a solution resistance, R_e (Figure 2-2(a)). For 1 M $NaNO_3$ at pH 8, the EIS data was indicative of mass-transfer limitations with a linear shape at low frequencies. Therefore, a Warburg impedance element (Eq. (2-4)) was also added in series with the R_t to represent the mass transfer limitation of the Faradaic reaction[112]

$$Z_w = \frac{\sigma}{\sqrt{\omega}} - \frac{\sigma}{\sqrt{\omega}}\boldsymbol{i} \tag{2-4}$$

where, Z_w is the impedance of a Warburg element and σ a function of the diffusion constant of the reacting species. For all other experimental test conditions, the Warburg constant, σ, was 0.

The CPE was included in the circuit to compensate for any surface non-homogeneity in the polycrystalline Cu-electrode and to improve the data fit.[109] To convert the CPE fitting parameters, Q and $\boldsymbol{\alpha}$, into an effective double layer capacitance C_{eff} with units of Farads, the Brug formula (Eq. (2-5)) was used. While many formalisms are used in the literature to convert CPE fitting parameters into an effective capacitance, the Brug formula was applied as it uses the solution resistance term to account for a distribution of time constants leading to a CPE behavior.[110,113]

$$C_{eff} = Q^{\frac{1}{\boldsymbol{\alpha}}}\left(\frac{R_e\,R_t}{R_e\ +\ R_t}\right)^{(1-\boldsymbol{\alpha})/\boldsymbol{\alpha}} \tag{2-5}$$

The effective impedance for the entire circuit is determined by Eq. (2-6),

$$Z_{eff} = R_e + \frac{Z_{CPE}\ (R_t + Z_w)}{Z_{CPE}\ +\ R_t + Z_w} \tag{2-6}$$

where, Z_{eff} is the effective impedance. Optimal values for R_e, R_t, Q, and $\boldsymbol{\alpha}$ were determined by using the nonlinear curve fitting function, *lsqcurvefit*, in MATLAB to fit the real and imaginary portions of Z_{eff} obtained from the Nyquist plot generated from EIS measurements. To maximize signal-to-noise ratio without using a Faraday cage, impedance values for $|Z_{eff}| < 105\ \Omega$ were used for data processing.[114]

EIS measurements were performed before and after chronoamperometry tests (Figure 2-2(b)). Therefore, initial and final values are available from these measurements for all relevant parameters (R_e, R_t, Q, $\boldsymbol{\alpha}$, and C_{eff}) and are listed in Table C-1 through Table C-6. The average charge transfer resistance (avg. R_t) and average effective capacitance (avg. C_{eff}) between the initial and final experiment were calculated for each trial. Even though these values change over the course of the CA measurement, average values are more relevant when comparing performance of different trials.

A series of tests, as shown in Figure 2-2(b), was performed on the polycrystalline planar Cu-electrodes using the test-cell in Figure 2-1 with solutions being stirred at 900 rpm. First, for the blank solution, an (1) OCV, (2) CV, and (3) CA were run right before the species reaction at every pH. No EIS was run for the blank solution since these did not have the same range in variability seen when NO_3^- was present in the electrolyte. Next, the sequence of tests with $NaNO_3$ was performed. An OCV was the initial step in the test sequence and was run for 10 min, or until stable potentials were measured. This was done to allow the electrode-solution interface to attain steady state before beginning the experiment. Next, an EIS scan was completed to determine the resistance and capacitance values, C_{eff}, R_t, and R_e (Eqs. (2-3)-(2-5)) before the constant-potential CA tests. Following this test, a CV was run for 1.5 cycles, starting from the OCV value, and ending at the starting point of the CA (see Table 2-1) with a scan rate of 20 mV s^{-1}. Getting a CV test prior to the CA measurement was useful for preconditioning the electrode surface, so smaller capacitive current jumps were seen at the beginning of the CA. The CA was run for 40 minutes at the potentials listed in Table 2-1 for the different pH values considered. The CA operating potentials were chosen to maximize the rate of selective NH_3 formation while minimizing possible competition coming from HER (Figure B-4) depicts the predicted Faradaic efficiencies and rates of ammonia formation estimated from the averaged response from the CVs).

Table 2-1: Potential ranges used in the CA and expected faradaic efficiency from the CV study

pH	**CA Potential (V vs RHE)**
8	-0.62 V
10	-0.6 V
14	-0.55 V

An OCV and an EIS measurement followed the CA to probe any surface capacitance and resistance changes post the constant-potential CA measurements. An OCV measurement preceded the 2nd EIS measurement to dissipate the local pH gradient back to a steady state value; a local pH gradient is expected to develop due to the release of hydroxide ions (OH^-) during the NO_3^- reduction reaction. The dissipation of this gradient following the experiment manifested as an immediate drop in the OCV potential measured right after the CA experiments for all pH and concentrations tested (Figure C-5). This allows for a reliable working electrode potential to be accessed throughout the 20-second-long EIS experiment, which depends on stable pH and potential readings. Additionally, a steady-state bulk solution phase enables correlating changes in R_t, before and after CA measurements, with changes in the NO_3^- concentrations or possibly the Cu surface, without any convoluting effects due to pH changes.

2.2.5 Concentration Measurements for NO_3^-, NO_2^-, and NH_3

Concentrations of NO_3^-, NO_2^-, and NH_3 were tracked using transmission measurements obtained in a UV-Vis spectrophotometer (UV-2600, Shimadzu). All analyses were done using a fast scan rate (4,000 nm min^{-1}) and a wavelength probe every 0.5 nm. Absorbance-concentration calibration curves were obtained over an identified range of species concentrations where the absorbance-concentration calibration curve was linear. Sample solutions were diluted appropriately to ensure the validity of using the calibration curves.

NO_3^- has a characteristic absorption peak at 303 nm, whereas NO_2^- has a characteristic peak at 355 nm with an additional absorption feature at 303 nm. Calibration curves obtained for these species are in Figure D-1 and Figure D-2, where we also report the measured molar absorption coefficient (L mol^{-1} cm^{-1}) following Beer's law (Eq. (E-1)) at these wavelengths. Because NO_2^- exhibits substantial absorption at a wavelength of 303 nm (~1.3 times that of NO_3^- at equivalent concentrations), the measured absorbance at this wavelength was deconvoluted in the presence of both NO_3^- and NO_2^- species. To do this, extracted molar absorption coefficients were applied to determine respective species concentrations (Table D-1).

Ammonia concentration was detected by using the salicylate method as described in Giner-Sanz et al.[115] A blue indophenol-like dye forms when ammonia is present in solution and has been found to be reliable for ammonia concentrations up to 60 μM.[116] In highly alkaline solutions (pH > 13.5), the characteristic peak of the formed dye is located at 650 nm, but the peak shifts towards larger wavelengths as the pH decreases.[117] Therefore, the measured samples were diluted using 1 M NaOH such that both the pH and concentration ranges were suitable for characterization. Calibration curves (Figure D-3) were repeated three times and measured with respect to DI water as the baseline. For all measurements, the final ammonia concentrations were determined by removing the signal from the supporting solution: the salicylate reagents were added to DI water to capture the contributions of NH_3 contaminations and of the colored reagents.

The calibration curves were obtained by using 10 μM – 50 μM solutions made from a 1 mM parent solution of ammonium chloride (ACS reagent, ≥99.5%, Sigma-Aldrich). Additional reagents used included a salicylate catalyst solution, composed of 2.75 M sodium salicylate (USP specifications, Sigma-Aldrich) and 0.95 mM sodium nitroferricyanide (III) dehydrate (≥99%, Sigma-Aldrich), and a hypochlorite solution composed of 90 vol% of 340 mM sodium citrate tribasic dehydrate (≥99.0%, Sigma-Aldrich) and 465 mM sodium hydroxide and 10 vol% of sodium hypochlorite aqueous (reagent grade, 4-4.99%, Sigma-Aldrich). Both reagents were made fresh for the analyses, with the salicylate solution kept in the dark. Solutions samples before and after CA tests were stored in the refrigerator and brought up to ambient temperature to perform the salicylate analyses. No effects are expected on the measured ammonia concentration due to aging for time periods less than 21 days. Fresh DI water was used in the preparation of the reagents and for the 1 M NaOH prepared for the dilutions. The diluted CA samples were analyzed in the following manner: 5 mL of the diluted sample solution were mixed with 0.6 mL of the salicylate catalyst solution, before adding 1 mL of the hypochlorite solution and mixing vigorously. The sample was then stored at room temperature and in ambient room light conditions, i.e., without any exposure to natural sunlight, for 1 hour before obtaining the absorbance spectra in the UV-Vis spectrophotometer.

2.2.6 Error Quantification

The largest errors stem from trial-to-trial variabilities, leading to a substantial spread in the measured currents during the CV and CA studies, and in the measured Faradaic efficiencies. Therefore, at least three separate trials were performed for each combination of the NO_3^- concentration and pH. Reagents and the buffer solutions for each test were prepared fresh within 24 hours of the study, and the NO_3^- or NO_2^- species were added right before the study was performed. For the concentration measurements, there are several possible sources of error for the final concentration value, such as the systematic error coming from solution preparation, the fit error from the calibration curves, and the trial-to-trial variation (Table 2-2). The full error propagation approach and species-specific error equations are included in Appendix E.

Table 2-2: Error associated with different components of the experimental set-up

Measurement	**Instrument**	**Error**
Mass	Scale	0.1 mg
Volume	Pipettes	4.39% (propagated error, Appendix E)
Concentration	Scale, pipette, and dilution	≤ 2.8 mM for NH_3 ≤ 5.1 mM for NO_2^- ≤ 0.16 M for 1M NO_3^- (initial) ≤ 0.41 M for 1M NO_3^- (final)
pH	pH meter	0.01 pH
Current	Potentiostat	10 mA on 5 A range
Potential	Potentiostat	20 V

2.2.7 Performance metrics

The concentrations of NH_3 and NO_2^- were quantified and used in Eq. (2-7) to find the quantity of charge passed during the experiment, Q_i, that resulted in either NH_3 or NO_2^- formation,

$$Q_i = C_i \,\rlap{/}V\, n_e F\,; \quad i = NO_2^-, NH_3 \tag{2-7}$$

where C_i is the measured concentration of NO_2^- and NH_3 in solution after the entire duration of the CA experiment, $\rlap{/}V$ = 7 mL is the cell volume, and n_e = 2 and 8 are the number of electrons exchanged respectively for NO_2^- and NH_3 formation. Eq. (2-8) was used to find the Faradaic efficiency FE_i of NO_3^- conversion to products including NO_2^-, NH_3, and H_2 at the potential fixed during the CA (Table 2-1),

$$FE_i = \frac{Q_i}{\int_0^{t_{CA}} I(t)\, dt}; \quad i = NO_2^-, NH_3, H_2 \tag{2-8}$$

where, $I(t)$ (in mA cm^{-2}) is the measured time-dependent current density, t (in seconds) is the time step and t_{CA} = 2400 s is the duration of the CA experiment. Any additional charge passed during the experiment that cannot be attributed towards NH_3 or NO_2^- formation could either be going towards H_2 formation or additional nitrogen reduction reactions. We estimated the FE_{H_2} by using the corresponding blank experiment while constraining its value such that net charge balance remained satisfied, i.e., sum of FE_{NH_3}, $FE_{NO_2^-}$ and FE_{H_2} cannot exceed 100%. Any additional passed charge that could not be attributed to NH_3, NO_2^-, or H_2 formation was assumed to be going towards additional species that were not detected in our measurements and was referred to as "unaccounted FE".

The rate of the nitrate-to-ammonia reaction $\dot{r}_{NH_3}$ (in g_N m^{-2} day^{-1}) was calculated using Eq. (2-9):

$$\dot{r}_{NH_3} = \frac{C_{NH_3}\, M_{\mathrm{N}}\, \cancel{V}}{SA\, t_{test}} \tag{2-9}$$

where M_{N} = 14 g mol^{-1} is the molar mass of nitrogen, SA (in m^2) is the surface area of the pH-specific planar electrode (Table B-1), and t_{test} = 0.0278 days is the duration of the chronoamperometry experiment.

Another standard metric is the overall energy required to convert NO_3^- to NH_3 per kilogram of nitrogen recovered (E_{NH_3} in MJ kg$_{\mathrm{N}}^{-1}$), shown in Eq. (2-10):

$$E_{NH_3} = \frac{V_{cell}\, Q_{total}}{C_{NH_3}\, \cancel{V}\, M_{\mathrm{N}}} \tag{2-10}$$

where V_{cell} (in V) is the measured potential across the cell and $Q_{total} = \int_0^{t_{CA}} I(t)\, dt$ is the total charge passed during the reaction (denominator in Eq. (2-8)).

2.3 Results and Discussion

2.3.1 Concentration and pH Effects on Cu Disk Electrodes

Figure 2-3 presents CVs for all combinations of $NaNO_3$ concentrations and pH tested, as well as the blank responses, using a Cu disk electrode. As will be shown in Figure 2-6, the experimental data cluster into two groups classified based on measured currents and to be conservative, Figure 2-3 presents the datasets that exhibit low currents at any potential for pH 8 and 14. However, for pH 10, all trials were taken into account as the data didn't cluster as prominently. Even though stabilized CV data are shown in Figure 2-3, the currents change significantly in the first 15 cycles (Figure A-1), which is indicative of adsorbed species reactions on the electrode surface, such as intermediate N-species in the nitrate reduction process, and possible deactivation due to H_2 adsorption.[87]

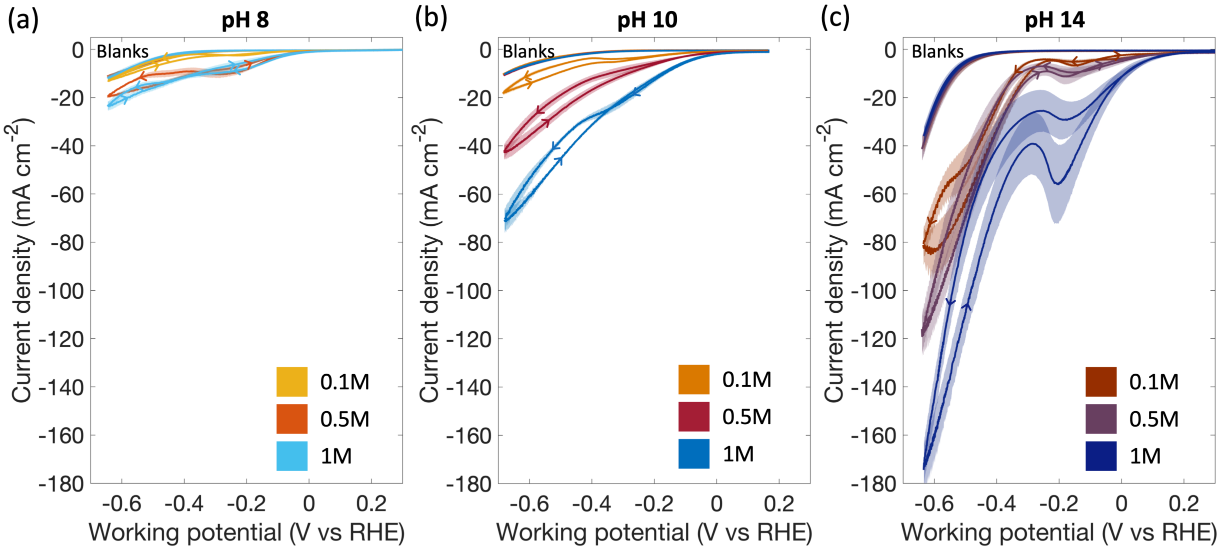

Figure 2-3: Cyclic voltammograms for 0.1 M, 0.5 M and 1 M $NaNO_3$ for (a) pH 8, (b) pH 10, and (c) pH 14 using a Cu disk electrode (Figure 2-1) with a scan rate of 20 mV s^{-1} and stir rate of 900 rpm. Average current density for the last and steady cycle is shown as a bold line with the shaded regions representing the standard deviation over at least 3 trials computed at every potential. Arrows indicate the direction of the sweep. Data in Figure 2-3(a) and Figure 2-3(b) for pH 8 and pH 10 is a selected subset of more experimental trials.

For all $NaNO_3$ concentrations tested, as pH increases the current densities attained for a fixed working electrode potential increase. Large gains are especially made when the pH changes from 10 to 14 and when $V_{WE} < -0.3$ V. For a 1 M concentration of $NaNO_3$, at -0.6 V the magnitude of the NO_3^- reduction current increases three-fold at pH 10, and seven-fold at pH 14, compared to the current density of 20 mA cm^{-2} obtained at pH 8. The rate of change of current densities with respect to concentration of $NaNO_3$ is pH dependent. This is explained by the combined influences of NO_3^- and OH^- concentration on kinetics and mass-transfer, and possibly a non-unity reaction order with respect to the adsorbed NO_3^- species for the rate-limiting NO_3^- to NO_2^- reduction reaction (Eq. (2-1)). At pH 8, while nearly comparable current densities are attained for both 0.5 M and 1 M $NaNO_3$ at all potentials, the current densities reached by 0.1 M $NaNO_3$ are 5 times smaller. This is indicative of kinetic/surface limitations being more dominant for the larger $NaNO_3$ concentrations, as well as higher levels of HER occurring for potentials lesser than -0.14 V.[97] This underscores that H_2 adsorption is a significant concern for smaller $NaNO_3$ concentrations. At pH 10, we observe roughly proportional variations with concentration at any potential for 0.5 M and 1 M $NaNO_3$. However, it breaks down for the 0.1 M $NaNO_3$ case, especially for potentials ranging from -0.1 V to -0.33 V, where the current densities are a half to a third of the values obtained with 0.5 M $NaNO_3$. This behavior is attributed to a bulk-limited production and consumption of intermediate species, likely NO_2^-, which also leads to a distinct peak in this potential window. For pH 14, the NO_3^--to-NO_2^- reduction current increases with NO_3^- concentration for potentials in the range of -0.25 V – 0.2 V due to the increase in driving forces. For more cathodic potentials, V_{WE} < -0.25 V, the current densities of 0.1 M and 0.5 M $NaNO_3$ solutions are similar, whereas the current density of 1 M $NaNO_3$ is proportionally larger for the same potentials. This behavior for the smaller concentrations can be attributed to the increased likelihood of depletion of the NO_2^- formed at these potentials, which results in the mass-transfer-limited response for 0.1 M $NaNO_3$ when the working electrode potential ranges between -0.5 V and -0.6 V.

For most cases in Figure 2-3, larger current densities are observed on the reverse or anodic potential sweep from -0.6 V to 0.2 V. This is in part attributed to the surface being cleared off of adsorbed H_2 species when the potential scan changes direction, thereby reversing H-poisoning on the Cu surface.[87,94] Similar outcomes have been previously reported by Perez-Gallent et al.[87] For all $NaNO_3$ concentrations, pH 8 is relatively more affected by this H-poisoning effect such that it results in slightly anodic current densities for 0.1 M $NaNO_3$.

To further understand the features/onsets in the CVs in Figure 2-3, Figure 2-4 shows the comparison of CVs obtained with the blank, 1 M $NaNO_3$ and 1 M $NaNO_2$ solutions as a function of pH. Key features and onsets in the polarization curve when NO_3^- is present are marked as C_1-C_4, with the equivalent features marked on the NO_2^- curve with C_1^*- C_3^*. The onset potential, C_1,

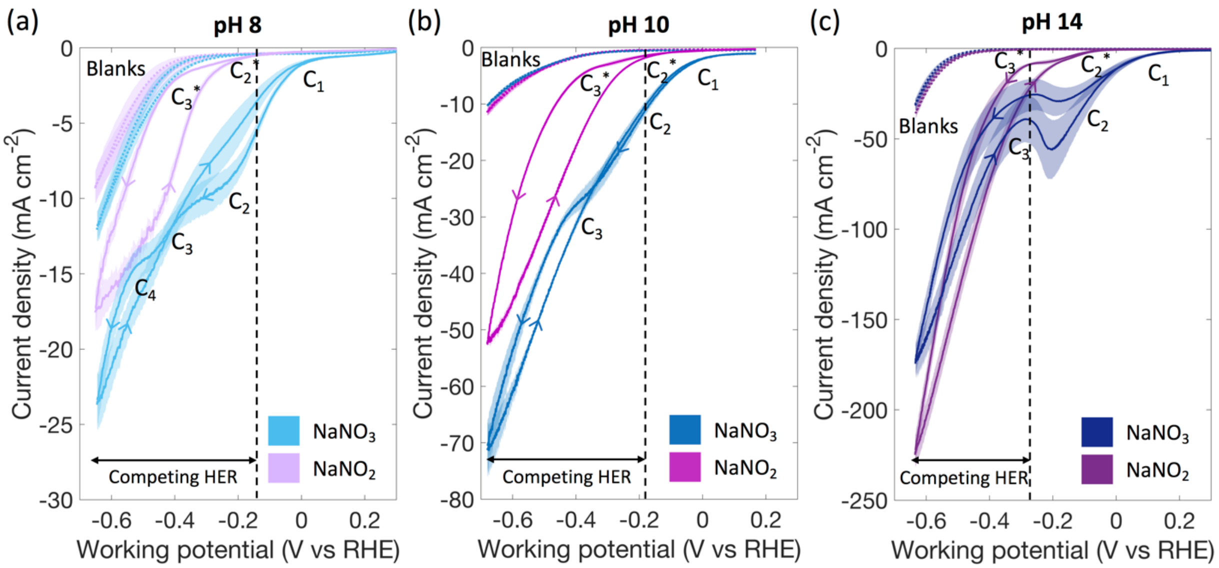

Figure 2-4: Cyclic voltammograms for pH and 1 M $NaNO_3$ and 1 M $NaNO_2$ concentrations for a Cu disk electrode obtained with a scan rate of 20 mV s^{-1} and a stir rate of 900 rpm at: (a) pH 8, (b) pH 10, and (c) pH 14. The blanks associated with each trial condition are shown as dotted lines. The onset of the blank is indicated by the vertical dashed line. Average current density for the last and steady cycle is shown as a bold line, with the shaded regions representing the standard deviation over all trials calculated at each potential.

corresponds to the NO_3^- to NO_2^- reduction reaction (Eq. (2-1)) as it is the onset feature that is consistently absent in the NO_2^- reduction response. Despite proton coupled electron transfer occurring during the NO_3^- to NO_2^- reduction reaction, the C_1 onset potential decreases and moves towards its equilibrium potential (0.835 V) with increase in pH – 0.012 V, 0.04 V, and 0.20 V for pH 8, 10, and 14 respectively. This trend points towards more favorable kinetics with increasing pH and can be attributed to differences in pH-dependent adsorption/desorption energies of reactant/product species.[97,118,119] For more negative potentials, the next onset is C_2, which is also present in the NO_2^- reduction curve, C_2^*, for potentials in the range of -0.1 V to -0.2 V. Only pH 8 has C_2 as a prominent feature on the NO_3^- curve, which possibly indicates kinetically slower rate of NO_2^- production at pH 8 compared to its consumption to form N-intermediates (Figure 2-4(a)). The subsequent common onset potential for all pH and concentration conditions tested is C_3 and C_3^* in the -0.2 V to -0.4 V range. This secondary change in slope is attributed to NO_2^-

transformation to many possible N-species including hydroxylamine (NH_2OH), nitric oxide (NO), and ammonia (NH_3). Reyter et al. attributed the C_2/C_2^* features with NO_2^- transformation to NH_2OH while the C_3/C_3^* features were associated with NH_3 formation from NO_2^-.[85] However, for pH 8 and 10, the C_3/C_3^* onsets overlap with the potential window where hydrogen evolution reaction (HER) can compete with NO_3^- reduction. For HER, the measured onsets are -0.14 V, -0.18 V and -0.27 V for pH 8, 10 and 14 respectively. Therefore, the extent of competition from HER is the smallest at pH 14, and consistent with theoretical evaluations of HER on Cu surfaces.[97] Finally, pH 8 exhibits a unique onset at -0.52 V, C_4, in the cathodic sweep when NO_3^- is present. This could possibly be due to transformations involving adsorbed H_2 species as H-poisoning has been shown to be more prominent at lower pH, but it is difficult to determine the root source by only using data from the CV.[85,97]

When a large cathodic potential of -0.6 V is applied at pH 8 and pH 10 with 1 M $NaNO_3$ and $NaNO_2$ solutions, the currents attained with only NO_3^- present overpowers the current from only NO_2^- present in the solution. This is attributed to the larger local NO_2^- concentration, produced from NO_3^- reduction (C_1), which can sustain larger NO_2^- or any other intermediate transformation to NH_3 at these potentials. However, for pH 14 the larger current densities arise when the bulk electrolyte is $NaNO_2$ instead of $NaNO_3$. This is because the local NO_2^- concentration is getting depleted at a faster rate relative to the rate of generation of NO_2^- from NO_3^-. Therefore, a larger concentration of NO_2^- in the bulk helps sustain these large currents. The same outcome of smaller currents with NO_3^- versus NO_2^- present in the bulk electrolyte was also observed for 0.1 M $NaNO_3$ at pH 10 (Figure A-3). This is driven by the slower rate of NO_2^- production on the surface from NO_3^- compared to the rate of NO_2^- transport from the bulk to electrode surface.

Overall, Figure 2-4 enables qualitative identification of reaction onsets and correlations to reactant/product and intermediate species through comparisons of CVs with different species. However, more comprehensive product quantification as a function of applied potential is required to conclusively deduce kinetic mechanisms.

Figure 2-5 shows the pH and $NaNO_3$ concentration dependence of the Tafel kinetic parameters extracted from the average data (filled markers in Figure 2-5) from the trials presented in Figure 2-3 as well as the spread in values when the individual trials were fitted (vertical lines with empty markers in Figure 2-5). The Tafel kinetics were extracted for the stabilized last cycle at the C1 onset where only the NO_3^- to NO_2^- reduction reaction is taking place. All values and corresponding goodness of fit (R^2) are listed in Table A-1. Consistent with the results in Figure 2-3, the exchange current densities increase dramatically with increasing pH for all $NaNO_3$ concentrations. For all concentrations, the exchange current density increases by a steeper margin as pH increases from 8 to 10 and slows down from pH 10 to 14. This could suggest a change of the NO_3^- reduction mechanism from near neutral to alkaline conditions. There is also a strong dependence on pH for the fitted α_c. Similar findings have recently reported pH dependencies of α_c for HER, where α_c varies with pH due to the surface coverage of H^+ species as well as competing available HER pathways, in both theoretical and experimental works.[120,121] Bulk NO_3^- concentration also impacts the fitted values for j_0 and α_c, which indicates a NO_3^- adsorption-controlled reduction to form NO_2^-.[94] For all pH, the kinetic parameters change by a small extent for the 0.1 M and 0.5 M $NaNO_3$ cases and more significantly for 1 M $NaNO_3$ in solution. Notably, at pH 8, the exchange current density, j_0, increases in magnitude by a factor of 20 when increasing the concentration from 0.1 M $NaNO_3$ to 1 M $NaNO_3$, whereas at pH 10, the j_0 decreased by a

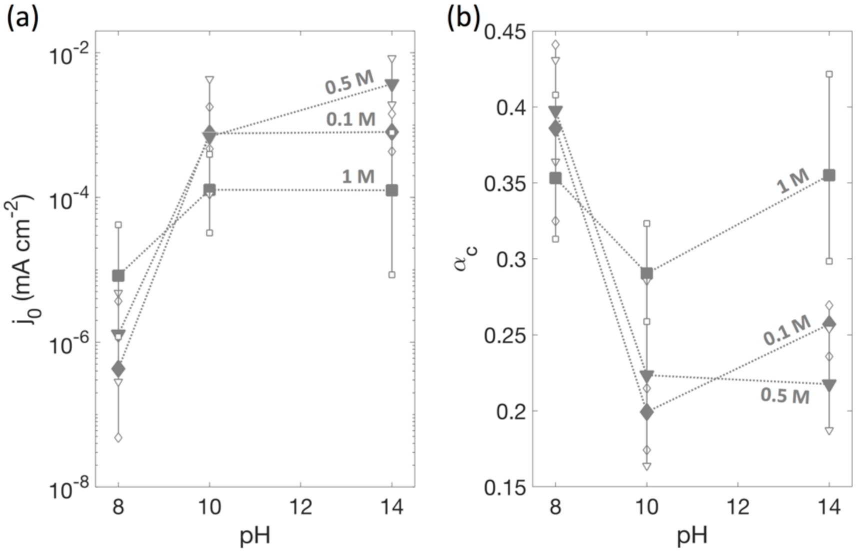

Figure 2-5: Tafel kinetics extracted from the CVs obtained with a Cu disk electrode for all pH and $NaNO_3$ concentrations in the NO_3^- to NO_2^- onset potential region: (a) exchange current densities j_0 (mA cm^{-2}) and (b) charge transfer coefficients α_c. The filled markers indicate the values extracted for the average behavior across all trials and the vertical lines with empty markers as endpoints indicate the range of values covered by the individual trials.

factor of 6. The decrease in j_0 is counterbalanced by the 45% larger α_c for 0.1 M as compared to 1 M $NaNO_3$.

To deconvolute the interdependencies between the fitted values of j_0 and α_c in Figure 2-5, we also obtained best-fit values by constraining α_c to be only pH dependent by averaging its values over the 3 concentrations measured, which resulted in $\alpha_C \propto 1.303 \times 10^7 [H^+] + 0.2495$ ($R^2 = 0.929$). With this constraint, the fit values for j_0 were monotonic with respect to NO_3^- concentration with reasonably good quality of fits to the data ($R^2 > 0.94$ for the averaged runs, $R^2 > 0.7$ for the individual trials, Table A-2). From these fits, the exchange current density is found to increase logarithmically with pH and linearly with bulk NO_3^- concentration (Figure A-5). Overall, the deduced kinetic parameters suggest a more pronounced change with pH from 8 to 10, compared to changes in pH from 10 to 14. While the exchange current density exhibits a strong dependence on both pH and NO_3^- concentration, the charge-transfer coefficient dependence on pH can be reasoned physically due to the proton-coupled electron transfer reactions for NO_3^-/NO_2^- reduction and the competition for surface sites between adsorbed NO_3^- and OH^- species on the electrode surface. Extracting these parameters not only allows for a better understanding of how the reactions of interest are taking place as the electrolyte composition is varied, but can also be used for modeling proposed devices as shown in Chapter 3.

Figure 2-3 and Figure 2-4 indicate that there is a substantial trial-to-trial deviation in the polarization curves obtained at any pH. This deviation when averaged over all concentrations increases with pH with maximum values of 2, 6, and 21 mA cm^{-2} for pH 8, 10, and 14, respectively. Additionally, for all concentrations and especially for 0.5 M $NaNO_3$, pH 10 has a distinct shape as compared to pH 8 and pH 14. We predict that these effects are a consequence of trial-to-trial variations in the crystallographic texture (surface roughness and exposed grain facets) of the polycrystalline Cu electrode, leading to variations in the active sites in contact with the electrolyte. Figure 2-6 interrogates these factors more comprehensively and presents data for individual trials for 0.5 M $NaNO_3$ as a function of pH. The same Cu disk electrode subjected to identical pretreatment procedures to obtain Figure 2-3 and Figure 2-4 was used in this dataset. For pH 8 and pH 14, the 5 trials for each pH cluster into two groups of datasets – *"high current density" (HCD)* data for 2 trials and *"low current density" (LCD)* for the remaining 3 trials. The HCD data were not present consistently for all concentrations for pH 14 and pH 8. It was present only for 0.5 M $NaNO_3$ at both pH values and for 0.1 M $NaNO_3$ for pH 8. For pH 10, the datasets lie in between the two types of responses and therefore categorizing them as one or the other is inconclusive. The HCD datasets are different from the LCD datasets in two attributes. The HCD data reaches larger NO_3^- reduction currents especially for more cathodic potentials and has a smaller onset potential for NO_3^- to NO_2^- reduction, especially at pH 14. This results in the loss of some of the features described in Figure 2-4 – the distinctive peaks or changes in slopes for the

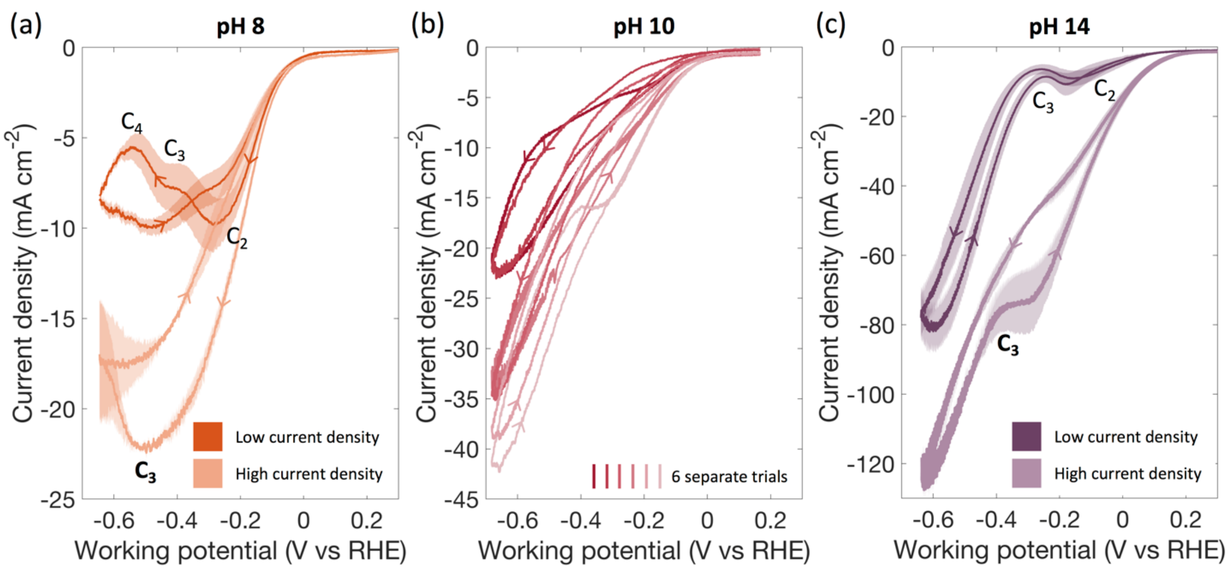

Figure 2-6: Cyclic voltammograms for 0.5 M $NaNO_3$ for a Cu disk electrode with a scan rate of 20 mV s^{-1} and a stir rate of 900 rpm at (a) pH 8, (b) pH 10 and (c) pH 14. For (a) and (c), two different clusters of measured datasets are observed and average current density values over multiple trials (at least 2) are shown in bold and the shaded regions represent the standard deviation. For (b), data from all trials are shown.

NO_2^- reduction, C_2, is difficult to distinguish for the HCD curves, and the features associated with N-species intermediate reduction, C_3, have shifted to more negative potentials as compared to the LCD data. Such variations can stem from the lack of control on the surface finish of the electrode and therefore the electrochemically active surface area (ECSA) from one trial to another. It could also arise due to differences in the active facets in the electrode that are catalyzing the reactions, e.g., Cu(100) vs Cu(111) in a polycrystalline surface. Combined insights from DFT calculations by Hu et al. and single-crystal electrode experiments by Pérez-Gallent et al. are suggestive of substantial facet effects on the kinetics and the measured current-voltage behavior of Cu catalysts.[87,97] These differences in behavior have been attributed to the presence of Cu_2O at the Cu/electrolyte interface, since Cu_2O is known to grow at different rates depending on the Cu facets due to differences in the surface energies and atomic packing of the facets.[88] Thus, we infer that the features associated with the HCD and LCD datasets are suggestive of the behaviors reported for the single-crystal Cu(100) and Cu(111) electrodes, respectively.[87] To further deconstruct contributions from ECSA and facets on trial-to-trial deviations, EIS measurements were performed and its results are subsequently discussed.

2.3.2 Activity, Selectivity and Stability Measurements on Cu Planar Electrodes

Figure 2-7 depicts transient current densities from the CA measurements (Section 2.2.4) when held at a potential of roughly -0.6 V for all pH and concentrations of both 0.1 M and 1 M $NaNO_3$. Data in Figure 2-7 has been obtained from 3 trials and corresponding average and standard deviation values are shown. Like the trends in the CVs in Figure 2-3, steady-state current densities increase with an increase in pH and $NaNO_3$ concentration. At all conditions, there is a rapid decline in currents in the initial 5 minutes, when the diffusive species flux through the boundary layer is unable to sustain large current densities. Steady-state currents are attained for 1 M $NaNO_3$ at pH 8 and pH 14 within 15 minutes for both solutions. However, for pH 10, even at 40 minutes currents are continually decreasing even though the rate of change is significantly smaller than at the start of the CA test. This is conceivably due to competing adsorption of PO_4^{3-} ions from the buffer on the reaction sites in place of N-species. A prior voltammetry study on a Cu(100) surface supports this hypothesis and has demonstrated the likelihood of PO_4^{3-} adsorption for pH 6.8 – 11.2.[122] This effect is likely also exacerbated by the local pH increase above the bulk value of 10, due to OH^- production during both NO_3^- reduction and hydrogen evolution. Above pH 10, PO_4^{3-} is present at the same order of magnitude as the majority species HPO_4^{2-}. This behavior is not observed at pH 8 because $H_2PO_4^-$ and HPO_4^{2-} species are dominant compared to the insignificant concentrations of PO_4^{3-} (Figure D-5). Therefore, for future investigations with highly alkaline waste stream sources where phosphate is expected to be present in significant concentrations, e.g., low-level nuclear wastes,[46] this competing surface adsorption effect should be considered. At pH 14 for0.1 M $NaNO_3$, while the currents do not rapidly decay as in the case of pH 10, it does not attain

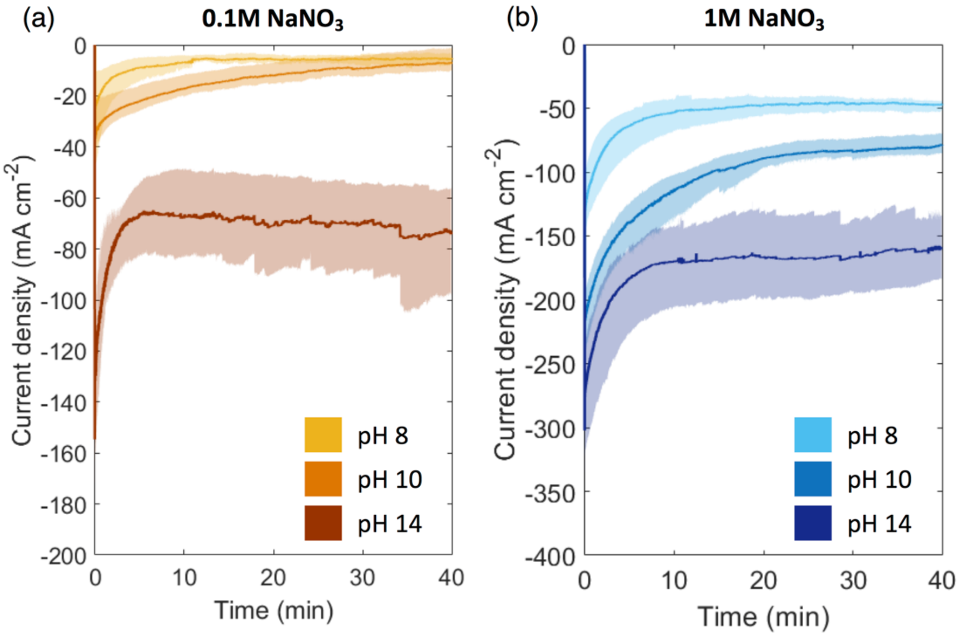

Figure 2-7: Chronoamperometry studies for pH 8, 10, and 14 for NaNO$_3$ concentrations of (a) 0.1 M and (b) 1 M. Average current density for all trials is shown in the bold line, with the shaded regions representing the standard deviation of 3 experimental trials. Experiments were completed with planar Cu electrodes with geometric areas in Table B-1, where the working electrode was subject to the voltages in Table 2-1, and with a stir rate of 900 rpm.

a steady-state value as in pH 8. Instead, cathodic currents gradually become more negative after the initial drop-off in the first 5 minutes, and this trend continues for the remainder of the test until reaching 40 minutes. Similar to the CV data in Section 2.3.1, pH 14 measurements lead to substantial spread in the measured data. This aspect is further interpreted in the EIS measurements (Section 2.3.4).

Compared to the current density expected from the CVs (Figure 2-3) at the applied potentials listed in Table 2-1, the planar electrode results in larger steady-state current densities, by up to a factor of 16, at equivalent pH and NaNO$_3$ concentrations. For example, at pH 8 and 0.1 M NaNO$_3$, while approximately -0.35 mA cm^{-2} of current density is expected from CV measurements, a steady-state current density of -5.4 mA cm^{-2} is observed in the CA measurements. At pH 8 and 1 M NaNO$_3$, this factor is ~5 times, and at pH 14, it is ~1.4. These outcomes are attributed to (a) increased surface roughness, (b) improved bubble detachment, and (c) larger localized pH values near the surface of the planar electrode when compared to the disk electrode. Increased surface roughness is expected for the planar Cu electrode due to manufacturing and polishing imperfections (as observed in the optical microscope images of the different Cu planar electrode surfaces shown in Figure B-1 to Figure B-3). Moreover, we anticipate improved buoyancy and detachment of nucleated H_2 bubbles on the planar Cu electrode with its exposed vertical surface to the electrolyte (Figure 2-1). While these two factors are pertinent, it is unlikely that they alone can explain the near tenfold increase in current densities measured, for example in the case of 0.1 M $NaNO_3$ in pH 8. Therefore, we expect that the local pH environment also plays a significant role. It is reasonable to expect that a relatively larger local pH will develop during the CA measurements compared to the CVs, because the electrode is held at a fixed potential for a significantly longer duration. Additionally, specific to our experimental setup, the stir bar does not spin as effectively for the planar electrode used in the CAs as compared to the disk electrode used in the CVs. Hence, a larger concentration boundary layer is likely for the CA tests, which can sustain larger local pH gradients due to the production of OH^- through the NO_3^- reduction reactions. This could therefore result in larger currents due to enhanced kinetics with increasing pH (Figure 2-5). In part, this effect also explains why the current densities increase more for the CA as compared to the CV measurements at the lower pH values, where the relative change in pH will be significantly larger than at a higher pH due to the logarithmic nature of the pH scale.

Figure 2-8 shows the product quantification and Faradaic efficiencies based on the constant potential measurements (Figure 2-7) for all pH and concentration combinations. Species concentrations for NO_3^-, NO_2^- and NH_3 were measured for every trial performed and the average value was used to compute the average Faradaic efficiency (Eq. (2-8)) in Figure 2-8(a). Error is computed by factoring in both systematic error due to concentration measurements (Table 2-2), and random error due to trial-to-trial deviations (Appendix E). The largest errors are observed for FE_{NH_3} at pH 14 because of large trial-to-trial deviations (17.8% for 1 M and 43.5% for 0.1 M $NaNO_3$).

For both pH 8 and pH 10, the average selectivity towards NH_3 shows a dependency on the $NaNO_3$ concentration. Larger average FE_{NH_3} are obtained with 0.1 M $NaNO_3$, reaching 40 ± 18% and 40 ± 20%, whereas with 1 M $NaNO_3$ it is 25 ± 5.9% and 26 ± 4.6% for pH 8 and 10 respectively. However, even with experimental uncertainties, there is lesser accumulation of NO_2^- in the final solution for 0.1 M $NaNO_3$ when compared to the 1 M $NaNO_3$ electrolyte at these pH conditions. For 1 M $NaNO_3$ at pH 8 and 10, roughly half of the total current is driving NO_3^- reduction to NO_2^- (average $FE_{NO_2^-}$ of 45% and 46%), and therefore much of the reduced NO_3^- remains as NO_2^-. This accumulation of NO_2^- is indicative of slower rates of NO_2^- to NH_3 reduction at low pH on Cu surfaces and aligns with results in Figure 2-3. The highest FE_{NH_3} is at pH 14, reaching an average value of 46 % for both concentrations (± 11% for 1 M and ± 21% for 0.1 M $NaNO_3$) and is accompanied by a low $FE_{\mathrm{NO}_2^-}$ of 5.1 ± 0.56%. This indicates that while the selectivity for NH_3 production on average is low at roughly 50%, the NO_3^- reduction is nearly fully selective towards NH_3 for both concentrations at pH 14.

Due to the exponential nature of the polarization curves and competing reactions, the applied potential will have a significant effect on the measured Faradaic efficiencies. The Faradaic efficiencies for NH_3 formation, FE_{NH_3}, for a polycrystalline Cu electrode in a dual-compartment batch cell have been reported to be 21% at -0.64 V in 0.1 M $NaNO_3$ at pH 14, whereas it increases to 85% at an applied potential of -0.44 V for a 0.02 M $NaNO_3$ and pH 14 electrolyte.[85,123] For comparison, in this study for an applied potential of -0.55 V, the FE_{NH_3} of 46 ± 21% and 46 ±

11% for 0.1 M and 1 M $NaNO_3$ concentrations is within the previously reported range of 21 – 85% at pH 14.

Figure 2-8(b) compares the measured and estimated amount of NO_3^- consumption. The measured NO_3^- consumption is obtained from the difference between spectrophotometric measurements of initial and final NO_3^- concentrations, whereas the estimated value of NO_3^-

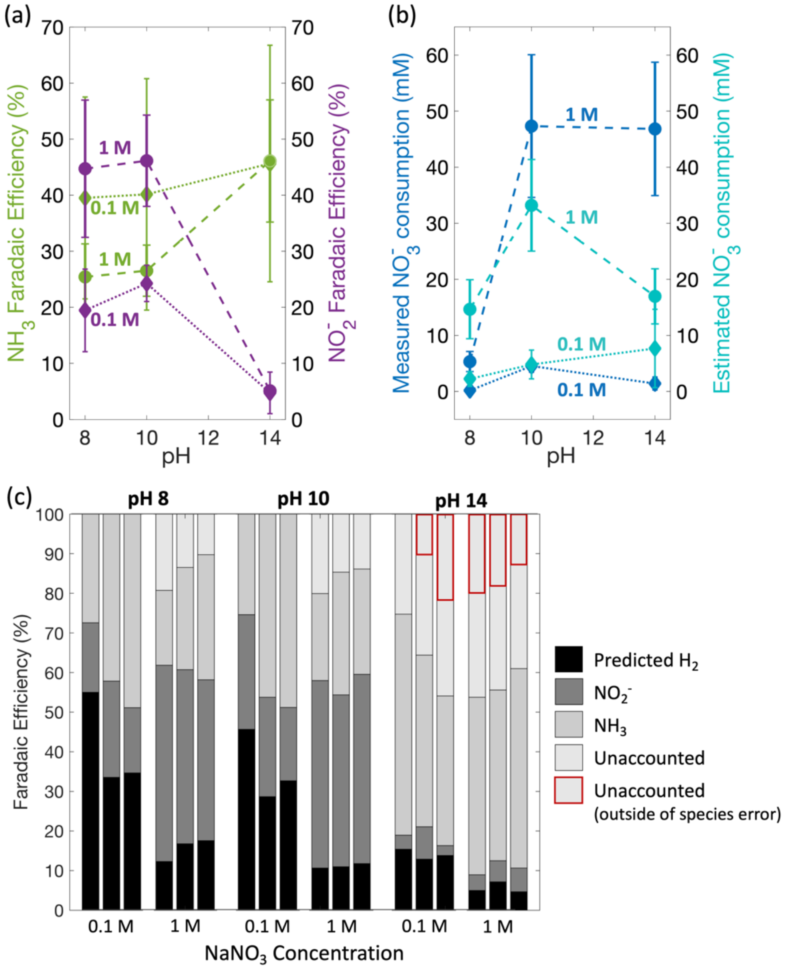

Figure 2-8: (a) Average and standard deviations in Faradaic efficiency to NH_3 (green) and NO_2^- (purple) at pH 8, 10, and 14 for 0.1 M and 1 M NaNO3. (b) Average and standard deviations in measured NO_3^- consumption (blue) and estimated NO_3^- consumption (teal); (c) trial-to-trial breakdown of Faradaic efficiency to NO_2^-, NH_3, predicted H_2, and unaccounted products. All data for this figure are from experiments completed with planar Cu electrodes with geometric areas in Table B-1, where the working electrode was subject to the voltages in Table 2-1, and with a stir rate of 900 rpm. Average values in 2-8(a) and 2-8(b) are obtained by averaging over all trials in Figure 2-7, and error bars account for both random (trial-to-trial) and systematic errors (Table 2-2); 2-8(c) does not show uncertainties in the Faradaic efficiency to NO_2^- and NH_3. Instead, the red box indicates the portion of the unaccounted products that lies outside of the systematic error coming from the NH_3 and NO_2^- measurements.

consumption is the sum of the measured NH_3 and NO_2^- concentrations. Therefore, significant discrepancy, where the measured NO_3^- consumption is larger than the estimated NO_3^- consumption even after factoring in experimental uncertainties, point to either the formation of N-products that are not NH_3 or NO_2^-, the loss of NH_3 produced through oxidation at the anode, or the formation of other byproducts that are not N-based (such as H_2). These results are co-interpreted with Figure 2-8(c) that shows the trial-by-trial breakdown of Faradaic efficiencies by end products. The error in the Faradaic efficiencies stemming from the NO_2^- and NH_3 measurements leads to errors in the unaccounted Faradaic efficiencies. Therefore, Figure 2-8(c) highlights using the red outlines the minimum amount of unaccounted charge after factoring in these measurement errors. Data from Figure 2-8(c) is presented in Table E-5 with the appropriate error ranges.

Consistent discrepancies between measured and estimated NO_3^- consumption are observed for pH 14 (Figure 2-8(b)), and this is correlated with up to ~20% unaccounted charge in Figure 2-8(c). For 0.1 M $NaNO_3$, while the estimated consumption of NO_3^- is much larger than the measured value, they are within measurement uncertainties largely due to trial-to-trial variations (Figure 2-8(c), Table E-4). For this 0.1 M case, excess estimated NO_3^- concentration compared to the measured NO_3^- consumption is indicative of an unlikely NO_3^- loss in the solution post CA tests and cannot be directly correlated with unaccounted charge in Figure 2-8(c) for two trials. A more likely cause is attributed to the formation of CuO_x species, which can interfere with absorption in the 300 – 450 nm spectrum, where both NO_3^- and NO_2^- have characteristic absorption peaks (Figure D-4).[124] This therefore results in an underestimation of the measured NO_3^- consumption and possibly an overestimation of the NO_2^- formed. There is a significant amount of unaccounted charge in Figure 2-8(c) for all trials at 1 M $NaNO_3$, which is also correlating with smaller values of estimated compared to measured NO_3^- consumption. This indicates that there was either additional charge going to NO_2^- formation, or to other uncharacterized N-species, or to oxidation of the produced NH_3, which is feasible in a 3-electrode cell without any membranes separating the catholyte and the anolyte. Therefore, it is likely that the net Faradaic efficiencies towards all N-products for 1 M $NaNO_3$ at pH 14 are likely higher by up to 20%.

At pH 10 for both concentrations, the average values for measured and estimated consumption are within the error bounds of one another. The unaccounted charge from Figure 2-8(c) is also within the error bounds of the concentration measurement, indicating that all N-species are accounted for within the error bounds of this experiment. However, at pH 8 for both concentrations, like pH 14 and 0.1 M $NaNO_3$, the estimated consumption of NO_3^- is larger compared to the measured value. This is despite the lack of unaccounted charge in Figure 2-8(c) at the same condition. This disparity is therefore attributed to an outlier in the 3 experimental trials performed at pH 8, which results in substantial trial-to-trial error at pH 8 (Table E-4). Therefore, we cannot draw much from this disparity in Figure 2-8(b) for this condition because the average and standard deviation for the true population, or even a larger sample set, may significantly change from what is reported due possible outliers.

2.3.3 Energy Intensity for NH_3 Recovery

The implications of measured current densities (Figure 2-7) and product distribution (Figure 2-8) on system-level performance are quantified by evaluating the rate of nitrogen recovery, $\dot{r}_{NH_3}$ (Eq. (2-9)) and the energy intensity of this process to form ammonia, E_{NH_3} (Eq. (2-10)) in Figure 2-9. The trends for energy intensity are largely driven by the Faradaic efficiencies for NH_3 production, FE_{NH_3}, where smaller values of FE_{NH_3} require larger amounts of energy to produce the same amount of NH_3. For 1 M $NaNO_3$, the energy intensity is roughly uniform within measurement errors from pH 8 to 10, and then decreases considerably as the pH increases further

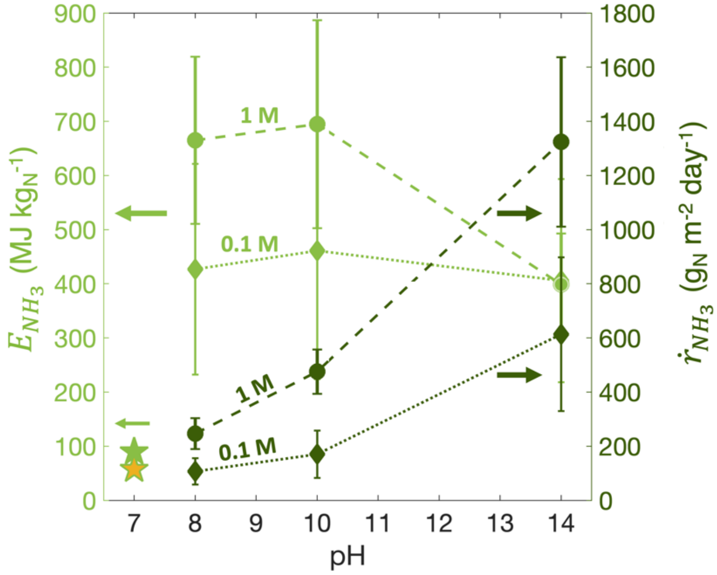

Figure 2-9: Energy intensity for ammonia recovery, E_{NH_3} (MJ kg$_N^{-1}$), and rate of ammonia production, $\dot{r}_{NH_3}$ (g$_N$ m^{-2} day^{-1}), as a function of pH 8, 10, and 14 for 0.1 M and 1 M $NaNO_3$. Energy intensity values estimated for the standard biological nitrification-denitrification approach (green star), and for the Sharon-Anammox process (yellow star) are included for comparison. All data for this figure are from experiments completed with planar Cu electrodes with geometric areas in Table B-1, where the working electrode was subject to the voltages in Table 2-1, and with a stir rate of 900 rpm. Average values for energy intensity and rate of ammonia production are obtained by averaging over all trials in Figure 2-7, and error bars account for both random (trial-to-trial) and systematic errors (Table 2-2).

to 14. At 0.1 M $NaNO_3$, the energy intensity is nearly constant within measurement uncertainties for all pH. The near-constant energy intensity values between pH 8 and 10 at both concentrations are explained by the similarity in their FE_{NH_3} values (Figure 2-8). The extent of the reduction of E_{NH_3} from pH 8 to 14 at 1 M concentration is large, decreasing from an average value of665 MJ kg$_N^{-1}$ to 399 MJ kg$_N^{-1}$ due to the concentration and pH dependence on the rate of increase in FE_{NH_3}. From pH 10 to pH 14, while the average FE_{NH_3} for 1 M $NaNO_3$ increases by 20% it only increases by 5.5% for 0.1 M $NaNO_3$. For pH 14, the energy intensity E_{NH_3} values for both concentrations are nearly the same due to their similar FE_{NH_3}. The trends for the rate of ammonia production monotonically increases with pH and concentration. Therefore, the larger rates of ammonia production with increasing pH do not translate directly into gains in the energy intensity.

Consequently, while pH 14 is evidently attractive from an energy intensity standpoint as compared to pH 8, the pH 10 case is not.

For comparison, Figure 2-9 also shows the energy intensity for producing ammonia, via the traditional Haber-Bosch process, from N_2 obtained from wastewater treatment using: (1) a traditional nitrification-denitrification process with a process intensity of 45 MJ kg_N^{-1} and (2) the SHARON-Annamox process with an energy intensity of 10-16 MJ kg_N^{-1}.[46] Even when considering parasitic energy requirements such as pumping and aeration, the energy intensities are expectedly small because the microbes are efficient at metabolizing nitrogen-contaminants.[125,126] To these estimates, the Haber-Bosch process, with an energy intensity of 44.4 MJ kg_N^{-1}, was additionally included to convert the recovered N_2 to NH_3.[127] This results in energy intensities for ammonia recovery less than 100 MJ kg_N^{-1} for the biological processes. This stacks up with outcomes from this study with a projected energy intensity of 427 MJ kg_N^{-1} at pH 8 for an electrocatalytic process using unoptimized Cu surfaces and applied potentials. Therefore, there is significant room for innovations in catalyst development and optimization of operating conditions to make electrochemical NO_3^- treatment more competitive with biological processes at near-neutral pH. However, a comparison cannot be made for the more alkaline conditions ($pH \geq 10$), where there are negative effects on the microbes due to their pH-sensitivity. Under these conditions the electrocatalytic approach poses to offer more lucrative nutrient recovery solutions. Additionally, Figure 2-9 results are specific and sensitive to the applied potentials at the working electrodes listed in Table 2-1. This can dramatically influence the rates and the Faradaic efficiencies as a function pH and $NaNO_3$ concentration. For example, Jaramillo et al. revealed such differences in their work using a titanium electrode, where an optimal potential of -1.25 V for pH = 13 and -1 V for pH = 10.95 were found from a surveyed range of 0 to -2 V vs RHE.[86] Therefore, further optimization of the applied working electrode potential is also warranted with Cu electrodes, especially at pH 8 and 10.

2.3.4 Correlating Impedance Measurements with Trial-to-Trial Variations

Figure 2-10 shows the average charge transfer resistance, R_t, extracted from EIS measurements (Section 2.4, Appendix C) plotted against the measured charge (Eq. (2-7)) for NO_3^- reduction to form NO_2^- and NH_3, i.e., $Q_{NO_2^-} + Q_{NH_3}$. Since the R_t was measured at a voltage (-0.1 V) where only NO_3^- to NO_2^- is expected to occur (Figure C-4) and this is the rate determining step of the reaction on Cu,[93,107] the R_t should influence charge passed to all reduced N-products, as calculated from Eq. (2-7). Our results show that R_t is strongly correlated (having a Pearson correlation coefficient of -0.79 with a P-value of 0.0001) to the charge transferred for NO_2^- or NH_3 production for both the 0.1 M and 1 M $NaNO_3$ data sets. Based on the slope of the fit line, a

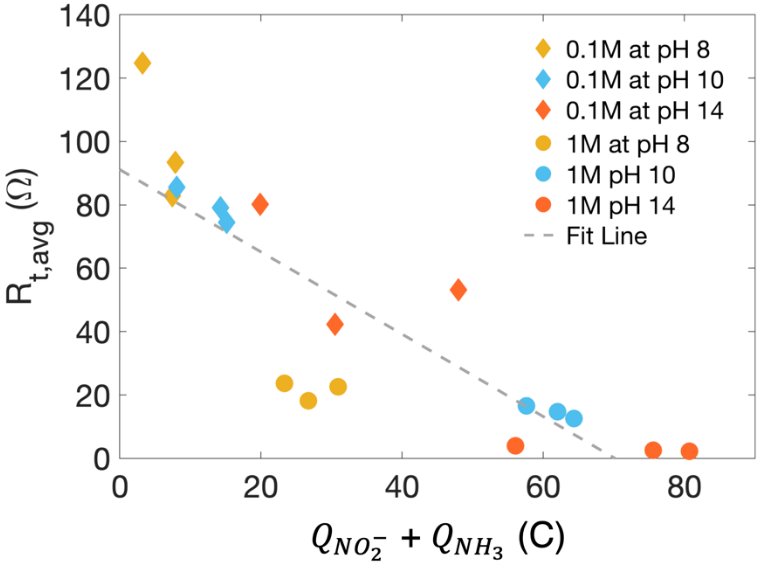

Figure 2-10: Correlation, using trial-by-trial experimental data, between the average of initial and final values of the charge-transfer resistance, R_t, and the charge passed for NO_3^- reduction to NO_2^- and NH_3, $Q_{NO_2^-} + Q_{NH_3}$, for 0.1 M and 1 M $NaNO_3$ at pH 8, 10, and 14. Best-fit charge-transfer resistance values are obtained from electrochemical impedance spectroscopy data measured with planar Cu electrodes at a potential of -0.1 V. Lower R_t leads to higher charge passed to NO_3^- reduction products, as shown by the fit line. Systematic errors in the determination of $Q_{NO_2^-} + Q_{NH_3}$ (Table 2-2) is not explicitly shown in this dataset.

decrease in R_t leads to higher NO_3^- reduction current to form either NO_2^- or NH_3. Additionally, lower R_t occurs for all 1 M concentrations of $NaNO_3$, which confirms we are probing a NO_3^--concentration dependent reaction rate. Average values are used in Figure 2-10, but even with error bars arising from systematic errors in the concentration determination of NO_2^- and NH_3 (Table E-5, Figure 2-8), the predicted trends for R_t against $Q_{NO_2^-} + Q_{NH_3}$ still hold true.

To obtain surface information from the EIS data, the effective double layer capacitance for all trials, C_{eff} (Eq. (2-5)) is correlated with both the charge associated with any species other than H_2 measured in the blank experiment, i.e., $Q_{NO_2^-} + Q_{NH_3} + Q_u$ (Eq. (2-6)), in Figure 2-11(a) and (b), and the charge associated with NO_3^- reduction to NO_2^- and NH_3, i.e. $Q_{NO_2^-} + Q_{NH_3}$(Eq. (2-6), in Figure 2-11(c) and (d). The double layer capacitance C_{eff} can be expressed as a product of the

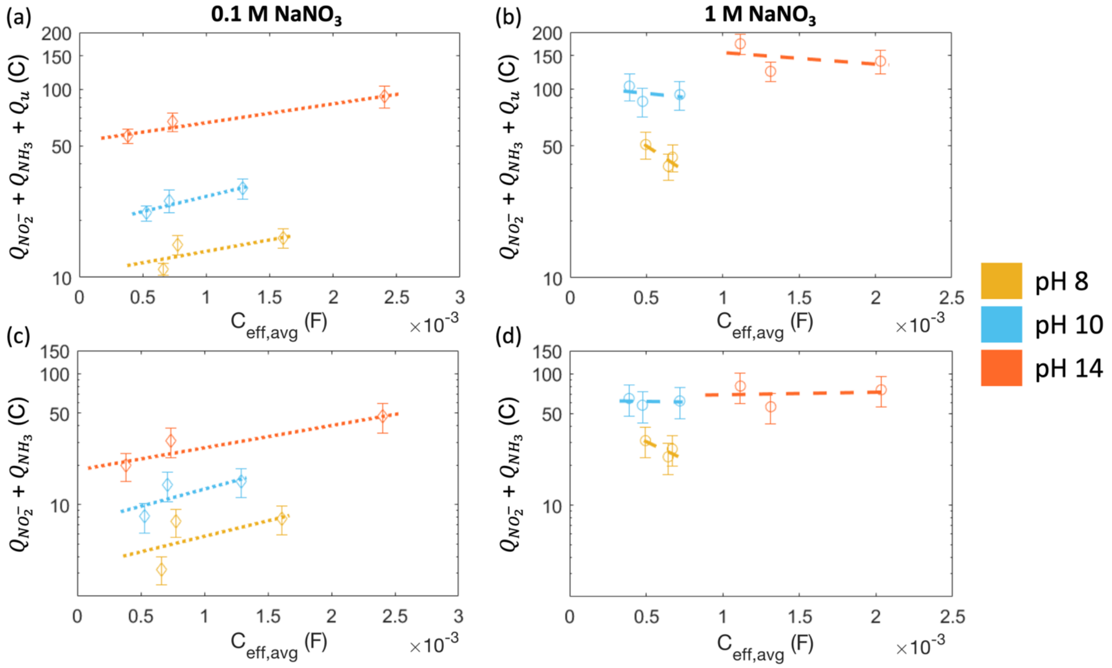

Figure 2-11: Correlations using trial-by-trial experimental data between the net charge passed and the average of the initial and final effective double-layer capacitance, C_{eff}. (a, b) show the charge for NO_2^-, NH_3, and unaccounted products and (c, d) only consider NO_2^- and NH_3. The C_{eff} is split by concentration, with (a, c) showing 0.1 M and (b,d) showing 1 M $NaNO_3$ for pH 8, 10, and 14. Trendlines in the data (dotted and dashed) are included at every pH. Best-fit double-layer capacitance values are calculated from electrochemical impedance spectroscopy data obtained with planar Cu electrodes at a potential of -0.1 V. The error bars for $Q_{NO_2^-} + Q_{NH_3}$ include the contributions from systematic error (Table 2-2).

area-specific capacitance of the surface, C_s, and the electrochemically active surface area (ECSA). For a polycrystalline surface, different facets may have unique specific capacitance values, and therefore the extracted C_{eff} is an area-weighted sum of all these facets, $C_{eff} = \sum_{facets} C_{s,i} \mathrm{ECSA}_i$. Typically, on a homogenous surface, a higher C_{eff} would be indicative of a higher ECSA and higher currents, resulting in larger magnitudes of charge transferred.[111]

The trendlines for the 0.1 M $NaNO_3$ data in both Figure 2-11(a) and (c) indicate that an increase in the C_{eff} leads to an increase in the charge magnitude for NO_3^- reduction. This fits with the hypothesis that a larger ECSA results in larger currents. From trial-to-trial, there is variation in the roughness of the exposed Cu facets, which leads to variation in the currents at this concentration. In contrast, for 1 M $NaNO_3$, the currents are not limited by the ECSA and larger magnitudes of charge towards NO_3^- reduction are obtained relative to the 0.1 M $NaNO_3$ case at comparable C_{eff} for any pH. Additionally, looking at the trial-to-trial trends within any given pH, the charge magnitude decreases (Figure 2-11(b) and Figure 2-11(d) for pH 8) or remains unaffected (Figure 2-11(d) for pH 10 and 14) with increasing C_{eff} consistently across all pH values. Since these trends cannot be explained by only a changing ECSA, this outcome is instead correlated with a kinetically more active Cu facet with a lower area-specific capacitance. That is, if a kinetically less active facet has a larger area-specific capacitance when compared to a more active facet, at equivalent ECSA, a larger double layer capacitance will be obtained for the less active facet and will be correlated with a smaller magnitude of charge for the reactions. This effect explains the decrease in the charge magnitude (Figure 2-11(b) and 2-11(d) for pH 8) with an increase in C_{eff}. The lack of correlation between the C_{eff} and the charge for NO_2^- and NH_3 formation at pH 10 and 14 (Figure 2-11(d)) likely arises from opposing contributions from the facet-dependent area-specific capacitance and its corresponding ECSA or is due to unaccounted N-product charge

(Figure 2-8(c)). To corroborate these analyzed trends, additional surface characterization such as atomic force microscopy should be used to track the trial-to-trial variations in the electrode surfaces before and after each experiment.

2.4 Conclusion

In this study, we explore the effects of pH (8, 10 and 14), concentration (0.1, 0.5 and 1 M $NaNO_3$), and catalyst facets on electrocatalytic NO_3^- reduction on polycrystalline copper (Cu) electrodes. Cyclic voltammetry with Cu disk electrodes informs the landscape of electron-transfer reactions and helps quantify Tafel kinetic parameters for nitrate-to-nitrite reduction. Chronoamperometry is performed at select working electrode potentials to probe activity, selectivity, and stability of Cu planar electrodes. In conjunction with chronoamperometry, electrochemical impedance spectroscopy is applied to diagnose underlying contributors to measurement uncertainties.

Cyclic voltammograms reveal the interplay of NO_3^- concentration and pH on the polarization behavior. Measured current densities in general increase with concentration and pH, with the rate of increase with concentration being pH dependent. Through direct comparisons of cyclic voltammograms obtained with a blank, $NaNO_2$, and $NaNO_3$ electrolytes, consistent onset features are present at all pH and $NaNO_3$ concentrations for the NO_3^- to NO_2^- reduction, and for the further reduction of NO_2^- to other N-intermediates and NH_3. Best fit values for the Tafel kinetic parameters – exchange current density and the charge-transfer coefficient – for the NO_3^- to NO_2^- reduction step is affected by both pH and NO_3^- concentration. The impact of pH is more dominant on the charge-transfer coefficient because of the proton/hydroxide coupled electron transfer reactions.

Measured activity and current densities follow similar trends with respect to pH and $NaNO_3$ concentration in the fixed potential tests with chronoamperometry. While current stabilizes for pH 8 and 14 within the first 10 mins, the stability at pH 10 is compromised due to the presence of Na_2HPO_4 buffer and competing effects of PO_4^{3-} adsorption on the electrode surface. In addition, localized pH gradients influence substantial deviations from equivalent data obtained from cyclic voltammetry, especially at pH 8. At any $NaNO_3$ concentration, the Faradaic efficiency of NO_3^- reduction to NH_3 increases with pH, but more pronouncedly from 10 to 14. While at pH 14 the Faradaic efficiency (~46% average values) for NH_3 formation remains unaltered with concentration, for pH 8 and 10, selectivity towards NH_3 production increases with decreasing NO_3^- concentration due to a larger accumulation of NO_2^- in the electrolyte. Therefore, in these conditions, NO_2^- competes with the production of NH_3. By interpreting measured Faradaic efficiencies together with discrepancies between measured and estimated NO_3^- consumption, we identify that there is greater likelihood of oxidation of NH_3 or the formation of uncharacterized reduced N-species at pH 14 with 1 M $NaNO_3$. Trends in energy intensity for ammonia recovery followed suit with the Faradaic efficiencies with the lowest value (399 MJ kg_N^{-1}) estimated for pH 14, and average energy intensities being significantly smaller for 0.1 M compared to 1 M $NaNO_3$ at pH 8 and 10. Comparisons with energy intensities for biological processes establish the need for significant improvement in catalysts at near-neutral pH while demonstrating the appeal of electrocatalytic approaches for strongly alkaline conditions.

Even after much standardization and control of experiments, substantial trial-to-trial variations prevailed in both the cyclic voltammetry and chronoamperometry datasets. These variations led to the polarization curves clustering in two groups, especially at pH 8 and 14. In the fixed potential tests, these variations led to steady current densities deviating by as much as

21 mA cm^{-2} at pH 14. Fitted data for the charge-transfer resistance and the effective double layer capacitance obtained from electrochemical impedance measurements provide important insights on the sources of experimental uncertainties. We show that the charge-transfer resistance and the effective capacitances changes from one trial to another even under the same testing conditions. The charge-transfer resistances are inversely proportional with the charge transferred for NO_3^- reduction to either NO_2^- or NH_3. From the capacitance data, we interpret how different trials can influence both the electrochemically active surface area and the facet-dependent area-specific capacitances. Even though it is expected that polycrystalline Cu will be comprised of different facets with different kinetic activities, the relative importance of these different facets depends on $NaNO_3$ concentration. At 0.1 M $NaNO_3$, the N-reducing charge to form NO_2^- or NH_3 is more strongly related to the electrochemical surface area. Whereas, for the 1 M $NaNO_3$ concentration, the facet-dependent specific capacitance plays a more significant role. The impedance-based diagnostics introduced in this study can serve as a powerful technique in tandem with other more direct surface characterization techniques to explicitly quantify facet effects on electrochemical reactivities.

Collectively, this study presents important findings and insights to advance electrocatalytic ammonia recovery from wastewater nitrates with commercially viable polycrystalline Cu electrodes. We have additionally uniquely applied impedance-based diagnostic tools to uncover factors stemming from the electrode surface that contributes to experimental uncertainties.

Chapter 3 Harnessing Photoelectrochemistry for Wastewater Nitrate Treatment Coupled with Resource Recovery

Adapted with permission from: Barrera, L., & Bala Chandran, R. (2021). Harnessing Photoelectrochemistry for Wastewater Nitrate Treatment Coupled with Resource Recovery. *ACS Sustainable Chemistry & Engineering*, *9*, 3688–3701.

3.1 Introduction

Excessive anthropogenic production of nitrogen fertilizers combined with fossil-fuel combustion has significantly disrupted the natural nitrogen cycle,[83,128,129] leading to the contamination of groundwater and other surface-water bodies with various reactive forms of nitrogen — nitrates (NO_3^-), nitrites (NO_2^-), ammonia (NH_3), ammonium (NH_4^+) and organic nitrogen. These contaminants result in environmental threats such as algal blooms, suffocation of aquatic wildlife, and health risks in humans, e.g. excessive amounts of nitrates in drinking water causes methemoglobinemia ("blue baby" syndrome).[41–43,130,131] While several strategies have been reported to recover value-added products — energy from biogas and chemicals including biopolymers, bio-oils, and biochar from organic contaminants — far less emphasis has been placed on nutrient (i.e. nitrogen) and energy recovery from nitrogen contaminants.[30,132–134]

This study focuses on evaluating the feasibility of a photoelectrochemical approach to recover nitrogen nutrients from NO_3^- contaminants present in ion-exchange brines[25,34–36] and treated wastewater.[30,37–39] The state-of-the-art nitrification-denitrification processes for wastewater treatment are biological approaches that utilize microbes to consume and remove the excess nutrients.[135,136] However, the conventional two-stage biological nitrification-denitrification process is energy intensive, consuming up to 45 MJ kg_N^{-1},[125,137,138] not effective in effluent streams that harbor conditions unsuitable for microbial growth,[83,139] and has not been optimized for resource recovery.[134] Proof-of-concept bioprocesses, including the Sharon-Anammox and the coupled aerobic−anoxic nitrous decomposition operation (CANDO) have been proposed to lower the energy intensity and to promote energy recovery from N-contaminants, but are yet to be adopted for large scale wastewater treatment.[125,140] Ion-exchange,[52,131,141] electrodialysis,[142,143] and reverse osmosis[144,145] are used to treat nitrates (and other ions) at an industrial scale for drinking water applications, but result in the production of a secondary nitrate-concentrated brine that requires further treatment.[146] Hence, there is an increasing demand to develop wastewater treatment technologies to harness renewable energy, to be effective for a wide range of effluent stream conditions and to facilitate resource recovery in the form of nutrients and energy. To meet these critical needs, photoelectrochemical devices offer the potential to couple sunlight with electron-transfer reactions to treat and transform nitrogen-contaminants to value-added chemicals and therefore facilitate nitrogen recovery.

Prior work has provided theoretical limits for the solar-to-fuel energy conversion efficiencies and established guidelines to select semiconductor and co-catalysts/electrocatalysts to optimize the efficiency for photoelectrochemical water splitting devices, which generate hydrogen and oxygen from water using light absorbers and electrocatalysts.[69,75,77,78,111,147–153] However, the same extent of understanding is not available for photoelectrochemical nitrate treatment devices. Photocatalytic nitrate reduction has been investigated predominantly with TiO_2-based light absorbers with NO_3^- reduction often paired with sacrificial hole-scavengers (methanol, oxalic acid, and formic acid).[154–157] However, TiO_2 limits process efficiencies due to the low sunlight absorption and the presence of hole-scavengers lead to toxicity concerns for water treatment applications. Comprehensive reviews have been reported on electrochemical denitrification, i.e. NO_3^- to N_2 conversion, including investigations on metallic and bimetallic electrocatalysts for NO_3^- to N_2 and NH_3 conversion, and studies that probe fundamental reaction mechanisms.[18,59,85,158–168] However, the focus in a majority of these studies has been on electrocatalytically reducing NO_3^- to N_2, which poses formidable kinetic (reactivity and selectivity) challenges. Therefore, there is a lack of knowledge on the ideal performance limits and the impacts of materials parameters on the performance of a photoelectrochemical approach to recover nitrogen nutrients from wastewater.

The objective of this study is to theoretically predict the solar-to-chemical energy conversion efficiencies and the rate of recovery of nitrogen for a photoelectrochemical device that is operating on treated wastewater with predominantly nitrate contaminants (Figure 3-1). A notable innovation introduced in the modeling approach developed is the capability to account for the effects of competing hydrogen evolution and the oxygen reduction reactions that can compete with the desired nitrate reduction reaction at the cathode, within a simplified, yet powerful, equivalent circuit modeling framework. The model developed is used to obtain the impacts of material parameters, including the light-absorber band gaps, electrocatalyst exchange current densities and charge-transfer coefficients for the desired and the competing reactions, and operating nitrate concentration in the waste stream, on all the performance metrics. These results are interpreted to provide guidelines to select materials for the light absorbers and electrocatalysts to maximize resource (nitrogen) recovery. Furthermore, the predicted performance metrics are used to compare the proposed approach with the state-of-the-art nitrogen removal/recovery technologies – the Sharon-Annamox process[125,169] and ammonia stripping using electrochemical flow reactors.[138]

3.2 Photoelectrochemical Device for Wastewater Nitrate Treatment

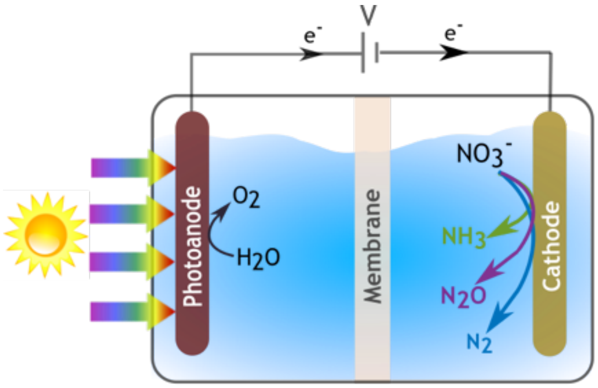

Oxidation		Reduction	
$2\ OH^- \rightarrow ½\ O_2(g) + H_2O + 2\ e^-$	$E^0 = 1.23$ V	$NO_3^- + 6\ H_2O + 8\ e^- \rightarrow NH_3(g) + 9\ OH^-$	$E^0 = 0.82$ V
Net Reaction, R1:	$NO_3^- + 2\ H_2O \rightarrow NH_3\ (g) + OH^- + 2\ O_2\ (g)$		$E^0_{R1} = -0.41$ V
$2\ OH^- \rightarrow ½\ O_2(g) + H_2O + 2\ e^-$	$E^0 = 1.23$ V	$2\ NO_3^- + 5\ H_2O + 8\ e^- \rightarrow N_2O(g) + 10\ OH^-$	$E^0 = 1.12$ V
Net Reaction, R2:	**$2\ NO_3^- + H_2O \rightarrow N_2O\ (g) + 2\ OH^- + 2\ O_2\ (g)$**		$E^0_{R2} = -0.11$ V
$2\ OH^- \rightarrow ½\ O_2(g) + H_2O + 2\ e^-$	$E^0 = 1.23$ V	$2\ NO_3^- + 6\ H_2O + 10\ e^- \rightarrow N_2(g) + 12\ OH^-$	$E^0 = 1.25$ V
Net Reaction, R3:	$2\ NO_3^- + H_2O \rightarrow N_2\ (g) + 2\ OH^- + 5/2\ O_2\ (g)$		$E^0_{R3} = 0.02$ V

Figure 3-1: Schematic of a photoelectrochemical device for treating wastewater nitrate contaminants. Selective water oxidation at the photoanode and only NO_3^- reduction to form NH_3 (R1), N_2O (R2) or N_2 (R3) are depicted for simplicity. All the standard potentials, E^0, for aqueous solutions at 25°C are reported vs. NHE based on a 1 atm standard state for H_2. Unless otherwise mentioned all species are in the aqueous phase.[170,171] A negative E^0 for a net reaction indicates that it is thermodynamically uphill, while a positive E^0 indicates reaction spontaneity.

In this work, we propose a photoelectrochemical device to pair water oxidation with nitrate reduction (Figure 3-1). A photoactive semiconductor anode absorbs incident sunlight and is electrically connected to the cathode. The holes generated at the photoanode surface effect the oxygen evolution reaction (OER) while at the cathode surface the electrons effect the nitrate reduction reaction (NO3RR) to the desired products including NH_3/NH_4^+ and N_2O. An ion-exchange membrane may be present to facilitate ion transport while preventing gas crossover between the electrodes. Compared to the removal of NO_3^- contaminants as N_2, the transformation to NH_3/NH_4^+ and N_2O recovers the N-nutrients and upgrades the *energetic value* of the reactive-nitrogen contaminant species. Aqueous NH_3/NH_4^+ can be reused as a fertilizer and/or oxidized to generate electricity in an ammonia fuel-cell, and gaseous NH_3 can be used as a fuel to generate heat and produce electricity.[54,172,173] Despite being a potent greenhouse gas, N_2O is also a powerful oxidizer, especially for the combustion of rocket-fuel and biogas and for supercharging applications as it increases the energy released during the combustion of CH_4 by 37% as compared to using O_2 as an oxidizer.[56,57,132] In prior work, bioprocesses have demonstrated viable energy and resource recovery during wastewater denitrification through the formation of N_2O by coupling N-removal to high-rate and high-efficiency N_2O generation.[132,133,140,174]

While outside the scope of this work, product separation and collection for NH_3/NH_4^+ and N_2O could pose significant challenges. Therefore, this aspect needs to be considered in the design and evaluation of practical devices. For separating NH_3/NH_4^+, (bio)electrochemical approaches coupled with gas-permeable membranes have been demonstrated to be more energy efficient as compared to air stripping for ammonia recovery.[138,175] As for N_2O, it can be separated and recovered by stripping it out of solution,[132,176] with the possibility of enhanced stripping efficiencies and therefore lower energy consumption with the addition of salts.[177] Reactor design and operation can also be engineered to ensure no loss of N_2O to the atmosphere, for example with non-aerated liquid surfaces and floating enclosures to collect the N_2O formed.[178]

3.3 Theory & Numerical Model

A zero-dimensional (0-D), equivalent circuit model was developed to determine operating current densities and potentials, where the semiconductor light absorber was modeled as an ideal diode in series with the electrochemical reactions, which were modeled as variable resistors to account for the electrocatalyst current-overpotential behavior (Figure 3-2). A nomenclature of symbols is included in the ESI. While the chemical composition of wastewater effluents can vary significantly depending on its source (Figure 1-1), to simplify our analysis, a *"model waste stream"* comprising of only NO_3^- contaminants with varying concentrations, from 0.1 mM to 1000 mM, was considered. It was assumed that both the anode and cathode were exposed to the same electrolyte composition and the pH conditions, which were modeled based on the catalysts identified for selective NH_3 and N_2O production, will be discussed in Table 3-2. A flow-reactor design is assumed for the analysis with a steady concentration of NO_3^- concentration in the bulk electrolyte. Even though species transport within the electrolyte is not explicitly modeled, diffusion-limited mass-transfer across the concentration boundary layer has been considered.

For the electrochemical reactions, kinetic and mass-transfer potential losses were considered. Selective oxidation of water (OER) was assumed at the anode (Eq.(3-1a)), whereas non-selective reduction reactions were modeled at the cathode by considering parallel current pathways and by enforcing potential equality (Eq. (3-1a)) in the parallel branches; the overall operating potential of the diode is given by Eq. (3-2).

$$V_{\mathrm{anode}} = E_{\mathrm{eq,OER}} + \eta_{\mathrm{OER}} \tag{3-1a}$$

$$V_{\mathrm{cathode}} = \begin{cases} E_{\mathrm{eq,NO3RR}} + \eta_{\mathrm{NO3RR}} \\ E_{\mathrm{eq,HER}} + \eta_{\mathrm{HER}} \\ E_{\mathrm{eq,ORR}} + \eta_{\mathrm{ORR}} \end{cases} \tag{3-1b}$$

$$V_{\mathrm{op}} = V_{\mathrm{anode}} - V_{\mathrm{cathode}} \tag{3-2}$$

Selective OER is a simplifying assumption to model the electrochemical reactions at the anode. Depending upon the local pH conditions at the electrode surface, reduced products from the NO3RR could also get oxidized. However, there is a rather low likelihood for the oxidation of N_2O (pH = 1) and NH_3/NH_4^+ (pH = 14) on the respective OER catalysts and the pH conditions that were modeled.[95,139] At the cathode, in addition to the desired NO3RR, competing hydrogen evolution (HER) and oxygen reduction (ORR) reactions were also modeled. The HER has been reported to compete with the NO3RR in prior work with Cu catalysts;[83,95,107] the ORR was

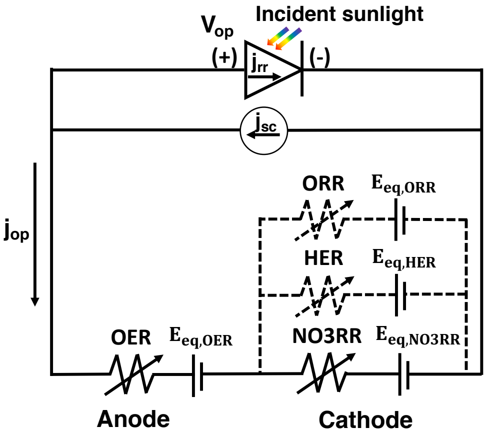

Figure 3-2: Equivalent circuit diagram to model the operation and performance of the photoelectrochemical device in Figure 3-1. The semiconductor light-absorber was modeled as a photodiode and the electrochemical reactions as variable resistors with minimum electrical loads corresponding to the thermodynamic potentials for the corresponding reactions. Selective oxygen evolution reaction (OER) at the anode and parallel reactions were modeled at the cathode including the desired NO3RR, and the competing HER and ORR. Desired reactions in the circuit are indicated by the solid lines and the undesired and competing reactions at the cathode are indicated by the dashed lines.

considered due to the O_2 produced at the anode, which can crossover and react at the cathode surface.

The Nernstian potential, E_{eq}, was included (Eq. (3-3)) as the minimum electrical load at the cathode and the anode.

$$E_{\mathrm{eq}} = E^0 + \frac{R_c\, T}{n_e\, F} \ln\left(\frac{a_O^{\nu_O}}{a_R^{\nu_R}}\right) \tag{3-3}$$

Current conservation, Eq. (3-4), was satisfied in the circuit, while taking into account the parallel and competing reactions occurring at the cathode. The sign convention adopted implements the reduction current densities to be negative and the oxidation current density to be positive.

$$j_{\mathrm{op}} = j_{\mathrm{OER}} = -\sum_{r=\mathrm{NO3RR,ORR,HER}} j_r \tag{3-4}$$

3.3.1 Light Absorber

The semiconductor light absorber was modeled as a diode with the pertinent governing equations and key assumptions summarized in Table 3-1.[69,75,77,78,147,151–153] Ideal diode behavior with only radiative recombination (Eqs. (3-5)-(3-7)) and a large optical path length was assumed to keep the analyses general and to analyze a wide range of light absorber bandgaps. The valence and the conduction band edge positions are not explicitly modeled, however, they are assumed to straddle the appropriate redox potentials of the catalysts and/or the electrolyte redox species, as required for device operation. This approach allows for a more generic analysis that is parametrized on the basis of the light-absorber band gaps and is similar to prior work on photoelectrochemical systems for solar water splitting.[75,153] However, the trends predicted for the impacts of the material band gaps on the performance metrics are expected to be valid even with more realistic recombination models. Sunlight attenuation by water is not a concern because light absorption is most effective in the ultraviolet, visible and in the near-infrared wavelengths for the

Table 3-1: List of the governing equations for the semiconductor light absorber in the equivalent circuit (0-D) model

Physics modeled	**Governing equations and key assumptions**
Current-potential behavior of the semiconductor	Shockley-Queisser detailed-balance model[151] $j_{\mathrm{op}} = j_{\mathrm{sc}} - j_{\mathrm{rr}}\left(e^{\frac{q_e V_{\mathrm{op}}}{n_d k_{\mathrm{B}} T}} - 1\right)$ (3-5) ***(i)*** Optically thick semiconductor absorbs all the above-band-gap photons to ensure that current density is not limited by the material design, i.e. planar electrodes,[151] photocatalytic particle suspension reactors,[69] nanowires,[179] etc. ***(ii)*** Negligible optical losses due to reflection at the surface of the light absorber to keep the analysis generic and applicable over a wide range of material bandgaps ***(iii)*** Ideal diode with only radiative recombination dictated by the rate of thermal emission of photon at ambient temperature, T = 298.15 K
Short-circuit current density, j_{sc}	$j_{\mathrm{sc}} = q_e \int_{\upsilon_{\mathrm{g}}=\frac{E_g}{k_{\mathrm{B}}T}}^{\infty} \phi_{\mathrm{solar}}(\upsilon)\ \mathrm{d}\upsilon$ (3-6) ***(i)*** Electron-hole (e^-/h^+) pairs are generated by each and every incident photon with energy larger than its band gap of E_g ***(ii)*** Excited-state charge carriers rapidly thermalize to the band edges and each absorbed photon produces only one e^-/h^+ pair
Radiative recombination current density, j_{rr}	$j_{\mathrm{rr}} = 2\, q_e \left(\frac{2\pi}{c^2}\right) \int_{\upsilon_{\mathrm{g}}}^{\infty} \frac{\upsilon^2}{e^{\frac{h\,\nu}{k_{\mathrm{B}}T}} - 1}\ \mathrm{d}\upsilon$ (3-7) ***(i)*** Light absorber is surrounded by a blackbody at the same temperature as that of the diode that is at T = 298.15 K [151]

semiconductor material band gaps that yielded non-zero efficiencies, whereas water predominantly absorbs in the mid-infrared wavelengths.

3.3.2 Electrochemical Reactions

Potential losses for the electrochemical reactions included the mass-transfer ($\eta_{i,\mathrm{mt}}$) and the kinetic ($\eta_{i,\mathrm{k}}$) overpotentials for all the redox reactions considered, i.e., r = OER, NO3RR, HER, and ORR (Eqs. (3-8) and (3-9)).

$$\eta_i = \eta_{r,\mathrm{k}} + \eta_{r,\mathrm{mt}} \tag{3-8}$$

The mass-transfer overpotential was included to account for the bulk concentration-dependent limiting current densities for all redox species (NO_3^-/NO_2^- for NO3RR, H_2O/H_2 for HER, and O_2/OH for ORR) except for the OER. For the OER, this mass-transfer overpotential component in Eq. (3-8) is assumed to be negligibly small because of the large concentration of the reacting species, $c_{\mathrm{H_2O}}$ = 55.5 M (pH = 1) and $c_{\mathrm{OH^-}}$ = 1 M (pH = 14). Equation (3-9) accounts for the mass-transfer overpotential,

$$\eta_{r,\mathrm{mt}} = \frac{R_c\, T}{F\, n_e} \ln\left(\frac{\left(1 - \frac{j_r}{j_{l,r,c}}\right)^{\nu_{r,c}}}{\left(1 - \frac{j_r}{j_{l,r,a}}\right)^{\nu_{r,a}}} \right) \tag{3-9}$$

where, j_l is the limiting current density for the cathodic (c) and anodic (a) half-reactions. Limiting current densities were calculated assuming diffusion-limited species transport (Eq. (3-10)) of the oxidized (O) or reduced species (R), with a concentration boundary layer thicknesses of 10 µm, δ_{BL} = 10 µm, which is a reasonable assumption for planar electrode architectures with a laminar flow regime,[180]

$$j_{l,r,a/c} = \pm \frac{n_e\, F\, D_{\mathrm{R/O}}\, \boldsymbol{c}_{\mathrm{R/O,bulk}}}{\delta_{BL}\, \nu_{\mathrm{R/O}}} \tag{3-10}$$

Laminar flow conditions and a concentration boundary layer thickness of 10 μm leads to conservative estimates for the limiting current densities, whereas in larger-scale and industrial electrochemical flow reactors, enhanced mixing is expected, which results in smaller boundary layer thicknesses that can sustain even larger limiting current densities.[181]

Butler-Volmer equations were applied to model reversible electron transfer reactions (Eq. (3-11)) and irreversible cathodic reactions (Eq. (3-12)),

$$j_r = j_{0,\mathrm{ref},r} \left(\frac{\boldsymbol{c}_{\mathrm{R,bulk}}}{\boldsymbol{c}_{\mathrm{R,bulk,ref}}} \right)^{(\nu_{\mathrm{R}}\, \alpha_{c,r})/n_e} \left(\frac{\boldsymbol{c}_{\mathrm{O,bulk}}}{\boldsymbol{c}_{\mathrm{O,bulk,ref}}} \right)^{(\nu_{\mathrm{O}}\, \alpha_{a,r})/n_e} \left(\exp\left(\frac{\alpha_{a,r}\, \eta_{r,\mathrm{k}}}{R_c\, T/F} \right) - \exp\left(\frac{-\alpha_{c,r}\, \eta_{r,\mathrm{k}}}{R_c\, T/\, F} \right) \right) \qquad (3\text{-}11)$$

$$j_r = j_{0,\mathrm{ref},r} \left(\frac{\boldsymbol{c}_{\mathrm{O,bulk}}}{\boldsymbol{c}_{\mathrm{O,bulk,ref}}} \right)^{1-\alpha_{c,r}/n_e} \left(-\exp\left(\frac{-\alpha_{c,r}\, \eta_{r,\mathrm{k}}}{R_c\, T/\, F} \right) \right) \qquad (3\text{-}12)$$

where, $j_{0,\mathrm{ref},r}$ is the reference surface- and concentration-dependent exchange current density of the r^{th} reaction (for a selected electrocatalyst, the larger the $j_{0,r}$ value, the faster the rate is for both the anodic and cathodic directions of the reversible redox reactions); α_a and α_c are the charge-transfer coefficients indicating the symmetry of the activation barrier for the reaction. Equation (3-11) was applied to model the kinetics for the OER, HER, and ORR, whereas Eq. (3-12) was used for the NO3RR. Unless specified otherwise, atmospheric conditions (1 atm, 25° C), with a mole-fraction of 20.9% of O_2(g), trace amounts of H_2(g) (0.5 ppm) and balance N_2, was assumed for the gaseous species. Dissolved gas concentrations, $\boldsymbol{c}_{\mathrm{O_{2,aq,bulk}}}$ and $\boldsymbol{c}_{\mathrm{H_{2,aq,bulk}}}$, were obtained by assuming equilibrium between the gaseous and the aqueous forms of the respective species. Henry's law constants reported at 25° C were used for these calculations,[55] leading to O_2(aq) and H_2(aq) concentrations of 2.8×10^{-1} mM and 3.9×10^{-7} mM, respectively, in the bulk electrolyte.

A literature review was performed to identify the state-of-the-art catalysts for the OER and NO3RR, based on which the kinetic parameters $(j_{0,\mathrm{ref},r}, \alpha_{c,r}, \alpha_{a,r})$ were determined for these reactions (Table 3-2). For the NO3RR, catalysts were selected based on satisfying two criteria: (a) the availability of kinetic parameters, or cyclic voltammograms or Tafel plots from which kinetic parameters can be extracted, and (b) the inclusion of product composition analyses to determine the selectivity to the desired nitrate reduction products.[107,123,158–160,162–164,182] It was determined that Cu (pH of 14) and Sn-Pt (pH of 1) exhibited high product selectivity for the reduction of NO_3^- to NH_3 and N_2O respectively.[107,160] The extracted kinetics from the previously studied polycrystalline Cu catalyst (Table A-2) for 0.1 M $NaNO_3$ under pH 14 and pH 8 conditions were included as well for comparison. Kinetic parameters obtained at pH 14 are largely comparable to reported data by other investigators for Cu at pH 14 and 0.1 M $NaNO_3$ conditions. The kinetics for the NO3RR was modeled by considering the irreversible reduction of NO_3^- to NO_2^- as the rate-determining step.[83,139]

$$NO_3^- + H_2O + 2\ e^- \rightarrow NO_2^- + 2\ OH^- \qquad E^0 = 0.835 \text{ V v/s NHE} \qquad (3\text{-}13)$$

Because of the high product selectivity (> 98%) reported for the state-of-the-art catalysts, we assumed full selectivity in the transformation of NO_2^- to the desired products for the selected catalysts. This is a simplifying assumption to overcome the lack of mechanistic information to model the sequence of elementary steps needed for the various nitrogen-products considered in this study.[83] However, for the kinetic inputs from our experimental studies on polycrystalline Cu catalyst, we reported Faradaic efficiencies for the same electrolyte conditions for a fixed potential of -0.55 V vs RHE (Figure 2-8). At pH 14 for both 0.1 M and 1 M $NaNO_3$ the reported Faradaic efficiency for the formation of NH_3 was FE_{NH_3} = 46% and at pH 8, the reported Faradaic efficiency towards NH_3 formation was FE_{NH_3} = 39.5% for 1 M and FE_{NH_3} = 25% for 0.1 M.

For the pH conditions considered, the most suitable OER catalysts were identified to be IrO_2 (pH = 14), CoMnOx (pH = 8), and RuO_2 (pH = 1).[69,149,183–185]

3.3.3 Modeling Competing Reactions

The electrocatalytic parameters ($j_{0,\text{ref},r}$, $\alpha_{c,r}$, $\alpha_{a,r}$) for the competing reactions (ORR and HER) at the cathode were determined such that the impact of the "*worst-case*" on the efficiency and rates of nitrogen-recovery from the products formed could be investigated. The largest exchange current density, $j_{0,\text{ref},r}$, for the competing HER was based on the kinetics reported for Pt at both pH = 1 and pH = 14 (Table 3-2). The HER was modeled to be fully reversible with α_c = α_a = 0.5, as justified by experimentally reported measurements for various catalysts.[186,187] For the ORR, the $j_{0,\text{ref},r}$ was selected based on reported values for Pt for a pH of 1 and 14,[188–191] and the ORR cathodic charge-transfer coefficient was assumed to be α_c = 0.9 to model a surface that is favorable to ORR.

Overall, we have a consistent system of algebraic equations (up to 12 when competing reactions are included) that are simultaneously solved for the variables – $j_{\text{op}}, V_{\text{op}}, \eta_{\text{OER,k}}, j_{\text{NO3RR}}, \eta_{\text{NO3RR,k}}, \eta_{\text{NO3RR,mt}}, j_{\text{HER}}, \eta_{\text{HER,k}}, \eta_{\text{HER,mt}}, j_{\text{ORR}}, \eta_{\text{ORR,k}}, \eta_{\text{ORR,mt}}$. The system of equations was

Table 3-2: Reactions modeled with relevant pH, reference exchange current density, $j_{0,\text{ref}}$; charge transfer coefficients, α_c and α_a; N/A for the charge-transfer coefficients implies the use of the irreversible equation form (Eq. (3-12)); bulk reference concentrations, $c_{\text{bulk,ref}}$, extracted from the literature or from own experiments for the catalysts are listed; pH 1 used for N_2O and pH 8 and 14 data used for NH_3 production

Reaction	**pH**	**Catalyst**	**Kinetic Parameters for Eqs. (3-11) and (3-12)**			
			$j_{0,\text{ref}}$ (A m^{-2})	α_c	α_a	$c_{\text{bulk,ref}}$ (mM)
OER[69,149,183–185]	1	RuO_2	6.68×10^{-4}	0.1	1	c_{H^+} = 1000; $c_{\text{O}_2\text{,aq}}$ =1.3
	8	CoMnOx	3.44×10^{-7}	0.09	0.91	c_{OH^-} = 10^{-3}; $c_{\text{O}_2\text{,aq}}$ = 1.3
	14	IrO_2	0.48	0.63	0.39	c_{OH^-} = 1000; $c_{\text{O}_2\text{,aq}}$ = 1.3
NO3RR[107,160]	1	Sn-Pt	2.12×10^{-3}	0.54	N/A	$c_{\text{NO}_3^-}$ =10; c_{H^+} = 100
	8	Cu - ours	4.83×10^{-6}	0.38	N/A	$c_{\text{NO}_3^-}$ =100; c_{OH^-} = 10^{-3}
	14	Cu - ours	5.13×10^{-3}	0.27	N/A	$c_{\text{NO}_3^-}$ =100; c_{OH^-} = 1000
	14	Cu	1.12×10^{-2}	0.30	N/A	$c_{\text{NO}_3^-}$ =100; c_{OH^-} = 1000
HER[187,192]	1	Pt	10	0.5	0.5	c_{H^+} = 1000; $c_{\text{H}_2\text{,aq}}$ = 0.78
	14					c_{OH^-} = 1000; $c_{\text{H}_2,aq}$ = 0.78
ORR[188–191]	1	Pt	10^{-1}	0.9	0.1	c_{H^+} = 100; $c_{\text{O}_2\text{,aq}}$ =1.3
	14		10^{-5}			c_{OH^-} = 1000; $c_{\text{O}_2\text{,aq}}$ =1.3

solved using the *fsolve* function in Matlab R2018a, with a function tolerance of 10^{-4}, an optimality tolerance of 10^{-4}, a step tolerance of 10^{-4}, an average finite difference step size of 1.5×10^{-4}, and with the default solver algorithm (trust-region dogleg) or in instances when the convergence was challenging, the Levenberg-Marquardt algorithm was applied.[193]

3.3.4 Performance Metrics

The efficiency of converting the incident solar power (1 Sun or 1000 W m^{-2}) to the output chemical power was obtained using Eq. (3-14), where $\dot{R}_i$ is the molar flux of NH_3 and N_2O produced, and Δg_i^0 is the standard state free-energy change for the respective oxidation reactions (Table 3-2). The molar flux, $\dot{R}_i$, of NH_3 and N_2O (in mol m^{-2} s^{-1}) is related to the nitrate reduction current density, j_{NO3RR}, as shown in Eq. (3-15). The Faradaic efficiency of NO3RR was assumed to be 100% or fully selective towards the desired end-product for all cases, except when the Cu polycrystalline catalyst inputs from 0 were used.

$$\eta_{\mathrm{solar-to-chemical},i} = \frac{\dot{R}_i |\Delta \mathrm{g}_i^0|}{1000}; i = \mathrm{NH_3, N_2O} \quad (3\text{-}14)$$

$$\dot{R}_i = \frac{FE_i\, |j_{\mathrm{NO3RR}}|}{n_{e,\mathrm{total}}\, F}; i = \mathrm{NH_3, N_2O} \quad (3\text{-}15)$$

The oxidation of gaseous NH_3 with O_2 was modeled, $\Delta \mathrm{g}^0_{\mathrm{NH_3/H_2O}}$= -339 kJ mol^{-1}, whereas gaseous N_2O was used as an oxidizer to combust CH_4, $\Delta \mathrm{g}^0_{\mathrm{CH_4,N_2O/H_2O}}$ = -308.7 kJ mol^{-1}. Solar energy conversion efficiencies for the NO_3^--to-N_2 transformation is not reported because the N_2 produced has to first be reduced to NH_3/NH_4^+ to facilitate energy recovery, and this step in itself is highly energy intense.[194,195] For comparison, when solar-to-hydrogen efficiencies are computed for photoelectrochemical water-splitting devices, the molar rate of H_2 production with $\Delta \mathrm{g}^0_{\mathrm{H_2/H_2O}}$ = 237.4 kJ mol^{-1} is used.

The rate of nitrogen-removal and nitrogen-recovery, $\dot{r}_\mathrm{N}$ (in $\mathrm{g_N\ m^{-2}\ day^{-1}}$) are equal and directly proportional to the molar flux, $\dot{R}_i$, of the products formed from the nitrate contaminants (Eq. (3-16)). In Eq. (3-16), $M_\mathrm{N} = 14$ g $\mathrm{mol^{-1}}$, is the molar mass of atomic-nitrogen and t_day = 86400 s $\mathrm{day^{-1}}$. Therefore, a larger solar-to-chemical efficiency is also indicative of improved rates of nitrogen removal/recovery in our analyses.

$$\dot{r}_\mathrm{N} = \dot{R}_i\, M_\mathrm{N}\, t_\mathrm{day};\ i = \mathrm{NH_3, N_2O} \tag{3-16}$$

The specific energy intensity E_N (in MJ $\mathrm{kg_N^{-1}}$) (Eq. (3-17)) is a measure of the total energy required per unit mass of nitrogen removed and is commonly used as a metric to compare various technologies from an energy-consumption standpoint. The calculation in Eq. (3-17) assumed that the device steadily operates at the predicted current-density, j_op, and operating potential, V_op. Therefore, there is lack of dependence on current-density for the E_N calculation, as the current-density term appears both in the numerator (total energy consumption) and the denominator (total mass of nitrogen removed).

$$E_\mathrm{N} = \frac{V_\mathrm{op}\, n_e\, F}{M_\mathrm{N}} \tag{3-17}$$

3.4 Results & Discussion

3.4.1 Solar-to-Chemical Efficiencies and Nitrogen Removal/Recovery Rates

Figure 3-3 presents the equivalent-circuit model predictions for the solar energy conversion efficiencies (Eq. (3-14)) for NH_3 and N_2O production as a function of the semiconductor band gaps and electrocatalytic parameters. A bulk NO_3^- concentration of 100 mM, which is approximately the average of the NO_3^- concentration in the point-source effluents in Figure 1-1, was used in these calculations, and selective OER and NO3RR was modeled to estimate the upper limits for the solar energy conversion efficiencies. Irrespective of the catalytic parameters modeled, the solar-to-chemical efficiency initially increases with an increase in the semiconductor band gap until an optimum point, after which, the efficiency decreases. The optimum arises because of the tradeoffs between the increased light absorption for the smaller band gaps and the decreased radiative recombination losses for the larger band gaps. For state-of-the-art catalysts, peak solar-to-chemical efficiencies are 10.1% and 7.3%, corresponding to peak nitrogen removal/recovery rates of 395.3 g_N m^{-2} day^{-1} and 260.3 g_N m^{-2} day^{-1}, for N_2O and NH_3 formation respectively. The trends for the nitrogen removal/recovery rates are not shown in Figure 3-3 because they exactly match with the trends obtained for the solar-to-chemical efficiencies. The higher efficiencies and recovery-rates for the production of N_2O relative to NH_3 is due to the more effective catalysis for the NO3RR with the Sn-Pt catalyst as compared to Cu. Therefore, at peak efficiencies, relatively smaller kinetic overpotentials resulted for N_2O as compared to NH_3 – 412 mV v/s 689 mV for the NO3RR (Figure 3-3 (b) and (c)). *Ideal* efficiency plots were obtained by imposing rapid kinetics for the NO3RR, i.e. $\eta_{\text{red}} = 0$, with state-of-the-art OER catalysts. The optimal solar-to-chemical efficiencies for the *ideal* case more than double, from 7.3% to 17%, for NH_3 and increase from 10.1% to 16.3% for N_2O, as compared to the *state-of-the-art* NO3RR catalysts. The solar-to-chemical efficiency for N_2O formation is relatively less sensitive to the kinetic parameters modeled for NO3RR, as opposed to NH_3 formation, because the OER overpotentials dominate the potential losses in the former. This dramatic boost in overall performance, achieved by eliminating the nitrate-reduction kinetic overpotential, indicates that effective nitrate reduction electrocatalysts can significantly boost the efficiencies for any light-absorber and that the performance predictions are highly sensitive to the catalytic parameters modeled. To place these efficiencies in context, Figure 3-3

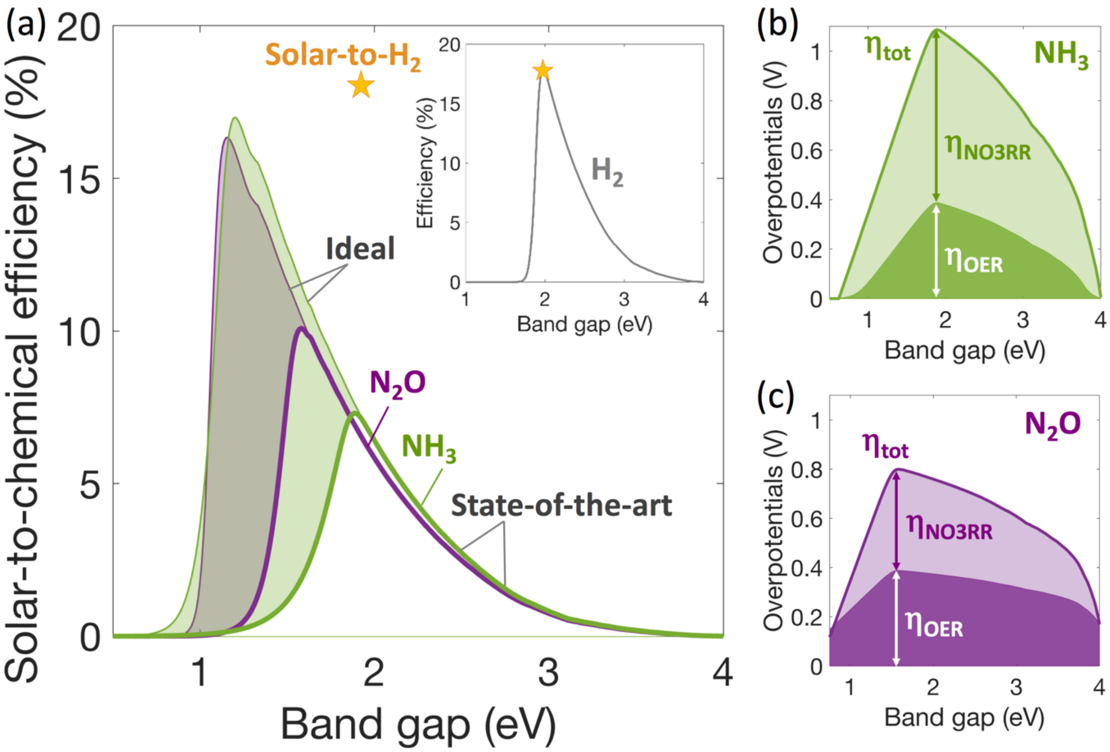

Figure 3-3: (a) Solar-to-chemical energy conversion efficiencies, $\eta_{\text{solar-to-chemical}}$, for water oxidation and NO_3^- reduction to NH_3 (green) and N_2O (purple) with RuO_2, Cu (pH 14) and IrO_2, Sn-Pt (pH 1) catalysts for the OER and the NO3RR, respectively. Solar-to-hydrogen efficiency in the inset was computed for RuO_2 (OER) and Pt (HER) catalysts at pH=1; maximum solar-to-H_2 efficiency is represented as a star.[153] The thick solid lines and the thin solid lines represent efficiencies with state-of-the-art and ideal nitrate reduction catalysts. Total kinetic overpotential, η_{total}, and the split between the oxidation (OER) overpotential, η_{OER}, (dark shaded area) and the NO3RR overpotential, η_{NO3RR}, (light shaded area) is shown for (b) NH_3 (green) and (c) N_2O (purple). Standard state potential from Eq. (3-3) was used and a 100 mM NO_3^- species concentration was modeled; $E^0_{\text{NO3RR}} = 0.835$ V vs NHE.

also depicts the maximum solar-to-hydrogen conversion efficiency of 18% for a photoelectrochemical water splitting device with a single light-absorber (band gap of 1.96 eV) and with state-of-the-art OER and HER catalysts.[153] The optimal efficiencies for the two processes are comparable when ideal/rapid NO3RR reduction kinetics were assumed because the kinetic overpotentials for the state-of-the-art HER catalysts are much smaller than that for the NO3RR catalysts. With state-of-the-art catalysts, the theoretical limits for the peak nitrogen-removal rates are comparable to the maximum removal rates, of 520 g_N m^{-2} day^{-1}, reported in (bio)electrochemical flow/continuous reactors for ammonia recovery.[138]

Figure 3-4 depicts the effect of varying the bulk NO_3^- concentration, $c_{NO_3^-,bulk}$, on the solar-to-chemical efficiency and the rate of nitrogen removal/recovery, while assuming selective NO3RR catalysis to form NH_3 (Figure 3-4(a) and (c)) or N_2O (Figure 3-4(b) and (d)). The bulk concentration of NO_3^- was varied from 0.1 mM to 1000 mM, representing the order-of-magnitude variation in the NO_3^- concentrations corresponding to the EPA limit in drinking water to the presence of NO_3^- in concentrated wastewater sources such as ion-exchange brines (Figure 1-1). Overall, for any concentration modeled, converting the NO_3^- to N_2O, as compared to NH_3, results in larger efficiencies and nitrogen removal/recovery rates (12.01% v/s 9.68% at 1000 mM) because of the more effective NO3RR catalysis for the former with Sn-Pt catalysts (Figure 3-3). There is a logarithmic scaling in the maximum efficiencies and the nitrogen removal/recovery rates with the NO_3^- concentration, because of the larger driving force and therefore lower kinetic overpotentials for the electron-transfer reactions (Eq. (3-12)).

For $c_{NO_3^-,bulk}$ = 10, 100 and 1000 mM, the transport of NO_3^- from the bulk solution to the electrode surface does not impact the operating current densities at any band gap of the semiconductor as the mass-transfer limited current density (Eq. (3-10)) for the NO3RR is much larger than the short-circuit density of the light-absorber. For these concentrations, when the band gaps are smaller than the optimal value, the concentration dependent NO3RR kinetics limits both the efficiency and nitrogen removal/recovery rates. For the same range of NO_3^- concentration, when the band gaps are larger than 2 eV, the performance is insensitive to changes in the concentration because light-absorption in the semiconductor limits the performance. However, for the two smaller concentrations, $c_{NO_3^-,bulk} = 0.1$ mM and 1 mM, there is a mass-transfer limited operational regime in addition to the kinetics and light-absorption limited performance. In this regime, there is little-to-no effect of the band gap on the performance, resulting in the *plateau*

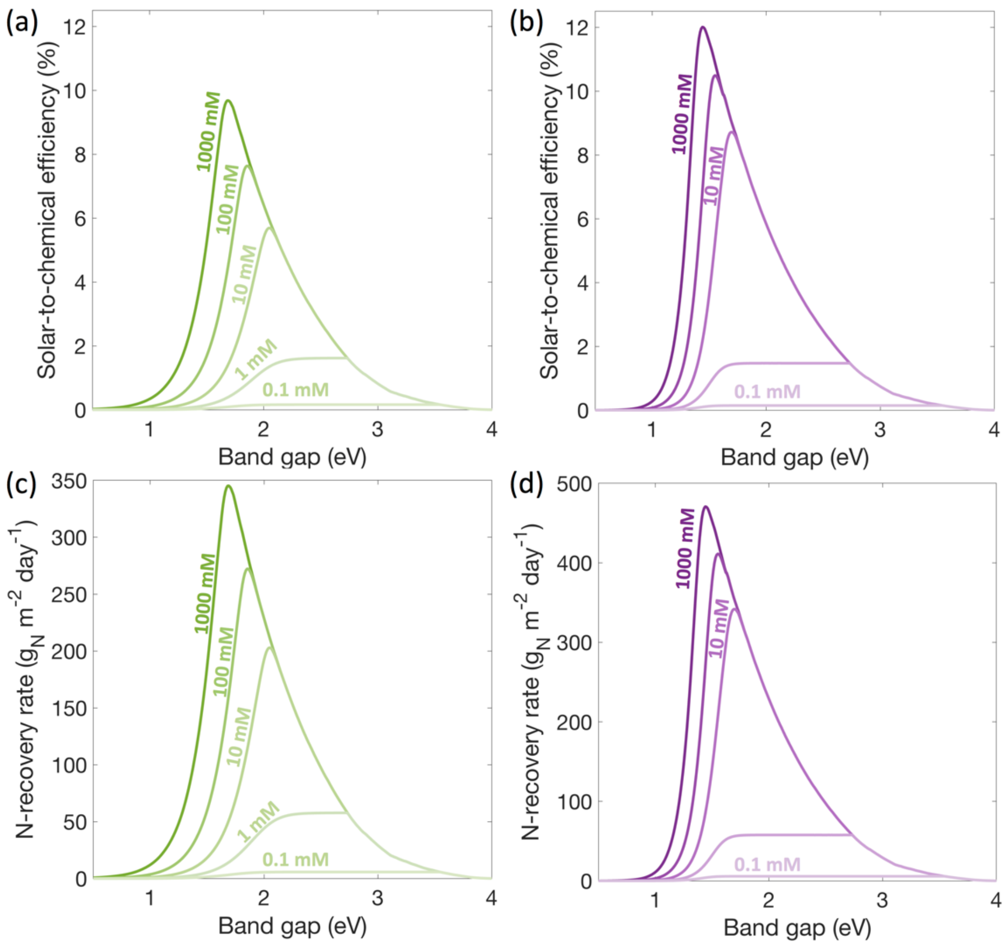

Figure 3-4: Concentration effects on the solar-to-chemical efficiencies ((a) and (b)) and the nitrogen-removal rates ((c) and (d)) with complete selectivity to desired reactions assumed: for (a) and (c), for the NO_3^--to-NH_3 conversion at pH 14, selective OER on IrO_2 and selective NO3RR on Cu was assumed; for (b) and (d), for the NO_3^--to-N_2O conversion at pH 1, selective OER on RuO_2 and selective NO3RR on Sn-Pt was assumed. For all these calculations, a headspace with standard atmospheric conditions (1 atm, 25˚C) with 20.9% of O_2, trace amounts of H_2 (0.5 ppm) and balance N_2 was assumed to determine thermodynamic reaction potentials.

region observed in Figure 3-4(a) and (b). In these conditions, the operating current density of the device (Eq. (3-4)), is predominantly limited by the rate of diffusion of the reacting NO_3^- species from the bulk electrolyte to the electrocatalyst surface. For NH_3 production, mass-transfer limited efficiencies of 1.62% and 0.16% are predicted for the band gaps of 2.15 – 2.75 eV and 1.65 – 2.75 eV, with $\boldsymbol{c}_{\mathrm{NO_3^-,bulk}}$ = 1 mM and 0.1 mM respectively. Therefore, the bulk NO_3^- concentration in the waste steam not only has an impact the maximum attainable efficiencies and the nitrogen recovery rates, but also affects how sensitive the performance is to the light-absorber band gaps.

Similar trends with respect to concentration are observed for both the solar-to-chemical efficiency to NH_3 and nitrogen-removal rate when a non-selective NO3RR reaction is assumed (Figure 3-5). For pH 14 (Figure 3-5(a)), the maximum values solar-to-chemical efficiencies, here 3.80% for 1000 mM as compared to 9.68% (Figure 3-4(a)), are now reached at larger band gaps. This decrease represents a larger shift than expected from the decrease in Faradaic efficiency towards NH_3 formation (100% changed to 46%) due to the additional change in the kinetic

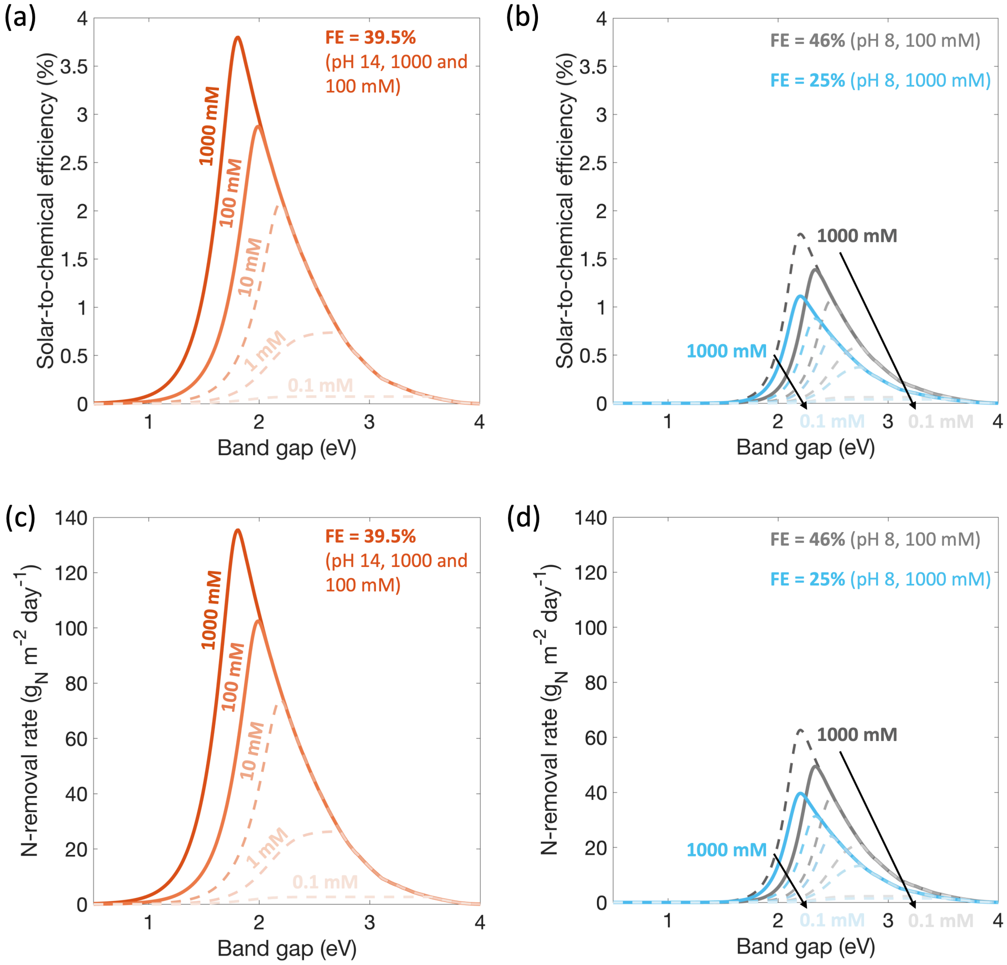

Figure 3-5: Concentration effects on the solar-to-chemical efficiencies ((a) and (b)) and the nitrogen-removal rates ((c) and (d)) with measured Faradaic efficiencies to desired reactions assumed: for (a) and (c), for the NO_3^--to-NH_3 conversion at pH 14, selective OER on IrO_2 and $FE = 39.5\%$ for NO3RR on Cu was assumed; for (b) and (d), for the NO_3^--to-NH_3 conversion at pH 8, selective OER on CoMnOx and $FE = 46\%$ (gray) and $FE = 25\%$ (blue) for NO3RR on Cu was assumed. Bold solid lines represent the FE implemented for the concentration at which it was measured (Chapter 2), dashed lines represent an assumed FE value being implemented. For all these calculations, a headspace with standard atmospheric conditions (1 atm, 25˚C) with 20.9% of O_2, trace amounts of H_2 (0.5 ppm) and balance N_2 was assumed to determine thermodynamic reaction potentials.

parameters implemented. For pH 8 (Figure 3-5(b)), two sets of lines are shown for the different Faradaic efficiencies reported in Figure 2-8: for 100 mM, FE = 46% was measured (implemented for gray lines) and for 1000 mM, FE = 25% was measured (implemented for blue lines). This results in an increase in the solar-to-chemical efficiencies as the concentration increases from 1000 mM to 100 mM, reaching a maximum of 1.11% at 2.2 eV and 1.39% at 2.34 eV respectively. The discrepancy between the implementation of the measured Faradaic efficiencies (solid lines) and the assumed values (dashed lines) for a same concentration exemplifies that extrapolating the system's behavior from one concentration to another does not hold at pH 8. It also highlights the need to measure the Faradaic efficiencies at more concentrations to better estimate the behavior of the proposed device for different wastewater compositions. Additionally, for the nitrogen-removal rates, it was assumed that all nitrogen removed was recovered as ammonia due to its possible uses. This however underestimates the total amount of NO_3^- removed, in particular for pH 8, as there were significant amounts of NO_2^- formed as well under those pH conditions (Figure 2-8).

Figure 3-6 reveals the extent to which the competing reactions influences the solar-to-chemical efficiencies. The green and the purple shaded areas (for NH_3 and N_2O respectively) represent the absolute change in efficiency, from assuming selective catalysis to when the *worst-case* was modeled for the competing reactions. Four semiconductor materials are mapped with selected band gaps—Si (1.1 eV), MoS_2 (1.75 eV), $BiVO_4$ (2.5 eV), and TiO_2 (3.1 eV). All materials other than Si have suitable valence band edges to function as a photoanode for the OER, whereas Si could be applicable as a photocathode material for the NO3RR.[196,197] Three bulk NO_3^- concentrations of 1000, 10, and 1 mM were selected to highlight the trends. Consider the results for the NO_3^--to-NH_3 transformation (Figure 3-6(a)). For all bandgaps, competing reactions result in lower solar-to-chemical efficiencies and nitrogen removal/recovery rates. The peak efficiencies, from Figure 3-4 are reduced by 9% and 63% for 1000 mM and 1 mM NO_3^- respectively. For any band gap, the relative decrease in the efficiency becomes larger when the bulk concentration of NO_3^- becomes smaller (Figure F-1). This outcome is due to the increase in the NO3RR mass-transfer overpotential with a decrease in the NO_3^- concentration, which in turn increases the driving force for the competing reactions. For the intermediate band gap materials —MoS_2 (1.75 eV) and $BiVO_4$ (2.5 eV) – ORR occurs at the mass-transfer limited current density of ~21 A m^{-2} for all NO_3^- concentrations (blue circles in Figure 3-6(b)). However, the rate of competing HER band gap, the relative decrease in the efficiency becomes larger when the bulk concentration of NO_3^- becomes smaller (Figure F-1). This outcome is due to the increase in the NO3RR mass-transfer overpotential with a decrease in the NO_3^- concentration, which in turn increases the driving force for the competing reactions. For the intermediate band gap materials —MoS_2 (1.75 eV) and $BiVO_4$ (2.5 eV) – ORR occurs at the mass-transfer limited current density of ~21 A m^{-2} for all NO_3^- concentrations (blue circles in Figure 3-6(b)). However, the rate of competing HER increases when the NO_3^- concentration decreases below 10 mM (yellow circles in Figure 3-6(b)). For $\boldsymbol{c}_{\mathrm{NO}_3^-,\mathrm{bulk}} >$ 1 mM, mass-transfer limited H_2 oxidation occurs instead of H_2 evolution because the cathode potential is larger than the equilibrium potential of H^+/H_2, $V_{\mathrm{cathode}} > E_{\mathrm{eq,HER}}$ = 0.19 V v/s RHE. For a bulk NO_3^- concentration of 1 mM and a band gap of 2.5 eV, while the NO3RR is mass-transfer limited when selective NO3RR was modeled (open green circles in Figure 3-6(b)), this limitation ceases to exist when competing reactions were taken into account at the cathode (filled green circles in Figure 3-6(b)). This trend is also evident in the shift of the operating potential and current densities of the diode (open versus closed black circles on the diode curve in Figure 3-6(b)). For both Si (1.1 eV) and TiO_2 (3.1 eV), the baseline efficiencies without the competing reactions are small due to the lack of driving potential at the cathode for the NO3RR in Si and because of

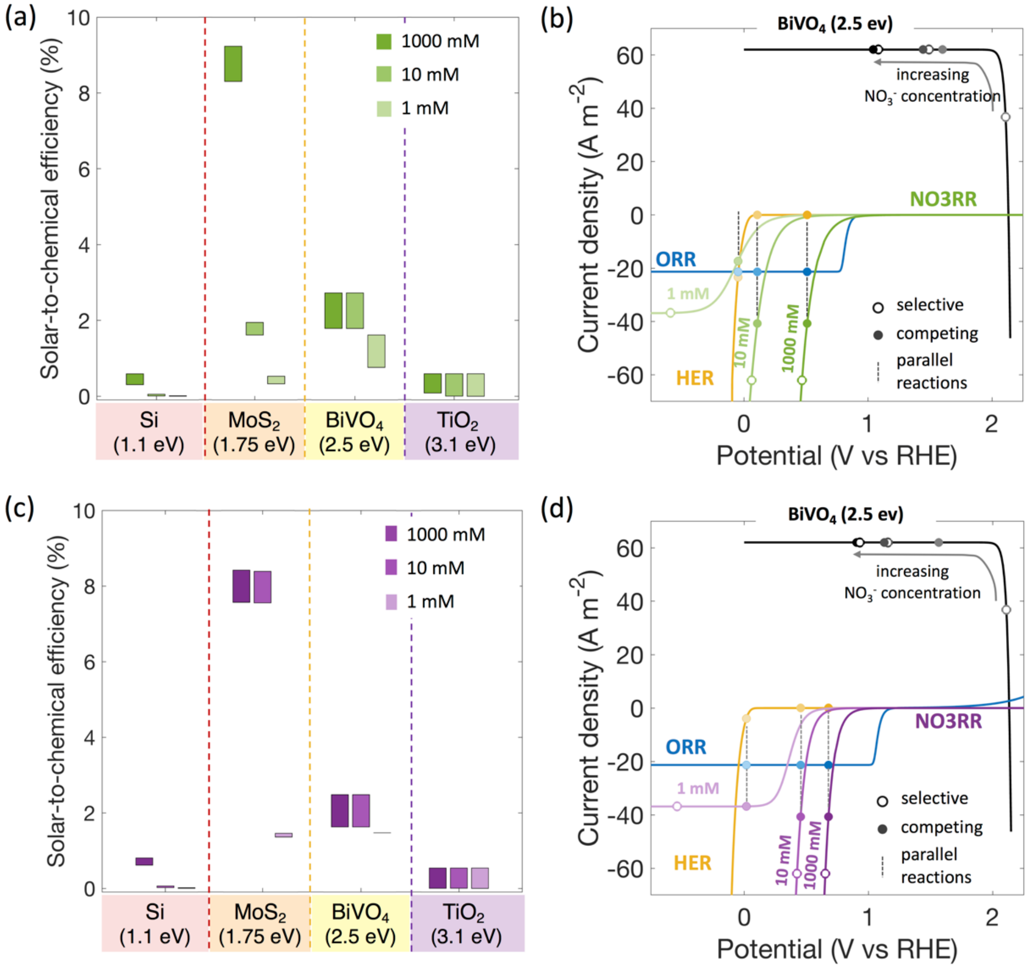

Figure 3-6: Solar-to-chemical efficiency for (a) NH_3 production and (c) N_2O production when competing HER and ORR reactions are implemented at the cathode with *worst-case* kinetic parameter values (Table 3-2). (b,d) To further illustrate the driving forces for the competing reactions, the current-voltage behavior for the diode (black) assuming $BiVO_4$ with a band gap of 2.5 eV and the parallel and competing electrochemical reactions at the cathode. Open symbols on the current-voltage plot represent models that assumed selective reactions whereas the filled symbols include the competing reactions. The operating point, j_{op} and V_{op}, is shown on the diode curve (black circles); the cathode potential and current densities for (b) NH_3 production (green) or (d) N_2O production (purple); HER (yellow); and ORR (blue).

the limited visible light absorption for TiO_2. In both these instances, mass-transfer limited ORR predominates at the cathode as compared to the NO3RR; H_2 oxidation occurs at negligibly small, mass-transfer limited rates of 3.87×10^{-5} A m^{-2}, for all NO_3^- concentrations in the bulk.

For the NO_3^--to-N_2O transformation (Figure 3-6(c)), overall trends are largely similar to what was previously discussed for the NO_3^--to-NH_3 transformation. A subtle difference occurs with respect to the effects of competing HER for the low NO_3^- concentrations (≤ 1 mM). While

HER becomes more significant at these NO_3^- concentrations for NH_3 production, it is not the case for N_2O formation because of the lower kinetic potential losses. Therefore, the current onset occurs at a much lower potential on the Sn-Pt catalyst for N_2O formation as compared to the Cu catalyst for NH_3 production. For example, with the $BiVO_4$ light-absorber with a 2.5 eV bandgap, Figure 3-6(d) reveals that the NO3RR is mass-transfer limited for both with and without competing reactions, and therefore the efficiency does not change (Figure 3-6(c)). The conversion of NO_3^- to N_2O benefits from more efficient catalytic parameters modeled as compared to NH_3, especially at the low NO_3^- concentrations.

Overall, even with large driving forces for the competing reactions established by the *worst-case* parameters modeled herein, these results indicate that the competing reactions do not significantly influence the performance (at most 10% relative change in efficiencies and the nitrogen removal/recovery rates) when the NO_3^- concentrations are large ($\geq$ 100 mM) and with optimally selected band gaps. In these cases, the most dominant competing reaction at the cathode is the ORR, which is mass-transfer-limited to current-densities less than 21 A m^{-2}, which is at least five times lesser than the NO3RR current densities.

3.4.2 Comparison with state-of-the-art nitrogen-removal technologies

We compared the proposed device with two tertiary technologies that are currently used for nitrogen removal and recovery – (1) electrochemical ammonia stripping, which recovers NH_3/NH_4^+,[138] and (2) the Sharon-Anammox process, which is one of the most energy efficient biological route to remove NH_3/NH_4^+ contaminants as N_2.[125,169] These three pathways were compared on the basis of the nitrogen-removal rates and the mass-specific energy intensity (Table 3-3). While all three processes qualify as nitrogen-removal technologies, there are substantial disparities in the implementation (Table 3-3). The Sharon-Anammox process removes NH_3/NH_4^+

contaminants present as N_2 without nutrient recovery, electrochemical ammonia stripping only separates contaminants that are already in the form of NH_3/NH_4^+, and finally the proposed photoelectrochemical approach transforms NO_3^- to NH_3/NH_4^+ to both remove and recover the nutrients present. For the sake of this comparison, we assumed bulk NO_3^- concentrations of 1, 10, and 100 mM, state-of-the-art catalysts for NH_3/NH_4^+ production and did not consider competing reactions (Cu demonstrates greater than 98% selectivity for NH_3 production at pH 14). Figure 3-6 indicates that the competing reactions do not substantially alter the performance for the 100 mM and 10 mM cases; for 1 mM NO_3^- concentration, not accounting for competing reactions could overestimate the N-removal rate by a factor larger than 2 and underestimate the mass-specific energy intensity by 40%.

For the nitrogen-removal rates, the proposed photoelectrochemical approach achieves rates that are comparable with electrochemical flow reactors for ammonia-stripping — 272.2 and

Table 3-3: Process description, nitrogen-removal rates and mass-specific energy intensity comparisons for the Sharon-Annamox, electrochemical flow reactor for ammonia stripping and the photoelectrochemical approach discussed in this work.

Process Details & Performance Metrics (Units)	**Nitrogen Removal and Recovery Technologies**				
	Sharon-Anammox	Electrochemical ammonia stripping	Photoelectrochemical device		
Process details	NH_4^+ to N_2 transformation with NO_2^- as the electron mediator; batch reactor	Physical separation and concentration of NH_4^+ contaminants by applying an electrical bias; flow reactor	Solar-driven electrochemical transformation of NO_3^- to NH_3/NH_4^+; flow reactor		
Nitrogen-removal rates (g_N m^{-2} day^{-1})	10	384	272.2 (100 mM)	203 (10 mM)	57.7 (1 mM)
Mass-specific energy intensity (MJ kg_N^{-1}) for nitrogen removal at a rate of 10 g_N m^{-2} day^{-1}	10-16	2.4	7.9	9.4	26.3

203 g_N m^{-2} day^{-1} for NH_3 production from 100 mM and 10 mM bulk NO_3^- concentration respectively. The Sharon-Anammox process is implemented in a batch reactor with N-removal rates on the order of 2 kg_N m^{-3} d^{-1}.[125,169] While batch reactors offer simplicity in terms of component and reactor design, they often have lower conversion rates as compared to flow reactors because the reactant concentration decreases with time, which reduces the driving force for the reactions.[198] An areal reaction rate of 10 g_N m^{-2} day^{-1} is estimated by assuming a biofilm/membrane surface area of 200 m^2 m^{-3} (Section 0 for calculation details). Therefore, the mass-specific energy intensities for all three N-removal technologies were compared at this fixednitrogen removal rate of 10 g_N m^{-2} day^{-1}. To obtain a volumetric reaction rate for the proposed device requires further multiphysics analyses for flow and species transport, which is outside the scope of the present work, but will be done in future work. About 10–16 MJ kg_N^{-1} is estimated to be required by the Sharon-Anammox process, including aeration, pumping and other parasitic power inputs at the plant-scale.[125,169] A specific energy intensity of ~2.4 MJ kg_N^{-1} is estimated, without any consideration of parasitic energy requirements, for the electrochemical ammonia stripping reactor.[138] In comparison, at equivalent nitrogen-removal rates, the energy intensity for the photoelectrochemical approach for the bulk NO_3^-concentration of 100 mM is 7.9 MJ kg_N^{-1}, out of which 2.9 MJ kg_N^{-1} is required for the NO_3^-–to–NH_4^+ transformation, 2.6 MJ kg_N^{-1} is estimated for pumping in a flow reactor,[153] and an energy requirement of 2.4 MJ kg_N^{-1} was additionally included to recover the NH_3/NH_4^+ formed via electrochemical ammonia stripping. The energy intensity for the NO_3^-–to–NH_4^+ transformation increases as the concentration is decreased, with a three-fold increase from 100 mM (7.9 MJ kg_N^{-1}) to 1 mM (26.3 MJ kg_N^{-1}) due to the mass-transport limited reaction rates. Therefore, the proposed approach has the potential to be competitive with one of the most energy-efficient nitrogen-removal technologies, the Sharon-Anammox process,

for bulk NO_3^- concentrations larger than 10 mM, with the added dual benefits of harnessing sunlight to treat and remove reactive-nitrogen (NO_3^-) contaminants while also recovering nutrients as NH_3/NH_4^+ (or N_2O).

3.5 Conclusions

In summary, we propose and analyze the performance of a solar-powered wastewater nitrate treatment process that couples water oxidation with nitrate reduction to produce value-added chemicals such as NH_4^+/NH_3 and N_2O. A numerical model was developed to predict the influences of material- and operational- parameters on solar-to-chemical efficiencies and the nitrogen removal/recovery rates. Important modeling innovations were introduced to quantify the influences of reacting species concentrations in the bulk solution and the competing hydrogen evolution and oxygen reduction reactions on the performance.

For a bulk NO_3^- concentration of 100 mM, results predict peak solar-to-chemical efficiencies of 7% and 10%, and nitrogen removal/recovery rates of 260 $g_N\,m^{-2}\,day^{-1}$ and 395 $g_N\,m^{-2}\,day^{-1}$, for NH_3 and N_2O production with Cu and Sn-Pt catalysts respectively; optimal light-absorber band gaps are 1.89 eV and 1.58 eV respectively. For NO_3^- concentrations larger than or equal to 10 mM, efficiencies and the nitrogen removal/recovery rates are limited either by the nitrate reduction kinetics or the light-absorber current-voltage behavior. However, for smaller NO_3^- concentrations, there is a mass-transfer limited operating regime, wherein the efficiencies and the nitrogen removal/recovery rates are unaffected by changes in the light-absorber band gap and the electrocatalytic parameters. In this regime, the operating current densities are only limited by the rate of diffusion of the NO_3^- ions, from the bulk to the surface of the electrocatalyst. Competing hydrogen evolution and oxygen reduction reactions were modeled with *worst-case* parameters deduced from kinetics for these reactions on a Pt-catalyst. For large concentrations ($\geq$ 100 mM) of nitrates and optimally selected light-absorber band gaps, oxygen reduction is the more dominant competing reaction and is mass-transfer limited. The driving force for the hydrogen evolution reaction increases for the smaller NO_3^- concentrations and for increasing light-absorber band gaps. Model predictions were used to map selected band gaps with real semiconductor materials for NH_3 and N_2O production. For example, MoS_2 with a band gap of 1.75 eV can yield high efficiencies and nitrogen removal rates for NO_3^--to-NH_3 conversion, when NO_3^- concentrations are larger than 10mM. For smaller NO_3^- concentrations, the efficiency remains largely unaffected with variations in the light absorber band gap due to mass-transfer limitations. Therefore, efficiencies obtained for MoS_2 and materials with larger band gaps, e.g., $BiVO_4$, (2.5 eV) are comparable. The proposed photoelectrochemical device is comparable and competitive with the Sharon-Anammox process, which is one of the most efficient biological pathways to remove ammonia present in wastewater as nitrogen and offers the potential to harness solar energy for resource recovery from nitrogen-contaminants in wastewater.

On the whole, theoretical analyses in this study indicate that transforming wastewater nitrates to value-added chemicals, including NH_3 and N_2O, by utilizing sunlight can be a promising new approach to achieve resource recovery, in the form of value-added chemicals and energy, from wastewater. Future investigations will focus on experimental measurements to assess the realistic performance of the catalysts and semiconductor materials identified in this work and in evaluating coupled transport and kinetics to aid reactor design and operation.

Chapter 4 Revealing the Role of Competing Reactions and Mass-Transfer Effects in Photocatalytic Solar Hydrogen Production Systems

Adapted in part from a manuscript under preparation: *Barrera, L., Ardo, S., Bala Chandran, R., "Revealing the Role of Competing Redox Reactions and Mass-Transfer Limitations in Current–Voltage Characteristics for Photocatalysis".*

4.1 Introduction

At the core of photocatalysis is semiconductor mediated redox reactions powered by photons/electromagnetic waves.[199,200] This enables the conversion of abundant yet intermittent and diffuse sunlight to storable and transportable chemical fuels,[64,201–203] including hydrogen,[67–69,75,204–207] carbon monoxide for synthesis gas[208–214] and methanol[213–220] by using water and carbon dioxide as feedstocks. Photocatalysis also has extensive oxidative applications, for example, to treat organic contaminants in water[221–223] and air,[223,224] and to effect methane transformations.[225–231] We have developed a powerful and elegant equivalent circuit modeling framework for photocatalytic and photoelectrochemical systems alike to predict solar-to-fuel energy conversion efficiencies as a function of material thermodynamic and kinetic parameters, while factoring in reaction selectivity and mass-transfer limitations. Predictions of selectivity and the inclusion of mass-transfer effects is a unique distinction and departure from state-of-the-art techniques, which are tailored towards efficiency predictions for externally biased or heterogeneous junction photoelectrochemical electrodes. Even though this study specifically focuses on performance predictions for a Z-scheme photocatalytic solar water splitting system,[69,75,232] the approach developed here is broadly applicable to predict, understand, and control device performance with rectifying semiconductor-electrolyte junctions.

On the surface of a photocatalyst, photo-excited charge carriers that do not recombine will drive at least one reduction and oxidation reaction respectively at the conduction and valence bands to maintain charge neutrality. Figure 4-1 depicts photocatalytic oxidation of a redox shuttle, represented as D/D^+ ($D \rightarrow D^+ + e^-$) with hydrogen evolution ($H^+ + e^- \rightarrow \frac{1}{2} H_2$); D/D^+ can be H_2O/O_2, Fe(III)/Fe(II), or I^-/IO_3^- depending on the system. However, thermodynamic driving forces favor the opposite reactions – the reduction of the redox shuttle and/or oxidation of hydrogen (Figure 4-1(b)). Such backward/undesired reactions have been observed even with cocatalysts during photocatalysis.[233–236] The challenge of reaction selectivity is most stark in two-step/dual-compartment Z-scheme photocatalysis reactors with soluble redox shuttles that relay electrons between oxygen and hydrogen evolving light absorbers.[66,69] Reactors based on this concept facilitate intrinsic spatial separation of H_2 and O_2 to promote safe operation at high efficiencies, and are projected to be lucrative from a technoeconomic standpoint for solar hydrogen production.[237,238] Therefore, there is a critical need to predict reaction selectivity and determine how performance is influenced by the redox shuttle kinetic parameters. Additionally, particle-based reactor architectures either as suspensions[66,69] or sheets[67,239] are more likely to be subject to mass-transfer limitations due to any one or all of these factors: (i) ineffective stirring/mixing on the particle-scale; (ii) redox shuttle species concentrations that are restricted to small quantities due to their contribution to the attenuation of visible light absorption and their species solubility; and (iii) small redox shuttle diffusivities, especially for large molecules like quinones.[69]

Modeling tools that are analogous to detailed-balance efficiency predictions in photovoltaic cells already exist for photovoltaic-electrolyzer, photoelectrochemical and

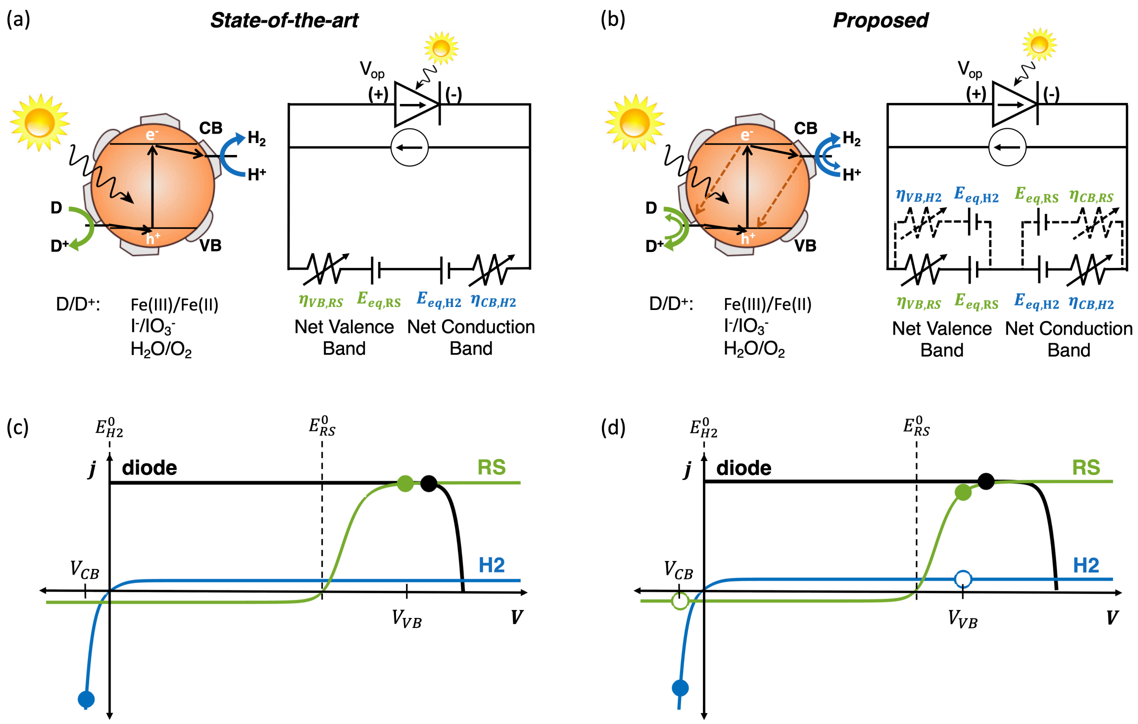

Governing equations

Diode:

$$j = j_{sc} - j_{rr}\left(\exp\left(\frac{q_e\,V}{n_d\,k_B\,T}\right) - 1\right)$$

Mass-transfer limited Butler-Volmer kinetics: $V = E^0 + \eta_{kin} + \eta_{mt}$

$$j = j_0\left(1 - \frac{j}{j_{l,a}}\right)^{\nu_R\,\alpha_c}\left(1 - \frac{j}{j_{l,c}}\right)^{\nu_O\,\alpha_a}\left(\exp\left(\frac{\alpha_a\,\eta_{\mathrm{kin}}}{R\ T/n_e\ F}\right) - \exp\left(\frac{-\alpha_c\,\eta_{\mathrm{kin}}}{R\ T/n_e\ \ F}\right)\right) \quad \text{and} \quad \eta_{\mathrm{mt}} = \frac{R\,T}{n_e F}\log\left(\frac{\left(1 - \frac{j}{j_{l,c}}\right)^{\nu_O}}{\left(1 - \frac{j}{j_{l,a}}\right)^{\nu_R}}\right)$$

Figure 4-1: Particle schematics and equivalent circuit diagrams for (a) the state-of-the-art scenario, where only desired reduction (H^+/H_2) and desired oxidation (D/D^+) reactions are taking place, and (b) the hereby proposed scenario, where additional competing back-reactions (indicated by the dashed lines) are allowed. Intersection plots of the diode curve (black) with the reaction curves (green for the redox shuttle reaction (RS), blue for the hydrogen reaction (H2)) (c) when only selective reactions are implemented and (d) competing reactions are considered as well, with desired reactions shown as full markers and competing reactions shown as empty markers. The operating point of the device is indicated by the black marker on the diode curve. Governing equations for the current densities implemented shown in the box.

photocatalytic systems.[75–78,153,240–242] Most of these models pair the current-voltage behavior of an ideal photodiode with electrochemical loads due to reaction kinetics and ohmic/solution resistance.[76,153] Many of the studies have also looked at the behavior of multiple semiconductor diodes in series, for tandem or multijunction set-ups,[75–77,153] with recent studies extending their modeling capabilities to account for different configurations and photon matching.[241,242] Even with such comprehensive predictive tools and foundational knowledge in the literature, all of these studies unanimously discount the effects of competing/parallel reaction pathways (Figure 4-1). This aspect has been considered in a limited extent in our prior work.[46,69] Bala Chandran et al. considered Z-scheme photocatalysis with a suspension of particles and modeled competing reactions based on an operating potential derived from the assumption of perfect selectivity, which will likely overestimate the extent of back reactions.[69] Barrera et al. modeled competing reactions at the conduction band for a specific application of NO_3^- reduction, with selective reactions modeled at the valence band and only considering a single light absorber.[46] The majority of the tools previously discussed were only applicable for a single light-absorber, whereas particle systems are better represented by many light absorbers. Motivated by these knowledge gaps, this study develops and furthers an equivalent-circuit based modeling framework that accounts for parallel/competing reaction pathways and mass-transfer limited current densities. Furthermore, we establish a path to better relate detailed-balance performance predictions for particle-based photocatalytic reactor concepts, and we apply this formulation to an array of thin, semitransparent, light absorbers that are optically in series.

4.2 Theory & Numerical Model

The behavior of a photoelectrochemical device was captured using a modified traditional zero-dimensional (0-D) equivalent circuit model such that both the desired pair of the hydrogen (H2) and redox shuttle (RS) electrochemical reactions (hydrogen evolution and redox shuttle oxidation) and unwanted competing reactions (hydrogen oxidation and redox shuttle reduction) could be sustained. As seen on Figure 4-1(b), the competing reactions were added to the equivalent circuit as additional pathways (dotted line resistors) at both the conduction band (CB) and valence band (VB) of the semiconductor light absorber. Similar to the approach described in Chapter 3.3, the electrochemical reactions, modeled as variable resistors to account for the electrocatalyst current-overpotential behavior, were placed in series with a semiconductor light absorber. The same potential and current density equalities (Eq. (3-1a) to Eq. (3-4)) were enforced across the parallel branches of the circuit. The sign convention implemented for the current density is still reduction current densities as negative and oxidation current densities as positive. A distinction to the previous Nernst potential definition (Eq. (3-3)) is that the activities of all reacting species were assumed to be equal to 1.

In addition, the ensemble behavior of the particles in a Z-scheme reactor was captured in a 0-D equivalent circuit model by modeling multiple or N slabs of light absorbers within a reactor. This indicates a shift from a single optically thick slab to a stack of N optically thin light absorbers, which still absorb the same total amount of light. Each light absorber slab was assumed to be behaving independently from one another while still being governed by the same material properties and the equalities listed in Eq. (3-1a) to Eq. (3-4).

4.2.1 Light absorber behavior

Individual semiconductor light absorbers were modeled as an ideal diode with only radiative recombination as the loss mechanism for any generated electron-hole pair. The band gap of the material was always assumed as 1.55 eV (Table 4-1), with the specific positions for the valence and conduction band edges not explicitly modeled. Instead, it was assumed that the band edges straddle the required redox potentials for the device to operate.

The light intensity profile of the incoming AM 1.5 spectrum was modeled using Beer's law and by assuming a total optical absorptance A_{total} of the semiconductor material (Figure 4-2). Parametrizing A_{total}, such that it remains constant at 99% of light absorbed and is wavelength-independent allowed for results to be determined by the total optical thickness τ (Eq. (4-1)),

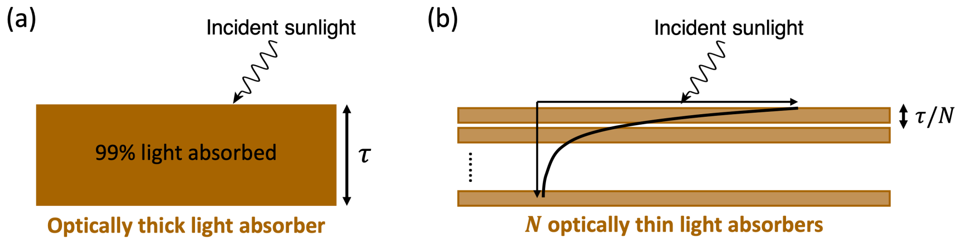

Figure 4-2: Schematics depicting (a) a single (N = 1) optically thick light absorber and (a) an ensemble of optically thin light absorbers with Beer's Law implemented, with τ/N representing the optical thickness of each light absorber assumed to be present.

thereby agnostic to material-specific spectral absorption coefficients and physical thickness of the semiconductor material. Additionally, no parasitic absorption by the electrolyte composed of water and redox shuttle ions was assumed to be taking place.

$$\tau = -\ln(1 - A_{\text{total}}) \tag{4-1}$$

When modeling $N > 1$ light absorbers, the optical thickness of an individual light absorber slab was inversely related to the total optical thickness by the number of slabs considered (Figure 4-2). This allowed for the implementation of a height dependence on the amount of light absorbed by each slab when a vertical stacking of the slabs was assumed, which in turn affected the maximum possible current density that can be sustained by each light absorber within the stack. The current-potential behavior of the semiconductor light absorber was modeled using the Shockley-Queisser detailed-balance model, like in Section 3.3.1, with the values for an optically thick slab shown in Table 4-1. The previous short circuit current density $j_{\text{sc},n}$ and radiative recombination current density $j_{0,\text{rr}}$ definitions were modified to account for the appropriate light intensity (Eq. (4-2) and Eq. (4-3)) with the implementation of Beer's Law.

$$j_{\text{sc},n} = q_e \int_0^{\lambda_g} N_{0,\lambda} \left(\exp\left(-\tau \frac{(n-1)}{N}\right) - \exp\left(-\tau \frac{n}{N}\right) \right) d\lambda \tag{4-2}$$

$$j_{0,\mathrm{rr}} = \frac{2\,\pi\, q_e}{h^2\,\mathrm{c}} \int_{0}^{\lambda_g} \exp\left(-\frac{h\,\mathrm{c}}{k_B T\,\lambda}\right)\left(\underbrace{1-\exp\left(-\frac{\tau}{N}\right)}_{\text{absorptance per slab}}\right) d\lambda \tag{4-3}$$

Where q_e is the electron charge, k_{B} = 1.38 x 10^{-23} J K^{-1} is the Boltzmann constant, $N_{0,\lambda}$ is the incident AM 1.5 spectrum, n = 1, 2, …, N is the slab number starting from the top of the stack, h = 6.626 x 10^{-34} m^2 kg s^{-1} is Planck's constant, c = 3 x 10^8 m^{-1} is the speed of light, λ is the wavelength of light, and λ_g is the characteristic wavelength of the semiconductor light absorber.

4.2.2 Selective coating implementation

A selective coating was implemented as a uniform layer covering the entirety of the slab surface. The reactions were assumed to be taking place at the semiconductor/coating or the catalyst/coating interface, such that species transport through the coating was considered consistently for all species present but Pt kinetics for the H2 reaction could still be implemented. The coating can be characterized by the coating thickness and the permeability $P_{e,i}$ of the RS species through the coating,

$$P_{e,i} = D_{eff,i}\, S_i \tag{4-4}$$

where, for a species i, $D_{eff,i}$ is the effective diffusion coefficient through the coating and S_i is partition coefficient. The effective diffusion coefficient $D_{eff,i}$ was defined as a factor of the bulk diffusion coefficient D_i. The partition coefficient S_i, also known as the solubility parameter, was defined as the ratio of species concentrations within the coating and liquid electrolyte phases at equilibrium,

$$S_i = \frac{\boldsymbol{c}_i^*}{\boldsymbol{c}_i} \tag{4-5}$$

where $\boldsymbol{c}_i^*$ (in M) is the concentration of the i-th species in the coating and $\boldsymbol{c}_i$ (in M) is the concentration of the i-th species in the liquid electrolyte. Note S_i = 1 is achieved when the equilibrium concentrations of the species i in the coating and liquid phases are equal, which also represents the scenario where there is no coating. Both $S_i < 1$ and $S_i > 1$ are physically possible irrespective of whether the species is getting made or consumed at the electrode surface. For a same coating, S_i can be different values for each species considered and depends on temperature, chemical composition of the coating, and physical characteristics of the coating such as density. S_i should generally be inversely related to density, as the higher percentage of volume occupied by the solid atoms of the coating material means that there is less physical space that can be occupied by the species of interest.[243]

4.2.3 Electrochemical reactions

The electrochemical reactions were modeled to include potential losses coming from both mass-transfer ($\eta_{b,k,\mathrm{mt}}$) and kinetic ($\eta_{b,k,\mathrm{kin}}$) overpotentials (Eq. (4-6)) for all of the redox reactions considered, i.e. b, k = VB,RS; VB,H2; CB,RS; CB,H2, as well as the contributions from the partition coefficients S_i:

$$\eta_{b,k} = \eta_{b,k,\mathrm{mt}} + \eta_{b,k,\mathrm{kin}} \tag{4-6}$$

The mass-transfer overpotential $\eta_{b,k,\mathrm{mt}}$ is defined by Eq. (4-7):

$$\eta_{b,k,\mathrm{mt}} = \frac{R_c\, T}{n_{e,k}\, F} \log\left(\frac{\left(S_{O,k} \left(1 - \frac{j_{b,k}}{j_{l,k,c}}\right)\right)^{\nu_{O,k}}}{\left(S_{R,k} \left(1 - \frac{j_{b,k}}{j_{l,k,a}}\right)\right)^{\nu_{R,k}}} \right) \tag{4-7}$$

Where $j_{b,k}$ was defined using mass-transport limited Butler-Volmer kinetics:

$$\begin{gathered} j_{b,k} = j_{0,k} \left[S_{R,k}\, a_{R,k} \left(1 - \frac{j_{b,k}}{j_{l,k,a}}\right)\right]^{\nu_{R,k}\, \alpha_{c,k}} \left[S_{O,k}\, a_{O,k} \left(1 - \frac{j_{b,k}}{j_{l,k,c}}\right)\right]^{\nu_{O,k}\, \alpha_{a,k}} \\ \left(\exp\left(\alpha_{a,k}\, \eta_{b,k,\mathrm{kin}}\, k_{mf}\, n_{e,k}\right) - \exp\left(-\alpha_{c,k}\, \eta_{b,k,\mathrm{kin}}\, k_{mf}\, n_{e,k}\right)\right) \end{gathered} \tag{4-8}$$

With $j_{0,k}$ as the reference exchange current density, $\alpha_{c/a,k}$ as the charge transfer coefficient, and k_{mf} as the thermal voltage, assuming $\nu_{O,k} = \nu_{R,k} = 1$ and $\alpha_{c,k} + \alpha_{a,k} = 1$. For the full derivation, see Appendix H.

While the concentration overpotential accounts for the Nernstian penalty of having concentration differences between the surface of a co-catalyst and the bulk solution, the kinetic overpotential is influenced by the electrocatalytic parameters, the exchange current density, the charge-transfer coefficient, and the surface concentration of the redox species. This surface species concentration is dictated by the ratio of operating to respective limiting current. Therefore, changing limiting currents affects both the concentration and kinetic overpotentials. The limiting current density $j_{l,k,c/a}$ for the cathodic (c) or anodic (a) reaction was calculated using Eq. (4-9):

$$j_{l,i,a/c} = \pm \frac{n_{e,i}\, F\, \boldsymbol{c}_{i,\mathrm{bulk}}}{\dfrac{\delta_{BL}}{D_{0,R/O}} + \dfrac{t_c}{P_{e,i}}};\ i = H^+, H_2, Fe^{3+}, Fe^{2+} \qquad (4\text{-}9)$$

Where $\boldsymbol{c}_{i,\mathrm{bulk}}$ is the bulk species i concentration, δ_{BL} is the boundary layer thickness, $D_{0,R/O}$ is the bulk diffusion coefficient, and t_c is the coating thickness.

To broadly consider these interconnected influences, limiting currents of individual species (H_2, D^+, D) were varied over several orders of magnitude, with the limiting current for D ($j_{l,RS,a}$) varied with respect to the short circuit current density of the diode (factors of 1e-2 - 1). Asymmetry factors, g_l, were introduced and varied from 1e-4 to 10 to compare the undesired/competing redox reactions to the desired redox shuttle oxidation current, at the valence band ($g_{l,VB} = j_{l,H2,a}/j_{RS,a}$) and conduction band ($g_{l,CB} = |j_{l,RS,c}|/j_{RS,a}$). The cathodic hydrogen evolution reaction was assumed to be comparatively much larger than the short circuit current density of the diode ($j_{l,H2,c}/j_{sc}$ = -1000) to reflect significantly higher concentration of H^+ compared to other species in an acidic environment and large H_2O concentration. In addition to the limiting currents, the exchange current density ($j_{0,RS}$ = 1e-5 – 1e3 A m^{-2}), the asymmetry in the charge transfer

Table 4-1: Assumed constants and parameter space

Parameter	Value	
Semiconductor and optical properties		
Band gap	1.55 eV	
Short-circuit current density j_{sc}	270 A m^{-2}	
Radiative recombination current density j_{rr}	6.22e-20 A m^{-2}	
Reaction kinetics		
Reaction k	RS	H2
Redox shuttle potential E_k^0	0.3 – 1.23 V	0 V
Reference exchange current density $j_{0,k}$	1e-5 – 1e3 A m^{-2}	10 A m^{-2}
Anodic charge transfer coefficient $\alpha_{a,k}$	0.01 – 0.99	0.5
Limiting current density ratios		
$j_{l,RS,a}/j_{\mathrm{sc}}$	1, 0.01	
$g_{l,CB} = \lvert j_{l,RS,c}\rvert/j_{l,RS,a}$	1e-4 – 10	
$g_{l,VB} = j_{l,H2,a}/j_{l,RS,a}$	1e-4 – 10	
Partition coefficients for RS reaction		
$S_{O,RS}$	1e-1 - 10	
$S_{R,RS}$	1e-2 - 10	

coefficient ($\alpha_{a,RS}$ = 0.01 – 0.99, where $\alpha_{c,RS} + \alpha_{a,RS} = 1$) for the RS reaction were also parametrized. All parameter ranges are summarized in Table 4-1.

Figure 4-3 shows different regimes of operation depending on the limiting current densities and the electrocatalytic parameters (Table 4-1) modeled by considering Fe(II)/Fe(III) as the redox shuttle paired with hydrogen evolution (H^+/H_2) reacting on a single, optically thick light absorber with a band gap of 1.55 eV. In the mass-transfer limited regime, the minimum limiting current density amongst the desired reactions, in this case for Fe(II) oxidation $j_{l,RS,a}$, is much smaller as compared to the diode short-circuit current j_{sc}, with $j_{l,RS,a}/j_{sc}$ = 1e-2. Therefore, the operating current densities are restricted to being lesser than the mass-transfer limited Fe(II) oxidation current density. As this ratio of limiting current density to the short-circuit current density increases, $j_{l,RS,a}/j_{sc} \geq 1$, we move towards a light absorption limited regime where the operating point is restricted by the magnitude of the short-circuit current density, which is influenced by the

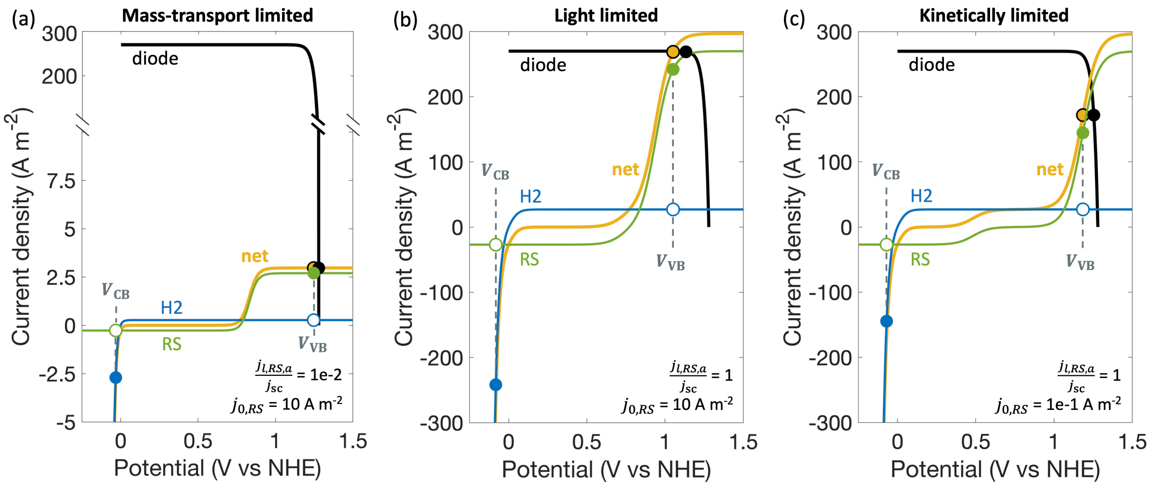

Figure 4-3: Intersection plots depicting diode curve (black), individual reaction curves (H2: hydrogen in blue, RS: redox shuttle in green), and summed reaction curve (yellow), showing (a) mass-transport limited behavior, (b) light-limited behavior, and (c) kinetically limited behavior. The desired reaction are shown by the filled markers, the undesired competing reaction shown by the empty markers, and the behavior at the conduction band and valence band are indicated by V_{CB} and V_{VB}, respectively. For all cases shown, $\alpha_{a,RS} = 0.5$, $g_{l,VB}$ = 1e-1, $g_{l,CB}$ = 1e-1, and $j_{l,H2,c}/j_{sc}$ = -1000.

bandgap, the optical properties, and the incident spectrum on the light absorber (Eq. (4-2)). For the same condition as in the light-absorption-limited case, if we modeled different electrocatalytic parameters ($j_{0,RS}$ = 10 A m^{-2} in Figure 4-3(b) vs $j_{0,RS}$ = 1e-1 A m^{-2} in Figure 4-3(c)), while the maximum operating current density is still dictated by j_{sc}, the operating point is restrained by the large kinetic overpotential for Fe(II) oxidation reaction, and so illustrates the kinetics-limited case.

4.2.4 Solver set-up

Figure 4-4 depicts a graphical illustration of the solution procedure. For each combination of inputs, the appropriate diode equation (black line) and current density-potential reaction curves (blue and green lines) were calculated. Across the same potential range, the total reaction current density (yellow bolded line) was calculated as the sum of the two reactions considered here. The intersection point of the diode curve and the summed reaction curve was used as the starting point of the solver $(V_{\mathrm{in}}, j_{\mathrm{in}})$[244] from which the resulting V_{CB} and V_{VB} values were deduced, as shown in the subplots for step 3. If the potential equality (Eq. (4-10)) was not respected, the operating point

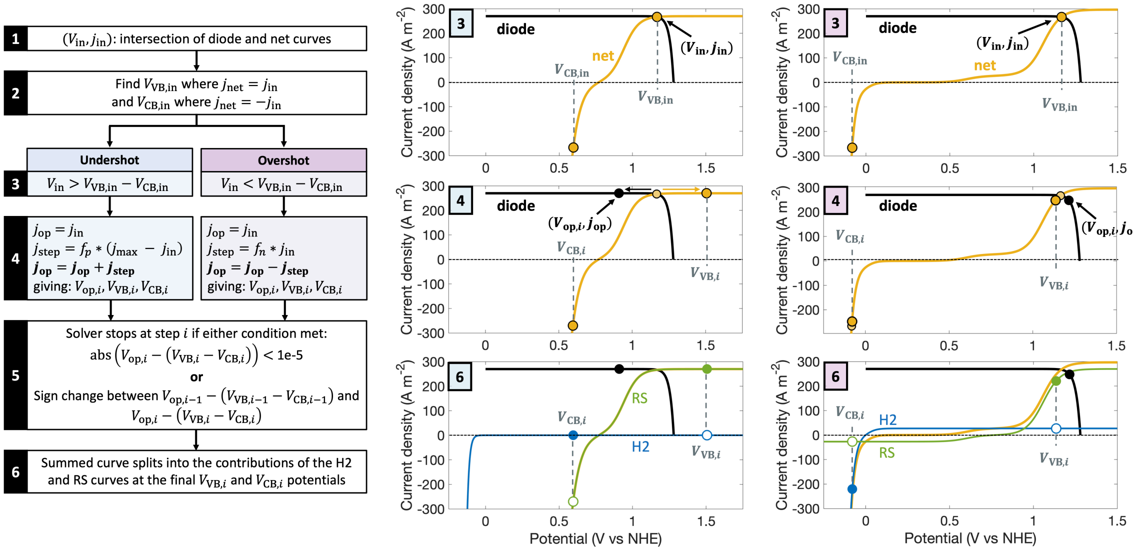

Figure 4-4: Algorithm flow chart with intersection plots depicting steps 3, 4, and 6 for both cases (undershot and overshot). Step 3: the intersection of the diode and summed curves is the starting point ($V_{\text{in}}, j_{\text{in}}$ shown as the yellow marker) that determines the initial $V_{\text{CB,in}}$ and $V_{\text{VB,in}}$. Step 4: shifting the operating point to larger (undershot) or smaller (overshot) current densities. Step 6: When the stopping criteria is met, the operating points on each curve can be calculated, with the desired reaction shown with the filled markers, the undesired competing reaction shown with the empty markers, and the behavior at the conduction band and valence band indicated by $V_{\text{CB},i}$ and $V_{\text{VB},i}$, respectively.

on the diode was shifted in a step-wise manner for i steps until the governing potential equality was respected. The direction of the shift depended on whether the initial guess undershot or overshot the potential equality, such that the operating current density was either increased or decreased, respectively (subplots for step 4). Note that the current density bounds were respected by taking a total number of steps smaller than $1/f_p$ or $1/f_n$, where f_p and f_n are the fractions (both $\leq$ 4e-4) used to determine j_{step}. In addition, for the case where j_{in} was increased by j_{step}, j_{step} was defined with respect to the difference between j_{in} and the maximum current density that can be sustained by the system j_{max} (here the minimum between j_{sc} and the sum of the anodic limiting current densities).

The algorithm stopped when either of the following stopping criteria were met (step 5): the potential equality (Eq. (4-10)) was respected within a tolerance of 1e-5; the potential equality difference changed sign between steps $i - 1$ and i (the operating point was then found from the intersection of the V_{op} and $V_{\mathrm{VB}} - V_{\mathrm{CB}}$ lines between steps $i-1$ and i). The V_{VB} and V_{CB} potentials were then used to determine the contributions of each reaction at the valence and conduction band respectively (step 6). With the stopping criteria met such that the potential equality (Eq. (4-10)) and the diode equation (Eq. (4-11)) are satisfied, the current density equalities (Eq. (4-12)) were respected within 0.5% of the j_{op}.

$$V_{op} = V_{VB} - V_{CB} \tag{4-10}$$

$$j_{op} = j_{sc,n} - j_{rr}\left(\exp\left(\frac{q_e\,V_{op}}{n_d\,k_B\,T}\right) - 1\right) \tag{4-11}$$

$$j_{op} = j_{VB,RS} + j_{VB,H2} = -(j_{CB,RS} + j_{CB,H2}) \tag{4-12}$$

4.2.5 Performance metrics

Several performance metrics were considered to quantify the behavior of the system. The solar-to-hydrogen (STH) efficiency of converting the incident solar power (1 Sun or 1000 W m^{-2}) to hydrogen was calculated using Eq. (4-13):

$$STH = \frac{\dfrac{-(j_{CB,H2} + j_{VB,H2})}{n_{e,H2}\,F}\,\Delta \mathrm{g}^{0}_{\mathrm{H_2/H_2O}}}{1000} \tag{4-13}$$

Where $\Delta \mathrm{g}^{0}_{\mathrm{H_2/H_2O}} = 237.4$ kJ mol^{-1} is the standard state free-energy change for the net desired oxidation and reduction reactions. It was assumed that the HER-driving compartment of the modeled Z-scheme reactor was paired with a perfectly complementary OER-driving compartment, such that no additional mass-transport or potential losses needed to be considered. The current densities at both CB and VB were considered here, such that a net consumption of the formed H_2 is possible, due to the assumed activities of 1 throughout the reactor, and so negative STH efficiencies could be calculated.

A reaction selectivity (S_{rxn}) was computed based on the molar reaction rates of the desired products as compared to the net rate of product generation at both the valence and the conduction bands using Eq. (4-14).

$$S_{rxn,VB} = \frac{\frac{|j_{VB,RS}|}{n_{e,RS}}}{\frac{|j_{VB,RS}|}{n_{e,RS}} + \frac{|j_{VB,H2}|}{n_{e,H2}}};\ S_{rxn,CB} = \frac{\frac{|j_{CB,H2}|}{n_{e,H2}}}{\frac{|j_{CB,RS}|}{n_{e,RS}} + \frac{|j_{CB,H2}|}{n_{e,H2}}} \qquad (4\text{-}14)$$

4.3 Parametric sweeps for a single slab

Figure 4-5(a) compares the solar-to-hydrogen efficiency dependence on the electrocatalytic parameters when ideally selective and competing reactions were modeled for mass-transfer and light-limited regimes based on the Fe(II)/Fe(III) oxidation current density for a single optically thick planar absorber. The H^+/H_2 reaction was assumed to occur on Pt co-catalysts, with fixed electrocatalytic parameters of $j_{0,H2}$ = 10 A m^{-2} and $\alpha_{a,H2} = \alpha_{c,H2} = 0.5$ for all cases unless otherwise mentioned. Additionally in Figure 4-5, the back reactions of hydrogen oxidation and Fe(III) reduction occur at smaller limiting current densities when compared to Fe(II) oxidation, $g_{l,VB}$ = 1e-1 and $g_{l,CB}$ = 1e-1, as well as all partition coefficients S_i were assumed to be 1. For comparison, the maximum possible STH efficiency that can be attained when the operating current density equals the short-circuit current density is 33%. As anticipated, all else being the same, optimal STH efficiencies decrease and occur at lower exchange current densities when competing reaction pathways were modeled compared to selective reactions (Figure 4-5(a)). This illustrates the substantial thermodynamic driving forces for back reactions for both Fe(II)/Fe(III) and H^+/H_2 species. Notably, results indicate that when exchange current density and anodic charge-transfer coefficient for the Fe(II)/Fe(III) reaction becomes small enough, net H_2 consumption occurs due to oxidation at the valence band resulting in negative STH efficiencies. In the mass-transfer limited regime, $j_{l,RS,a}/j_{sc}$ = 1e-2, while the maximum STH efficiency is at least two orders of magnitude smaller than the 33% attained in the light absorption limited region when $j_{l,RS,a}/j_{sc}$ = 1, the STH efficiency exhibits similar extents of deviations in efficiencies between modeling selective and competing reactions.

Trends for STH efficiency with respect to the exchange current density, $j_{0,RS}$, and anodic charge-transfer coefficient, $\alpha_{a,RS}$, are similar whether selective or competing reactions were

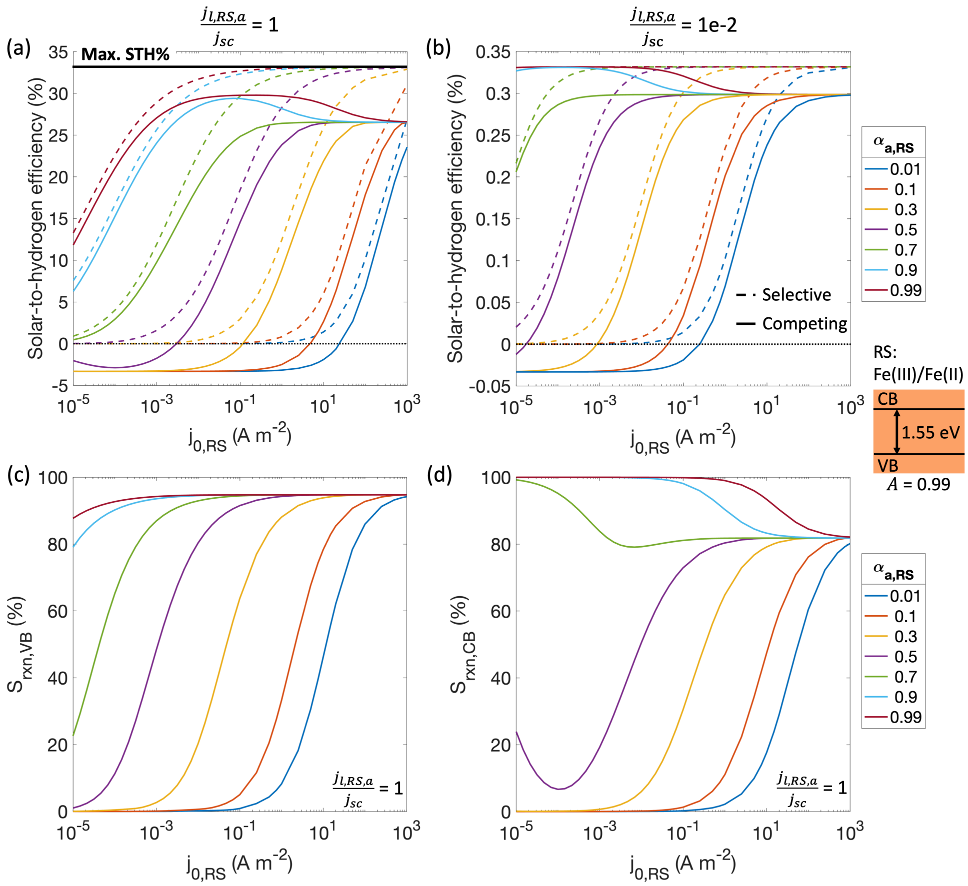

Figure 4-5: Solar-to-hydrogen efficiencies for selective reactions (dashed lines) and with competing reactions (solid lines) for (a) $j_{l,RS,a}/j_{sc}$ = 1 and (b) $j_{l,RS,a}/j_{sc}$ = 1e-2. Selectivity (S_{rxn}) towards the desired reaction (when competing reactions are implemented) for $j_{l,RS,a}/j_{sc}$ = 1 at (c) the valence band (VB) (d) the conduction band (CB). Black line indicates the maximum possible STH efficiency that could be reached assuming a fully ideal redox reaction. The light absorber was assumed to be optically thick (absorptance A of 0.99) with a band gap of 1.55 eV. The additional limiting current densities assumed were: $g_{l,VB} = j_{l,H2,a}/j_{l,RS,a}$ = 1e-1, $g_{l,CB} = |j_{l,RS,c}|/j_{RS,a},$ = 1e-1, and $j_{l,H2,c}/j_{sc}$ = -1000. The redox shuttle pair assumed here was Fe(III)/Fe(II). All S_i = 1. RS: redox shuttle reaction. H2: hydrogen reaction.

modeled. With increase in $j_{0,RS}$ STH efficiency initially increases up to its optimal value, due to lower kinetic overpotentials, and then decreases because of increased competition from the redox shuttle reduction reaction – Fe(III)/Fe(II) ((Figure 4-5(a) and (b)). Likewise, due to an increase in driving force for desired reactions, STH efficiencies monotonically increase with increase in $\alpha_{a,RS}$ with an associated decrease in minimum $j_{0,RS}$ required to attain optimal STH efficiencies. For instance, when $j_{0,RS} > 5$ A m^{-2} all charge transfer coefficients tend towards an efficiency of 26.53% for $j_{l,RS,a}/j_{sc} = 1$ (Figure 4-5(a)) and 0.30% for $j_{l,RS,a}/j_{sc} =$ 1e-2 (Figure 4-5(b)).

Figure 4-5(c) and (d) illustrate that the calculated STH efficiencies are dictated by the product of reaction selectivity at the valence and the conduction bands. For all $\alpha_{a,RS}$, the selectivity towards the redox shuttle oxidation reaction (Fe(II)/Fe(III)) at the valence band increases with $j_{0,RS}$, but has a ceiling of 94.74%. The upper bound is dictated by the mass-transfer limited hydrogen oxidation current density due its low solubility in water (0.78 mM in equilibrium with 1 atm H_2 at 300 K) (Figure 4-5(c)). Thus, for a high enough value of exchange current density and any charge-transfer coefficient, the maximum STH efficiency is restricted to 29.79% in Figure 4-5(a). Reaction selectivity at the conduction band towards H_2 evolution (H^+/H_2) (Figure 4-5(d)) is also influenced by the electrocatalytic parameters for the redox shuttle. Specifically, the trends with respect to the exchange current density changes depend on a threshold value for the charge-transfer coefficient. For $\alpha_{a,RS} < 0.5$, the selectivity monotonically increases with $j_{0,RS}$ because of the increase in driving forces for redox shuttle reaction: overall larger current densities can be sustained by the system, such that more H_2 evolution can take place as compared to redox shuttle reduction. For $\alpha_{a,RS} \geq 0.5$, there is an additional initial decrease in the selectivity as $j_{0,RS}$ increases from 1e-5 to 1e-4 A m^{-2} (for $\alpha_{a,RS} = 0.5$) and from 1e-5 to 5e-2 A m^{-2} (for $\alpha_{a,RS} > 0.5$) due to increasing competition from the redox shuttle reaction at the conduction band.

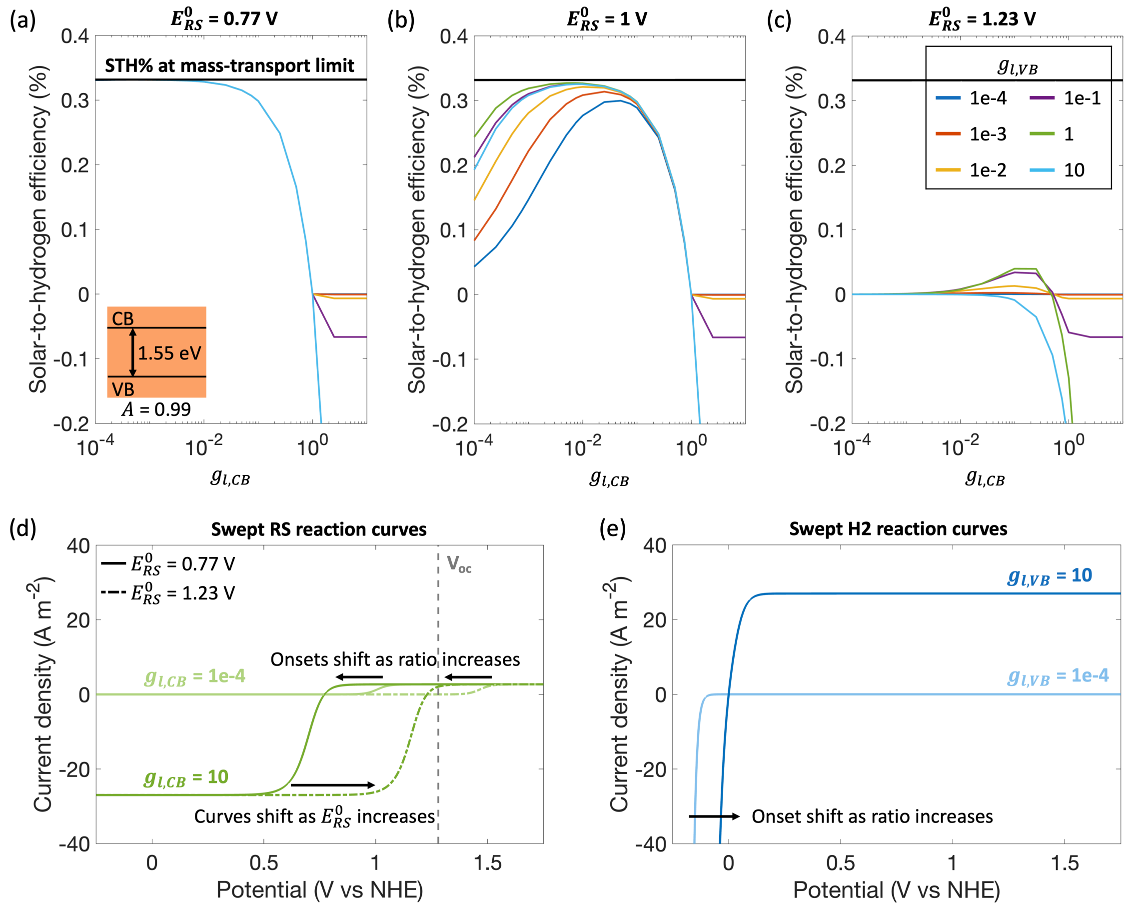

Figure 4-6: Solar-to-hydrogen efficiencies for competing reactions implemented for different redox shuttle pairs: (a) E^0_{RS} = 0.77 V (Fe^{3+}/Fe^{2+}), (b) E^0_{RS} = 1 V (I^-/IO_3^-), and (c) E^0_{RS} = 1.23 V (H_2O/O_2). (d) RS reaction curves for different assumed E^0_{RS} values (solid lines for 0.77 V and dash-dot lines for 1.23 V) as $g_{l,CB} = |j_{l,RS,c}|/j_{l,RS,a}$ is varied from 1e-4 (light green) to 10 (dark green). (e) H2 reaction curves for $g_{l,VB} = j_{l,H2,a}/j_{l,RS,a}$ varied from 1e-4 (light blue) to 10 (dark blue). For all plots, $j_{l,RS,a}/j_{sc}$ = 1e-2, $j_{0,RS}$ = 10 A m^{-2} and $\alpha_{a,RS}$ = 0.5, all S_i = 1, and a single optically thick light absorber with an absorptance A of 0.99 and optical thickness of 4.61, with a band gap of 1.55 eV was considered. RS: redox shuttle. H2: hydrogen.

Figure 4-6 considers a mass-transfer limited regime for redox shuttle oxidation with $j_{l,RS,a}/j_{sc}$ = 1e-2 (Figure 4-3(a)), fixed kinetic parameters for the redox shuttle ($j_{0,RS}$ = 10 A m^{-2} and $\alpha_{a,RS}$ = 0.5), and fixed partition coefficients (S_i = 1) to illustrate the effects of: (i) the asymmetry factors, g_l, that compare the undesired/competing redox reactions to the desired redox shuttle oxidation current density, at the valence ($g_{l,VB} = j_{l,H2,a}/j_{RS,a}$ ranging from 1e-4 to 10), and conduction ($g_{l,CB} = |j_{l,RS,c}|/j_{RS,a}$ ranging from 1e-4 to 10), and (ii) the thermodynamic potentials of the redox shuttle, E^0_{RS}. Larger asymmetry factors in the limiting current densities increase the driving force for back reactions when operating in a mass-transfer limited regime. Differences in E^0_{RS} were considered to assess influences of different redox shuttles, for example E^0_{RS} = 0.77 V, 1 V and 1.23 V vs NHE are representative of Fe(II)/Fe(III), I^-/IO_3^- and H_2O/O_2 redox shuttles, respectively. These potentials have been previously shown to influence optimal STH efficiencies in Z-scheme solar water splitting systems.[75]

For all cases, as the thermodynamic potential of the redox shuttle increases, the maximum STH efficiency reached decreases, with a more significant drop from E^0_{RS} = 0.77 V to 1.23 V (Figure 4-6(a)-(c)). With the increase in E^0_{RS}, the operating potential shifts towards the open circuit potential of the light absorber modeled (1.28 V, Figure 4-6(d)), which decreases the operating current density and therefore the STH efficiency. For a small enough E^0_{RS} as compared to the open-circuit potential of the light absorber (Figure 4-6(a)), the STH efficiency generally decreases with an increase in the asymmetry factor for redox shuttle reduction ($g_{l,CB}$). It levels off when the STH efficiency is more limited by the H2 oxidation current at the valence band. For instance, when $g_{l,VB}$= 1e-1, STH efficiency decreased for $g_{l,CB}$ from 0.33% to -0.07% but attains a plateau thereafter. Similarly, when $g_{l,VB}$= 1, the STH efficiency plateaus at -0.7%.

As the E^0_{RS} increases, there is a greater influence of the competing hydrogen reaction on the predicted STH efficiency. Additionally, at these potentials, the effect of H2 oxidation on STH efficiency, as quantified by $g_{l,VB}$, switches trends depending upon the asymmetry factor at the conduction band, $g_{l,CB}$. For E^0_{RS} = 1 V and 1.23 V and any fixed limiting current density for H2 oxidation, $g_{l,VB}$, the STH efficiency counterintuitively initially increases with increasing asymmetry for the redox shuttle reduction limiting current, $g_{l,CB}$. This is due to the tradeoffs in the benefits of decreasing onset potentials, thanks to increasing surface concentrations of the reduced species (Eq. (4-8)) and increasing competing redox shuttle reduction with increasing $g_{l,CB}$. For instance, as $g_{l,CB}$ increases, the onset potential for redox shuttle oxidation decreases driven by the increase in the surface concentration of the reduced redox shuttle species – Figure 4-6(d) shows that the onset potential decreased by 20 mV when $g_{l,CB}$ increases from 1e-4 to 10 for E_{RS}^{0} = 1.23 V. Consequently, an optimum $g_{l,CB}$ arises and lies between 5e-3 and 5e-1 for 1 V and between 5e-2 and 5e-1 for 1.23 V for all $g_{l,VB}$ modeled. The trends with respect to $g_{l,VB}$ can be explained similarly with more anodic onsets for H2 evolution with increase in limiting current densities for H2 oxidation (Figure 4-6(e)). Therefore, for larger E_{RS}^{0} values there is a greater benefit in having a larger asymmetry factor for $g_{l,VB}$, in our predictions up to a value of 1. When $g_{l,VB}$ becomes 10, worse performances results from the increased loss of H_2 produced to oxidation at the valence band.

Overall, the thermodynamic potential of the redox shuttle not only affects the STH efficiency magnitude, but also the extent to which the asymmetry factors in limiting current densities for redox shuttle reduction and H2 oxidation penalize the performance.

The presence of a selective coating affects the transport of ions to the reacting surface, and this behavior can be captured by varying the limiting current densities as well as the partition coefficient (Eq. (4-5)), as shown in Figure 4-7. When the partition coefficient S_i is equal to 1, the ratio of the species concentrations within the coating and in the bulk solution are the same, thus indicating that any changes in the limiting current densities are due to the effective diffusion coefficient contributions to the permeability (Eq. (4-4), (4-9)). For all situations considered here, the selective coatings were assumed to have partition coefficients of 1 for the H^+ and H_2 species as supported by experimental findings.[243,245] For the Fe(II) species, we varied the partition coefficient $S_{R,RS}$ from 1e-2 to 10 independently from the different limiting current density ratios

(Figure 4-7(a)). When operating in the kinetic regime, we observe a clear increase for the STH efficiency as the $S_{R,RS}$ is increased. This is thanks to a decreasing onset of the redox oxidation reaction as the ratio becomes more favorable towards oxidation (inset). The dependence on $S_{R,RS}$, however, becomes less prevalent for the mass-transport and light-limited regimes.

As expected from Figure 4-6, we observe a decreasing STH efficiency as the competing redox shuttle reduction increases, across all limiting current density ratio combinations. The notable outlier is when $g_{l,CB}$ = 1e-4, which severely affects the onset of the RS curve. This results in the STH efficiency also showing a dependence on the $S_{O,RS}$ value (Figure 4-7(b)), with a decreasing STH efficiency as the $S_{O,RS}$ increases from 1e-1 to 10. For all other values of $g_{l,CB}$, no significant dependence on $S_{O,RS}$ was observed.

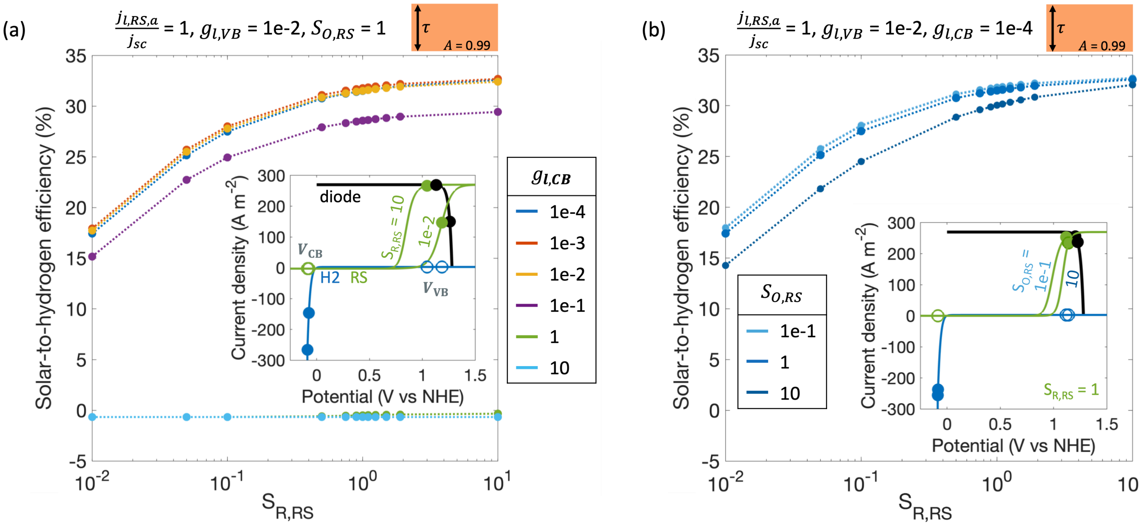

Figure 4-7: (a) Solar-to-hydrogen efficiencies for $j_{l,RS,a}/j_{sc}$ = 1, $g_{l,VB} = j_{l,H2,a}/j_{l,RS,a}$ = 1e-2 and $S_{O,RS}$ = 1 for varying $g_{l,CB} = |j_{l,RS,c}|/j_{l,RS,a}$ and $S_{R,RS}$ values. Inset depicting intersection plot for $S_{R,RS}$ = 1e-2 - 10 when $g_{l,CB}$ = 1e-2. (b) Solar-to-hydrogen efficiencies for $j_{l,RS,a}/j_{sc}$ = 1, $g_{l,VB}$ = 1e-2 and $g_{l,CB}$ = 1e-4 for varying $S_{O,RS}$ and $S_{R,RS}$ values. Inset depicting intersection plot for $S_{O,RS}$ = 10 and 1e-1 when $S_{R,RS}$ = 1. The light absorber was assumed to be optically thick (absorptance A of 0.99) with a band gap of 1.55 eV. The redox shuttle pair assumed here was Fe(III)/Fe(II).

4.4 Parametric sweep for an ensemble of light absorbers

Figure 4-8 predicts the performance of an array of light absorbers modeled as thin, planar, semitransparent slabs, with the number of absorbers, N, ranging from 1 – 1000. The results for N = 1 case are identical to what has been shown in Figure 4-5 and Figure 4-6, and for all cases of N the total absorptance of incident sunlight is fixed at 99%. We model influences of N by considering the mass-transfer limited regime, $j_{l,RS,a}/j_{sc}$ = 1e-2 (Figure 4-3(a)). Even within this regime, two distinct trends emerge for how the number of light absorbers influences STH efficiency as dictated by the asymmetry factor for the redox shuttle reduction current ($g_{l,CB}$, Figure 4-8(a) and (b)). When this asymmetry factor is larger than 1e-1 (Figure 4-8(b) shows results for $g_{l,CB}$ = 1), increasing the number of light absorbers results in decreasing STH efficiencies because of a larger number of light absorbers driving the back reactions, i.e., reduction of the redox shuttle (Fe(III)/Fe(II)) instead of H2 evolution. However, when the asymmetry factor is less than or equal to 1e-1, $j_{l,RS,a}/j_{sc} \leq$ 1e-1, there is an optimum number of light absorbers that maximizes net STH efficiency. An optimum number balances the multiplicative gain from positive STH efficiencies produced per light absorber operating in the mass-transfer limited regime with the light absorbers in the bottom driving back reactions for H2 oxidation and/or redox shuttle reduction. This is further evident in the trend that for a fixed asymmetry factor for the redox shuttle, the optimal number of light absorbers decreases with increase in asymmetry factors for H2 oxidation.

Figure 4-8(c) and (d) compile optimal STH efficiencies and the corresponding number of light absorbers as a function of asymmetry factors for redox shuttle reduction and H2 oxidation ($g_{l,CB}$ and $g_{l,VB}$). For the specific case modeled in Figure 4-8, asymmetry factors larger than 1e-2 either for redox shuttle reduction or H2 oxidation substantially penalize the STH efficiencies due to the domination of back reactions. Furthermore, the greater of the two asymmetry factors will more strongly influence the STH efficiency. For every decade of change in $g_{l,CB}$ beyond 1e-2, absolute changes in STH efficiency of more than 20 percentage points occur for $g_{l,VB} \leq$ 1e-2. Whereas, when $g_{l,CB} <$ 1e-2, the STH efficiency changes by more than 6 percentage points for every decade of change in $g_{l,VB}$. As the asymmetry factors increase, the optimal number of light absorbers required to attain maximum STH efficiency rapidly decreases, where beyond g_l = 1,

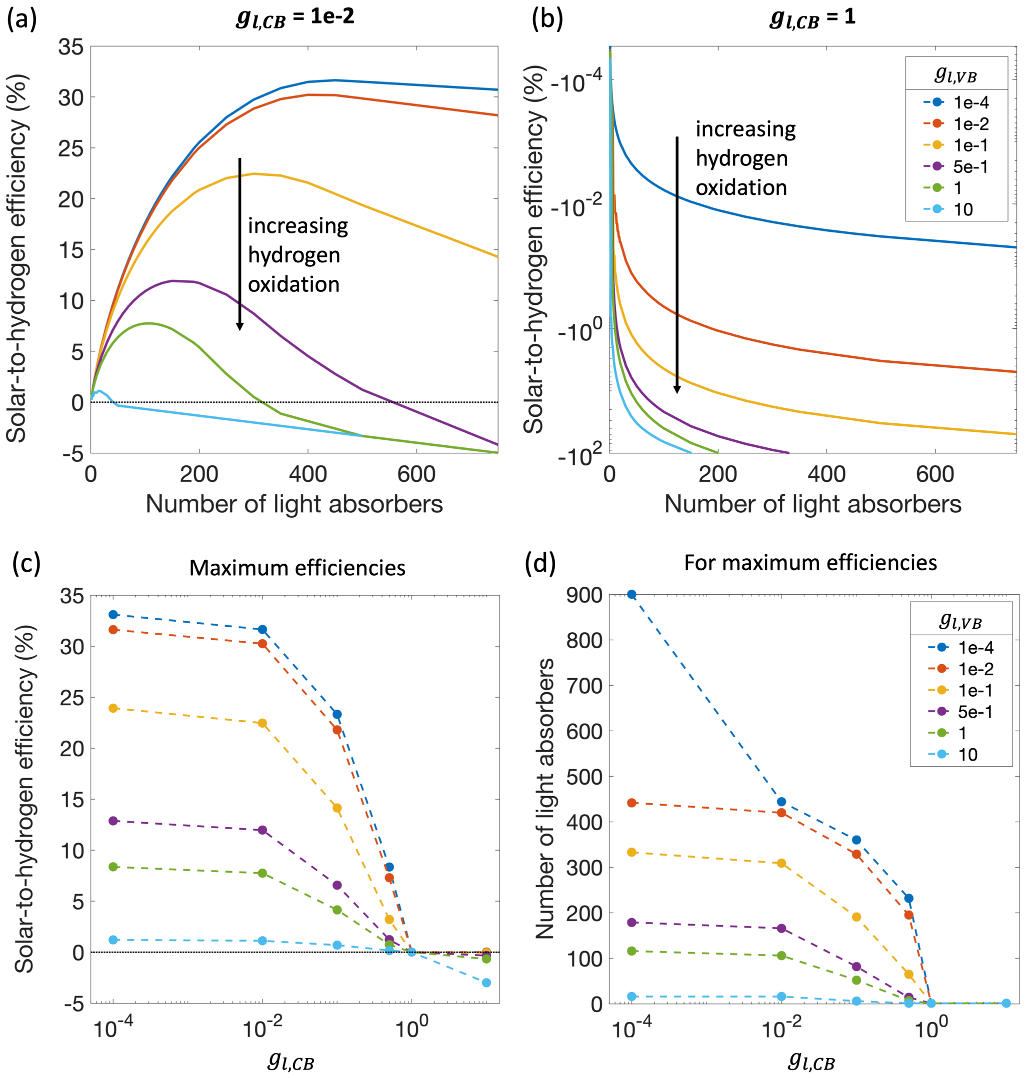

Figure 4-8: Solar-to-hydrogen efficiencies for an increasing number of light absorbers for (a) $g_{l,CB} = |j_{l,RS,c}|/j_{l,RS,a}$ = 0.01 and (b) $g_{l,CB}$ = 1, with $g_{l,VB} = j_{l,H2,a}/j_{l,RS,a}$ = 1e-4 – 10. (c) Maximum solar-to-hydrogen efficiencies and (d) corresponding number of slabs are tracked with respect to $g_{l,CB}$ and $g_{l,VB}$. For all plots, $j_{l,RS,a}/j_{sc}$ = 1e-2, $j_{0,RS}$ = 10 A m^{-2}, $\alpha_{a,RS}$ = 0.5, and S_i = 1. The total absorptance A was maintained at 0.99 for an ensemble of semitransparent optically thin slabs with a band gap of 1.55 eV. The redox shuttle pair assumed here was Fe(III)/Fe(II).

the optimal number is just N = 1 because N > 1 just drives back reactions. A notable change in slope in the optimal number of light absorbers, going from 442 to 900, occurs when $g_{l,CB}$ decreases from 1e-2 to 1e-4 for $g_{l,VB}$ = 1e-4. This is compared to all other values of $g_{l,VB}$ where the optimal number levels off when $g_{l,CB} \leq$ 1e-2. The increase results from the severe asymmetry limiting the overall current densities that can be sustained, such that a larger number of light absorbers is required to reach similar efficiencies as well as be hindered by the unwanted back reactions.

We can additionally vary the partition coefficient $S_{R,RS}$ with respect to the limiting current density ratios for the ensemble case. As shown on Figure 4-9, we can track the maximum solar-to-hydrogen efficiencies reached for different limiting current densities, with Figure 4-9(a) depicting the maximums for $j_{l,RS,a}/j_{sc}$ ranging from 1e-2 to 10 when the asymmetry is favorable towards the desired reactions ($g_{l,CB} = g_{l,VB}$ = 1e-2) and Figure 4-9(b) depicting the maximums for $j_{l,RS,a}/j_{sc}$ ranging from 1e-2 to 1 when the asymmetry is unfavorable towards the desired reactions

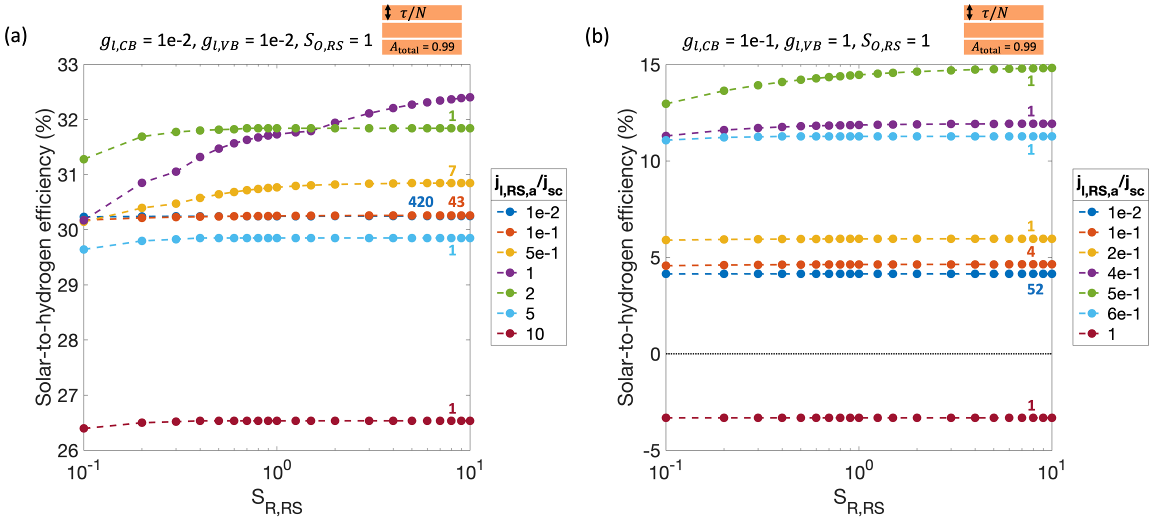

Figure 4-9: Maximum solar-to-hydrogen efficiencies for (a) $g_{l,CB} = \left|j_{l,RS,c}\right|/j_{l,RS,a}$ = 1e-2 and $g_{l,VB} = j_{l,H2,a}/j_{l,RS,a}$ = 1e-2 and (b) $g_{l,CB}$ = 1e-1 and $g_{l,VB}$ = 1. The number of light absorbers required to reach the maximum solar-to-hydrogen efficiencies are listed for each $j_{l,RS,a}/j_{sc}$ combination. For (a), $j_{l,RS,a}/j_{sc}$ = 1 reaches its maximum values for a decreasing number of light absorbers as $S_{R,RS}$ increases, going from 3 to 1. For all plots, the total absorptance A was maintained at 99%, $j_{0,RS}$ = 10 A m^{-2} and $\alpha_{a,RS}$ = 0.5, $S_{O,RS}$ = 1, and the redox shuttle pair assumed here was Fe(III)/Fe(II).

($g_{l,CB}$ = 1e-1 and $g_{l,VB}$ = 1). Any larger $g_{l,CB}$ or $g_{l,VB}$ values result in negative STH efficiencies for all $j_{l,RS,a}/j_{sc}$ assumed.

When favorable asymmetry in the competing reactions is implemented (Figure 4-9(a)), the largest variation with respect to $S_{R,RS}$ is observed when $j_{l,RS,a}/j_{sc}$ = 1 (purple line), with the STH efficiency increasing by 2.2 percentage points to reach 32.40% as $S_{R,RS}$ goes from 1e-1 to 10. In addition, the number of light absorbers required to reach maximum STH notably increases with $S_{R,RS}$: for small partition coefficients ($S_{R,RS}$ < 0.3) indicating a depletion of Fe^{2+} within the coating, the maximum STH efficiency is reached for 3 slabs of light absorbers; for partition coefficients around unity (0.3 ≤ $S_{R,RS}$ < 1.5), it is reached at 2; for large partition coefficients ($S_{R,RS}$ > 1.5) indicating an accumulation of Fe^{2+} within the coating, the maximum solar-to-hydrogen efficiency is reached for a single slab. This gradual decrease in the required number of light absorbers is due to shift in the onset of the RS curve as the $S_{R,RS}$ goes from 1e-1 to 10 (inset of Figure 4-7(a)), such that the system goes from the kinetics-limited to the light-limited regime. Less significant dependencies on $S_{R,RS}$ are observed for $j_{l,RS,a}/j_{sc}$ = 5e-1. For $j_{l,RS,a}/j_{sc}$ < 5e-1, the device is operating under mass-transport limited conditions, resulting in the expected multiplicative effect from Figure 4-8: all maximum efficiencies are reached for when more than a single light absorber is considered. The contribution from $S_{R,RS}$ is limited here as the mass-transport effects dominate over the RS kinetics effects. This is additionally highlighted by the same STH efficiencies being reached for $j_{l,RS,a}/j_{sc}$ = 1e-1 and $j_{l,RS,a}/j_{sc}$ = 1e-2, with the number of light absorbers compensating for the order of magnitude change between the two cases (43 slabs as compared to 420 slabs, respectively). For $j_{l,RS,a}/j_{sc}$ ≥ 2, the maximum STH efficiencies were all reached for a single light absorber by operating under light-limited conditions when $S_{R,RS}$ > 0.3. The decrease in STH efficiencies results from the increasing contributions from the competing reactions.

When unfavorable asymmetry in the competing reactions is implemented (Figure 4-9(b)), with $g_{l,CB}$ = 1e-1 and $g_{l,VB}$ = 1, the largest variation with respect to $S_{R,RS}$ is observed when $j_{l,RS,a}/j_{sc}$ = 5e-1 (green line), with the STH efficiency increasing by 1.86 percentage points as $S_{R,RS}$ goes from 1e-1 to 10. The shift is again due to the device shifting from operating under the kinetics-limited regime to the light-limited regime. Under light-limited conditions, the maximum STH efficiency reached by $j_{l,RS,a}/j_{sc}$ = 5e-1 is 14.82% when $S_{R,RS}$ = 10. It remains less than half of the total maximum STH that can possibly be sustained (33%) due to the combined contributions of both competing reactions. Similarly to Figure 4-9(a), the trend in the maximum STH efficiencies shift around the optimum point reached at $j_{l,RS,a}/j_{sc}$ = 5e-1: for $j_{l,RS,a}/j_{sc}$ < 5e-1, the STH efficiencies increase with $j_{l,RS,a}/j_{sc}$ as the device moves from mass-transport limited to the kinetic-limited regime; for $j_{l,RS,a}/j_{sc}$ > 5e-1, the STH efficiencies decrease with increasing $j_{l,RS,a}/j_{sc}$ as the device is light-limited and has growing contributions from the competing reactions. Overall the contribution from $S_{R,RS}$ is limited when unfavorable asymmetry is implemented as the operating point of the device is dominated by the competing reactions.

Thus, when considering an ensemble of light absorbers, the solar-to-hydrogen efficiencies most depend on the assumed limiting current densities as opposed to the implemented partition coefficients, unless $S_{R,RS}$ is highly unfavorable ($S_{R,RS}$ < 0.5) where the STH efficiency can be decreased by up to 0.5 percentage points. For a single light absorber, the dependencies on $S_{R,RS}$ remain large when the device is operating within the kinetics-limited regime and are small for mass-transport limited cases, especially when unfavorable asymmetry for the desired reactions are assumed.

4.5 Conclusion

A simple yet powerful equivalent circuit modeling framework was developed to explore the effects of competing reactions, mass-transport limitations, reaction kinetics, and selective coating properties on the solar-to-hydrogen efficiency. The reaction kinetics of the redox shuttle reaction, the exchange current density and the charge transfer coefficient, were found to have a significant effect on the predicted solar-to-hydrogen efficiency both when selective and competing reactions were assumed. For selective reactions, the maximum possible efficiency is reached for smaller exchange current density as the reaction becomes more favorable towards the oxidation reaction. When competing reactions are considered, a similar trend emerges for cathodic to anodic charge-transfer coefficients ($\alpha_{a,RS} \leq 0.7$), but the solar-to-hydrogen efficiency reached in the plateau region is determined by the assumed limiting current densities of the competing reactions. For the highly anodic charge transfer coefficients ($\alpha_{a,RS} \geq 0.9$), there is an optimum value reached due to the device behavior shifting from being kinetically-limited to being light-limited.

The dependencies of the limiting current densities of the different reactions taking place were explored using several non-dimensional ratios, representative thermodynamic redox potentials (Fe^{3+}/Fe^{2+}, IO_3^-/I^-, H_2O/O_2), and partition coefficients. Varying the ratio of the limiting redox shuttle anodic reaction with respect to the diode equation affects the overall magnitude of the current density that can be sustained. Varying the ratio of the limiting redox shuttle cathodic and hydrogen anodic reactions with respect to the redox shuttle anodic reaction quantifies the extent of the competitive reactions assumed to be taking place. Overall, for small E^0 values, the solar-to-hydrogen efficiency is affected by the extent of competing redox shuttle reduction, whereas for larger E^0 values both reactions affect the overall efficiencies. Varying the partition coefficient, or the ratio of Fe^{2+} within the coating with respect to Fe^{2+} in the bulk solution, results in increasing efficiencies as the amount of Fe^{2+} within the coating is assumed to accumulate. This follows from the decrease of the onset as the partition coefficient increases and results in the partition coefficient having limited effects on the mass-transport and light-limited regimes.

In addition, ensemble effects were probed to better model the behavior of a suspension of light absorbers. The largest benefit in increasing the amount of light absorbers was observed for severely mass-transport cases with minimal competing reactions taking place. The optimum point as the number of slabs increased resulted from the interplay between the multiplicative effect of having more light absorbers driving the desired reaction and the increasing light limitation at the bottom of the reactor, resulting in the bottom light absorbers driving undesired reactions. In addition, the partition coefficient has a limited effect on the maximum efficiency when the ensemble is operating under mass-transport or light-limited conditions. The maximum efficiency reached is highly dependent on both asymmetry factors assumed for the competing reactions and tends towards negative values for increasingly competitive reactions.

Overall, the intricate interdependencies of the considered parameter inputs highlight the power of this simple model to explore the effects of competing reactions, mass-transport limitations, reaction kinetics, partition coefficients, and ensemble behavior.

Chapter 5 Summary and Future Work

This dissertation focused on the evaluation of electrochemical nutrient recovery from wastewater nitrates and the development of detailed-balance models for photocatalytic systems for solar hydrogen production. Electrocatalytic formation of ammonia from nitrate reduction on Cu was experimentally investigated in different electrolyte compositions, representative of existing wastewater streams. An equivalent circuit model was developed to incorporate the effects of competing reactions and mass-transport limitations within a standard framework and calculate their influences on solar-to-fuel efficiency and product selectivity.

5.1 Thesis summary and limitations

5.1.1 Wastewater resource recovery – experimental and modeling findings

Chapter 2 presented experimental investigations to determine the electrocatalytic performance of polycrystalline Cu electrodes in different electrolyte conditions for nitrate concentrations ranging from 0.1 M to 1 M $NaNO_3$ and pH conditions going from 8 to 14. Measured current densities from cyclic voltammograms were both concentration and pH dependent, with current densities increasing by almost 7 times for a pH change from 8 to 14 at an applied potential of -0.6 V vs RHE for 1 M. This data was used to extract the exchange current density and charge transfer coefficients for the rate-determining NO_3^- to NO_2^- reduction step, and a larger dependence on pH was quantified for the extracted charge transfer coefficients. Chronoamperometry was used to quantify end-product selectivity/Faradaic efficiency by measuring concentrations of NO_3^-, NO_2^-, and NH_3 using UV-Vis spectroscopy. The NH_3 Faradaic efficiency increases with pH, with the largest increase seen between pH 10 and pH 14, at any NO_3^- concentration. When the concentration of NO_3^- is increased from 0.1 M to 1 M, the Faradaic efficiency at pH 14 remains stable around 46% but the efficiencies for pH 8 and pH 10 decrease due to increasing NO_2^- competition. Using these Faradaic efficiencies, the energy intensity for ammonia recovery was estimated as 427 MJ kg_N^{-1} for 0.1 M $NaNO_3$ solutions at pH 8, which is ~4 times larger than the estimated energy intensity of < 100 MJ kg_N^{-1} for biological processes. While the energy requirements are not competitive yet due in part to the unoptimized reactor conditions implemented, these are promising findings for the application of electrochemical wastewater nitrate treatment within the understudied near-neutral range using a commercially available polycrystalline Cu electrode.

Measured data indicated significant trial-to-trial variations, which motivated the use of electrochemical impedance spectroscopy to understand and diagnose the contributors to this outcome. These measurements allow to track the charge-transfer resistance and effective capacitances for all of the different trials. The dependencies on the electrochemically active surface area and facet-dependent area-specific capacitances vary between the tested nitrate concentrations: for 1 M $NaNO_3$, the charge going towards NO_2^- and NH_3 formation is strongly correlated with the facet-dependent specific capacitance, whereas for 0.1 M $NaNO_3$, it is more strongly correlated with the electrochemical surface area. On the whole, this study generated new experimental data to determine pH and concentration dependencies for ammonia formation on Cu and additionally introduced impedance-based diagnostic tools to identify underlying contributors to measurements due to surface composition.

Limitations of this work concern the limited scope of the Faradaic efficiencies data and the lack of additional product detection outside of NO_3^-, NO_2^- and NH_3. During the chronoamperometry tests, the Faradaic efficiencies measured were dependent on both pH and NO_3^- concentrations, and as shown in Figure 3-5, these variations can affect the predicted solar-to-chemical efficiencies greatly when used in the modeling framework. Furthermore, previous studies have established the potential dependence of the Faradaic efficiencies, as well as the interplay between potential and pH to reach maximum efficiencies.[85,86,123] These efforts highlight the need for a more populated data set to better understand the behavior of polycrystalline Cu electrode to treat different wastewater nitrate compositions. With this in mind, an expanded product quantification protocol should also be developed such that all charge consumed can be properly attributed to the formed products. Additional dissolved species that could be measured are: N_2H_4 which can be detected using UV-Vis spectroscopy; NH_2OH which can be quantified using Fourier-transform infrared spectroscopy.[85,87] Gaseous species like N_2, N_2O, NO, and H_2 can be analyzed using on-line electrochemical mass spectrometry and gas chromatography (once the high-solubility gases are stripped from the solution).[85,87]

In Chapter 3, an equivalent circuit model framework was developed to probe the effects of NO_3^- concentration and competing reactions on the solar-to-chemical efficiency and nitrogen removal rates for a photocatalytic nitrate reduction process. For larger concentrations of NO_3^- ($\geq$ 10 mM), both metrics are governed by the assumed kinetics and the light absorber behavior. This resulted in an optimal band gap found for each concentration. For smaller concentrations of NO_3^- (< 10 mM), mass-transport limitations negate any contributions from the assumed kinetics and light absorber behavior. Competing hydrogen reduction and oxygen reduction were considered at the cathode and resulted in a decrease in the proposed efficiencies, with oxygen reduction dominating at larger concentrations and hydrogen reduction becoming more important for smaller concentrations and larger band gaps. Limitations of this work include treating the semiconductor material as an ideal diode, as this results in much larger efficiencies than what will be reached in a real PV-electrolyzer set-up. Furthermore, oxidation reactions at the anode other than water oxidation should be explored to treat additional wastewater pollutants and possibly avoid the large thermodynamic potential required by the water oxidation reaction.

5.1.2 Photocatalytic solar water-splitting

In Chapter 4, the hydrogen evolving compartment of a Z-scheme solar reactor was modeled using an equivalent circuit modeling framework. The effects of competing reactions, reaction kinetics, mass-transport limitations, and ensemble behavior on the solar-to-hydrogen efficiencies were explored. For $\alpha_{a,RS} \leq 0.7$, the maximum solar-to-hydrogen efficiency tends towards the same value (26.5% for the light-limited case, 0.3% for the mass-transport limited case), with the plateau region reached for smaller exchange current density values as the reaction becomes more anodic. For $\alpha_{a,RS} \geq 0.9$, a maximum solar-to-hydrogen efficiency (29.8% for the light-limited case, 0.33% for the mass-transport limited case) is reached due to a shift in the operating regime (kinetic to light-limited). The predicted efficiencies were also found to be sensitive to the assumed limiting current densities for the competing reactions as well as the assumed electrochemical potential of the redox shuttle. As the partition coefficients were varied in tandem with the limiting current density ratios, the largest effect on the solar-to-hydrogen efficiencies were observed in the kinetically-limited regime. Finally, the performance of an ensemble of light absorbers was calculated, where the multiplicative effect on the solar-to-hydrogen efficiency was observed as the number of light absorbers increased only when the limiting currents for at least one of the desired reactions is significantly smaller than the short-circuit current density of the light absorber, i.e.,

$j_{RS,a} \leq$ 1e-2 j_{sc}. If this is not the case, additional light absorbers simply increase the amount of current density driving the undesired reactions and result in a general decrease in the total solar-to-hydrogen efficiency. For a high number of light absorbers, the overall efficiency can decrease due to the light absorbers at the bottom of the reactor driving more of the undesired reactions.

Limitations of this work is the driving assumption that the H_2-evolving compartment is perfectly paired with an O_2-evolving compartment. Not only is this crucial for the calculation of the solar-to-hydrogen efficiency (as the energy output results from H_2 combustion) but also in the underlying assumption of the redox shuttle behavior: the reaction rates in both compartments are sufficiently paired that local depletions or diffusion-limited behaviors across compartments is not considered.

5.2 Thesis impact

Unique contributions from this work included investigations of the previously under-examined effects of near-neutral pH conditions on the formation of ammonia using a polycrystalline Cu electrode, and the application of electrochemical impedance spectroscopy to quantify *in situ* surface structure changes. We coupled these findings with energy consumption estimates to better understand the application of electrochemistry for wastewater nitrates remediation and the promising results indicate that further reactor design could make polycrystalline Cu a viable electrode for scalable nitrate treatment.

Furthermore, the incorporation of competing reactions and mass-transport limitations in the formulation of the equivalent circuit model is unique to this work. These models were applied for the first time to capture the behavior of sunlight-driven electrochemical reduction of nitrate to ammonia and nitrous oxide and to understand the effects of band gap, nitrate concentration, and competing reaction effects. This modeling framework could be further leveraged to inform the design of a PV-electrolyzer set-up, which would allow to offset part of the energy requirement for the wastewater nitrate remediation by using solar energy. Finally, specifically for photocatalytic hydrogen production, the incorporation of competing reactions and mass-transport limitations in the formulation of the equivalent circuit model was used to better inform the behavior of a photocatalyst suspension reactor. The impact of this effort results from the simple and elegant modeling framework that captures extensive competing reactions, mass-transport limitations, and ensemble behavior within a graphical approach. This allows for easy adjustments with respect to the kinetics, mass-transport assumptions, selective coatings, and thermodynamic potentials, as shown in Chapter 4, but can also be further modified in a straightforward manner to include, among other features, additional competing reactions and other light intensity profiles.

5.3 Future work

5.3.1 Effects of competing ions present in real waste streams

Chronoamperometry data obtained with pH 10 exhibits starkly unstable current densities and deviations compared to current responses obtained at pH 8 and pH 14. This is attributed to the presence of interfering PO_4^{3-} ions in the buffer solution, which competitively adsorb to the electrode surface. As shown in Figure 1-1, phosphates are a common wastewater pollutant, in addition to sulfates, chlorides (Cl^-), and perchlorates.[25,34–36] For instance, the presence of Cl^- ions in solution can lead to NH_3 being more easily oxidized to N_2. Quantifying the effect of interfering ions in solution is crucial for the development of competitive nutrient recovery from wastewater streams, where the scalability of this process will depend in part on the extent of parasitic energy requirements for removing competing ions.

5.3.2 Nitrate reduction in an electrochemical flow reactor

The steady-state response of a polycrystalline Cu electrode for pH 8 and pH 14 was investigated within a three-electrode batch reactor set-up. For pH 10, the current density response was shown to be unstable due to the presence of interfering PO_4^{3-} ions, which could possibly be formed thanks to a local pH gradient through the boundary-layer on the electrode surface. Furthermore, the unaccounted charge at pH 14 (outside of the measurement error) has been attributed in part to the possible NH_3 oxidation taking place due to cross-over from the cathode to the anode. This motivates the development of an electrochemical flow reactor where the operating conditions control the boundary-layer formation and can be used to draw further insight on the performance of a polycrystalline Cu electrode. Additionally, a flow reactor would allow the implementation of time-dependent product quantification through the use of on-line measurement techniques, such that product loss through cross-over would be minimized.

5.3.3 Resolving local species concentrations in tandem with reaction rate predictions

The ensemble model currently assumes that the species concentration/activity remains the same for all light absorbers present in the ensemble, which is representative of a scenario of extremely rapid species transport/mixing. This results in the underlying assumption that all the light absorbers behave independently from one another. These assumptions are summarized by maintaining the activities of all species at unity throughout the model, and results in negative efficiencies (net consumption of H_2) being possible. However, in a real reactor, when the local concentration of H_2 is decreases, the driving force for H_2 oxidation should automatically decrease. For this reason, species concentrations should be updated as a function of the reaction rates. Such an implementation can also consider the parasitic light absorption by the redox species. The rate of production/consumption of a colored redox species can also influence the light intensity profile within the reactor.

5.3.4 Case study with a suspension of particles instead of an ensemble of thin semitransparent slabs

The current model assumes that the ensemble behaves like a stack of thin semitransparent slabs, where the light intensity profile is governed by Beer's law where only absorption is modeled. In a particle suspension system, both absorption and scattering events dictated by particle size distribution and concentration will influence the intensity profiles along the depth of the reactor. The existing framework can be adjusted in several manners to incorporate these updated light intensity profiles. The short-circuit current density and the radiative recombination current density can be calculated using the new light intensity profiles instead of the Beer's Law within the existing framework. In addition, optical properties from real materials can be implemented as opposed to assuming an ideal optical thickness. Finally, the number of sections within the particle suspension should be chosen such that the absorption profile throughout the height of the reactor, integrated across each section, roughly matches the light absorption profile used as an input.

Appendix A Cyclic Voltammetry Studies

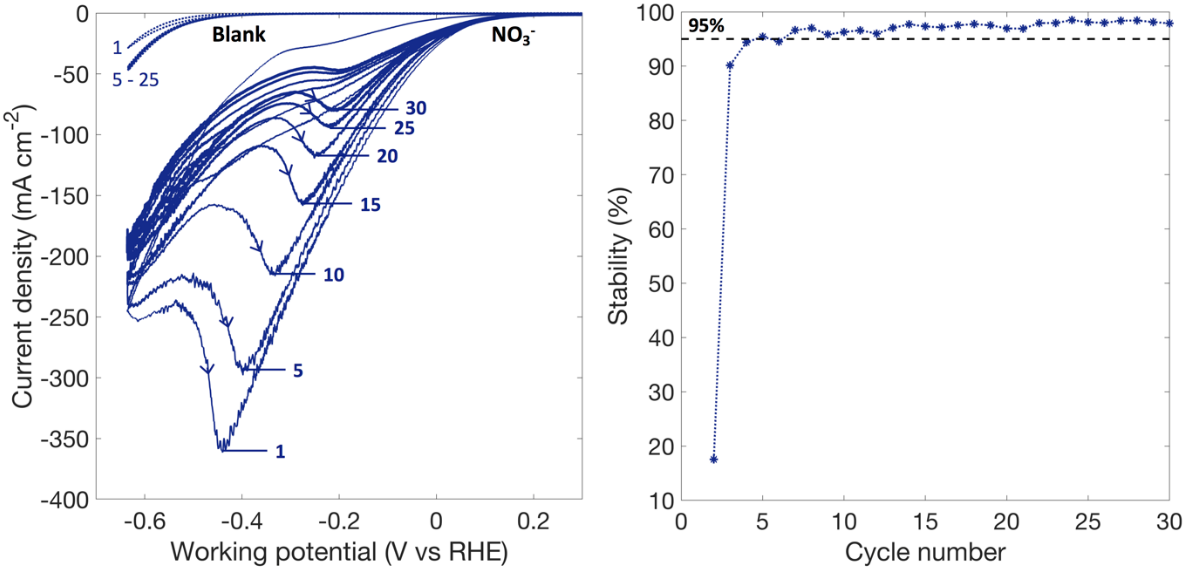

Figure A-1: (a) Cyclic voltammogram for 1 M $NaNO_3$ at pH 14 for cycles 1 through 30. The blank cycles are shown as dotted lines. (b) Cycle stability calculated for each sequential pair of cycles (ex: the stability of cycle 30 was calculated as the change in current density over all potentials with respect to cycle 29). A CV was considered stable if the last five cycles were over 95% stable (cut-off shown as dashed line).

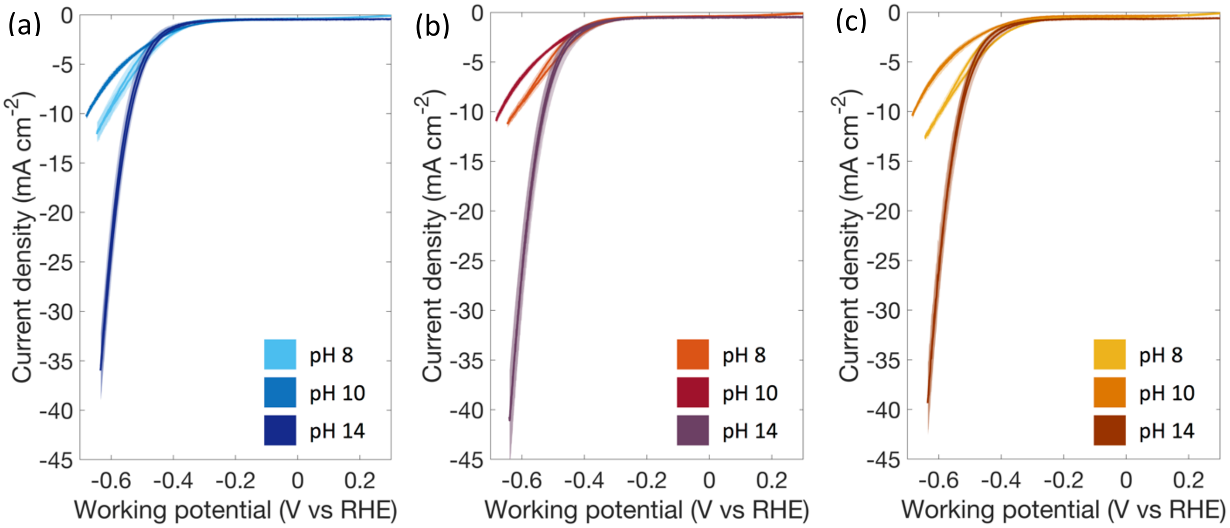

Figure A-2: Cyclic voltammogram for the average blank response at each pH (8, 10, 14) for (a) 0.1 M $NaNO_3$, (b) 0.5 M $NaNO_3$, and (c) 1 M $NaNO_3$. The average was taken across all trials (before the $NaNO_3$ was run) using the last cycle.

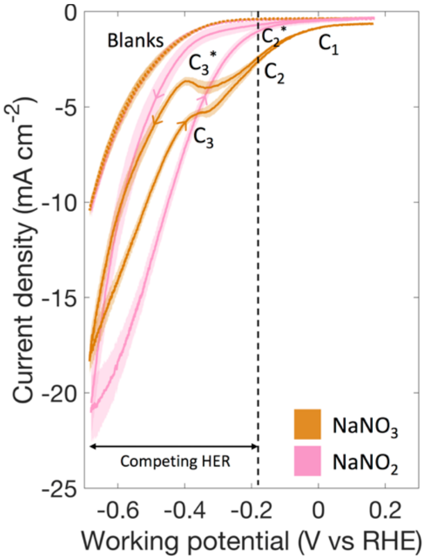

Figure A-3: Cyclic voltammograms for pH 10 and 0.1 M $NaNO_3$ and 0.1 M $NaNO_2$ concentrations. The blanks associated with each trial condition are shown as dotted lines. The onset of the blank is indicated by the dashed line. Average current density for the last cycle is shown as a bold line, with the shaded regions representing the standard deviation between the different runs calculated at each potential point. Scan rate: 20 mV s^{-1}; stir rate: 900 rpm.

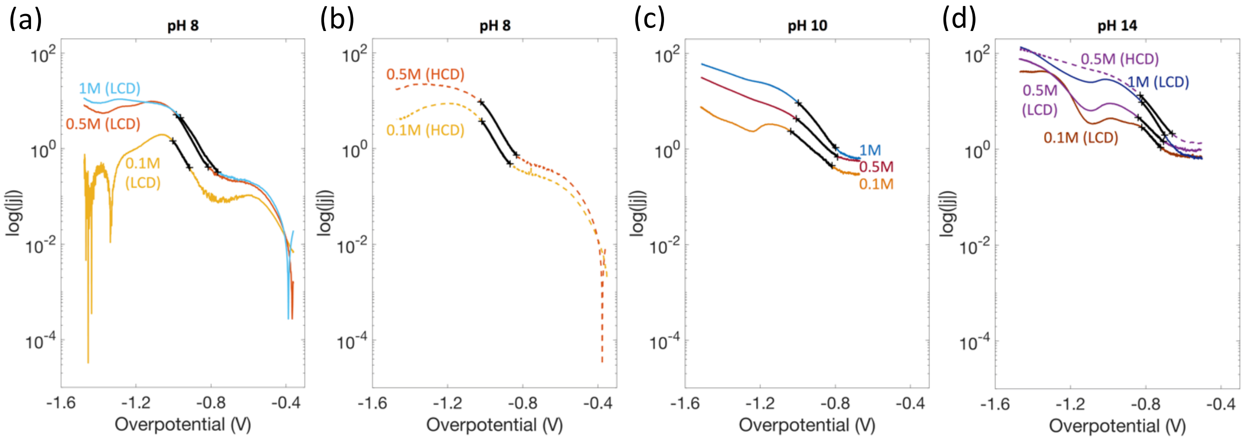

Figure A-4: Average Tafel current density with respect to overpotential ($\eta = V_{WE} - E^0_{RDS}$), where E^0_{RDS} = 0.835 vs RHE for the (a) LCD cases at pH 8 and all $NaNO_3$ concentrations, (b) HCD cases at pH 8 and 0.1 M and 0.5 M $NaNO_3$, (c) pH 10 and all $NaNO_3$ concentrations, and (d) both types (LCD for all $NaNO_3$ concentrations and HCD for 0.5 M $NaNO_3$) at pH 14. Stable current density values from the cathodic sweep are used with the blank current deducted for each data type. Low current density (LCD) runs are shown as solid lines and high current density (HCD) runs are shown as dashed lines.

Table A-1: Tafel kinetics extracted for each concentration/pH pairing shown in Figure A-4

pH	$c_{\mathbf{NaNO_3}}$ **(M)**	**Type**	**Average**			**Range**		
			j_0 (mA cm^{-2})	α_c	R^2	j_0 (mA cm^{-2})	α_c	R^2
8	0.1	HCD	1.71e-6	0.37	0.998	3.22e-7 – 4.62e-6	0.33 – 0.41	0.995-0.998
	0.5	HCD	4.33e-6	0.37	0.998	2.49e-6 – 7.35e-6	0.35 – 0.39	0.997
	0.1	LCD	4.28e-7	0.39	0.997	4.81e-8 – 3.68e-6	0.33 – 0.44	0.993-0.995
	0.5	LCD	1.28e-6	0.40	0.999	2.84e-7 – 4.82e-6	0.36 – 0.43	0.997-0.998
	1	LCD	8.31e-6	0.35	0.998	1.19e-6 – 4.18e-5	0.31 – 0.41	0.995-0.998
10	0.1		7.64e-4	0.2	0.999	4.69e-4 – 1.78e-3	0.17 – 0.22	0.993-0.997
	0.5		6.90e-4	0.22	0.998	1.10e-4 – 4.33e-3	0.16 – 0.29	0.986-0.998
	1		1.27e-4	0.29	0.997	3.23e-5 – 3.93e-4	0.26 – 0.32	0.993-0.998
14	0.5	HCD	1.16e-3	0.29	0.999	8.73e-4 – 1.44e-3	0.29 – 0.30	0.999
	0.1	LCD	8.02e-4	0.26	0.996	4.30e-4 – 1.42e-3	0.24 – 0.27	0.971-0.998
	0.5	LCD	3.69e-3	0.22	0.997	1.92e-3 – 8.38e-3	0.19 – 0.26	0.97-0.997
	1	LCD	1.25e-4	0.36	0.999	8.53e-6 – 7.89e-4	0.3 – 0.42	0.992-0.999

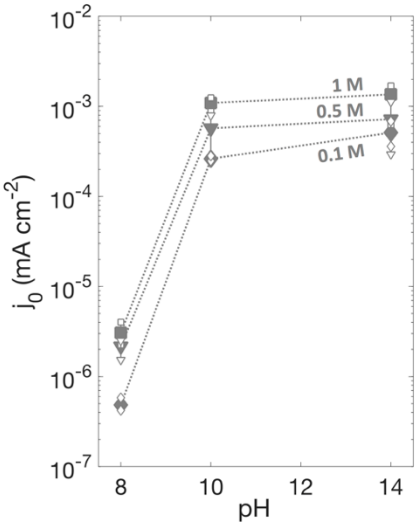

Figure A-5: Exchange current densities j_0 (mA cm^{-2}) extracted from the CVs for all pH and NaNO$_3$ concentrations in the NO$_3^-$ to NO$_2^-$ onset potential region using the fixed α_c values listed in Table A-2. The filled markers indicate the values extracted for the average behavior across all trials and the vertical lines with empty markers as endpoints indicate the range of values covered by the individual trials. All values can be found in Table A-2.

Table A-2: Tafel kinetics extracted for each concentration/pH pairing shown in Figure A-5.

pH	$c_{\mathrm{NaNO_3}}$ **(M)**	**Type**	**Average**			**Range**		
			j_0(mA cm^{-2})	α_c	R^2	j_0(mA cm^{-2})	α_c	R^2
8	0.1	HCD	1.02e-6	0.38	0.996	7.58e-7 – 1.26e-6	0.38	0.973-0.995
	0.5	HCD	2.63e-6		0.996	2.50e-6 – 2.69e-6		0.990-0.997
	0.1	LCD	4.83e-7		0.997	4.23e-7 – 5.81e-7		0.961-0.993
	0.5	LCD	2.16e-6		0.998	1.53e-6 – 2.50e-6		0.985-0.996
	1	LCD	3.07e-6		0.991	2.25e-6 – 4.02e-6		0.946-0.994
10	0.1		2.63e-4	0.23	0.977	2.48e-4 – 2.82e-4	0.23	0.898-0.989
	0.5		5.72e-4		0.997	2.64e-4 – 7.97e-4		0.831-0.995
	1		1.09e-3		0.953	8.77e-4 – 1.25e-3		0.908-0.984
14	0.5	HCD	2.01e-3	0.27	0.995	1.73e-3 – 2.24e-3	0.27	0.992-0.996
	0.1	LCD	5.13e-4		0.993	3.60e-4 – 6.83e-4		0.949-0.998
	0.5	LCD	7.22e-4		0.961	2.95e-4 – 1.12e-3		0.711-0.997
	1	LCD	1.36e-3		0.945	6.26e-4 – 1.70e-3		0.867-0.990

Appendix B Chronoamperometry Experiments

B.1 Surface Area Measurements for Cu Planar Electrodes

Table B-1: pH Specific Electrode Areas Used in the Chronoamperometry Results

pH	**Area (cm^2)**
8	0.255
10	0.306
14	0.315

B.2 Optical Images of Electrode Surface

Optical microscope images were taken for each pH-specific electrode used. Roughness was not measured explicitly. However, comparative roughness can be observed from the microscope images. While pH 10 and pH 14 electrodes appear generally to have a similar level of roughness (Figure B-2 and Figure B-3 respectively), the pH 8 electrode shows significantly more surface scratches than the others (Figure B-1). This level of additional roughness to the pH 8 electrode could be an additional factor that led to pH 8 CA experiments having up to 14 times higher current density than the CV experiments, even though the pH 14 experiments are only twice as large during the CA experiments compared to the CV experiments.

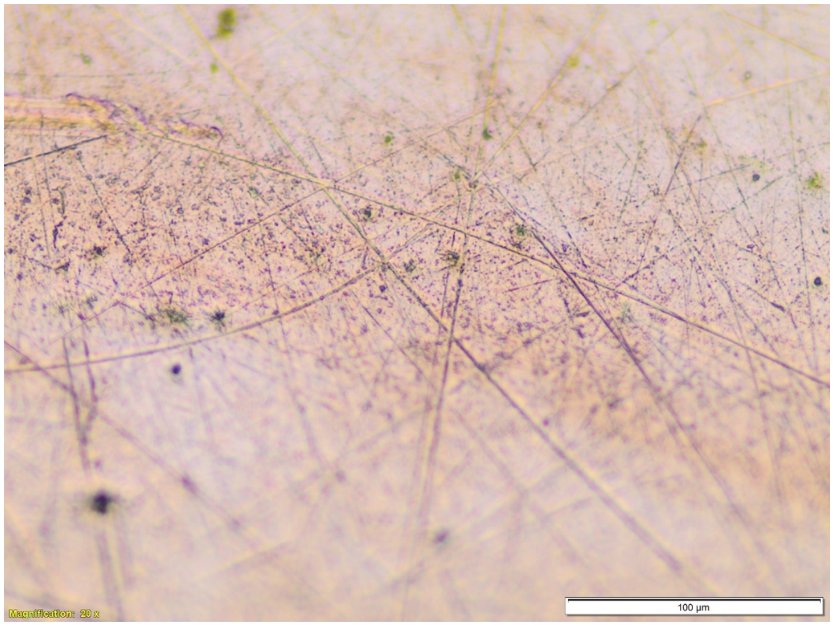

Figure B-1: Optical microscope images of the pH 8 electrode, showing significant surface roughness and scratches. Image taken at 20 times zoom. Scale bar shown on image.

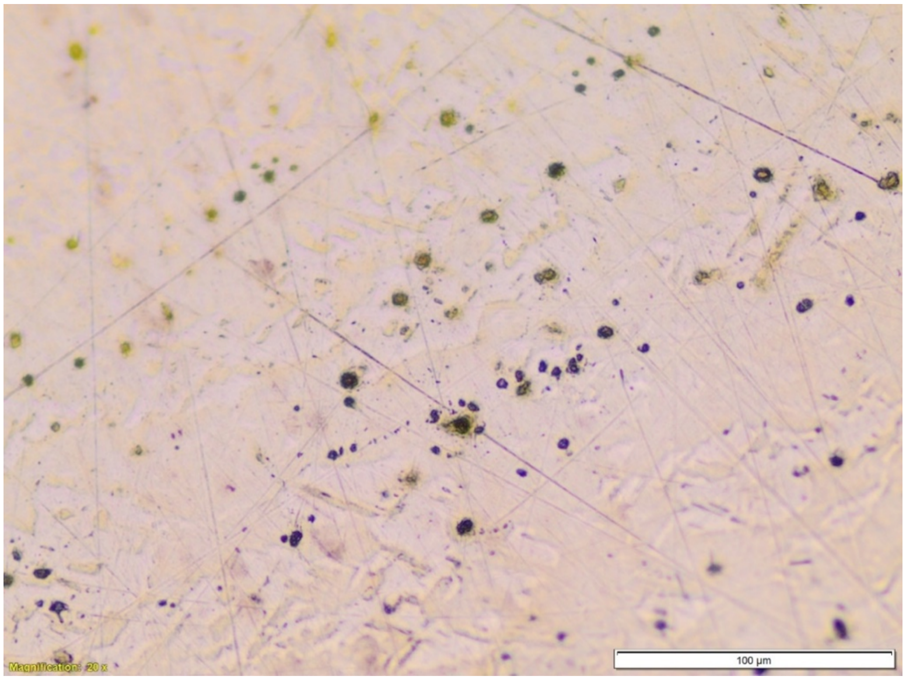

Figure B-2: Optical microscope images of the pH 10 electrode, showing significantly reduced scratching than the pH 8 electrode. Pitting of the Cu surface is present. Image taken at 20 times zoom. Scale bar shown on image.

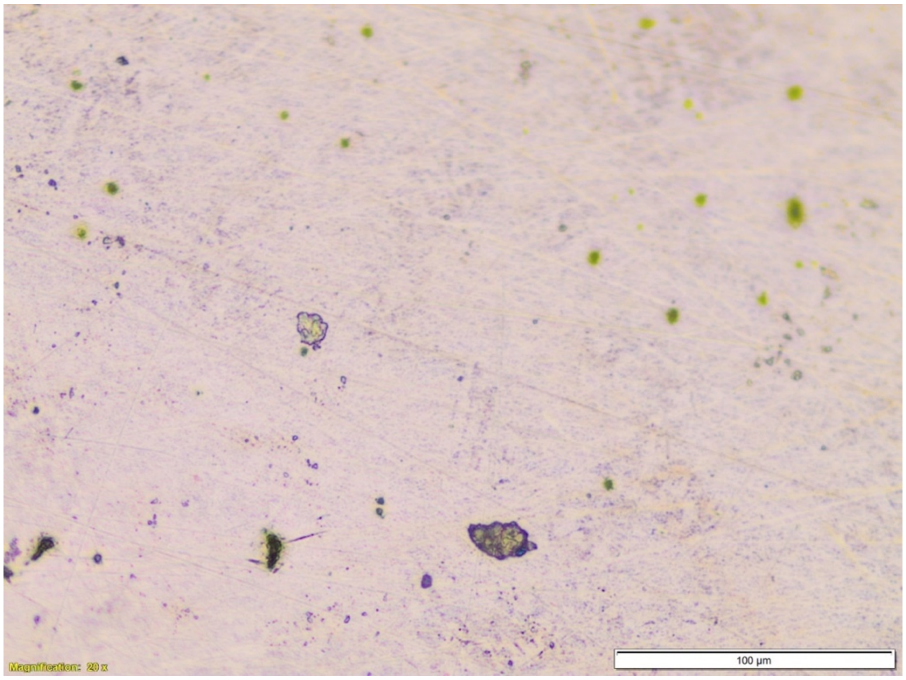

Figure B-3: Optical microscope images of the pH 14 electrode, showing significantly reduced scratching than the pH 8 electrode but also lesser pitting compared to pH 10 electrode. Image taken at 20 times zoom. Scale bar shown on image.

B.3 Choosing CA Operating Potentials

The CA operating potentials – -0.62 V, -0.6 V and -0.55 V v/s RHE for pH 8, 10, and 14 respectively – were chosen to maximize the rate of NH_3 formation. From CVs we noticed that we needed to operate at potentials lesser than -0.4 V to be in the NH_3 production region, as opposed to other intermediate N-species production. Since H_2 formation begins to increasingly compete with HER at large enough cathodic potentials, < -0.65 V, the selected potential was chosen within this bounded range. Figure B-4 shows the predicted rate of NH_3 formation, assuming all current not going to H_2 production (as predicted by the blank) is going toward NH_3 formation.

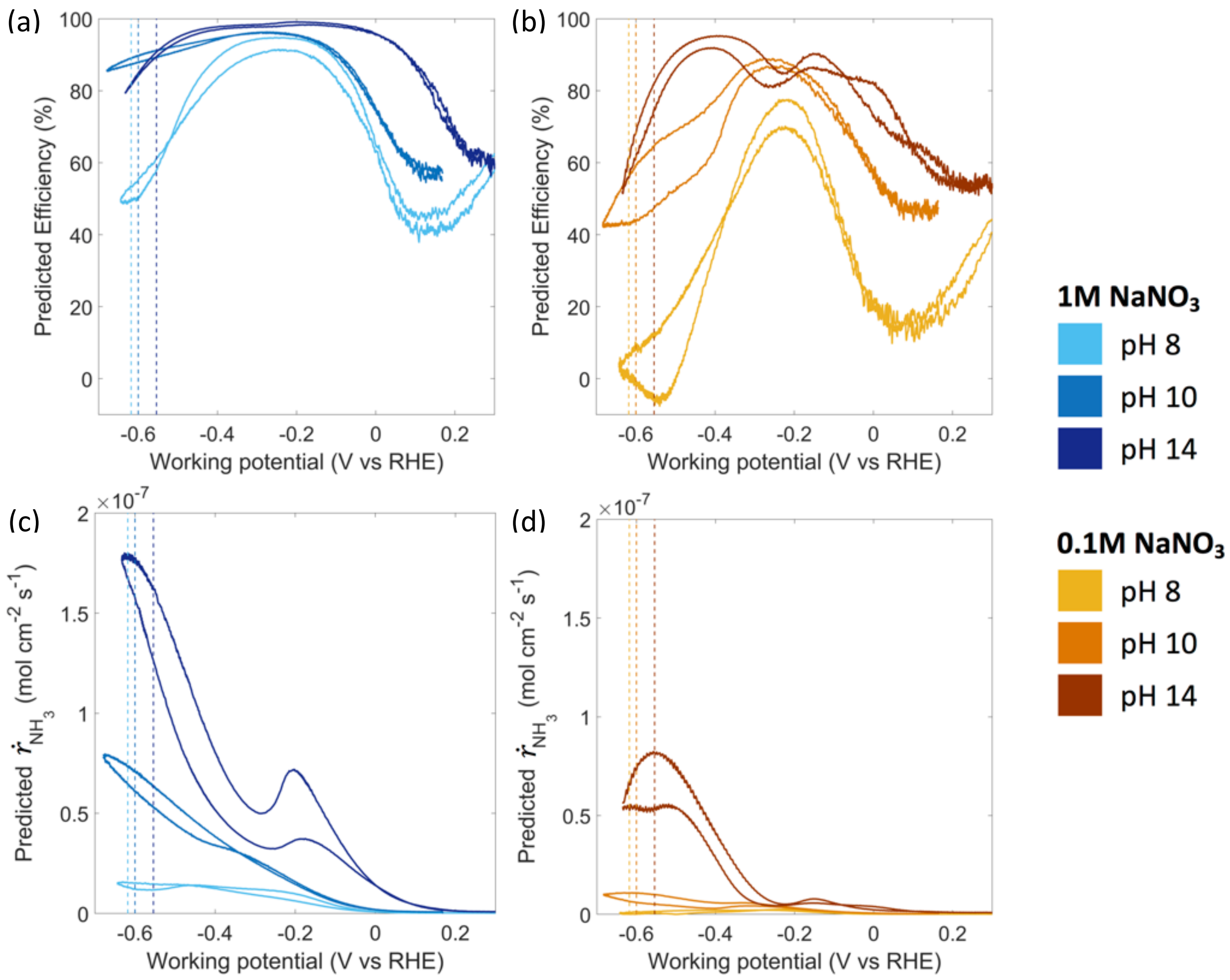

Figure B-4: Predicted efficiency towards NH_3 formation and predicted rate of NH_3 formation vs working potential for all pH and concentrations, using the average current density response from the CVs shown in Figure 2-3.

Appendix C Electrochemical Impedance Spectroscopy

To extract the desired EIS parameters of $\boldsymbol{Q}$, $\boldsymbol{\alpha}$, R_t, and R_e, a MATLAB curve fitting code was used to fit the real and imaginary portions of the impedance to construct a Nyquist impedance curve. Before curve fitting commenced, data was processed to remove noisy values. Since using a Faraday cage was not realistic for our set up, in order to maximize signal-to-noise ratio, impedance values of for $|Z| < 105\ \Omega$ were used for data processing.[246] If a value of more than 105 Ω was recorded, the current was essentially too low to confidently measure without a Faraday cage. After data processing, the circuit was modeled as shown in Figure 2-2. The MATLAB function then calculates the effective impedance of the modeled circuit and extracts the real and imaginary portions of the data fit. The nonlinear curve fitting function of *lsqcurvefit* was used to find the best-fit parameters. Parameters obtained from the curve fit are reported with their 95% confidence intervals, obtained from the Jacobian of the curve fit. The Jacobian is used to calculate confidence intervals using the function *nlparci*. Error from the respective fitting parameters was propagated accordingly to obtain a confidence interval for C_{eff}, which was calculated from $\boldsymbol{Q}$ and $\boldsymbol{\alpha}$. Curve fits of the different EIS experiments are shown below in Figure C-1 to Figure C-3. Extracted parameters from each curve fit are shown in Table C-1 to Table C-6.

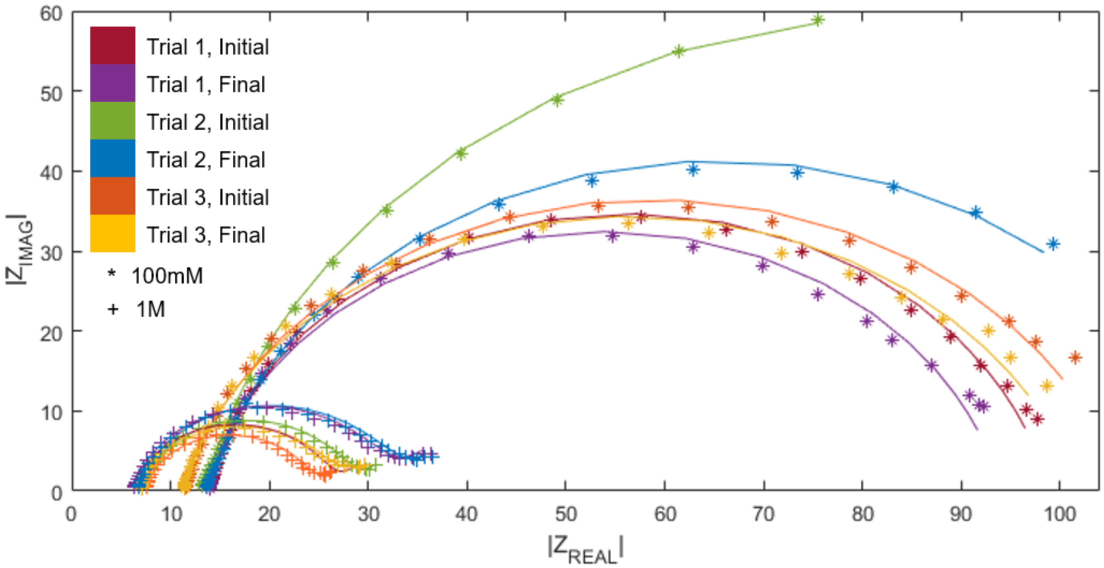

Figure C-1: Nyquist impedance data points and best fit curves for all pH 8 data. All trials have both an initial and final data fit. 1 M $NaNO_3$ data is show by + and 0.1 M data is shown by * symbols. pH 8 1 M data was fit using a Warburg impedance element in series with a CPE, to account for the mass transfer limitation seen in the shape of the curve.

Table C-1: Extracted fit values and confidence intervals for EIS curve fitting parameters for 1 M $NaNO_3$ at pH 8 trials. Confidence intervals are shown to the right of each fitted parameter in the same units as the parameter. i: initial, f: final.

Trial		R_e (Ω)	R_t (Ω)	Q (F s$^{\alpha-1}$)	α (-)	W (Ω s$^{-1/2}$)	C_{eff} (F)	R^2
1	i	6.39 ± 0.12	19.74 ± 0.24	1.26E-04 ± 9.56E-06	0.88 ± 0.01	7.76 ± 0.58	4.43E-04 ± 2.57E-05	1.00
	f	6.19 ± 0.22	25.40 ± 0.49	1.36E-04 ± 1.52E-05	0.87 ± 0.02	13.46 ± 1.14	5.48E-04 ± 4.99E-05	0.99
2	i	6.90 ± 0.12	21.26 ± 0.25	1.39E-04 ± 9.74E-06	0.87 ± 0.01	8.43 ± 0.58	5.49E-04 ± 3.09E-05	1.00
	f	6.55 ± 0.20	26.05 ± 0.49	1.67E-04 ± 1.73E-05	0.86 ± 0.02	11.50 ± 1.13	7.38E-04 ± 6.47E-05	0.99
3	i	7.41 ± 0.15	16.76 ± 0.29	1.53E-04 ± 1.63E-05	0.88 ± 0.02	6.93 ± 0.68	5.79E-04 ± 4.69E-05	0.99
	f	6.90 ± 0.17	19.59 ± 0.37	1.82E-04 ± 2.02E-05	0.86 ± 0.02	9.30 ± 0.87	7.60E-04 ± 6.70E-05	0.99

Table C-2: Extracted fit values and confidence intervals for EIS curve fitting parameters for 0.1 M $NaNO_3$ at pH 8 trials. Confidence intervals are shown to the right of each fitted parameter in the same units as the parameter. i: initial, f: final.

Trial		R_e (Ω)	R_t (Ω)	Q (F s$^{\alpha-1}$)	α (-)	C_{eff} (F)	R^2
1	i	13.39 ± 0.18	146.06 ± 2.73	1.12E-04 ± 4.33E-06	0.87 ± 0.01	5.41E-04 ± 2.68E-05	1.00
	f	13.75 ± 0.28	103.35 ± 1.26	1.49E-04 ± 6.31E-06	0.86 ± 0.01	7.88E-04 ± 4.96E-05	1.00
2	i	13.71 ± 0.29	85.16 ± 0.68	1.56E-04 ± 6.05E-06	0.87 ± 0.01	7.10E-04 ± 4.22E-05	1.00
	f	13.57 ± 0.44	80.51 ± 1.05	1.74E-04 ± 1.09E-05	0.86 ± 0.01	8.38E-04 ± 8.16E-05	0.99
3	i	11.02 ± 0.42	95.53 ± 1.22	2.06E-04 ± 1.10E-05	0.83 ± 0.01	1.41E-03 ± 1.16E-04	1.00
	f	10.74 ± 0.49	91.36 ± 1.38	2.49E-04 ± 1.57E-05	0.82 ± 0.01	1.81E-03 ± 1.80E-04	0.99

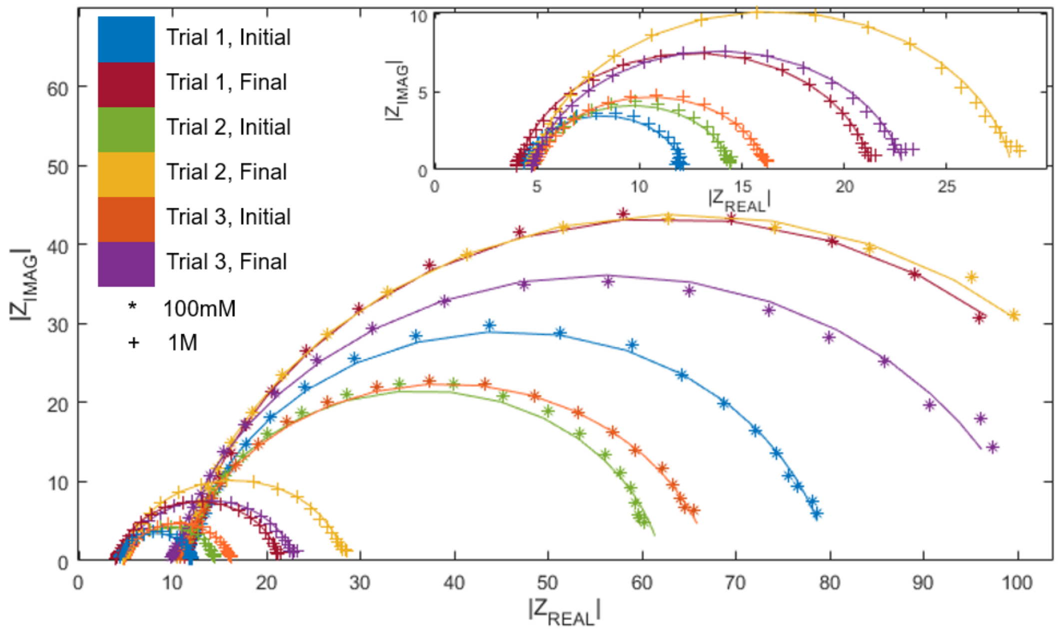

Figure C-2: Nyquist Impedance data points and best fit curves for all pH 10 data. All trials have both an initial and final data fit. 1 M $NaNO_3$ data is show by + and 0.1 M data is shown by * symbols. The inset of the plot shows a close-up view of the 1M $NaNO_3$ data.

Table C-3: Extracted fit values and confidence intervals for EIS curve fitting parameters for 1 M $NaNO_3$ at pH 10 trials. Confidence intervals are shown to the right of each fitted parameter in the same units as the parameter. i: initial, f: final.

Trial		R_e (Ω)	R_t (Ω)	Q (F $s^{\alpha-1}$)	α (-)	C_{eff} (F)	R^2
1	i	4.28 ± 0.12	7.83 ± 0.16	1.27E-04 ± 1.98E-05	0.92 ± 0.02	2.77E-04 ± 2.39E-05	0.97
	f	4.07 ± 0.08	17.27 ± 0.14	2.07E-04 ± 1.07E-05	0.91 ± 0.01	4.99E-04 ± 1.90E-05	1.00
2	i	4.78 ± 0.12	9.74 ± 0.17	1.87E-04 ± 2.35E-05	0.90 ± 0.02	5.22E-04 ± 4.08E-05	0.98
	f	4.79 ± 0.12	23.43 ± 0.20	1.74E-04 ± 9.69E-06	0.91 ± 0.01	4.29E-04 ± 1.99E-05	1.00
3	i	4.88 ± 0.08	11.38 ± 0.12	2.31E-04 ± 1.74E-05	0.88 ± 0.01	7.71E-04 ± 3.89E-05	0.99
	f	4.78 ± 0.12	18.15 ± 0.20	2.26E-04 ± 1.61E-05	0.89 ± 0.01	6.67E-04 ± 3.71E-05	0.99

Table C-4: Extracted fit values and confidence intervals for EIS curve fitting parameters for 0.1 M $NaNO_3$ at pH 10 trials. Confidence intervals are shown to the right of each fitted parameter in the same units as the parameter. i: initial, f: final.

Trial		R_e (Ω)	R_t (Ω)	Q (F $s^{\alpha-1}$)	α (-)	C_{eff} (F)	R^2
1	i	11.52 ± 0.25	68.36 ± 0.53	1.44E-04 ± 5.85E-06	0.90 ± 0.01	4.74E-04 ± 2.66E-05	1.00
	f	11.54 ± 0.19	102.83 ± 0.91	1.72E-04 ± 5.00E-06	0.89 ± 0.01	5.83E-04 ± 2.55E-05	1.00
2	i	10.91 ± 0.35	51.22 ± 0.71	1.61E-04 ± 1.23E-05	0.89 ± 0.01	5.54E-04 ± 5.46E-05	0.99
	f	10.78 ± 0.22	106.98 ± 1.00	2.15E-04 ± 6.42E-06	0.87 ± 0.01	8.67E-04 ± 4.03E-05	1.00
3	i	10.77 ± 0.21	56.64 ± 0.47	2.21E-04 ± 9.32E-06	0.85 ± 0.01	1.13E-03 ± 6.48E-05	1.00
	f	9.89 ± 0.29	92.32 ± 0.88	2.71E-04 ± 1.01E-05	0.85 ± 0.01	1.44E-03 ± 8.45E-05	1.00

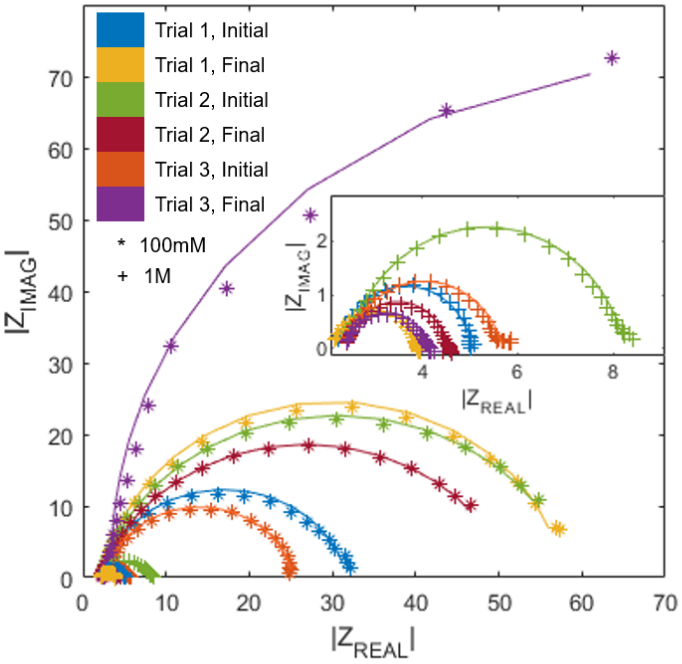

Figure C-3: Nyquist Impedance data points and best fit curves for all pH 14 data. All trials have both an initial and final data fit. 1 M $NaNO_3$ data is show by + and 0.1 M data is shown by * symbols. The inset of the plot shows a close-up view of the 1 M $NaNO_3$ data, which is nearly 1 order of magnitude smaller than the 0.1 M $NaNO_3$ data.

Table C-5: Extracted fit values and confidence intervals for EIS curve fitting parameters for 1 M $NaNO_3$ at pH 14 trials. Confidence intervals are shown to the right of each fitted parameter in the same units as the parameter.

Trial		R_e **(Ω)**	R_t **(Ω)**	Q **(F s$^{\alpha-1}$)**	α **(-)**	C_{eff} **(F)**	**R^2**
1	i	2.25 ± 0.02	2.80 ± 0.03	4.75E-04 ± 3.98E-05	0.88 ± 0.01	1.18E-03 ± 2.75E-05	0.99
	f	2.16 ± 0.04	1.75 ± 0.04	4.00E-04 ± 7.01E-05	0.88 ± 0.02	1.05E-03 ± 4.00E-05	0.97
2	i	2.42 ± 0.05	5.84 ± 0.08	4.31E-04 ± 3.87E-05	0.84 ± 0.01	1.61E-03 ± 6.30E-05	0.99
	f	2.44 ± 0.05	2.10 ± 0.06	4.03E-04 ± 8.75E-05	0.88 ± 0.03	1.01E-03 ± 5.81E-05	0.96
3	i	2.41 ± 0.06	3.28 ± 0.08	5.01E-04 ± 8.45E-05	0.83 ± 0.02	1.93E-03 ± 1.12E-04	0.98
	f	2.40 ± 0.05	1.75 ± 0.06	6.20E-04 ± 1.46E-04	0.83 ± 0.03	2.14E-03 ± 1.17E-04	0.95

Table C-6: Extracted fit values and confidence intervals for EIS curve fitting parameters for 0.1 M $NaNO_3$ at pH 14 trials. Confidence intervals are shown to the right of each fitted parameter in the same units as the parameter.

Trial		R_e **(Ω)**	R_t **(Ω)**	Q **(F s$^{\alpha-1}$)**	α **(-)**	C_{eff} **(F)**	**R^2**
1	i	2.16 ± 0.13	56.84 ± 0.45	5.41E-04 ± 1.51E-05	0.86 ± 0.01	1.79E-03 ± 4.12E-05	1.00
	f	2.11 ± 0.08	49.43 ± 0.29	7.14E-04 ± 1.44E-05	0.82 ± 0.00	3.02E-03 ± 4.41E-05	1.00
2	i	2.33 ± 0.23	29.36 ± 0.49	3.41E-04 ± 2.97E-05	0.89 ± 0.02	9.18E-04 ± 6.05E-05	0.99
	f	2.55 ± 0.33	55.12 ± 0.87	2.86E-04 ± 1.95E-05	0.93 ± 0.02	5.57E-04 ± 3.76E-05	0.99
3	i	2.85 ± 0.15	22.33 ± 0.29	3.03E-04 ± 2.21E-05	0.92 ± 0.01	6.19E-04 ± 3.47E-05	0.99
	f	3.46 ± 0.51	138.01 ± 7.79	1.81E-04 ± 1.67E-05	1.02 ± 0.02	1.48E-04 ± 1.85E-05	0.99

EIS was only performed before and after the nitrate reduction experiment at the potential of -0.1 V for all pH. This potential was chosen as it was more negative than the onset of nitrate reduction, but more positive than other reaction onsets, including HER and nitrite reduction.

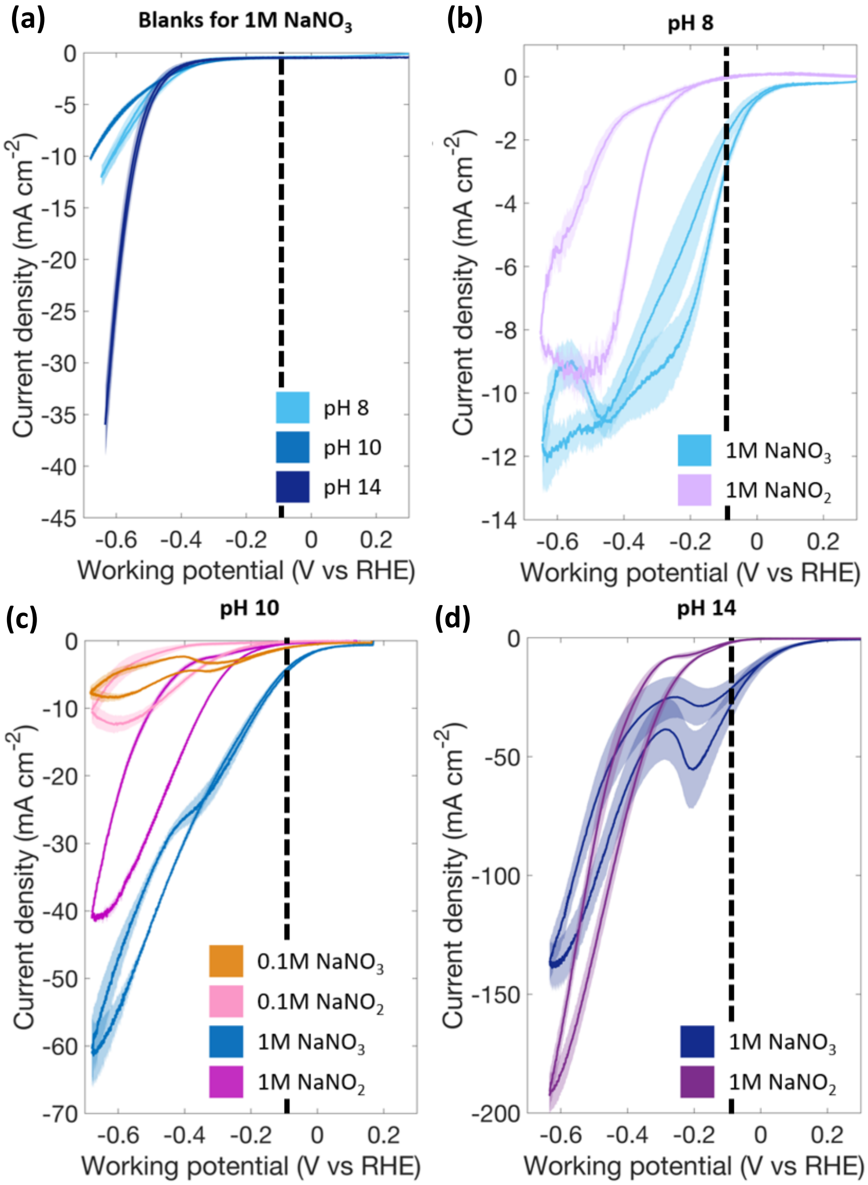

Figure C-4: Showing the EIS voltage in relation to different reaction onsets. (a) EIS operating voltage is more positive than the onset of HER in all blanks tested. (b) In the pH 8 solution, the EIS operating voltage takes place after the onset of the 1 M $NaNO_3$ data, but before the onset of the 1 M $NaNO_2$ data. (c) In the pH 10 solution, both 1 M and 0.1 M $NaNO_3$ onsets occur before the EIS onset, but the 0.1 M and the 1 M $NaNO_2$ onset occurs after. (d) In the pH 14 solution, the onset of the 1M $NaNO_3$ takes place more positive of the EIS potential, while the 1 M $NaNO_2$ onset is observed more negative of the EIS potential.

Figure C-4 shows the blanks and experimental data plotted together. The dotted line indicated the potential where EIS was performed. This potential is more positive than the blank onset and additional features of the CV data. Additionally, EIS was not performed on the blank as there is no other charge transfer reaction other than hydrogen evolution in the selected potential range (-0.4 – 0 V). Probing the PEIS spectra for hydrogen evolution was not considered best practice as gas formation may block reaction sites and lead to changing surface areas or our electrode, which would complicate our probing of the surface type.[247] Additionally, probing at potentials close to that of hydrogen evolution would lead to oxidation of the Cu electrode, in the more reactive pH 14 solution. An OCV was completed before the final EIS test, to ensure that local pH gradient, leading to a buildup of negative charge near the electrode surface had dissipated prior to running the EIS. If the local pH is changing over the course of the EIS experiment, then the potential of the experiment vs RHE, could not be held constant. The EIS experiment would last only around 20 seconds. However, as shown in Figure C-5, even over this short time the OCV would not hold constant. Instead, the OCV following the end of the experiment, shown a buildup of local negative charge, which could be both NO_3^-, NO_2^-, and OH^-, which proceeded to quickly dissipate after the reaction was finished. Since this experiment is an OH^- producing experiment and a local pH gradient is expected to develop, it is necessary to ensure the local pH gradient has dissipated before completing the EIS experiment. By observing a steady state OCV, we can be sure the bulk pH we measure is also the local pH near the electrode surface. Therefore, the second EIS experiment was only completed following a steady-state OCV.

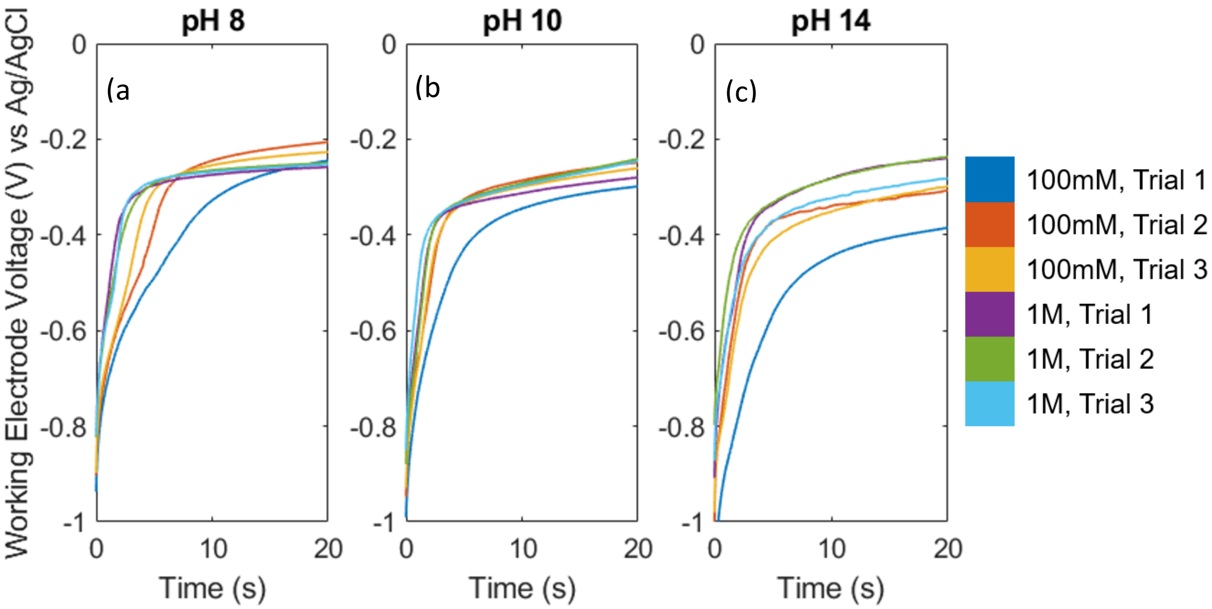

Figure C-5: The OCV in the first 20 seconds following the completion of the CA experiment for each trial at (a) pH 8, (b) pH 10, and (c) pH 14. The rapid drop shows the local and bulk concentrations of anions coming into equilibrium. Since this is a hydroxide producing reaction, OH^- is expected to be present in significant amounts. As OCV relaxes back to steady-state, any local pH gradient would have dissipated, meaning that our operating voltage for EIS is now a steady value vs RHE.

Appendix D Species Behavior in Solution

D.1 UV-Vis Calibration curves

For each species, the calibration curves were repeated at least 3 times and measured in different concentration orders to avoid any influence due to cross-contamination. The quartz cuvettes were also thoroughly rinsed with DI water and dried between each measurement. The molar absorption coefficients were extracted using Beer's Law (Table D-1).

When both NO_3^- and NO_2^- are present in solution, the concentration of NO_2^- was first determined to establish the amount of NO_2^- present in solution. Then, the resulting absorbance at 303 nm corresponding to the presence of NO_2^- was calculated, such that the measured absorbance at 303 nm was "corrected" by removing the contributions coming from NO_2^-. The measured concentration of NO_3^- was extracted from this corrected absorbance at 303 nm.

For NH_3, the effect of the supporting electrolyte and the colored salicylate reagents was minimized by removing the signal coming from the blank (0 µM).

Table D-1: Species-specific concentration ranges used to make the calibration curves, and the species-specific wavelengths used to extract the molar absorption coefficients.

Species	**Concentration range**	**Wavelength (nm)**	**Molar absorption coefficient, ε (L mol^{-1} cm^{-1})**	**Figure**
NO_3^-	10 mM – 100 mM	303	7.10e-3 ± 7.57e-5	Figure D-1
NO_2^-	1 mM – 50 mM	355 303	2.28e-2 ± 5.40e-5 9.19e-3 ± 3.35e-5	Figure D-2
NH_3	10 µM – 50 µM	650	2.27e-2 ± 2.1e-3	Figure D-3

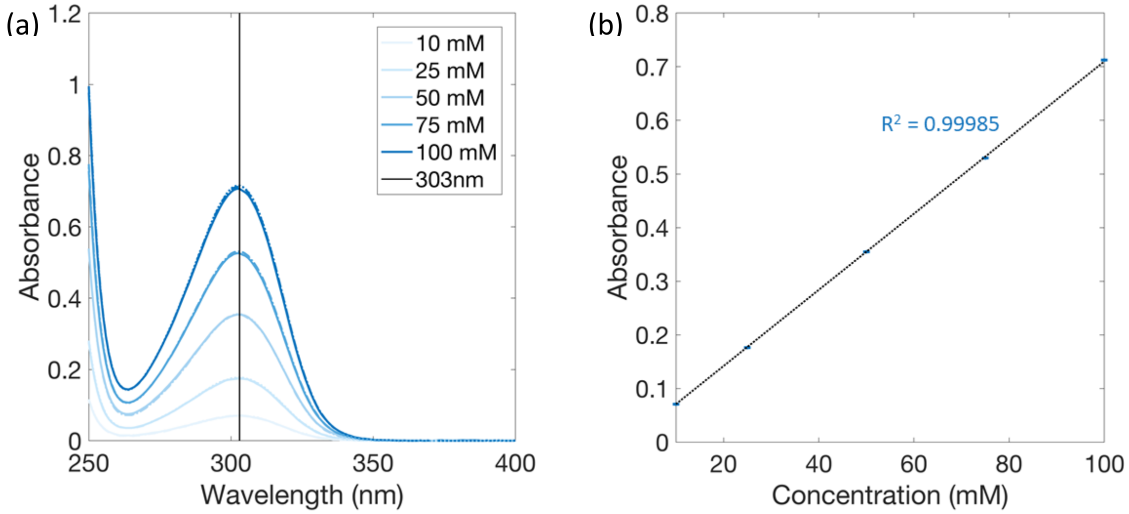

Figure D-1: (a) Wavelength-dependent absorbance for NO_3^- concentrations ranging from 10 mM to 100 mM, with the NO_3^- characteristic peak centered around 303 nm (b) Concentration-dependent maximum absorbance reached at 303 nm, fitted using Beer's Law.

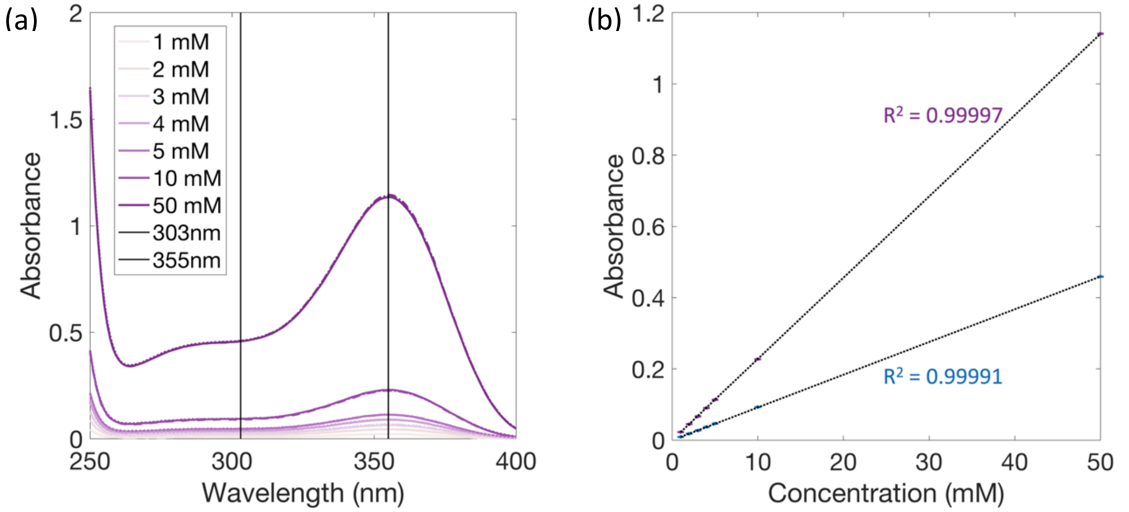

Figure D-2: (a) Wavelength-dependent absorbance for NO_2^- concentrations ranging from 1 mM to 50 mM, with the NO_2^- characteristic peak centered around 355 nm and secondary peak around 303 nm (b) Concentration-dependent maximum absorbance reached at 355 nm, and secondary peak at 303 nm, fitted using Beer's Law.

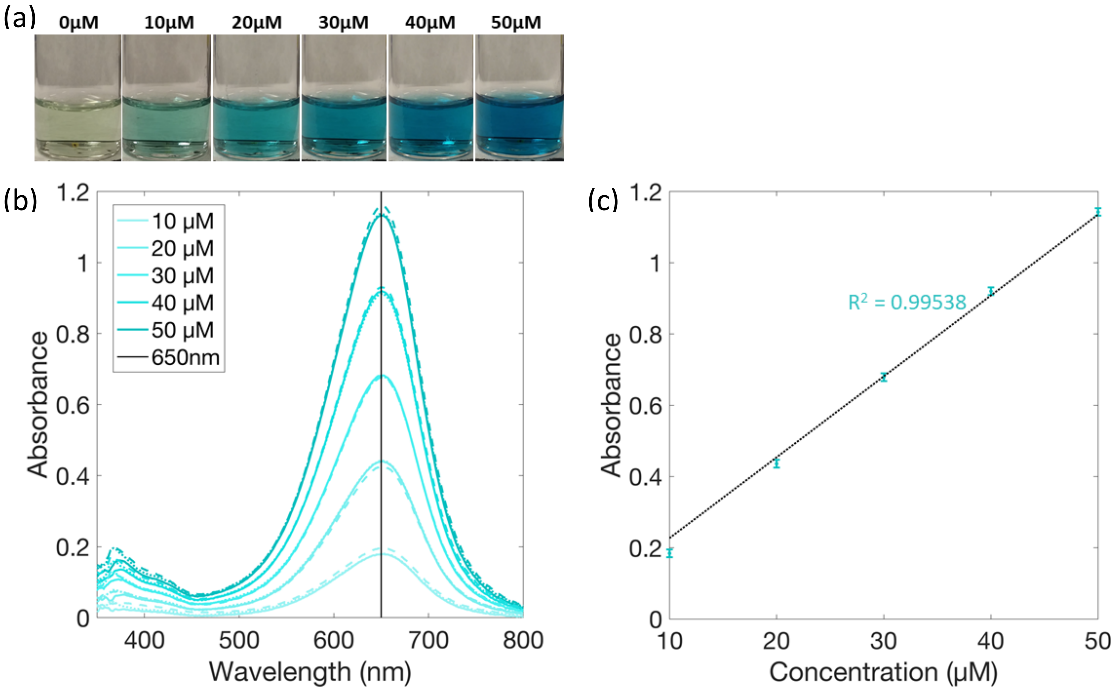

Figure D-3: (a) Prepared calibration samples using the salicylate method after 1 hour (b) Wavelength-dependent absorbance for NH_3 concentrations ranging from 10 μM to 50 μM as detected using the salicylate method, with the NH_3 characteristic peak centered around 650 nm (c) Concentration-dependent maximum absorbance reached at 650 nm, fitted using Beer's Law.

D.2 Interfering signal for NO_2^- concentration readings

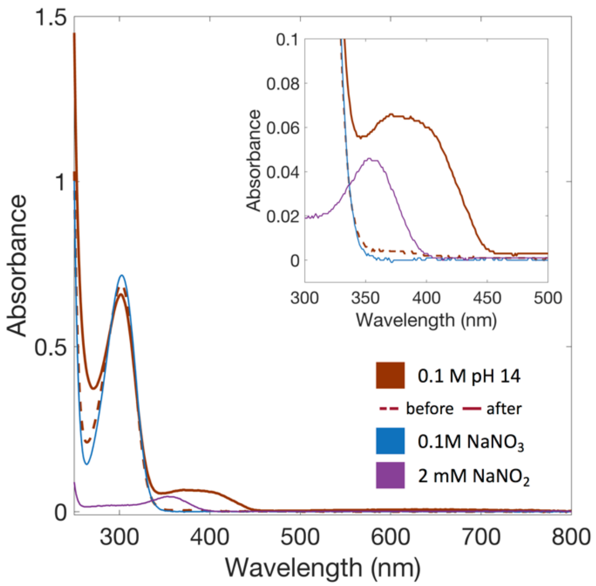

Figure D-4: UV-Vis reading for a trial at 0.1 M $NaNO_3$ and pH 14, compared to NO_3^- and NO_2^- calibration curves. (inset) Wavelength range where unexplained signal is taking place.

D.3 Bjerrum Plot for Phosphate Species

Table D-2: Equations and constant values for K_a (for phosphoric acid in water at 25°C)[248] used for equilibrium speciation calculations of a phosphate buffer

Eq.	Equilibrium constant	In water (25˚C)
(D-1)	$K_1 = \frac{[H^+][H_2PO_4{}^-]}{[H_3PO_4]}$	7.11 x 10^{-3}
(D-2)	$K_2 = \frac{[H^+][HPO_4{}^{2-}]}{[H_2PO_4{}^-]}$	6.34 x 10^{-8}
(D-3)	$K_3 = \frac{[H^+][PO_4{}^{3-}]}{[HPO_4{}^{2-}]}$	1.26 x 10^{-12}
(D-4)	$pKw = pOH + pH$	14

Declining currents in the pH 10 CA experiments are attributed to competitive adsorption by the phosphate buffer. PO_4^{3-} is reported by literature to be the major adsorbed species on the electrode surface in the range of pH 6.8 – 11.2.[122] This is true even when PO_4^{3-} is not the major species present in solution. However, as it becomes a more present ion in solution, the likelihood of adsorption of PO_4^{3-} becomes greater, due to higher concentration. Although PO_4^{3-} is not present in solution in a significant quantity when the buffer is first made, either at pH 8 or pH 10, we have hypothesized that the formation of a locally higher pH region is developing over the course of the experiment. This would cause the dashed lines in Figure D-5 to shift to the right. As the buffer composition shifts locally, for the pH 10, an increasing significant amount of PO_4^{3-} is made. However, for pH 8, there is not a significant amount of PO_4^{3-} formed. This causes a higher concentration of PO_4^{3-} in the pH 10 solution which can competitively adsorb to the electrode surface, blocking reaction sites for the NO_3^- reduction. As more PO_4^{3-} is formed, the reaction rate of the pH 10 experiment drops.

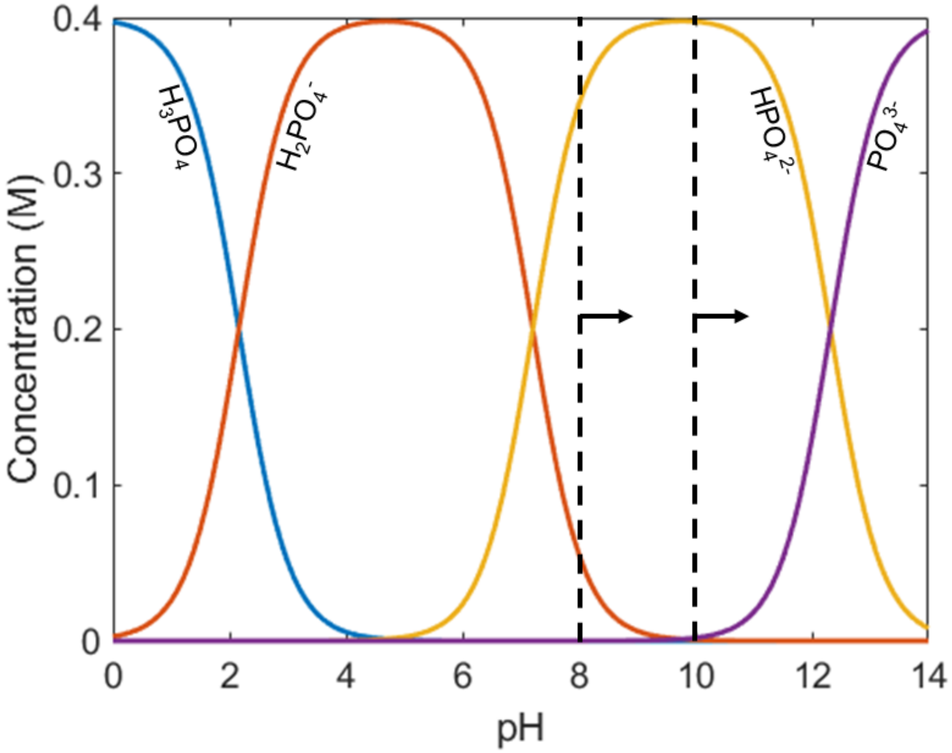

Figure D-5: Phosphate Bjerrum plot (calculated from the state equations listed in Table D-2) from 0 to 14 pH at 25°C with a total concentration of 0.4 M (as in the case of the pH 10 solutions used in this study). As pH 8 and 10 locally develop a higher pH, the phosphate species close to the electrode will shift based on the local pH. As pH 10 shifts locally, an increasing amount of PO_4^{3-} ions will develop. As pH 8 shifts higher locally, the amount of PO_4^{3-} ions will still be insignificant.

Appendix E Error Quantification

Species concentrations for NO_3^-, NO_2^-, NH_3 were obtained from absorbance measurements from the UV-Vis spectrophotometer. Calibration datasets were used to obtain a molar absorption coefficient, ϵ, from measured absorbance, $A_{cal,i}$ and species concentration, c_i, using Beer's law:

$$A_{cal,i} = \epsilon \, c_i \, l \tag{E-1}$$

Where ϵ is the slope from the fit across all concentrations and all trials and l = 1 cm.

Using Eq. (E-1), we can calculate the concentration distributions before and after the CA tests using the $A_{m,i}$ measurement obtained from UV-Vis spectrophotometry. The error in the concentration estimates was computed by accounting for the error coming from the calibration curves, the systematic error from the solution preparation, and the repeatability between trials. We define the following terms:

- $\frac{s_{\epsilon,fit}}{\epsilon}$ (Eq. (E-2)): the error from the fit from which the absorption coefficient, ϵ is obtained (which can be calculated using the standard error of the regression slope)
- $\frac{s_{c,cal}}{c_i}$ (Eq. (E-6)): the calibration measurement variability, which accounts for the trial-to-trial random error in the absorbance measurements as well as the error coming from the calibration solutions preparation
- $\frac{s_{c,sys}}{c_s}$ (Eq.(E-8)): the systematic error from preparing the nitrate solution, included for the initial nitrate concentration

- $\frac{s_{c,dil}}{c_i}$ (Eq. (E-9)): the dilution error applied when the sample required dilution before any UV-Vis measurement (applicable for all species apart from NO_3^- and NO_2^- readings for the 0.1 M stock solutions)
- $\frac{s_{t-t}}{\bar{c}_{s,m}}$ (Eq. (E-10)): the trial-to-trial error

E.1 Fit error

The error in the fitted ϵ can be computed based the standard error of regression slope:

$$\frac{s_{\epsilon,fit}}{\epsilon} = \frac{1}{\epsilon}\sqrt{\frac{\frac{1}{N-1}\Sigma_{i=1}^{N}\left(A_{cal,i} - \epsilon c_i l\right)^2}{\Sigma_{i=1}^{N}(c_i - \bar{c})^2}} \qquad \text{(E-2)}$$

Where: s_ϵ is the standard error for ϵ

N is the total number of data points (-1 comes from fitting for 1parameter)

$A_{cal,i}$ is the measured absorbance at calibration concentration c_i

$\epsilon c_i l$ is the estimated absorbance at c_i using the fitted ϵ

$\bar{c}$ is the average concentration across all calibration concentrations

$\frac{s_{\epsilon,fit}}{\epsilon}$ corresponds to the fit error with respect to the A_{cal} and c_{cal} measurements (the only sources of error in the calibration measurements).

We established calibration curves for NO_3^-, NO_2^-, NH_3, with their respective fit errors listed in Table E-1.

Table E-1: Errors from the calibration curves NO_3^-, NO_2^-, and NH_3 at the relevant wavelengths

Species	**$NO_3^-\|_{\lambda=303nm}$**	**$NO_2^-\|_{\lambda=303nm}$**	**$NO_2^-\|_{\lambda=355nm}$**	**$NH_3\|_{\lambda=650nm}$**
$s_{\epsilon,fit}$	2.34e-5 mM^{-1} cm^{-1}	2.00e-5 mM^{-1} cm^{-1}	2.94e-5 mM^{-1} cm^{-1}	4.36e-4 μM^{-1} cm^{-1}
ϵ	7.1e-3 mM^{-1} cm^{-1}	9.19e-3 mM^{-1} cm^{-1}	2.28e-2 mM^{-1} cm^{-1}	0.0227 μM^{-1} cm^{-1}
$\left(\frac{s_{\epsilon,fit}}{\epsilon}\right)$	0.0033	0.0022	0.0013	0.0192
$\left(\frac{s_{c,cal}}{c_i}\right)$	0.0879	0.0936	0.0887	0.141

E.2 Random error in the calibration solutions

The random error $s_{c,cal}$ for the concentration c_i can be computed by propagating the error from the absorbance measurements (Eq. (E-3)) and the error from the solution preparation (Eq. (E-4)-(E-6)). The error for the absorbance measurements was calculated using the standard deviation definition:

$$\frac{s_A}{\bar{A}_\iota} = \frac{1}{\bar{A}_\iota}\sqrt{\frac{1}{N}\Sigma_{i=1}^{N}(A_i - \bar{A}_\iota)^2} \tag{E-3}$$

Where: s_A is the standard deviation for A

N is the total number of data points

A_i is the measured absorbance at calibration concentration c_i

$\bar{A}_\iota$ is the average absorbance at calibration concentration c_i

To calculate the error from the solution preparation with respect to the calibration curves, we calculated the systematic error coming from the stock solution preparation $\left(\frac{s_{c,sys}}{c_{s,stock}}\right)$ as well as the error from the dilution procedure $\left(\frac{s_{c,dil}}{c_i}\right)$. We can calculate the systematic error $\frac{s_{c,sys}}{c_{s,stock}}$ using Eq. (E-4):

$$\frac{s_{c,sys}}{c_{s,stock}} = \sqrt{\left(\frac{\Delta m}{m_s}\right)^2 + \left(\frac{\Delta V}{V}\right)^2} \tag{E-4}$$

Where: $s_{c,sys}$ is the systematic error for $c_{s,s}$

$c_{s,stock}$ is the concentration of the stock solution

Δm is the error from the balance (Δm = 0.1 mg)

m_s is the mass of solute used to make the stock solution

$\Delta \text{Ꝟ}$ is the error from the pipettes (values listed in the table below)

Ꝟ is the volume of the prepared solution

The solutions could be prepared with pipettes of different sizes (no graduated cylinders were used). According to the manufacturer, our pipettes have the specifications listed in Table E-2 with respect to inaccuracy.

Table E-2: Pipettes specifications for SCILOGEX MicroPipette Pipettors

Pipette	$\frac{\Delta \text{Ꝟ}}{\text{Ꝟ}_{min}}$	$\frac{\Delta \text{Ꝟ}}{\text{Ꝟ}_{max}}$
0.5 – 10 μL	2.50 % at 1μL	1.00 %
10 – 100 μL	3.00 %	0.80 %
100 – 1000 μL	2.00 %	0.60 %

The most common volume measured was 1 mL using the 100 – 1000 μL pipette, but during the dilution process other volumes/pipettes were used as well. If we consider the largest relative uncertainty for each pipette, we obtain the following:

$$\left(\frac{\Delta \text{Ꝟ}}{\text{Ꝟ}}\right)_{all} = \sqrt{(0.0250)^2 + (0.0300)^2 + (0.0200)^2} = 0.0439$$

For a conservative error estimate, we will use 0.0439 as the error on the volume for all solutions.

To calculate $\frac{s_{c,sys}}{c_{s,stock}}$ for the calibration curves, we used the inputs from the stock solution used during the calibrations (Table E-3): the stock solution was diluted by different factors to reach the desired concentrations for the calibration curves.

Table E-3: Inputs for the systematic error calculation

Species	$c_{s,stock}$	m_s	Ꝟ	$\frac{s_{c,sys}}{c_{s,stock}}$
NO_3^-	100.00 mM	0.08500 g	10 mL	0.0439
NO_2^-	50.00 mM	0.01730 g	5 mL	0.0443
NH_3	1.0 mM	1.3 mg	5 mL	0.089

We can calculate $\frac{s_{c,dil}}{c_i}$ by using Eq. (E-5):

$$\frac{s_{c,dil}}{c_i} = \sqrt{\left(\frac{s_{c,sys}}{c_{s,stock}}\right)^2 + \left(\frac{s_{\cancel{V}}}{\cancel{V}}\right)^2 + \left(\frac{s_{\cancel{V}_{dil}}}{\cancel{V}_{dil}}\right)^2} \tag{E-5}$$

Where $\left(\frac{s_{c,sys}}{c_{s,stock}}\right)$ comes from Eq. (E-4) and $\left(\frac{s_{\cancel{V}}}{\cancel{V}}\right) = \left(\frac{s_{\cancel{V}_{dil}}}{\cancel{V}_{dil}}\right) = \left(\frac{\Delta\cancel{V}}{\cancel{V}}\right)_{all} = 0.0439$.

Thus, we can estimate $s_{c,cal}$ by calculating the standard deviation for each concentration using Eq. (E-6) and then taking the average value of the $\frac{s_{c,cal}}{c_i}$ ratio (listed in Table E-1):

$$\frac{s_{c,cal}}{c_i} = \sqrt{\left(\frac{s_A}{\bar{A}_i}\right)^2 + \left(\frac{s_{c,sys}}{c_{s,stock}}\right)^2 + \left(\frac{s_{c,dil}}{c_i}\right)^2} \tag{E-6}$$

E.3 Sample solution error

The solution error was calculated using Eq. (E-7):

$$\frac{s_{c,sol}}{c_s} = \sqrt{\left(\frac{s_{c,sys}}{c_s}\right)^2 + \left(\frac{s_{c,dil}}{c_{s,m}}\right)^2} \tag{E-7}$$

As a reminder, we are defining $s_{c,sys}$ as the error coming from preparing the solution before the CA experiment:

$$\frac{s_{c,sys}}{c_s} = \sqrt{\left(\frac{\Delta m}{m_s}\right)^2 + \left(\frac{\Delta\cancel{V}}{\cancel{V}}\right)^2} \tag{E-8}$$

Where c_s is the concentration of the prepared sample (0.1 M or 1 M $NaNO_3$) and m_s is the mass of the nitrate required to reach the initial concentration.

We are defining $s_{c,dil}$ as the error coming from diluting the reacted solution after the CA experiment:

$$\frac{s_{c,dil}}{c_{s,m}} = \sqrt{\left(\frac{s_{c,sys}}{c_s}\right)^2 + \left(\frac{s_{\cancel{V}}}{\cancel{V}}\right)^2 + \left(\frac{s_{V_{dil}}}{V_{dil}}\right)^2} \tag{E-9}$$

Where $c_{s,m}$ is the measured concentration of the diluted sample

E.4 Trial-to-trial variance in concentration measurement

The trial-to-trial error s_{t-t} for the average measured concentration $\bar{c}_{s,m}$ (across all trials for a pH and stock solution concentration combination) can be computed by using the standard deviation definition (Eq. (E-10)):

$$\frac{s_{t-t}}{\bar{c}_{s,m}} = \frac{1}{\bar{c}_{s,m}} \sqrt{\frac{1}{N_t} \Sigma_{i=1}^{N_t} \left(c_{s,m} - \bar{c}_{s,m}\right)^2} \tag{E-10}$$

Where N_t is the number of measurements across all trials.

The "NO_3^-, after, full" (in bold) measurement at 303 nm is the square sum of the $\frac{s_{t-t}}{\bar{c}_{s,m}}$ errors for the "NO_2^-, after" at 303 nm and "NO_3^-, after" at 303 nm, since the final concentration of NO_3^- is calculated by correcting for any NO_2^- contributions in the measured absorbance at 303 nm.

Table E-4: Trial-to-trial error across all pH and concentration combinations

Species	Wavelength (nm)	pH 8, 0.1 M	pH 8, 1 M	pH 10, 0.1 M	pH 10, 1 M	pH 14, 0.1 M	pH 14, 1 M
NO_3^-, before	303	1.44%	0.94%	7.04%	5.33%	8.48%	1.69%
NO_3^-, after	303	1.11%	1.68%	10.1%	5.82%	20.2%	1.65%
NO_2^-, after	303	36.8%	25.2%	9.35%	13.8%	76.9%	12.7%
NO_3^-, after, full	**303**	**37.1%**	**25.4%**	**13.8%**	**15.0%**	**79.5%**	**12.8%**
NO_2^-, after	355	37.1%	25.4%	9.07%	13.9%	77.9%	12.8%
NH_3, after	650	42.9%	17.3%	49.0%	7.58%	43.5%	17.8%

E.5 Total error for the measured concentration

Thus, we can propagate the error from the different sources for each species as follows such that the error is comparing like-to-like:

$$\frac{s_{c,NO3,in}}{c_{NO3,in,m}} = \sqrt{\left(\frac{s_{\epsilon,fit}}{\epsilon}\right)_{NO3}^{2} + \left(\frac{s_{c,cal}}{c_i}\right)_{NO3}^{2} + \left(\left(\frac{s_{c,sys}}{c_s}\right)_{NO3}^{2} + \left(\frac{s_{c,dil}}{c_{s,m}}\right)_{NO3}^{2}\right) + \left(\frac{s_{t-t}}{\bar{c}_{s,m}}\right)_{NO3}^{2}} \qquad \text{(E-11)}$$

$$\frac{s_{c,NO3,f}}{c_{NO3,f,m}} = \sqrt{\left(\frac{s_{\epsilon,fit}}{\epsilon}\right)_{NO3}^{2} + \left(\frac{s_{c,cal}}{c_i}\right)_{NO3}^{2} + \left(\frac{s_{c,dil}}{c_{s,m}}\right)_{NO3}^{2} + \left(\frac{s_{t-t}}{\bar{c}_{s,m}}\right)_{NO3}^{2} + \left(\frac{s_{c,NO2,f}}{c_{NO2,f,m}}\right)^{2}} \qquad \text{(E-12)}$$

$$\frac{s_{c,NO2,f}}{c_{NO2,f,m}} = \sqrt{\left(\frac{s_{\epsilon,fit}}{\epsilon}\right)_{NO2}^{2} + \left(\frac{s_{c,cal}}{c_i}\right)_{NO2}^{2} + \left(\frac{s_{c,dil}}{c_{s,m}}\right)_{NO2}^{2} + \left(\frac{s_{t-t}}{\bar{c}_{s,m}}\right)_{NO2}^{2}} \qquad \text{(E-13)}$$

$$\frac{s_{c,NH3,f}}{c_{NH3,f,m}} = \sqrt{\left(\frac{s_{\epsilon,fit}}{\epsilon}\right)_{NH3}^{2} + \left(\frac{s_{c,cal}}{c_i}\right)_{NH3}^{2} + \left(\frac{s_{c,dil}}{c_{s,m}}\right)_{NH3}^{2} + + \left(\frac{s_{t-t}}{\bar{c}_{s,m}}\right)_{NH3}^{2}} \qquad \text{(E-14)}$$

We used the following relation to quantify the error for the measured consumed nitrate (calculated by taking the difference between $c_{NO3,\mathrm{i}}$ and $c_{NO3,\mathrm{f}}$):

$$s_{c,NO3,m} = (c_{NO3,\mathrm{i}} - c_{NO3,\mathrm{f}})\sqrt{\left(\frac{s_{c,NO3,\mathrm{i}}}{c_{NO3,\mathrm{i},m}}\right)^{2} + \left(\frac{s_{c,NO3,\mathrm{f}}}{c_{NO3,\mathrm{f},m}}\right)^{2}} \qquad \text{(E-15)}$$

We used the following relation to quantify the error for the estimated consumed nitrate (calculated by assuming that the consumed c_{NO3} is equal to the sum of $c_{NO2,f,m}$ and $c_{NH3,f,m}$):

$$s_{c,NO3,est} = (c_{NO2,\mathrm{f},m} + c_{NH3,\mathrm{f},m})\sqrt{\left(\frac{s_{c,NO2,\mathrm{f}}}{c_{NO2,\mathrm{f},m}}\right)^{2} + \left(\frac{s_{c,NH3,\mathrm{f}}}{c_{NH3,\mathrm{f},m}}\right)^{2}} \qquad \text{(E-16)}$$

All s values have units of mM and are used to generate the error bars on Figure 2-8 and Figure 2-11.

E.6 Measured trial-by-trial error for species concentrations

Table E-5: Measured $FE_{NO_2^-}$ and FE_{NH_3} with the associated error ($\frac{s_{c,NO2,\mathrm{f}}}{c_{NO2,\mathrm{f},m}}$ and $\frac{s_{c,NH3,\mathrm{f}}}{c_{NH3,\mathrm{f},m}}$) without considering the contributions from trial-to-trial variation). The total species error is calculated as the sum of these errors and can be compared to the unaccounted charge in each trial.

Solution tested (trial)	$FE_{NO_2^-}$ **(%)**	$\frac{s_{c,NO2,\mathrm{f}}}{c_{NO2,\mathrm{f},m}}$	FE_{NH_3} **(%)**	$\frac{s_{c,NH3,\mathrm{f}}}{c_{NH3,\mathrm{f},m}}$	**Total species error (%)**	**Unaccounted (%)**
pH 8, 0.1 M (1)	17.58	0.089	27.45	0.155	24.37	0.00
pH 8, 0.1 M (2)	24.30	0.089	42.18	0.155	24.37	0.00
pH 8, 0.1 M (3)	16.47	0.089	48.89	0.155	24.37	0.00
pH 10, 0.1 M (1)	29.24	0.099	25.36	0.155	25.37	0.00
pH 10, 0.1 M (2)	25.06	0.102	46.26	0.155	25.69	0.00
pH 10, 0.1 M (3)	18.49	0.089	48.79	0.155	24.37	0.00
pH 14, 0.1 M (1)	3.56	0.105	55.83	0.155	25.96	25.25
pH 14, 0.1 M (2)	8.15	0.099	43.35	0.155	25.40	35.61
pH 14, 0.1 M (3)	2.50	0.089	37.76	0.155	24.37	45.94
pH 8, 1 M (1)	49.61	0.108	18.86	0.155	26.33	19.27
pH 8, 1 M (2)	43.95	0.108	25.79	0.155	26.33	13.50
pH 8, 1 M (3)	40.62	0.108	31.58	0.155	26.33	10.26
pH 10, 1 M (1)	47.32	0.108	21.97	0.155	26.33	20.07
pH 10, 1 M (2)	43.36	0.108	31.02	0.155	26.33	14.67
pH 10, 1 M (3)	47.74	0.108	26.61	0.155	26.33	13.88
pH 14, 1 M (1)	4.00	0.108	44.83	0.155	26.33	46.24
pH 14, 1 M (2)	5.32	0.108	43.16	0.155	26.33	44.38
pH 14, 1 M (3)	5.99	0.108	50.37	0.155	26.33	39.01

Appendix F Estimated Solar-to-Chemical Efficiencies and Nitrogen Removal/Recovery Rates

Figure F-1 shows the relative difference (RE) for the solar-to-chemical efficiency that was calculated with, $\eta_{\text{solar-to-chemical,comp}}$, and without, $\eta_{\text{solar-to-chemical,no comp}}$, competing reactions as function of the bulk NO_3^- concentration. Both HER and ORR were implemented with "*worst-case*" kinetic parameters. An increase in this relative difference corresponds to an increase in the effect of the competing reactions; a value of 100% implies that the efficiency value with competing reactions approached 0. On Figure F-1(a), the relative difference decreases with increasing concentration for all band gaps, with the largest values overall reached by TiO_2 and Si. For the formation of N_2O, on Figure F-1(b), the smaller concentrations show less of an effect due to the competing reactions, which follows from the mass-transport limited behavior of the NO3RR shown on Figure 3-6.

$$RE(\%) = \frac{\eta_{\text{solar-to-chemical,no comp}} - \eta_{\text{solar-to-chemical,comp}}}{\eta_{\text{solar-to-chemical,no comp}}} \tag{F-1}$$

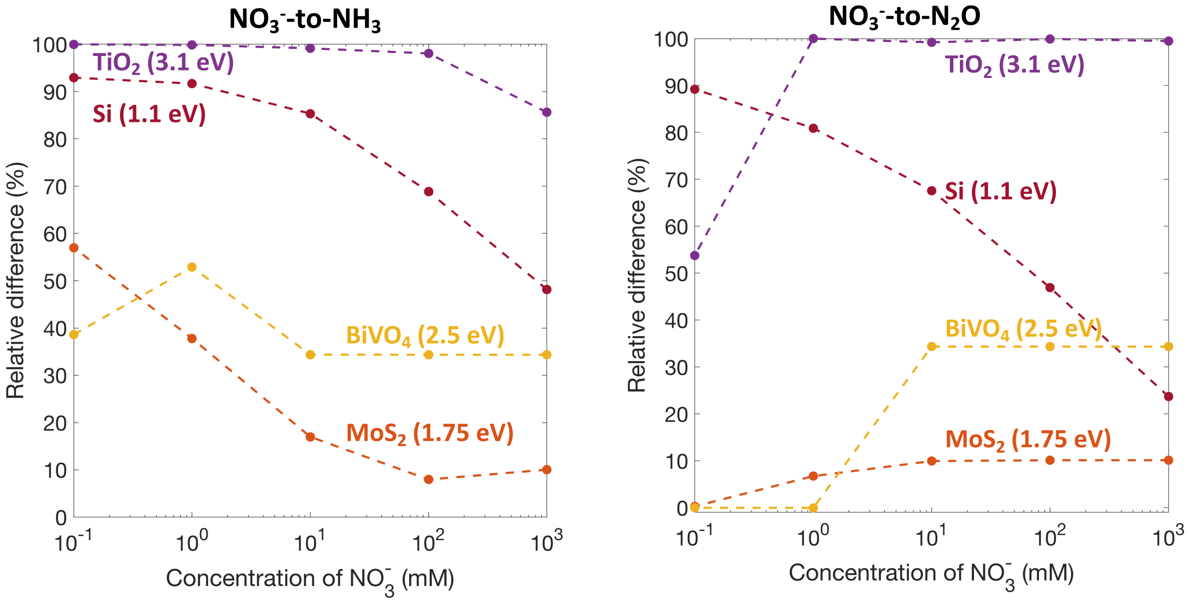

(a) (b)

Figure F-1: Relative difference (RE (%)) of the solar-to-chemical efficiencies with and without competing reactions as a function of NO_3^- concentration for Si (red), MoS_2 (orange), $BiVO_4$ (yellow) and TiO_2 (purple) as discussed in Figure 3-6 for the (a) NO_3^--to-NH_3 transformation and (b) NO_3^--to-N_2O transformation. RE value of 100% indicates that the solar-to-chemical efficiency with competing reactions is 0; smaller the RE value lesser the effect of competing reactions on the efficiency.

F.1 Comparison with state-of-the-art nitrogen-removal technologies

The ammonia stripping reactor recovers NH_3/NH_4^+ nutrients that are present in the solution in an electrochemical flow cell by applying an electric field.[138] This approach offers the advantages of high nitrogen-recovery rates, up to 384 g_N m^{-2} day^{-1}, because of improved mass-transport in flow reactors.[138] However, it relies on the presence of $NH_3/NH4^+$ in the waste stream, unlike our device that transforms the NO_3^- to NH_3 or N_2O already.

The Sharon-Anammox process is an energy-efficient, biological pathway to transform reactive-nitrogen contaminants present in the form of NH_3/NH_4^+ to N_2.[249] However, with this approach the nutrients in wastewater are not recovered but lost as N_2. Because this process is typically carried out in batch-reactors, volumetric nitrogen-removal rates of up to 2 kg_N m^{-3} day^{-1} have been reported.[125,169] To translate the volumetric rate to an areal rate, a biofilm/membrane with a conservatively low specific surface area of ~200 m^{-2} m^{-3} was assumed,[250] which results in an areal rate of approximately 10 g_N m^{-2} day^{-1}. Our estimate of 200 m^2 m^{-3} for the biofilm surface area is already conservatively low. Most reported biofilm/membrane surfaces easily have >500 m^2 m^{-3} in specific surface area of the biofilm/membrane.[251,252]

Appendix G Derivations for Equivalent Circuit Model: Selective Coating Implementation

G.1 Concentration fluxes at the electrode surface covered by a selective coating

The solubility parameter or the partition coefficient, S_i, is a thermodynamic property that is defined as the ratio of species i concentrations within the coating and liquid electrolyte phases at equilibrium (Eq. (4-5)):

$$S_i = \frac{\boldsymbol{c}_i^*}{\boldsymbol{c}_i}$$

Where $\boldsymbol{c}_i^*$ (in mol m^{-3}) is the concentration of species i in the coating, and $\boldsymbol{c}_i$ (in mol m^{-3}) is concentration of species i in the liquid electrolyte.

At steady-state conditions, the flux of the species in the diffusion boundary layer is equal to the flux in the overlayer/coating:

$$N_i = N_{i,DBL} = N_{i,coat}$$

$$j = -n_e\, F\, D_O \left(\frac{\boldsymbol{c}_{O,\text{bulk}} - \boldsymbol{c}_O(x = t_\text{c})}{\delta_{BL}}\right) = -n_e\, F\, D_{eff,O} \left(\frac{\boldsymbol{c}_O^*(x = t_\text{c}) - \boldsymbol{c}_O^*(x = 0)}{t_\text{c}}\right) \quad \text{(G-1)}$$

Where the negative sign denotes a cathodic current density j (in A m^{-2}), δ_{BL} is the boundary layer thickness; $\boldsymbol{c}_{O,\text{bulk}}$ (in mol m^{-3}) denotes species concentration in the bulk electrolyte far away from the diffusion boundary layer.

We can rewrite the flux in the coating as a function of S_O and the species concentrations in the electrolyte at any spatial location, such Eq. (G-1) becomes Eq. (G-2) in the electrolyte and Eq. (G-3) in the coating:

$$j = -n_e\, F\, D_O \frac{\boldsymbol{c}_{O,bulk} - \boldsymbol{c}_O(x = t_c)}{\delta_{BL}} \tag{G-2}$$

$$j = -n_e\, F\, \underbrace{D_{eff,O}\, S_O}_{P_O} \left(\frac{\boldsymbol{c}_O(x = t_c) - \boldsymbol{c}_O(x = 0)}{t_c} \right) \tag{G-3}$$

where, the overlayer permeability, $P_O = D_{e,O} S_O$ (in $\mathrm{m^2\ s^{-1}}$) is dictated by the product of the partition coefficient and the effective diffusivity for species O.

Eq. (G-3) has undergone a simple transformation of variables based on the partition function definition (Eq. (4-5)) such that both Eq. (G-2) and Eq. (G-3) depend on the same variable C_O. Here the C_O stands in as a hypothetical concentration of O in the liquid phase present at $x = 0$ and in equilibrium with O within the solid coating phase.

At limiting current density, the concentration at the electrode surface is $\boldsymbol{c}_O^*(x = 0) = \boldsymbol{c}_O(x = 0) = 0$, making:

$$j_{lim}^* = -n_e\, F\, P_O \frac{\boldsymbol{c}_O(x = t_c)}{t_c} \tag{G-4}$$

$$\boldsymbol{c}_{O,\mathrm{limiting}}(x = t_c) = \frac{-j_{lim}^*\, t_c}{n_e\, F\, P_O} \tag{G-5}$$

From Eq. (G-2), at limiting current, we can rewrite j_{lim}^* as:

$$j_{lim}^* = -n_e\, F\, D_O \frac{\boldsymbol{c}_{O,bulk} + \frac{j_{lim}\, t_c}{n_e\, F\, P_O}}{\delta_{BL}}$$

$$j_{lim}^* \left(1 + \frac{D_O\, t_c}{P_O\, \delta_{BL}} \right) = -\frac{n_e\, F\, D_O\, \boldsymbol{c}_{O,bulk}}{\delta_{BL}}$$

$$j_{lim}^* = -\frac{n_e\, F\, \boldsymbol{c}_{O,bulk}}{\left(\frac{\delta_{BL}}{D_O} + \frac{t_c}{P_O} \right)} \tag{G-6}$$

We should note that j_{lim}^{*} as defined in Eq. (G-6), with both a coating and a boundary-layer present, will only approach i_{lim} for a bare electrode (with the same boundary-layer thickness) when $\frac{P_j}{t_c}$ >> $\frac{D_j}{\delta_{BL}}$. We can rewrite Eq. (G-6) with respect to the boundary-layer and coating in isolation, such that:

$$j_{lim}^{*} = \frac{1}{j_{lim,DBL}} + \frac{1}{j_{lim,coat}} \tag{G-7}$$

If there were no coating (such that $P_O = D_O; t_c = 0$), the $\frac{1}{j_{lim,coat}}$ term would drop out and we retrieve the expected expression for limiting current density.

From Eq. (G-2),

$$j = -n_e\, F\, D_O \frac{\boldsymbol{c}_{O,bulk} - \boldsymbol{c}_O(x = t_c)}{\delta_{BL}}$$

$$\frac{\boldsymbol{c}_O(x = t_c)}{\boldsymbol{c}_{O,\mathrm{bulk}}} = 1 + \frac{j\, \delta_{BL}}{n_e\, F\, D_O\, \boldsymbol{c}_{O,bulk}}$$

Substitute value for $\boldsymbol{c}_{O,bulk}$ from Eq. (G-6), where, $\boldsymbol{c}_{O,bulk} = -\frac{j_{lim}^{*}\left(\frac{\delta_{BL}}{D_O}+\frac{t_c}{P_O}\right)}{n_e\, F}$:

$$\frac{\boldsymbol{c}_O(x = t_c)}{\boldsymbol{c}_{O,\mathrm{bulk}}} = 1 + \frac{j\, \delta_{BL}}{n_e\, F\, D_O \left(\frac{-j_{lim}^{*}\left(\frac{\delta_{BL}}{D_O} + \frac{t_c}{P_O}\right)}{n_e\, F} \right)}$$

$$= 1 - \frac{j\, \delta_{BL}}{j_{lim}^{*}\, D_O \left(\frac{\delta_{BL}}{D_O} + \frac{t_c}{P_O}\right)}$$

$$\frac{\boldsymbol{c}_O(x = t_c)}{\boldsymbol{c}_{O,\mathrm{bulk}}} = 1 - \left(\frac{\left(\frac{\delta_{BL}}{D_O}\right)}{\left(\frac{\delta_{BL}}{D_O} + \frac{t_c}{P_O}\right)} \right) \frac{j}{j_{lim}^{*}} \tag{G-8}$$

At any operating current density, from, Eq. (G-2) and Eq. (G-3), we have:

$$-n_e\,F\,D_O\,\frac{\boldsymbol{c}_{O,bulk}-\boldsymbol{c}_O(x=t_c)}{\delta_{BL}}=-n_e\,F\,P_O\left(\frac{\boldsymbol{c}_O(x=t_c)-\boldsymbol{c}_O(x=0)}{t_c}\right)$$

Collecting all terms for specific concentrations together, we have,

$$\boldsymbol{c}_O(x=t_c)\left(\frac{D_O}{\delta_{BL}}+\frac{P_O}{t_c}\right)=\frac{\boldsymbol{c}_O(x=0)}{t_c/P_O}+\frac{\boldsymbol{c}_{O,bulk}}{\delta_{BL}/D_O}$$

$$\frac{\boldsymbol{c}_O(x=0)}{t_c/P_O}=\boldsymbol{c}_O(x=t_c)\left(\frac{D_O}{\delta_{BL}}+\frac{P_O}{t_c}\right)-\frac{\boldsymbol{c}_{O,bulk}}{\delta_{BL}/D_O}$$

$$\frac{\boldsymbol{c}_O(x=0)}{\boldsymbol{c}_{O,\mathrm{bulk}}}=\frac{t_c}{P_O}\left(\frac{\boldsymbol{c}_O(x=t_c)}{\boldsymbol{c}_{O,\mathrm{bulk}}}\left(\frac{D_O}{\delta_{BL}}+\frac{P_O}{t_c}\right)-D_O/\delta_{BL}\right)$$

$$=\frac{t_c}{P_O}\left(\left(1-\left(\frac{\left(\frac{\delta_{BL}}{D_O}\right)}{\left(\frac{\delta_{BL}}{D_O}+\frac{t_c}{P_O}\right)}\right)\frac{j}{j_{lim}^{*}}\right)\left(\frac{D_O}{\delta_{BL}}+\frac{P_O}{t_c}\right)-\frac{D_O}{\delta_{BL}}\right)$$

$$=\frac{t_c}{P_O}\left(\frac{D_O}{\delta_{BL}}-\left(\frac{\frac{j}{j_{lim}}}{\left(\frac{\delta_{BL}}{D_O}+\frac{t_c}{P_O}\right)}\right)+\frac{P_O}{t_c}-\frac{P_O}{t_c}\left(\left(\frac{\left(\frac{\delta_{BL}}{D_O}\right)}{\left(\frac{\delta_{BL}}{D_O}+\frac{t_c}{P_O}\right)}\right)\frac{j}{j_{lim}^{*}}\right)-\frac{D_O}{\delta_{BL}}\right)$$

$$=\frac{t_c}{P_O}\left(\frac{P_O}{t_{coat}}-\frac{j}{j_{lim}}\left(\frac{1}{\left(\frac{\delta_{BL}}{D_O}+\frac{t_c}{P_O}\right)}+\frac{P_O}{t_c}\frac{\left(\frac{\delta_{BL}}{D_O}\right)}{\left(\frac{\delta_{BL}}{D_O}+\frac{t_c}{P_O}\right)}\right)\right)$$

$$=\frac{t_c}{P_O}\left(\frac{P_O}{t_c}-\frac{j}{j_{lim}^{*}}\left(\frac{1+\left(\frac{P_O\delta_{BL}}{D_O t_c}\right)}{\left(\frac{\delta_{BL}}{D_O}+\frac{t_c}{P_O}\right)}\right)\right)$$

$$=\frac{t_c}{P_O}\left(\frac{P_O}{t_c}-\frac{i}{i_{lim}^{*}}\left(\frac{\frac{D_O\,t_c+P_O\,\delta_{BL}}{D_O\,t_c}}{\left(\frac{D_O\,t_c+P_O\,\delta_{BL}}{D_O\,P_O}\right)}\right)\right)$$

$$= \frac{t_c}{P_O}\left(\frac{P_O}{t_c} - \frac{j}{j_{lim}}\left(\frac{P_O}{t_c}\right)\right) = 1 - \frac{j}{j_{lim}^*}$$

$$\frac{\boldsymbol{c}_O(x=0)}{\boldsymbol{c}_{O,\text{bulk}}} = 1 - \frac{j}{j_{lim}^*} \qquad \text{(G-9)}$$

Therefore, $\frac{\boldsymbol{c}_O(x=0)}{\boldsymbol{c}_{O,\text{bulk}}}$, which is the ratio of the surface to bulk species concentration in the electrolyte still retains the form that we'd expect without the coating.

G.2 Deriving mass-transport Butler-Volmer kinetics accounting for the presence of a selective coating

We can define the rate of an electrochemical reaction k as:

$$r_{b,k} = \frac{j_{b,k}}{n_{e,k}\, F} = k_{a,k}\, \boldsymbol{c}_{R,s}^{\nu_{R,k}} \exp\left(\frac{\alpha_{a,k}\, V}{R_c\, T/n_{e,k}\, F}\right) - k_{c,k}\, \boldsymbol{c}_{O,s}^{\nu_O} \exp\left(\frac{-\alpha_{c,k}\, V}{R_c\, T/n_{e,k}\, F}\right) \qquad \text{(G-10)}$$

Where $\boldsymbol{c}_{R,s}$ and $\boldsymbol{c}_{O,s}$ are the concentrations of species O and R at the electrode surface and $\eta_s = V - U$ is the surface overpotential defined with respect to the applied potential V and the surface electrochemical potential U.

At equilibrium, when η_s = 0, U can be defined as:

$$k_{a,k}\, \boldsymbol{c}_{R,s}^{\nu_{R,k}} \exp\left(\frac{\alpha_{a,k}\, U}{R_c\, T/n_{e,k}\, F}\right) = k_{c,k}\, \boldsymbol{c}_{O,s}^{\nu_{O,k}} \exp\left(\frac{-\alpha_{c,k}\, U}{R_c\, T/n_{e,k}\, F}\right)$$

$$\ln\left[k_{a,k}\, \boldsymbol{c}_{R,s}^{\nu_{R,k}} \exp\left(\frac{\alpha_{a,k}\, U}{R_c\, T/n_{e,k}\, F}\right)\right] = \ln\left[k_{c,k}\, \boldsymbol{c}_{O,s}^{\nu_{O,k}} \exp\left(\frac{-\alpha_{c,k}\, U}{R_c\, T/n_{e,k}\, F}\right)\right]$$

$$\ln\left[k_{a,k}\, \boldsymbol{c}_{R,s}^{\nu_{R,k}}\right] + \frac{\alpha_{a,k}\, U}{R_c\, T/n_{e,k}\, F} = \ln\left[k_{c,k}\, \boldsymbol{c}_{O,s}^{\nu_{O,k}}\right] - \frac{\alpha_{c,k}\, U}{R_c\, T/n_{e,k}\, F}$$

$$\frac{(\alpha_{a,k} + \alpha_{c,k})}{\frac{R_c\, T}{n_{e,k} F}} U = \ln\left[\frac{k_{c,k}\, c_{O,s}^{\nu_{O,k}}}{k_{a,k}\, c_{R,s}^{\nu_{R,k}}}\right] \qquad \text{(G-11)}$$

Eq. (G-11) can be re-arranged to be equivalent to the Nernstian potential only when $\alpha_{a,k} + \alpha_{c,k} = 1$

$$U = \underbrace{\frac{R_c\, T}{n_{e,k}\, F}\ln\left[\frac{k_{c,k}}{k_{a,k}}\right]}_{standard\ state\ potential} \quad + \quad \underbrace{\frac{R_c\, T}{n_{e,k}\, F}\ln\left(\frac{\boldsymbol{c}_{O,s}^{\nu_{O,k}}}{\boldsymbol{c}_{R,s}^{\nu_{R,k}}}\right)}_{Nernstian\ shift\ due\ to\ surface\ concentrations}$$

Inserting Eq. (G-11) into Eq. (G-10), we can define the exchange current density $j_{0,k}$:

$$\frac{j_{0,k}}{n_{e,k}\, F} = k_{a,k}\, \boldsymbol{c}_{R,s}^{\nu_{R,k}} \exp\left(\frac{\alpha_{a,k}\, U}{R_c\, T/n_{e,k}\, F}\right) = k_{a,k}\, c_{R,s}^{\nu_{R,k}} \exp\left(\frac{\alpha_{a,k}}{(\alpha_{a,k} + \alpha_{c,k})}\ln\left[\frac{k_{c,k}\, \boldsymbol{c}_{O,s}^{\nu_{O,k}}}{k_{a,k}\, \boldsymbol{c}_{R,s}^{\nu_{R,k}}}\right]\right)$$

$$= k_{a,k}^{\frac{\alpha_{c,k}}{(\alpha_{a,k}+\alpha_{c,k})}} \left(\boldsymbol{c}_{R,s}^{\nu_{R,k}}\right)^{\frac{\alpha_{c,k}}{(\alpha_{a,k}+\alpha_{c,k})}} \left(k_{c,k}\right)^{\frac{\alpha_{a,k}}{(\alpha_{a,k}+\alpha_{c,k})}} \left(\boldsymbol{c}_{O,s}^{\nu_{O,k}}\right)^{\frac{\alpha_{a,k}}{(\alpha_{a,k}+\alpha_{c,k})}}$$

$$j_{0,k} = n_{e,k}\, F\left(k_{a,k}\, c_{R,s}^{\nu_{R,k}}\right)^{\frac{\alpha_{c,k}}{(\alpha_{a,k}+\alpha_{c,k})}} \left(k_{c,k}\, c_{O,s}^{\nu_{O,k}}\right)^{\frac{\alpha_{a,k}}{(\alpha_{a,k}+\alpha_{c,k})}} \tag{G-12}$$

Now, if we expand the surface overpotential in Eq. (G-10), we can define the Butler-Volmer kinetics for a general equation:

$$j_{b,k} = n_{e,k}\, F\left[k_{a,k}\, \boldsymbol{c}_{R,s}^{\nu_{R,k}} \exp\left(\frac{\alpha_{a,k}\,(\eta_s + U)}{R_c\, T/n_{e,k}\, F}\right) - k_{c,k}\, \boldsymbol{c}_{O,s}^{\nu_{O}} \exp\left(\frac{-\alpha_{c,k}\,(\eta_s + U)}{R_c\, T/n_{e,k}\, F}\right)\right]$$

$$j_{b,k} = n_{e,k}\, F\left[k_{a,k}\, \boldsymbol{c}_{R,s}^{\nu_{R,k}} \exp\left(\frac{\alpha_{a,k}\, \eta_s}{R_c\, T/n_{e,k}\, F} + \frac{\alpha_{a,k}}{(\alpha_{a,k} + \alpha_{c,k})}\ln\left[\frac{k_{c,k}\, \boldsymbol{c}_{O,s}^{\nu_{O,k}}}{k_{a,k}\, \boldsymbol{c}_{R,s}^{\nu_{R,k}}}\right]\right)\right.$$

$$\left. - k_{c,k}\, \boldsymbol{c}_{O,s}^{\nu_{O,k}} \exp\left(\frac{-\alpha_{c,k}\, \eta_s}{R_c\, T/n_{e,k}\, F} - \frac{\alpha_{c,k}}{(\alpha_{a,k} + \alpha_{c,k})}\ln\left[\frac{k_{c,k}\, \boldsymbol{c}_{O,s}^{\nu_{O,k}}}{k_{a,k}\, \boldsymbol{c}_{R,s}^{\nu_{R,k}}}\right]\right)\right]$$

$$j_{b,k} = n_{e,k}\, F\left[k_{a,k}\, \boldsymbol{c}_{R,s}^{\nu_{R,k}} \left(\frac{k_{c,k}\, \boldsymbol{c}_{O,s}^{\nu_{O,k}}}{k_{a,k}\, \boldsymbol{c}_{R,s}^{\nu_{R,k}}}\right)^{\frac{\alpha_{a,k}}{(\alpha_{a,k}+\alpha_{c,k})}} \exp\left(\frac{\alpha_{a,k}\, \eta_s}{R_c\, T/n_{e,k}\, F}\right)\right.$$

$$\left. - k_{c,k}\, \boldsymbol{c}_{O,s}^{\nu_{O,k}} \left(\frac{k_{c,k}\, \boldsymbol{c}_{O,s}^{\nu_{O,k}}}{k_{a,k}\, \boldsymbol{c}_{R,s}^{\nu_{R,k}}}\right)^{-\frac{\alpha_{c,k}}{(\alpha_{a,k}+\alpha_{c,k})}} \exp\left(\frac{-\alpha_{c,k}\, \eta_s}{R_c\, T/n_{e,k}\, F}\right)\right]$$

$$
\begin{aligned}
j_{b,k} = n_{e,k}\, F \Bigg[&\left(k_{a,k}\, \boldsymbol{c}_{R,s}^{\nu_{R,k}}\right)^{\frac{\alpha_{c,k}}{(\alpha_{a,k}+\alpha_{c,k})}} \left(k_{c,k}\, \boldsymbol{c}_{O,s}^{\nu_{O,k}}\right)^{\frac{\alpha_{a,k}}{(\alpha_{a,k}+\alpha_{c,k})}} \exp\left(\frac{\alpha_{a,k}\, \eta_s}{R_c\, T/n_{e,k}\, F}\right) \\
&- \left(k_{c,k}\, \boldsymbol{c}_{O,s}^{\nu_{O,k}}\right)^{\frac{\alpha_{a,k}}{(\alpha_{a,k}+\alpha_{c,k})}} \left(k_{a,k}\, \boldsymbol{c}_{R,s}^{\nu_{R,k}}\right)^{\frac{\alpha_{c,k}}{(\alpha_{a,k}+\alpha_{c,k})}} \exp\left(\frac{-\alpha_{c,k}\, \eta_s}{R_c\, T/n_{e,k}\, F}\right)\Bigg]
\end{aligned}
$$

$$
j_{b,k} = j_{0,k} \left[\exp\left(\frac{\alpha_{a,k}\, \eta_s}{R_c\, T/n_{e,k}\, F}\right) - \exp\left(\frac{-\alpha_{c,k}\, \eta_s}{R_c\, T/n_{e,k}\, F}\right)\right] \tag{G-13}
$$

Which is the expected Butler-Volmer relation when we assume $\nu_{R,k} = \nu_{O,k} = 1$ and $\alpha_{a,k} + \alpha_{c,k} = 1$, such that $j_{0,k}$ simplifies to:

$$
\begin{aligned}
j_{0,k} &= n_{e,k}\, F\left(k_{a,k}\, \boldsymbol{c}_{R,s}^{\nu_{R,k}}\right)^{\frac{\alpha_{c,k}}{(\alpha_{a,k}+\alpha_{c,k})}} \left(k_{c,k}\, \boldsymbol{c}_{O,s}^{\nu_{O,k}}\right)^{\frac{\alpha_{a,k}}{(\alpha_{a,k}+\alpha_{c,k})}} \\
&= n_e\, F\, k_{a,k}^{\alpha_{c,k}}\, \boldsymbol{c}_{R,s}^{\alpha_{c,k}}\, k_{c,k}^{\alpha_{a,k}}\, \boldsymbol{c}_{O,s}^{\alpha_{a,k}}
\end{aligned} \tag{G-14}
$$

If we define $j_{b,k}$ with respect to a reference exchange current density $j_{0,\text{ref},k}$, defined at some reference concentration in the bulk, of $\boldsymbol{c}_{R,ref}$ and $\boldsymbol{c}_{O,ref}$, and we assume the presence of a selective coating on the surface of the electrode, then Eq. (G-13) becomes:

$$
\begin{aligned}
&j_{b,k} \\
&= j_{0,\text{ref},k} \left(\frac{\boldsymbol{c}_{R,s}}{\boldsymbol{c}_R^*}\right)^{\alpha_{c,k}} \left(\frac{\boldsymbol{c}_R^*}{\boldsymbol{c}_{R,\text{bulk}}}\right)^{\alpha_{c,k}} \left(\frac{\boldsymbol{c}_{R,\text{bulk}}}{\boldsymbol{c}_{R,\text{ref}}}\right)^{\alpha_{c,k}} \left(\frac{\boldsymbol{c}_{O,s}}{\boldsymbol{c}_O^*}\right)^{\alpha_{a,k}} \left(\frac{\boldsymbol{c}_O^*}{\boldsymbol{c}_{O,\text{bulk}}}\right)^{\alpha_{a,k}} \left(\frac{c_{O,\text{bulk}}}{c_{O,\text{ref}}}\right)^{\alpha_{a,k}} \\
&\qquad \left[\exp\left(\frac{\alpha_{a,k}\, \eta_s}{R_c\, T/n_{e,k}\, F}\right) - \exp\left(\frac{-\alpha_{c,k}\, \eta_s}{R_c\, T/n_{e,k}\, F}\right)\right]
\end{aligned} \tag{G-15}
$$

We know that at steady-state conditions (for the O species) we can apply (G-4) and (G-9) to get:

$$
\begin{aligned}
j_{b,k} = j_{0,\text{ref},k} &\left(1 - \frac{j_{b,k}}{j_{l,k,a}}\right)^{\alpha_{c,k}} (S_R)^{\alpha_{c,k}} \left(\frac{c_{R,\text{bulk}}}{c_{R,\text{ref}}}\right)^{\alpha_{c,k}} \\
&\left(1 - \frac{j_{b,k}}{j_{l,k,c}}\right)^{\alpha_{a,k}} (S_O)^{\alpha_{a,k}} \left(\frac{c_{O,\text{bulk}}}{c_{O,\text{ref}}}\right)^{\alpha_{a,k}} \left[\exp\left(\frac{\alpha_{a,k}\, \eta_s}{R_c\, T/n_{e,k}\, F}\right) - \exp\left(\frac{-\alpha_{c,k}\, \eta_s}{R_c\, T/n_{e,k}\, F}\right)\right]
\end{aligned} \tag{G-16}
$$

We assumed that the activity of all species was 1, such that $a_R = \frac{c_{R,\text{bulk}}}{c_{R,\text{ref}}} = a_O = \frac{c_{O,\text{bulk}}}{c_{O,\text{ref}}} = 1$.

G.3 Calculating upper and lower bounds for the mass-transport overpotentials

The mass-transport overpotential bounds occur when the current density tends towards the limiting current density. By definition, we know:

$$\eta_{b,k,\mathrm{mt}} = \frac{R_c\, T}{n_{e,k}\, F} \log\left(\frac{\left(\frac{\boldsymbol{c}_{\mathrm{O},s}}{\boldsymbol{c}_{\mathrm{O,ref}}}\right)^{\nu_{\mathrm{O},k}}}{\left(\frac{\boldsymbol{c}_{\mathrm{R},s}}{\boldsymbol{c}_{\mathrm{R,ref}}}\right)^{\nu_{R,k}}} \right) = \frac{R_c\, T}{n_{e,k}\, F} \log\left(\frac{\left(\frac{\boldsymbol{c}_{\mathrm{O},s}}{\boldsymbol{c}_{\mathrm{O}}^*} \frac{\boldsymbol{c}_{\mathrm{O}}^*}{\boldsymbol{c}_{\mathrm{O,bulk}}} \frac{\boldsymbol{c}_{\mathrm{O,bulk}}}{\boldsymbol{c}_{\mathrm{O,ref}}}\right)^{\nu_{\mathrm{O},k}}}{\left(\frac{\boldsymbol{c}_{\mathrm{R},s}}{\boldsymbol{c}_{\mathrm{R}}^*} \frac{\boldsymbol{c}_{\mathrm{R}}^*}{\boldsymbol{c}_{\mathrm{R}}} \frac{\boldsymbol{c}_{\mathrm{R,bulk}}}{\boldsymbol{c}_{\mathrm{R,ref}}}\right)^{\nu_{R,k}}} \right)$$

$$\eta_{b,k,\mathrm{mt}} = \frac{R_c\, T}{n_{e,k}\, F} \log\left(\frac{\left(\left(1 - \frac{j_{b,k}}{j_{l,k,c}}\right) S_O \left(\frac{c_{\mathrm{O,bulk}}}{c_{\mathrm{O,ref}}}\right)\right)^{\nu_{\mathrm{O},k}}}{\left(\left(1 - \frac{j_{b,k}}{j_{l,k,a}}\right) S_R \left(\frac{c_{\mathrm{R,bulk}}}{c_{\mathrm{R,ref}}}\right)\right)^{\nu_{R,k}}} \right)$$

We assumed that the activity of all species was 1, such that $a_R = \frac{c_{R,\mathrm{bulk}}}{c_{R,\mathrm{ref}}} = a_O = \frac{c_{O,\mathrm{bulk}}}{c_{O,\mathrm{ref}}} = 1$.

$$\eta_{b,k,\mathrm{mt}} = \frac{R_c\, T}{n_{e,k} F} \log\left(\frac{\left(S_O \left(1 - \frac{j_{b,k}}{j_{l,k,c}}\right)\right)^{\nu_{\mathrm{O},k}}}{\left(S_R \left(1 - \frac{j_{b,k}}{j_{l,k,a}}\right)\right)^{\nu_{R,k}}} \right) \tag{G-17}$$

Let S_O = S_R = 1 and $j_{b,k} = j_{l,k,a}(1-\epsilon)$, such that Eq. (G-17) becomes:

$$\eta_{b,k,\mathrm{mt}} = \frac{R_c\, T}{n_{e,k}\, F} \log\left(\frac{\left(1 - \frac{j_{b,k}}{j_{l,k,c}}\right)^{\nu_{\mathrm{O},k}}}{\left(1 - \frac{j_{b,k}}{j_{l,k,a}}\right)^{\nu_{R,k}}} \right) = \frac{R_c\, T}{n_{e,k}\, F} \log\left(\frac{\left(1 - \frac{j_{l,k,a}(1-\epsilon)}{j_{l,k,c}}\right)^{\nu_{\mathrm{O},k}}}{\left(1 - \frac{j_{l,k,a}(1-\epsilon)}{j_{l,k,a}}\right)^{\nu_{R,k}}} \right)$$

$$\begin{aligned} \eta_{b,k,\mathrm{mt}} = {} & \frac{R_c\, T}{n_{e,k}\, F} \log\left(\left(\frac{j_{l,k,c} - j_{l,k,a}(1-\epsilon)}{j_{l,k,c}} \right)^{\nu_{\mathrm{O},k}} \right) \\ & - \frac{R_c\, T}{n_{e,k}\, F} \log\left(\left(\frac{j_{l,k,a} - j_{l,k,a}(1-\epsilon)}{j_{l,k,a}} \right)^{\nu_{R,k}} \right) \end{aligned} \tag{G-18}$$

When ϵ << 1:

$$\eta_{b,k,\mathrm{mt}} = \frac{R_c\, T}{n_{e,k}\, F} \log\left(\left(\frac{j_{l,k,c} - j_{l,k,a}}{j_{l,k,c}} \right)^{\nu_{\mathrm{O},k}} \right) - \frac{R_c\, T}{n_{e,k}\, F} \log\left(\left(\frac{j_{l,k,a}\, \epsilon}{j_{l,k,a}} \right)^{\nu_{R,k}} \right)$$

$$= \frac{R_c\,T}{n_{e,k}\,F}\left[\nu_{O,k}\log\left(\left(\frac{j_{l,k,c}-j_{l,k,a}}{j_{l,k,c}}\right)\right)-\nu_{R,k}\log\left(\left(\frac{j_{l,k,a}\,\epsilon}{j_{l,k,a}}\right)\right)\right]$$

$$= \frac{R_c\,T}{n_{e,k}\,F}\left[\nu_{O,k}\log\left(\left(\frac{j_{l,k,c}-j_{l,k,a}}{j_{l,k,c}}\right)\right)-\nu_{R,k}\log(\epsilon)\right]$$

Let $z = \log(\epsilon)$ such that we can rewrite the expression as:

$$\eta_{b,k,\mathrm{mt}} = \frac{R_c\,T}{n_{e,k}F}\left[\nu_{O,k}\log\left(\frac{j_{l,k,c}-j_{l,k,a}}{j_{l,k,c}}\right)-\nu_{R,k}\,z\right] \tag{G-19}$$

We obtain a similar expression when $j_{b,k} = j_{l,k,c}(1-\epsilon)$.

This expression allows for $j_{b,k}$ much closer to the limiting current density values without incurring computational difficulties. We can establish the extreme bounds (upper and lower) of the mass-transport overpotential $\eta_{b,k,\mathrm{mt}}$ by setting z = -100.

Bibliography

1. Valin, H. *et al.* The future of food demand: Understanding differences in global economic models. *Agric. Econ. (United Kingdom)* **45**, 51–67 (2014).
2. United Nations Department of Economic and Social Affairs - Population Division. *World Population Prospects 2022: Summary of Results*. (2022).
3. Van Vuuren, D. P., Bouwman, A. F. & Beusen, A. H. W. Phosphorus demand for the 1970-2100 period: A scenario analysis of resource depletion. *Glob. Environ. Chang.* **20**, 428–439 (2010).
4. Albornoz, F. Crop responses to nitrogen overfertilization: A review. *Scientia Horticulturae* vol. 205 79–83 at https://doi.org/10.1016/j.scienta.2016.04.026 (2016).
5. Smith, P. *et al.* Agriculture, Forestry and Other Land Use (AFOLU). in *Climate Change 2014: Synthesis Report. Contribution of Working Groups I, II and III to the Fifth Assessment Report of the Intergovernmental Panel on Climate Change* (eds. Team, C. W., Pachauri, R. K. & Meyer, L. A.) (IPCC, 2014).
6. Alexandratos, N. & Bruinsma, J. *World Agriculture towards 2030/2050: the 2012 revision*. *WORLD AGRICULTURE* www.fao.org/economic/esa (2012).
7. Kyriakou, V., Garagounis, I., Vourros, A., Vasileiou, E. & Stoukides, M. An Electrochemical Haber-Bosch Process. *Joule* **4**, 142–158 (2020).
8. United States Department of Energy - Office of Energy Efficiency & Renewable Energy. *H2@Scale: Enabling affordable, reliable, clean, and secure energy across sectors*. https://www.energy.gov/eere/fuelcells/h2-scale.
9. United States Department of Energy - Office of Fossil Energy and Carbon Management. *Hydrogen Strategy: Enabling A Low-Carbon Economy*. (2020).
10. Sawyer, C. N., McCarty, P. L. & Parkin, G. F. Biochemical Oxygen Demand. in *Chemistry for environmental engineering and science* 604–624 (2003).
11. Narayanan, C. M. & Narayan, V. Biological wastewater treatment and bioreactor design: A review. *Sustainable Environment Research* vol. 1 at https://doi.org/10.1186/s42834-019-0036-1 (2019).
12. Ajeej, A., Thanikal, J. V., Narayanan, C. M. & Kumar, R. S. An overview of bio augmentation of methane by anaerobic co-digestion of municipal sludge along with microalgae and waste paper. *Renewable and Sustainable Energy Reviews* vol. 50 270–276 at https://doi.org/10.1016/j.rser.2015.04.121 (2015).
13. Ye, Y. *et al.* Nutrient recovery from wastewater: From technology to economy. *Bioresource Technology Reports* vol. 11 at https://doi.org/10.1016/j.biteb.2020.100425 (2020).
14. United States Environmental Protection Agency. *2018 Edition of the Drinking Water Standards and Health Advisories Tables*. (2018).
15. United States Environmental Protection Agency. *Technical Development Document for the Effluent Limitations Guidelines and Standards for the Oil and Gas Extraction Point Source Category*. vol. EPA-820-R- (2016).
16. United States Environmental Protection Agency. *Development document for final effluent limitations guidelines and standards for the iron and steel manufacturing point source category*. (2002).
17. United States Environmental Protection Agency. Industrial Wastewater Treatment Technologies Database. https://watersgeo.epa.gov/iwtt/guided-search.
18. Genders, J. D., Hartsough, D. & Hobbs, D. T. Electrochemical reduction of nitrates and

nitrites in alkaline nuclear waste solutions. *J. Appl. Electrochem.* **26**, 1–9 (1996).
19. Hasebe, Y. *et al.* High-rate nitrification of electronic industry wastewater by using nitrifying granules. *Water Sci. Technol.* **76**, 3171–3180 (2017).
20. Garcia-Rodriguez, O. *et al.* Mineralization of electronic wastewater by electro-Fenton with an enhanced graphene-based gas diffusion cathode. *Electrochim. Acta* **276**, 12–20 (2018).
21. Mousset, E., Wang, Z., Olvera-Vargas, H. & Lefebvre, O. Advanced electrocatalytic pre-treatment to improve the biodegradability of real wastewater from the electronics industry — A detailed investigation study. *J. Hazard. Mater.* **360**, 552–559 (2018).
22. Moreno, C., Farahbakhshazad, N. & Morrison, G. M. Ammonia removal from oil refinery effluent in vertical upflow macrophyte column systems. *Water. Air. Soil Pollut.* **135**, 237–247 (2002).
23. Ghasemi, Z., Younesi, H. & Zinatizadeh, A. A. Preparation, characterization and photocatalytic application of TiO2/Fe-ZSM-5 nanocomposite for the treatment of petroleum refinery wastewater: Optimization of process parameters by response surface methodology. *Chemosphere* **159**, 552–564 (2016).
24. Bockris, J. O. & Kim, J. Electrochemical Reductions of Hg(II), Ruthenium-Nitrosyl Complex, Chromate, and Nitrate in a Strong Alkaline Solution. *J. Electrochem. Soc.* **143**, 3801–3808 (1996).
25. Yang, T., Doudrick, K. & Westerhoff, P. Photocatalytic reduction of nitrate using titanium dioxide for regeneration of ion exchange brine. *Water Res.* **47**, 1299–1307 (2013).
26. Prasad, S., Weidner, J. W. & Farell, A. E. A Boundary-Layer Model of A Parallel-Plate Electrochemical Reactor Model for the Destruction of Nitrate and Nitrite in Alkaline Waste Solutions. *J. Electrochem. Soc.* **142**, 1152–1161 (1995).
27. Shivaraman, N. *et al.* A two-stage biological treatment system for ammonium-nitrate-laden wastewater. *World J. Microbiol. Biotechnol.* **17**, 447–453 (2001).
28. Maine, M. A. *et al.* Hybrid constructed wetlands for the treatment of wastewater from a fertilizer manufacturing plant: Microcosms and field scale experiments. *Sci. Total Environ.* **650**, 297–302 (2019).
29. Jianping, W., Xiaoqiang, J., Lei, P., Changlin, W. & Guozhu, M. Nitrifying treatment of wastewater from fertilizer production in a multiple airlift loop bioreactor. *Biochem. Eng. J.* **25**, 33–37 (2005).
30. National Research Council. Municipal Wastewater, Sewage Sludge, and Agriculture. in *Use of Reclaimed Water and Sludge in Food Crop Production* 17–45 (The National Academies Press, 1996).
31. Jianping, W., Wei, P. L. H., Liping, D. & Guozhu, M. The denitrification of nitrate contained wastewater in a gas-liquid-solid three-phase flow airlift loop bioreactor. *Biochem. Eng. J.* **15**, 153–157 (2003).
32. Akyol, A., Can, O. T., Demirbas, E. & Kobya, M. A comparative study of electrocoagulation and electro-Fenton for treatment of wastewater from liquid organic fertilizer plant. *Sep. Purif. Technol.* **112**, 11–19 (2013).
33. Gabaldon, C. *et al.* Biological nitrate removal from wastewater of a metal-finishing industry. *J. Hazard. Mater.* **148**, 485–490 (2007).
34. Huo, X., Vanneste, J., Cath, T. Y. & Strathmann, T. J. A hybrid catalytic hydrogenation/membrane distillation process for nitrogen resource recovery from nitrate-contaminated waste ion exchange brine. *Water Res.* **175**, 115688 1–12 (2020).

35. Liu, J., Choe, J. K., Sasnow, Z., Werth, C. J. & Strathmann, T. J. Application of a Re-Pd bimetallic catalyst for treatment of perchlorate in waste ion-exchange regenerant brine. *Water Res.* **47**, 91–101 (2013).
36. Van Ginkel, S. W., Tang, Y. & Rittmann, B. E. Impact of precipitation on the treatment of real ion-exchange brine using the H2-based membrane biofilm reactor. *Water Sci. Technol.* **63**, 1453–1458 (2011).
37. Nichols, K. M., Miles-Richardson, S. R., Snyder, E. M. & Giesy, J. P. Effects of exposure to municipal wastewater in situ on the reproductive physiology of the fathead minnow (Pimephales promelas). *Environ. Toxicol. Chem.* **18**, 2001–2012 (1999).
38. Odjadjare, E. E. O. & Okoh, A. I. Physicochemical quality of an urban municipal wastewater effluent and its impact on the receiving environment. *Environ. Monit. Assess.* **170**, 383–394 (2010).
39. Katz, B. G., Griffin, D. W. & Davis, J. H. Groundwater quality impacts from the land application of treated municipal wastewater in a large karstic spring basin: Chemical and microbiological indicators. *Sci. Total Environ.* **407**, 2872–2886 (2009).
40. Abdel Wahaab, R. & Alseroury, F. A. Wastewater treatment: a case study of electronics manufacturing industry. *Int. J. Environ. Sci. Technol.* **16**, 47–58 (2019).
41. Gruber, N. & Galloway, J. N. An Earth-system perspective of the global nitrogen cycle. *Nature* **451**, 293–296 (2008).
42. Terblanche, A. Health hazards on nitrates in drinking water. *Water SA* **17**, 77–82 (1991).
43. Heisler, J. *et al.* Eutrophication and harmful algal blooms: A scientific consensus. *Harmful Algae* **8**, 3–13 (2008).
44. United States Environmental Protection Agency - Office of Water. *Wastewater Technology Fact Sheet - Denitrification Filters*. (2007).
45. Kuntke, P. *et al.* (Bio)electrochemical ammonia recovery: progress and perspectives. *Appl. Microbiol. Biotechnol.* **102**, 3865–3878 (2018).
46. Barrera, L. & Bala Chandran, R. Harnessing Photoelectrochemistry for Wastewater Nitrate Treatment Coupled with Resource Recovery. *ACS Sustain. Chem. Eng.* **9**, 3688–3701 (2021).
47. Sri Shalini, S. & Joseph, K. Combined SHARON and ANAMMOX processes for ammoniacal nitrogen stabilisation in landfill bioreactors. *Bioresour. Technol.* **250**, 723–732 (2018).
48. Kim, Y. K. *et al.* The capacity of wastewater treatment plants drives bacterial community structure and its assembly. *Sci. Rep.* **9**, (2019).
49. Nancharaiah, Y. V., Venkata Mohan, S. & Lens, P. N. L. Recent advances in nutrient removal and recovery in biological and bioelectrochemical systems. *Bioresource Technology* vol. 215 173–185 at https://doi.org/10.1016/j.biortech.2016.03.129 (2016).
50. Lim, E. T., Jeong, G. T., Bhang, S. H., Park, S. H. & Park, D. H. Evaluation of pilot-scale modified A2O processes for the removal of nitrogen compounds from sewage. *Bioresour. Technol.* **100**, 6149–6154 (2009).
51. Wang, X., Xia, Y., Wen, X., Yang, Y. & Zhou, J. Microbial community functional structures in wastewater treatment plants as characterized by GeoChip. *PLoS One* **9**, (2014).
52. Dahab, M. F. Nitrate Treatment Methods: An Overview. in *Nitrate Contamination: Exposure, Consequence, and Control* (eds. Bogardi, I. & Kuzelka, R. D.) 351–369 (NATO ASI Series, 1991).

53. International Plant Nutrition Institute. *Nutrient Source Specifics - Ammonia*.
54. Afif, A. *et al.* Ammonia-fed fuel cells: A comprehensive review. *Renew. Sustain. Energy Rev.* **60**, 822–835 (2016).
55. Sander, R. Compilation of Henry's law constants (version 4.0) for water as solvent. *Atmos. Chem. Phys.* **15**, 4399–4981 (2015).
56. Parmon, V. N. N., Panov, G. I. I., Uriarte, A. & Noskov, A. S. S. Nitrous oxide in oxidation chemistry and catalysis: Application and production. *Catal. Today* **100**, 115–131 (2005).
57. Lide, D. R. Standard Thermodynamic Properties of Chemical Substances. in *CRC Handbook of Chemistry and Physics* (ed. David R. Lide) 5–22 (CRC Press, 2005).
58. Scherson, Y. D. *et al.* Nitrogen removal with energy recovery through N $_2$ O decomposition. *Energy Environ. Sci.* **6**, 241–248 (2013).
59. Garcia-Segura, S., Lanzarini-Lopes, M., Hristovski, K. & Westerho, P. Electrocatalytic reduction of nitrate : Fundamentals to full-scale water treatment applications. *Appl. Catal. B Environ.* **236**, 546–568 (2018).
60. Liu, J. X., Richards, D., Singh, N. & Goldsmith, B. R. Activity and Selectivity Trends in Electrocatalytic Nitrate Reduction on Transition Metals. *ACS Catal.* **9**, 7052–7064 (2019).
61. Min, B. *et al.* Powering the Remediation of the Nitrogen Cycle: Progress and Perspectives of Electrochemical Nitrate Reduction. *Ind. Eng. Chem. Res.* **60**, 14635–14650 (2021).
62. Theerthagiri, J. *et al.* Electrocatalytic conversion of nitrate waste into ammonia : a review. *Environ. Chem. Lett.* **20**, 2929–2949 (2022).
63. Zhang, X. *et al.* Recent advances in non-noble metal electrocatalysts for nitrate reduction. *Chem. Eng. J.* **403**, 126269 (2021).
64. Lewis, N. S. & Nocera, D. G. *Powering the planet: Chemical challenges in solar energy utilization*. www.pnas.orgcgidoi10.1073pnas.0603395103 (2006).
65. Lewis, N. S. Research opportunities to advance solar energy utilization. *Science* vol. 351 at https://doi.org/10.1126/science.aad1920 (2016).
66. Fabian, D. M. *et al.* Particle suspension reactors and materials for solar-driven water splitting. *Energy and Environmental Science* vol. 8 2825–2850 at https://doi.org/10.1039/c5ee01434d (2015).
67. Nishiyama, H. *et al.* Photocatalytic solar hydrogen production from water on a 100-m2 scale. *Nature* **598**, 304–307 (2021).
68. Takata, T. *et al.* Photocatalytic water splitting with a quantum efficiency of almost unity. *Nature* **581**, 411–414 (2020).
69. Bala Chandran, R., Breen, S., Shao, Y., Ardo, S. & Weber, A. Z. Z. Evaluating particle-suspension reactor designs for Z-scheme solar water splitting via transport and kinetic modeling. *Energy Environ. Sci.* **11**, 0–59 (2018).
70. Chen, S., Takata, T. & Domen, K. Particulate photocatalysts for overall water splitting. *Nat. Rev. Mater.* **2**, (2017).
71. Kudo, A. & Miseki, Y. Heterogeneous photocatalyst materials for water splitting. *Chem. Soc. Rev.* **38**, 253–278 (2009).
72. Wang, Z., Huang, X. & Wang, X. Recent progresses in the design of BiVO4-based photocatalysts for efficient solar water splitting. *Catal. Today* **335**, 31–38 (2019).
73. Xu, X. T., Pan, L., Zhang, X., Wang, L. & Zou, J. J. Rational Design and Construction of Cocatalysts for Semiconductor-Based Photo-Electrochemical Oxygen Evolution: A Comprehensive Review. *Adv. Sci.* **6**, (2019).

74. Pattanayak, P. *et al.* Recent progress in perovskite transition metal oxide-based photocatalyst and photoelectrode materials for solar-driven water splitting. *J. Environ. Chem. Eng.* **10**, (2022).
75. Keene, S., Bala Chandran, R. & Ardo, S. Calculations of theoretical efficiencies for electrochemically-mediated tandem solar water splitting as a function of bandgap energies and redox shuttle potential. *Energy Environ. Sci.* **12**, 261–272 (2019).
76. Winkler, M. T., Cox, C. R., Nocera, D. G. & Buonassisi, T. Modeling integrated photovoltaic-electrochemical devices using steady-state equivalent circuits. *Proc. Natl. Acad. Sci.* **110**, E1076–E1082 (2013).
77. Fountaine, K. T., Lewerenz, H. J. & Atwater, H. A. Efficiency limits for photoelectrochemical water-splitting. *Nat. Commun.* **7**, 1–9 (2016).
78. Shaner, M. R., Fountaine, K. T. & Lewerenz, H. J. Current-voltage characteristics of coupled photodiode-electrocatalyst devices. *Appl. Phys. Lett.* **103**, 143905 1–4 (2013).
79. Kehrein, P. *et al.* A critical review of resource recovery from municipal wastewater treatment plants-market supply potentials, technologies and bottlenecks. *Environ. Sci. Water Res. Technol.* **6**, 877–910 (2020).
80. van der Hoek, J. P., Duijff, R. & Reinstra, O. Nitrogen recovery from wastewater: Possibilities, competition with other resources, and adaptation pathways. *Sustain.* **10**, 4605 (2018).
81. Renfrew, D. *et al.* Where is the greatest potential for resource recovery in wastewater treatment plants? *Water Res.* **220**, 118673 (2022).
82. van Langevelde, P. H., Katsounaros, I. & Koper, M. T. M. Electrocatalytic Nitrate Reduction for Sustainable Ammonia Production. *Joule* **5**, 290–294 (2021).
83. Duca, M. & Koper, M. T. M. Powering denitrification: the perspectives of electrocatalytic nitrate reduction. *Energy Environ. Sci.* **5**, 9726 (2012).
84. Flores, K. *et al.* Outlining Key Perspectives for the Advancement of Electrocatalytic Remediation of Nitrate from Polluted Waters. *ACS ES&T Eng.* **2**, 746–768 (2022).
85. Reyter, D., Bélanger, D. & Roué, L. Study of the electroreduction of nitrate on copper in alkaline solution. *Electrochim. Acta* **53**, 5977–5984 (2008).
86. McEnaney, J. M. *et al.* Electrolyte engineering for efficient electrochemical nitrate reduction to ammonia on a titanium electrode. *ACS Sustain. Chem. Eng.* **8**, 2672–2681 (2020).
87. Pérez-Gallent, E., Figueiredo, M. C., Katsounaros, I. & Koper, M. T. M. Electrocatalytic reduction of Nitrate on Copper single crystals in acidic and alkaline solutions. *Electrochim. Acta* **227**, 77–84 (2017).
88. Butcher, D. P. & Gewirth, A. A. Nitrate reduction pathways on Cu single crystal surfaces: Effect of oxide and Cl−. *Nano Energy* **29**, 457–465 (2016).
89. Zeng, Y., Priest, C., Wang, G. & Wu, G. Restoring the Nitrogen Cycle by Electrochemical Reduction of Nitrate: Progress and Prospects. *Small Methods* **4**, 1–28 (2020).
90. Lim, J. *et al.* Structure Sensitivity of Pd Facets for Enhanced Electrochemical Nitrate Reduction to Ammonia. *ACS Catal.* **11**, 7568–7577 (2021).
91. Chen, G. F. *et al.* Electrochemical reduction of nitrate to ammonia via direct eight-electron transfer using a copper–molecular solid catalyst. *Nat. Energy* **5**, 605–613 (2020).
92. Inc, S. Daily Metal Price. https://www.dailymetalprice.com.
93. Dima, G. E., Vooys, A. C. A. De & Koper, M. T. M. Electrocatalytic reduction of nitrate at low concentration on coinage and transition-metal electrodes in acid solutions. *J.*

Electroanal. Chem. **554–555**, 15–23 (2003).

94. Reyter, D., Odziemkowski, M., Bélanger, D. & Roué, L. Electrochemically Activated Copper Electrodes. *J. Electrochem. Soc.* **154**, K36–K44 (2007).
95. Reyter, D. *et al.* Nitrate removal by a paired electrolysis on copper and Ti/IrO2 coupled electrodes - Influence of the anode/cathode surface area ratio. *Water Res.* **44**, 1918–1926 (2010).
96. Boczkaj, G. & Fernandes, A. Wastewater treatment by means of advanced oxidation processes at basic pH conditions: A review. *Chem. Eng. J.* **320**, 608–633 (2017).
97. Hu, T., Wang, C., Wang, M., Li, C. M. & Guo, C. Theoretical Insights into Superior Nitrate Reduction to Ammonia Performance of Copper Catalysts. *ACS Catal.* **11**, 14417–14427 (2021).
98. Raistrick, I. D. Application of Impedance Spectroscopy to Materials Science. *Annu. Rev. Mater. Sci.* (1986).
99. Pajkossy, T. & Jurczakowski, R. Electrochemical impedance spectroscopy in interfacial studies. *Curr. Opin. Electrochem.* **1**, 53–58 (2017).
100. Kashyap, D. *et al.* Application of electrochemical impedance spectroscopy in bio-fuel cell characterization: A review. *Int. J. Hydrogen Energy* **39**, 20159–20170 (2014).
101. Goyal, A. & Koper, M. T. M. The Interrelated Effect of Cations and Electrolyte pH on the Hydrogen Evolution Reaction on Gold Electrodes in Alkaline Media. *Angew. Chemie - Int. Ed.* **60**, 13452–13462 (2021).
102. Irvine, J. T. S., Sinclair, D. C. & West, A. R. Electroceramics: Characterization by Impedance Spectroscopy. *Adv. Mater.* **2**, 132–138 (1990).
103. Osornio-Villa, A. *et al.* Impedance spectroscopy of the low potential range electro-oxidation of glucose on a polycrystalline gold electrode undergoing surface reconstruction. *J. Electroanal. Chem.* **886**, 115130 (2021).
104. Kalinin, S. V., Suchomel, M. R., Davies, P. K. & Bonnell, D. A. Potential and Impedance Imaging of Polycrystalline BiFeO3 Ceramics. *J. Am. Ceram. Soc.* **85**, 3011–17 (2002).
105. Huo, X., Vanneste, J., Cath, T. Y. & Strathmann, T. J. A hybrid catalytic hydrogenation / membrane distillation process for nitrogen resource recovery from nitrate-contaminated waste ion exchange brine. *Water Res.* **175**, 115688 (2020).
106. Pourbaix, M. Copper. *Atlas of Electrochemical Equilibria in Aqueous Solutions* 384–392 (1966).
107. Reyter, D., Bélanger, D. & Roué, L. Study of the electroreduction of nitrate on copper in alkaline solution. *Electrochim. Acta* **53**, 5977–5984 (2008).
108. Guidelli, R. *et al.* Defining the transfer coefficient in electrochemistry: An assessment (IUPAC Technical Report). *Pure Appl. Chem.* **86**, 245–258 (2014).
109. Wang, S. *et al.* Electrochemical impedance spectroscopy. *Nat. Rev. Methods Prim.* **1**, 1–21 (2021).
110. Brug, G. J., van den Eeden, A. L. G., Sluyters-Rehbach, M. & Sluyters, J. H. The analysis of electrode impedances complicated by the presence of a constant phase element. *J. Electroanal. Chem.* **176**, 275–295 (1984).
111. McCrory, C. C. L., Jung, S., Peters, J. C. & Jaramillo, T. F. Benchmarking Heterogeneous Electrocatalysts for the Oxygen Evolution Reaction. *J. Am. Chem. Soc.* **135**, 16977–16987 (2013).
112. Bard, A. J. & Faulkner, L. R. Techniques Based on Concepts of Impedance. in *Electrochemical Methods: Fundamentals and Applications* 368–416 (John Wiley & Sons,

Inc., 2001).

113. Hirschorn, B. *et al.* Determination of effective capacitance and film thickness from constant-phase-element parameters. *Electrochim. Acta* **55**, 6218–6227 (2010).
114. Gamry. Faraday Cage: What Is It? How Does It Work? 1–3 (2018).
115. Giner-Sanz, J. J., Leverick, G. M., Pérez-Herranz, V. & Shao-Horn, Y. Salicylate Method for Ammonia Quantification in Nitrogen Electroreduction Experiments : The Correction of Iron III Interference. *J. Electrochem. Soc.* **167**, 134519 (2020).
116. Li, D., Xu, X., Li, Z., Wang, T. & Wang, C. Detection methods of ammonia nitrogen in water : A review. *Trends Anal. Chem.* **127**, 115890 (2020).
117. Zhao, Y. *et al.* Ammonia Detection Methods in Photocatalytic and Electrocatalytic Experiments : How to Improve the Reliability of NH3 Production Rates ? *Adv. Sci.* 1802109 (2019).
118. Tiwari, A. *et al.* Fingerprint Voltammograms of Copper Single Crystals under Alkaline Conditions: A Fundamental Mechanistic Analysis. *J. Phys. Chem. Lett.* **11**, 1450–1455 (2020).
119. Schouten, K. J. P., Gallent, E. P. & Koper, M. T. M. The electrochemical characterization of copper single-crystal electrodes in alkaline media. *J. Electroanal. Chem.* **699**, 6–9 (2013).
120. Gao, G. & Wang, L. W. A potential and pH inclusive microkinetic model for hydrogen reactions on Pt surface. *Chem Catal.* **1**, 1331–1345 (2021).
121. Haghighat, S. & Dawlaty, J. M. pH Dependence of the Electron-Transfer Coefficient: Comparing a Model to Experiment for Hydrogen Evolution Reaction. *J. Phys. Chem. C* **120**, 28489–28496 (2016).
122. Koga, O., Watanabe, Y., Tanizaki, M. & Hori, Y. Specific adsorption of anions on a copper (100) single crystal electrode studied by charge displacement by CO adsorption and infrared spectroscopy. *Electrochim. Acta* **46**, 3083–3090 (2001).
123. Mattarozzi, L. *et al.* Electrochemical reduction of nitrate and nitrite in alkaline media at CuNi alloy electrodes. *Electrochim. Acta* **89**, 488–496 (2013).
124. Dutta, B., Kar, E., Bose, N. & Mukherjee, S. Significant enhancement of the electroactive β-phase of PVDF by incorporating hydrothermally synthesized copper oxide nanoparticles. *RSC Adv.* **5**, 105422–405434 (2015).
125. Maurer, M., Schwegler, P. & Larsen, T. A. Nutrients in urine: Energetic aspects of removal and recovery. *Water Sci. Technol.* **48**, 37–46 (2003).
126. Fertilizers Europe. *Best available techniques for pollution prevention and control in the European fertilizer industry: Production of Ammonia*. *Water Science and Technology* (2000).
127. International Fertilizer Industry Association. *Energy Efficiency and CO2 Emissions in Ammonia Production: 2008-2009 Summary Report*. (2009).
128. Rockström, J. *et al.* A safe operating space for humanity. *Nature* vol. 461 472–475 at https://doi.org/10.1038/461472a (2009).
129. Gao, H., Scherson, Y. D. & Wells, G. F. Towards energy neutral wastewater treatment: methodology and state of the art. doi:10.1039/c4em00069b.
130. Falkowski, P. *et al.* The Global Carbon Cycle : A Test of Our Knowledge of Earth as a System. *Science (80-.).* **290**, 291–297 (2000).
131. Kapoor, A. & Viraraghavan, T. Nitrate Removal From Drinking Water—Review. *J. Environ. Eng.* **123**, 371–380 (1997).

132. Scherson, Y. D. *et al.* Nitrogen removal with energy recovery through N2O decomposition. *Energy Environ. Sci.* **6**, 241–248 (2013).
133. Schreiber, F., Wunderlin, P., Udert, K. M. & Wells, G. F. Nitric oxide and nitrous oxide turnover in natural and engineered microbial communities: Biological pathways, chemical reactions, and novel technologies. *Front. Microbiol.* **3**, 1–24 (2012).
134. Puyol, D. *et al.* Resource recovery from wastewater by biological technologies: Opportunities, challenges, and prospects. *Front. Microbiol.* **7**, 1–23 (2017).
135. Pabi, S., Amarnath, A., Goldstein, R. & Reekie, L. *Electricity Use and Management in the Municipal Water Supply and Wastewater Industries*. *Electric Power Research Institute* http://www.waterrf.org/PublicReportLibrary/4454.pdf (2013).
136. United States Environmental Protection Agency. Case Studies on Implementing Low-Cost Modifications to Improve Nutrient Reduction at Wastewater Treatment Plants. *United States Environ. Prot. Agency, Off. Wetl. Ocean. Watersheds, Off. Sci. Technol. Off. Wastewater Manag.* 22 (2015).
137. United States Environmental Protection Agency. Energy Efficiency in Water and Wastewater Facilities. 49 (2014).
138. Kuntke, P. *et al.* (Bio)electrochemical ammonia recovery: progress and perspectives. *Appl. Microbiol. Biotechnol.* **102**, 3865–3878 (2018).
139. Rosca, V., Duca, M., de Groot, M. T. & Koper, M. T. M. Nitrogen Cycle Electrocatalysis. *Chem. Rev.* **109**, 2209–2244 (2009).
140. Duan, H. *et al.* Recovery of Nitrous Oxide from Wastewater Treatment: Current Status and Perspectives. *ACS ES&T Water* (2020) doi:10.1021/acsestwater.0c00140.
141. Lehman, S. G., Badruzzaman, M., Adham, S., Roberts, D. J. & Clifford, D. A. Perchlorate and nitrate treatment by ion exchange integrated with biological brine treatment. *Water Res.* **42**, 969–976 (2008).
142. Clifford, D., Lin, C.-C., Horng, L.-L. & Boegel, J. *Nitrate Removal from Drinking Water in Glendale, Arizona*. (1987).
143. Kneifel, K., Lührs, G. & Wagner, H. Nitrate Removal by Electrodialysis for Brewing Water. *Desalination* **68**, 203–209 (1988).
144. Bohdziewicz, J., Bodzek, M. & Wąsik, E. The application of reverse osmosis and nanofiltration to the removal of nitrates from groundwater. *Desalination* **121**, 139–147 (1999).
145. Shaffer, D. L., Yip, N. Y., Gilron, J. & Elimelech, M. Seawater desalination for agriculture by integrated forward and reverse osmosis: Improved product water quality for potentially less energy. *J. Memb. Sci.* **415–416**, 1–8 (2012).
146. Samatya, S., Kabay, N., Yüksel, Ü., Arda, M. & Yüksel, M. Removal of nitrate from aqueous solution by nitrate selective ion exchange resins. *React. Funct. Polym.* **66**, 1206–1214 (2006).
147. Winkler, M. T., Cox, C. R., Nocera, D. G. & Buonassisi, T. Modeling integrated photovoltaic – electrochemical devices using steady-state equivalent circuits. *Natl. Acad. Sci.* (2013) doi:10.1073/pnas.1301532110.
148. Wang, Q. *et al.* Scalable water splitting on particulate photocatalyst sheets with a solar-to-hydrogen energy conversion efficiency exceeding 1%. *Nat. Mater.* (2016) doi:10.1038/nmat4589.
149. Jung, S., McCrory, C. C. L., Ferrer, I. M., Peters, J. C. & Jaramillo, T. F. Benchmarking nanoparticulate metal oxide electrocatalysts for the alkaline water oxidation reaction. *J.*

Mater. Chem. A **4**, 3068–3076 (2016).

150. McCrory, C. C. L. *et al.* Benchmarking Hydrogen Evolving Reaction and Oxygen Evolving Reaction Electrocatalysts for Solar Water Splitting Devices. *J. Am. Chem. Soc.* **137**, 4347–4357 (2015).
151. Shockley, W. & Queisser, H. J. Detailed Balance Limit of Efficiency of p-n Junction Solar Cells. *J. Appl. Phys.* **32**, (1961).
152. Xiang, C. *et al.* Modeling, Simulation, and Implementation of Solar-Driven Water-Splitting Devices. *Angew. Chemie - Int. Ed.* **55**, 12974–12988 (2016).
153. Hu, S., Xiang, C., Haussener, S., Berger, A. D. & Lewis, N. S. An analysis of the optimal band gaps of light absorbers in integrated tandem photoelectrochemical water-splitting systems. *Energy Environ. Sci.* **6**, 2984–2993 (2013).
154. Tugaoen, H. O., Garcia-Segura, S., Hristovski, K. & Westerhoff, P. Challenges in photocatalytic reduction of nitrate as a water treatment technology. *Sci. Total Environ.* **599–600**, 1524–1551 (2017).
155. Wehbe, N. *et al.* Comparative study of photocatalytic and non-photocatalytic reduction of nitrates in water. *Appl. Catal. A Gen.* **368**, 1–8 (2009).
156. Marks, R., Yang, T., Westerhoff, P. & Doudrick, K. Comparative analysis of the photocatalytic reduction of drinking water oxoanions using titanium dioxide. *Water Res.* **104**, 11–19 (2016).
157. Loeb, S. K. *et al.* The Technology Horizon for Photocatalytic Water Treatment: Sunrise or Sunset? *Environ. Sci. Technol.* **53**, 2937–2947 (2019).
158. Kuang, P., Natsui, K. & Einaga, Y. Comparison of performance between boron-doped diamond and copper electrodes for selective nitrogen gas formation by the electrochemical reduction of nitrate. *Chemosphere* **210**, 524–530 (2018).
159. Cattarin, S. Electrochemical reduction of nitrogen oxyanions in 1 M sodium hydroxide solutions at silver, copper and CuInSe2 electrodes. *J. Appl. Electrochem.* **22**, 1077–1081 (1992).
160. Yang, J., Duca, M., Schouten, K. J. P. & Koper, M. T. M. Formation of volatile products during nitrate reduction on a Sn-modified Pt electrode in acid solution. *J. Electroanal. Chem.* **662**, 87–92 (2011).
161. Katsounaros, I., Ipsakis, D., Polatides, C. & Kyriacou, G. Efficient electrochemical reduction of nitrate to nitrogen on tin cathode at very high cathodic potentials. *Electrochim. Acta* **52**, 1329–1338 (2006).
162. Yang, J., Calle-Vallejo, F., Duca, M. & Koper, M. T. M. Electrocatalytic reduction of nitrate on a Pt electrode modified by p-block metal adatoms in acid solution. *ChemCatChem* **5**, 1773–1783 (2013).
163. Chen, T., Li, H., Ma, H. & Koper, M. T. M. Surface Modification of Pt (100) for Electrocatalytic Nitrate Reduction to Dinitrogen in Alkaline Solution. *Langmuir* **31**, 3277–3281 (2015).
164. Gootzen, J. F. E., Lefferts, L. & van Veen, J. A. R. Electrocatalytic nitrate reduction on palladium based catalysts activated with germanium. *Appl. Catal. A Gen.* **188**, 127–136 (1999).
165. Martínez, J., Ortiz, A. & Ortiz, I. State-of-the-art and perspectives of the catalytic and electrocatalytic reduction of aqueous nitrates. *Appl. Catal. B Environ.* **207**, 42–59 (2017).
166. Barrabés, N. & Sá, J. Catalytic nitrate removal from water, past, present and future perspectives. *Appl. Catal. B Environ.* **104**, 1–5 (2011).

167. Dortsiou, M., Katsounaros, I., Polatides, C. & Kyriacou, G. Electrochemical removal of nitrate from the spent regenerant solution of the ion exchange. *Desalination* **248**, 923–930 (2009).
168. Bouzek, K., Paidar, M., Sadiâlkova, A. & Bergmann, H. Electrochemical reduction of nitrate in weakly alkaline solutions. *J. Appl. Electrochem.* **31**, 1185–1193 (2001).
169. Lackner, S. *et al.* Full-scale partial nitritation/anammox experiences - An application survey. *Water Res.* **55**, 292–303 (2014).
170. Plieth, W. J. Nitrogen. in *Encyclopedia of Electrochemistry of the Elements, Vol. VIII* (ed. Bard, A. J.) 321–479 (Marcel Dekker, Inc., 1978).
171. Singh, N. & Goldsmith, B. R. Role of Electrocatalysis in the Remediation of Water Pollutants. *ACS Catal.* 3365–3371 (2020) doi:10.1021/acscatal.9b04167.
172. Zamfirescu, C. & Dincer, I. Using ammonia as a sustainable fuel. *J. Power Sources* **185**, 459–465 (2008).
173. Lan, R. & Tao, S. Ammonia as a Suitable Fuel for Fuel Cells. *Front. Energy Res.* **2**, 35 (2014).
174. Gao, H. *et al.* Complete Nutrient Removal Coupled to Nitrous Oxide Production as a Bioenergy Source by Denitrifying Polyphosphate-Accumulating Organisms. *Environ. Sci. Technol.* **51**, 4531–4540 (2017).
175. Desloover, J., Abate Woldeyohannis, A., Verstraete, W., Boon, N. & Rabaey, K. Electrochemical resource recovery from digestate to prevent ammonia toxicity during anaerobic digestion. *Environ. Sci. Technol.* **46**, 12209–12216 (2012).
176. Scherson, Y. D., Woo, S. G. & Criddle, C. S. Production of nitrous oxide from anaerobic digester centrate and its use as a co-oxidant of biogas to enhance energy recovery. *Environ. Sci. Technol.* **48**, 5612–5619 (2014).
177. Kosse, P., Lübken, M., Schmidt, T. C. & Wichern, M. Quantification of nitrous oxide in wastewater based on salt-induced stripping. *Sci. Total Environ.* **601–602**, 83–88 (2017).
178. Czepiel, P., Crill, P. & Harriss, R. Nitrous Oxide Emissions from Municipal Wastewater Treatment. *Environ. Sci. Technol.* **29**, 2352–2356 (1995).
179. Deng, J. *et al.* Nanowire Photoelectrochemistry. *Chem. Rev.* **119**, 9221–9259 (2019).
180. Bard, A. J. & Faulkner, L. R. Mass Transfer by Migration and Diffusion. in *Electrochemical Methods Fundamentals and Applications* 146–148 (John Wiley & Sons, Inc., 2001).
181. Noël, T., Cao, Y. & Laudadio, G. The Fundamentals behind the Use of Flow Reactors in Electrochemistry. *Acc. Chem. Res.* **52**, 2858–2869 (2019).
182. Reyter, D., Chamoulaud, G., Bélanger, D. & Roué, L. Electrocatalytic reduction of nitrate on copper electrodes prepared by high-energy ball milling. *J. Electroanal. Chem.* **596**, 13–24 (2006).
183. Chang, C. & Wen, T. Kinetics of Oxygen Reduction at IrO2-Coated Titanium Electrode in Alkaline Solution. *J. Electrochem. Soc.* **143**, 1485–1491 (1996).
184. Huynh, M., Ozel, T., Liu, C., Lau, E. C. & Nocera, D. G. Design of template-stabilized active and earth-abundant oxygen evolution catalysts in acid. *Chem. Sci.* **8**, 4779–4794 (2017).
185. Weng, L. C., Bell, A. T. & Weber, A. Z. Modeling gas-diffusion electrodes for CO2 reduction. *Phys. Chem. Chem. Phys.* **20**, 16973–16984 (2018).
186. Pentland, N., Bockris, J. O. & Sheldon, E. Hydrogen Evolution Reaction on Copper, Gold, Molybdenum, Palladium, Rhodium, and Iron. *J. Electrochem. Soc.* **104**, 182–194 (1957).

187. Sheng, W., Gasteiger, H. A. & Shao-Horn, Y. Hydrogen Oxidation and Evolution Reaction Kinetics on Platinum : Acid vs Alkaline Electrolytes. *J. Electrochem. Soc.* **157**, 1529–1536 (2010).
188. Macia, M. D., Campina, J. M., Herrero, E. & Feliu, J. M. On the kinetics of oxygen reduction on platinum stepped surfaces in acidic media. *J. Electroanal. Chem.* **564**, 141–150 (2004).
189. Dong, Q., Santhanagopalan, S. & White, R. E. Simulation of the Oxygen Reduction Reaction at an RDE in 0.5M H2SO4 Including an Adsorption Mechanism. *J. Electrochem. Soc.* **154**, A888–A899 (2007).
190. Kuzume, A., Herrero, E. & Feliu, J. M. Oxygen reduction on stepped platinum surfaces in acidic media. *J. Electroanal. Chem.* **599**, 333–343 (2007).
191. Geniès, L., Faure, R., Durand, R. & Genie, L. Electrochemical reduction of oxygen on platinum nanoparticles in alkaline media. *Electrochim. Acta* **44**, 1317–1327 (1998).
192. Sheng, W., Myint, M., Chen, J. G. & Yan, Y. Correlating the hydrogen evolution reaction activity in alkaline electrolytes with the hydrogen binding energy on monometallic surfaces. *Energy Environ. Sci.* **6**, 1509–1512 (2013).
193. MathWorks. Symbolic Math Toolbox ^{TM} User's Guide 2018a. 1714–1724 at (2018).
194. Hirakawa, H., Hashimoto, M., Shiraishi, Y. & Hirai, T. Photocatalytic Conversion of Nitrogen to Ammonia with Water on Surface Oxygen Vacancies of Titanium Dioxide. *J. Am. Chem. Soc.* **139**, 10929–10936 (2017).
195. Suryanto, B. H. R. *et al.* Challenges and prospects in the catalysis of electroreduction of nitrogen to ammonia. *Nat. Catal.* **2**, 290–296 (2019).
196. Shaham-Waldmann, N. & Paz, Y. Away from TiO2: A critical minireview on the developing of new photocatalysts for degradation of contaminants in water. *Mater. Sci. Semicond. Process.* **42**, 72–80 (2016).
197. Gurudayal *et al.* Si photocathode with Ag-supported dendritic Cu catalyst for CO2 reduction. *Energy Environ. Sci.* **12**, 1068–1077 (2019).
198. Levenspiel, O. Ideal Reactors for a Single Reaction. in *Chemical Reaction Engineering* 90–101 (1999).
199. Bard, A. J. Design of semiconductor photoelectrochemical systems for solar energy conversion. *J. Phys. Chem.* **86**, 172–177 (1982).
200. Tan, M. X. *et al.* Principles and Applications of Semiconductor Photoelectrochemistry. in *Progress in Inorganic Chemistry* (ed. Kenneth D. Karlin) vol. 41 21–144 (1994).
201. T. Spitler, M. *et al.* Practical challenges in the development of photoelectrochemical solar fuels production. *Sustain. Energy Fuels* **4**, 985–995 (2020).
202. Ardo, S. *et al.* Pathways to electrochemical solar-hydrogen technologies. *Energy Environ. Sci.* **11**, 2768–2783 (2018).
203. Segev, G. *et al.* The 2022 solar fuels roadmap. *J. Phys. D. Appl. Phys.* **55**, 323003 (2022).
204. Bard, A. J. & Fox, M. A. Artificial Photosynthesis: Solar Splitting of Water to Hydrogen and Oxygen. *Acc. Chem. Res.* **28**, 141–145 (1995).
205. Wang, Z., Li, C. & Domen, K. Recent developments in heterogeneous photocatalysts for solar-driven overall water splitting. *Chem. Soc. Rev.* **48**, 2109–2125 (2019).
206. Hisatomi, T. & Domen, K. Reaction systems for solar hydrogen production via water splitting with particulate semiconductor photocatalysts. *Nat. Catal. 2019 25* **2**, 387–399 (2019).
207. Goto, Y. *et al.* A Particulate Photocatalyst Water-Splitting Panel for Large-Scale Solar

Hydrogen Generation. *Joule* **2**, 509–520 (2018).
208. Iwase, A. *et al.* Water Splitting and CO $_2$ Reduction under Visible Light Irradiation Using Z-Scheme Systems Consisting of Metal Sulfides, CoOx-Loaded BiVO $_4$, and a Reduced Graphene Oxide Electron Mediator. *J. Am. Chem. Soc.* **138**, 10260–10264 (2016).
209. Li, Z. *et al.* Selective Photocatalytic Reduction of CO2 to Syngas Over Tunable Metal-Perovskite Interface. *ChemSusChem* **15**, (2022).
210. Alsabeh, P. G. *et al.* Iron-catalyzed photoreduction of carbon dioxide to synthesis gas. *Catal. Sci. Technol.* **6**, 3623–3630 (2016).
211. Chauhan, D. K., Sharma, N. & Kailasam, K. A critical review on emerging photocatalysts for syngas generation via CO2 reduction under aqueous media: a sustainable paradigm. *Materials Advances* vol. 3 5274–5298 at https://doi.org/10.1039/d2ma00334a (2022).
212. Fu, Z. *et al.* A stable covalent organic framework for photocatalytic carbon dioxide reduction. *Chem. Sci.* **11**, 543–550 (2020).
213. White, J. L. *et al.* Light-Driven Heterogeneous Reduction of Carbon Dioxide: Photocatalysts and Photoelectrodes. *Chemical Reviews* vol. 115 12888–12935 at https://doi.org/10.1021/acs.chemrev.5b00370 (2015).
214. Nguyen, V. N. & Blum, L. Syngas and synfuels from H2O and CO2: Current status. *Chemie-Ingenieur-Technik* vol. 87 354–375 at https://doi.org/10.1002/cite.201400090 (2015).
215. Tjandra, A. D. & Huang, J. Photocatalytic carbon dioxide reduction by photocatalyst innovation. *Chinese Chem. Lett.* **29**, 734–746 (2018).
216. Prabhu, P., Jose, V. & Lee, J. M. Heterostructured Catalysts for Electrocatalytic and Photocatalytic Carbon Dioxide Reduction. *Advanced Functional Materials* vol. 30 at https://doi.org/10.1002/adfm.201910768 (2020).
217. Zhang, W., Mohamed, A. R. & Ong, W. J. Z-Scheme Photocatalytic Systems for Carbon Dioxide Reduction: Where Are We Now? *Angewandte Chemie - International Edition* vol. 59 22894–22915 at https://doi.org/10.1002/anie.201914925 (2020).
218. Bellardita, M., Loddo, V., Parrino, F. & Palmisano, L. (Photo)electrocatalytic Versus Heterogeneous Photocatalytic Carbon Dioxide Reduction. *ChemPhotoChem* vol. 5 767–791 at https://doi.org/10.1002/cptc.202100030 (2021).
219. Adekoya, D., Tahir, M. & Amin, N. A. S. Recent trends in photocatalytic materials for reduction of carbon dioxide to methanol. *Renewable and Sustainable Energy Reviews* vol. 116 at https://doi.org/10.1016/j.rser.2019.109389 (2019).
220. Roy, S. C., Varghese, O. K., Paulose, M. & Grimes, C. A. Toward solar fuels: Photocatalytic conversion of carbon dioxide to hydrocarbons. *ACS Nano* vol. 4 1259–1278 at https://doi.org/10.1021/nn9015423 (2010).
221. Wang, N., Zhang, X., Wang, Y., Yu, W. & Chan, H. L. W. Microfluidic reactors for photocatalytic water purification. *Lab on a Chip* vol. 14 1074–1082 at https://doi.org/10.1039/c3lc51233a (2014).
222. Bahnemann, D. Photocatalytic water treatment: Solar energy applications. *Sol. Energy* **77**, 445–459 (2004).
223. Zhang, X., Wang, J., Dong, X. X. & Lv, Y. K. Functionalized metal-organic frameworks for photocatalytic degradation of organic pollutants in environment. *Chemosphere* vol. 242 at https://doi.org/10.1016/j.chemosphere.2019.125144 (2020).
224. Escobedo, S. & Lasa, H. de. Photocatalysis for air treatment processes: Current technologies and future applications for the removal of organic pollutants and viruses.

Catalysts vol. 10 at https://doi.org/10.3390/catal10090966 (2020).
225. Li, Q., Ouyang, Y., Li, H., Wang, L. & Zeng, J. Photocatalytic Conversion of Methane: Recent Advancements and Prospects. *Angewandte Chemie - International Edition* vol. 61 at https://doi.org/10.1002/anie.202108069 (2022).
226. Sher Shah, M. S. A. *et al.* Catalytic Oxidation of Methane to Oxygenated Products: Recent Advancements and Prospects for Electrocatalytic and Photocatalytic Conversion at Low Temperatures. *Advanced Science* vol. 7 at https://doi.org/10.1002/advs.202001946 (2020).
227. Hu, D., Ordomsky, V. V. & Khodakov, A. Y. Major routes in the photocatalytic methane conversion into chemicals and fuels under mild conditions. *Applied Catalysis B: Environmental* vol. 286 at https://doi.org/10.1016/j.apcatb.2021.119913 (2021).
228. Navarro-Jaén, S. *et al.* Highlights and challenges in the selective reduction of carbon dioxide to methanol. *Nat. Rev. Chem. 2021 58* **5**, 564–579 (2021).
229. Yuliati, L. & Yoshida, H. Photocatalytic conversion of methane. *Chem. Soc. Rev.* **37**, 1592 (2008).
230. Xie, J. *et al.* Highly selective oxidation of methane to methanol at ambient conditions by titanium dioxide-supported iron species. *Nat. Catal.* **1**, 889–896 (2018).
231. Li, X., Wang, C. & Tang, J. Methane transformation by photocatalysis. *Nature Reviews Materials* vol. 7 617–632 at https://doi.org/10.1038/s41578-022-00422-3 (2022).
232. Ardo, S. *et al.* Pathways to electrochemical solar-hydrogen technologies. *Energy Environ. Sci.* **11**, 2768–2783 (2018).
233. SASAKI, Y., IWASE, A., KATO, H. & KUDO, A. The effect of co-catalyst for Z-scheme photocatalysis systems with an Fe3+/Fe2+ electron mediator on overall water splitting under visible light irradiation. *J. Catal.* **259**, 133–137 (2008).
234. Kato, H., Sasaki, Y., Shirakura, N. & Kudo, A. Synthesis of highly active rhodium-doped $SrTiO_3$ powders in Z-scheme systems for visible-light-driven photocatalytic overall water splitting. *J. Mater. Chem. A* **1**, 12327 (2013).
235. Qi, Y. *et al.* Inhibiting competing reactions of iodate/iodide redox mediators by surface modification of photocatalysts to enable Z-scheme overall water splitting. *Appl. Catal. B Environ.* **224**, 579–585 (2018).
236. Bie, C., Wang, L. & Yu, J. Challenges for photocatalytic overall water splitting. *Chem* vol. 8 1567–1574 at https://doi.org/10.1016/j.chempr.2022.04.013 (2022).
237. Pinaud, B. A. *et al.* Technical and economic feasibility of centralized facilities for solar hydrogen production via photocatalysis and photoelectrochemistry. *Energy Environ. Sci.* **6**, 1983–2002 (2013).
238. James, B. D., Baum, G. N., Perez, J. & Baum, K. N. *Technoeconomic Analysis of Photoelectrochemical (PEC) Hydrogen Production*. (2009).
239. Wang, Q. *et al.* Particulate photocatalyst sheets based on carbon conductor layer for efficient Z-scheme pure-water splitting at ambient pressure. *J. Am. Chem. Soc.* (2017) doi:10.1021/jacs.6b12164.
240. Surendranath, Y., Bediako, D. K. & Nocera, D. G. Interplay of oxygen-evolution kinetics and photovoltaic power curves on the construction of artificial leaves. *Proc. Natl. Acad. Sci. U. S. A.* **109**, 15617–15621 (2012).
241. Seger, B., Hansen, O. & Vesborg, P. C. K. A Flexible Web-Based Approach to Modeling Tandem Photocatalytic Devices. *Sol. RRL* **1**, (2017).
242. Holmes-Gentle, I. & Hellgardt, K. A versatile open-source analysis of the limiting

efficiency of photo electrochemical water-splitting. *Sci. Rep.* **8**, (2018).

243. Beatty, M. E. S., Gillette, E. I., Haley, A. T. & Esposito, D. V. Controlling the Relative Fluxes of Protons and Oxygen to Electrocatalytic Buried Interfaces with Tunable Silicon Oxide Overlayers. *ACS Appl. Energy Mater.* **3**, 12338–12350 (2020).
244. NS. Curve intersections. at https://www.mathworks.com/matlabcentral/fileexchange/22441-curve-intersections (2022).
245. Esposito, D. V. Membrane-Coated Electrocatalysts - An Alternative Approach to Achieving Stable and Tunable Electrocatalysis. *ACS Catalysis* vol. 8 457–465 at https://doi.org/10.1021/acscatal.7b03374 (2018).
246. Gamry Instruments. *Faraday Cage: What Is It? How Does It Work?* https://www.gamry.com/application-notes/instrumentation/faraday-cage/ (2018).
247. Shah, A. A., Al-Fetlawi, H. & Walsh, F. C. Dynamic modelling of hydrogen evolution effects in the all-vanadium redox flow battery. *Electrochim. Acta* **55**, 1125–1139 (2010).
248. Proton Transfer Reactions. in *Lange's Handbook of Chemistry* (ed. Speight, J. G.) 1.350 (McGraw-Hill, 2005).
249. van Dongen, L. G. J. ., Jetten, M. S. M. & van Loosdrecht, M. C. M. Process description. in *The Combined Sharon/Anammox Process: A sustainable method for N-removal from sludge water* vol. 6 7–12 (2001).
250. Xie, G. J., Cai, C., Hu, S. & Yuan, Z. Complete nitrogen removal from synthetic anaerobic sludge digestion liquor through integrating anammox and denitrifying anaerobic methane oxidation in a membrane biofilm reactor. *Environ. Sci. Technol.* **51**, 819–827 (2017).
251. Shi, Y. *et al.* Nitrogen removal from wastewater by coupling anammox and methane-dependent denitrification in a membrane biofilm reactor. *Environ. Sci. Technol.* **47**, 11577–11583 (2013).
252. Trojanowicz, K. & Plaza, E. Combining numerical simulation with response surface modelling for optimization of reject water partial nitritation/anammox in moving bed biofilm reactor. *Environ. Technol. (United Kingdom)* **0**, 1–13 (2020).